Assessment and development of de-orbiting technology for nanosatellites

By

Nicole Andrea Driver-211038237

Thesis submitted in fulfilment of the requirements for the degree Master of Engineering in Mechanical Engineering in the Faculty of Engineering and the Built Environment at the Cape Peninsula University of Technology

Supervisor: Prof. Graeme John Oliver

Bellville

December 2019

DECLARATION

Cape Peninsula University of technology

I, Nicole Andrea Driver 211038237, declare that the contents of this dissertation/thesis represent my own unaided work, and that the dissertation/thesis has not previously been submitted for academic examination towards any qualification. Furthermore, it represents my own opinions and not necessarily those of the Cape Peninsula University of Technology.

Signed: Driver Date: 12/12/2019

ABSTRACT

The accumulating space debris has been a developing problem for many years. Technological advances led to the creation of nanosatellites, which allows more affordable access to space. As a result, the number of satellite launches is rapidly increasing, which, translates into an increase in debris in the low earth orbit (LEO) and geostationary orbit (GEO). To comply with the Inter-Agency Space Debris Coordination Committee (IADC) requirement of a 25-year maximum orbital lifetime, nanosatellites must have an end of life strategy. Failure to meet these guidelines may not only cause catastrophic collisions but may make future space travel even more challenging. Consequently, orbital lifetime predictions must be completed for nanosatellites. Considering this, the aim of this thesis is to investigate the orbital lifetime predictions for the nanosatellite ZACube-2, and the effects on the orbital lifetime if ZACube-2 is fitted with deorbiting technology, specifically a drag argumentation device. An in-depth literature review regarding the current state of technology pertaining to nanosatellite de-orbiting was conducted. This was followed by studies regarding orbital dynamics and perturbation forces. Four case studies were simulated in NASA's Debris assessment software (DAS 2.0) using orbital parameters extracted from the two-line element (TLE) file. General information such as launch date and final mass was provided by F'SATI. The Baseline case study presented the orbital lifetime of ZACube-2, without any drag enhancement device. This was followed by case study 1,2 and 3 which represented ZACube-2 when fitted with three different drag enhancement devices. A comparison study indicated a reduction in all three cases.

A new inflatable cube de-orbiting device (ICDD) concept was also presented, and the effects it has on the orbital lifetime predictions are showcased in case study three. Two deployment concepts were considered and evaluated against design requirements. Solidworks software was used to model the most suitable concept as well as perform finite element analysis on the structure. Static analysis was followed by natural frequency analysis in which the natural frequencies of the components and assembled structure were extracted. The Soyuz launch vehicle's sinusoidal testing requirements were used to evaluate the structures survivability under dynamic loading. Based on the finite element , and harmonic analysis it was concluded that the structures will survive the launch conditions of the Soyuz launch vehicle. Furthermore, individual parameters affecting orbital lifetime predictions are also identified, in the form of a mass and cross-sectional sensitivity study and a ballistic coefficient versus orbital time study.

Keywords

Nanosatellites, De-orbiting, Cube satellites, CubeSats, ZACube-2, Drag Augmentation Devices

ACKNOWLEDGEMENTS

I wish to sincerely thank:

- My supervisor Professor Graeme Oliver, thank you or your guidance and support.
- Professor Robert van Zyl, Director at F'SATI.
- PLMCC and F'SATI for providing the space and the equipment required to conduct this research.
- I would like to acknowledge my fellow students at F’SATI who supported me greatly and were always willing to help.

The financial assistance of the National Research Foundation towards this research is hereby acknowledged, through the F'SATI program. Opinions expressed in this thesis and the conclusions arrived at, are those of the author, and are not necessarily to be attributed to the National Research Foundation.

DEDICATION

Firstly, I would like to lovingly dedicate this research to my parents, Wilma, Cecil, and brother Cecil Jnr. Whom has supported, encouraged and believed in me every step of the way. Thank you for all the love and unwavering support and prayers throughout this journey. Thank you for giving me the drive and discipline to achieve my goals, for this I will be eternally grateful. Secondly, thank you to my extended family and friends who always had words of motivation and encouragement to offer.

Contents

DECLARATION ii

ABSTRACT iii

ACKNOWLEDGEMENTS iv

LIST OF FIGURES vi

LIST OF TABLES ix

LIST OF ABBREVIATIONS x

1 Introduction 1

- 1.1 Background 1
- 1.2 Research Aims and Objectives 2
- 1.3 Research Assumptions 3
- 1.4 Research Significance 3
- 1.5 Thesis Outline Structure 5

2 Literature Review and Problem Definition 7

- 2.1 Introduction 7
- 2.2 CubeSats 7
  - 2.2.1 CubeSat Overview 7
  - 2.2.2 CubeSat General Requirements 8
  - 2.2.3 CubeSat Dispenser System 9
- 2.3 Historical Perspective 10
  - 2.3.1 Kepler and Newton’s Revolutionary Theories 10
  - 2.3.2 Space Age 12
- 2.4 Space Debris Problem 13
  - 2.4.1 Concerns and Dangers due to Space Debris 15
  - 2.4.2 Mitigation Guidelines 18
- 2.5 Space Environment Conditions 19
  - 2.5.1 Radiation Environment 19
  - 2.5.2 Space Vacuum 20

2.5.3 Thermal Environment 20

2.6 Nanosatellite De-orbiting Technologies and Strategies....21

2.6.1 Method 1: Inflatable Drag Augmentation Devices 21

2.6.2 Method 2: De-orbiting Sail System 24

2.6.3 Method 3: Electrodynamic tethers (EDT)....26

2.6.4 Deorbiting method Evaluation Tool 29

2.7 Overview of DAS and STELA de-orbiting software packages....30

2.7.1 Debris Assessment Software (DAS 2.0)....30

2.7.2 The Semi-analytic Tool for End of Life Analysis software (STELA) 31

2.7.3 Comparison and evaluation of DAS and STELA 32

3 Orbital Mechanics 34

3.1 Introduction 34

3.2 Newton’s Laws of Motion and Gravitation (Equation of motion)....34

3.3 Kepler laws of planetary motion 35

3.4 Two-Body Problem....36

3.4.1 Two-body equation assumptions.....36

3.4.2 Equations of motion in an inertial frame 36

3.5 Kepler’s Equation 38

3.6 A solution to The Two-Body Equation of Motion 39

3.7 Position in Orbit....40

3.7.1 Maximum and Minimum Velocities in an Elliptical Orbit....40

3.8 Laws of Conservation....41

3.8.1 Mechanical Energy 41

3.8.2 Angular Momentum 42

3.9 Classical Orbital Elements 43

3.9.1 Semi-Major Axis 44

3.9.2 Eccentricity 44

3.9.3 Inclination 45

3.9.4 Right Ascension of the Ascending Node 45

3.9.5 Argument of Perigee..46

3.9.6 True Anomaly 46

3.10 Orbit Types 47

3.10.1 Low Earth Orbit (LEO)...47

3.10.2 Polar Orbit 47

3.10.3 Medium Earth Orbit (MEO)..47

3.10.4 Sun-Synchronous (SSO)..47

3.10.5 Geosynchronous Earth Orbit (GEO) 48

3.10.6 Geostationary Orbit 48

4 Orbital Perturbations..49

4.1 Orbital Perturbations 49

4.2 Third-Body Perturbation 50

4.3 Earth’s Oblateness..51

4.4 Oscillating and Mean Orbital Elements 52

4.5 Gravity Potential Theory..53

4.6 Solar Radiation Pressure 55

4.7 Atmospheric Drag 56

4.8 Atmospheric Density 57

4.8.1 Atmospheric Density Models..57

4.8.2 Jacchia-Roberts Model...57

4.8.3 Mass Spectrometer and Incoherent Scatter Model 58

4.8.4 Cosmos Satellite-Derived Density Model 58

4.8.5 Effects of Atmospheric Density Model on Orbital Lifetime Predictions. 58

4.9 NORAD Two-Line Elements Set 59

4.9.1 Two-Line Elements of ZACube-2 60

5 Software Simulation Environment..61

5.1 Introduction 61

5.2 DAS 2.0 Simulation Environment 61

5.3 Propagators used in DAS 2.0 62

5.4 Scientific Decimal time 62

5.5 Data Preparation for Orbital Lifetime Analysis Baseline Case 63

5.5.1 Data Preparation for ZACube-2 with no Drag Enhancement Device. . 64

5.5.2 Data Preparation for Case Study 1: Inflatable Pillow Device 64

5.5.3 Data Preparation for Case 2 Solar Sail 64

5.5.4 Data Preparation of Case Study 3: New Inflatable Cube Design Concept 64

6 Results and Discussion 65

6.1 Introduction 65

6.2 Orbital Lifetime Assessment Process 65

6.3 Simulation Results 66

6.3.1 Baseline Case: Orbital Lifetime Predictions for ZACube-2 with no Drag Enhancement Device 66

6.3.2 Case Study 1: Orbital lifetime Prediction for ZACube-2 with Inflatable Pillow Structure. 68

6.3.3 Case Study 2: Orbital Lifetime Predictions of ZACube-2 Fitted with a Drag Sail 70

6.3.4 Case Study 3: Orbital Lifetime Predictions of ZACube-2 Fitted with a 0.49m^2 cube concept 71

6.4 Mass Sensitivity Study 73

6.5 Cross-Sectional Area Analysis 74

6.6 Ballistic Coefficient vs Orbital Lifetime 74

6.7 Deployment Mechanism Concept Design 75

6.7.1 Concept 1: Deployment Using the mini frangibolts Actuator 75

6.7.2 Concept 2: Deployment Using Micro Latching Actuator 76

6.7.3 New Concept Evaluation 77

6.8 Overview of the New Inflatable Cube De-Orbiting Device (ICDD) Concept 78
6.8.1 Inflatable Cube Structure 79
6.8.2 Inflatable Cube Material Selection 80
6.8.3 Mass Analysis of the Inflatable Cube De-Orbiting Device Concept 81
6.8.4 Finite Element Analysis of the Housing 81
6.8.5 FEA Results Using Soyuz Rocket Longitudinal Static Load on the Housing 82
6.8.6 FEA Results Using Soyuz Rocket Lateral Static Load on the Housing 83
6.8.7 FEA Results Using Soyuz Rocket Longitudinal Static Load on the Lid 84
6.8.8 FEA Results Using Soyuz Rocket Lateral Static Load on the Lid 84
6.8.9 FEA Results Using Worst-Case Scenario Longitudinal Loading on the Housing 85
6.8.10 FEA Results Using Worst-Case Lateral Loading on the Housing 85
6.8.11 FEA Results Using Worst-Case Scenario Longitudinal Loading Conditions on the Lid 86
6.8.12 FEA Results Using Worst-Case Scenario Lateral Loading Conditions on the Lid 86
6.8.13 Summary of Longitudinal and Lateral FEA results 87
6.8.14 Location of De-orbiting Device and Fitment 87
6.8.15 Deployment sequence for De-orbiting Device 88
6.9 Discussion 89
6.9.1 Parameters Affecting the Orbital Lifetime. 90
6.9.2 Effects of Mass and Cross-sectional Sensitivity Study 90
6.9.3 Ballistic Coefficient (BC) 91
6.9.4 Inflatable Cube De-Orbiting Device Discussion 92
6.9.5 Modal and Harmonic Analysis Discussion 94
7 Conclusions and Recommendations 95

7.1 Overall Conclusion 95

7.1.1 Conclusion Summary 100

7.2 Recommendations and Further work 100

7.2.1 Deployment Mechanism 101

7.2.2 Inflatable Gas 101

7.2.3 Gas Cylinder Design...101

7.2.4 Concept Attitude Variation 102

8 REFERENCES 103

APPENDICES .... A

Appendix A Design Specification for a 3U CubeSat .... A

Appendix B Velocity Calculations at Perigee and Apogee for ZaCube-2............ B

Appendix C Change in velocity required to induce a decaying orbit for ZaCube-2 C

Appendix D Baseline Case Study Input Data .... D

Appendix E Case Study 1 Input Data .... F

Appendix F Case Study 2 Input Data .... H

Appendix G Case Study 3 Input Data .... J

Appendix H Ballistic Coefficient Calculations L

Appendix I Mass Sensitivity Study Data .... M

Appendix J Cross-sectional Area Analysis Data .... N

Appendix K Debris Mitigation Guidelines.. N

Appendix L Upilex-Ca Material Specifications... P

Appendix M Soyuz Rocket Sinusoidal Vibrations and g-loading range .... Q

Appendix N Perturbation included in DAS orbit propagators .... Q

Appendix O Modal and Harmonic Analysis .... R

LIST OF FIGURES

Figure 2.1: ZACube-1 on the left and ZACube-2 on the right 8
Figure 2.2: P-POD CubeSat Dispenser 9
Figure 2.3: Computer generated of orbital debris in LEO 14
Figure 2.4: LEO environment projection 15
Figure 2.5: Size of fragments and potential effects of space systems 16
Figure 2.6: Growth of fragments in earth’s environment 17
Figure 2.7 Inflatable device container 21
Figure 2.8: Pillow geometry 22
Figure 2.9: Inflated areocube-3 balloon on the left and inflation system on the right 22
Figure 2.10: GOLD system concept 23
Figure 2.11: Deployment sequence of the gossamer de-orbiting sail system 24
Figure 2.12: CanX-7 de-orbiting device 25
Figure 2.13: Engineering model prototype of the Terminator Tape module 26
Figure 2.14: Nanoterminator tape module fitted on a 1U CubeSat. 26
Figure 2.15: Performance predictions for Nanoterminator 27
Figure 2.16:Plasma brake concept 28
Figure 3.1: Kepler's first Law 35
Figure 3.2: Kepler’s Second Law 35
Figure 3.3:(a) Two masses in an inertial frame (b) Free-body diagram of the masses 36
Figure 3.4: Two body system representation 37
Figure 3.5: Eccentric anomaly 38
Figure 3.6: Orbital plane containing position and velocity vectors 43
Figure 3.7: Semi-Major Axis 44
Figure 3.8: Inclination 45
Figure 3.9: Right ascending node 45
Figure 3.10: Argument of perigee 46
Figure 3.11: True anomaly 46
Figure 3.12: Orbital types 48
Figure 4.1: Orbital element perturbation 50
Figure 4.2: Zonal harmonics 53
Figure 4.3: Orbital lifetime vs atmospheric model 58
Figure 4.4: Two-line elements 59

Figure 5.1:DAS main window 61
Figure 6.1: Orbital lifetime assessment process 65
Figure 6.2: ZACube-2 orbital lifetime prediction when fitted with no drag enhancement device 66
Figure 6.3: Graphical output for ZACube-2 orbital lifetime prediction with no drag enhancement device 67
Figure 6.4: Delta-V required for decaying orbit with area-to-mass of 0.008m^2 68
Figure 6.5: ZACube-2‘s orbital lifetime prediction when fitted with inflatable pillow structure 69
Figure 6.6: Graphical output of the orbital lifetime prediction of ZACube-2 with inflatable pillow structure 69
Figure 6.7: ZACube-2 orbital lifetime prediction when fitted with 10m^2 drag sail 70
Figure 6.8: Graphical output of the Orbital Lifetime Prediction of Zacube-2 when fitted with 10m^2 drag sail 71
Figure 6.9: ZACube-2 Orbital Lifetime Prediction when fitted with 0.49m^2 inflatable cube structure..72
Figure 6.10: Graphical output of the Orbital Lifetime Prediction of ZACube-2 when fitted with the new inflatable cube concept 0.49m^2 72
Figure 6.11: CubeSat Mass Variation study for ZACube-2.......................................73
Figure 6.12: Cross-Sectional Variation Study 74
Figure 6.13: Ballistic Coefficient vs Orbital Lifetime Predictions for Zacube-2...........74
Figure 6.14: Concept 1 75
Figure 6.15: Concept 2 76
Figure 6.16: New concept design 78
Figure 6.17: Inflatable cube concept deployed 79
Figure 6.18: von Mises stress on housing under longitudinal Soyuz launch conditions 82
Figure 6.19: Housing displacement under longitudinal Soyuz launch conditions 82
Figure 6.20: von Mises stress of housing under Soyuz lateral launch conditions......83
Figure 6.21: Housing displacement under Soyuz lateral launch conditions...............83
Figure 6.22: von Mises stress on lid (left) and displacement of lid (right) under Soyuz longitudinal launch conditions..84
Figure 6.23: von Mises stress on lid (left) and displacement of lid (right) under Soyuz lateral launch conditions 84

Figure 6.24: von Mises stress (left) and displacement (right) of housing under worst-case launch conditions 85
Figure 6.25: von Mises stress (left) and displacement (right) of housing under worst-case lateral launch conditions 85
Figure 6.26: von Mises stress (left) and displacement (right) of lid under worst-case longitudinal launch conditions...86
Figure 6.27: von Mises stress (left) and displacement (right) of lid under worst-case lateral launch conditions 86
Figure 6.28: Device location 87
Figure 6.29: Operational sequence of device 88
Figure 7.1: Deployment mechanism..101

LIST OF TABLES

Table 2:1 Advantages and disadvantages of method 1...23
Table 2:2: Advantages and disadvantages of de-orbiting method 2..........................25
Table 2:3: Advantages and disadvantages of method 3..28
Table 2:4: Concept considerations 29
Table 2:5: Concept evaluation..29
Table 2:6: Key differences between DAS and STELA...32
Table 5:1: Orbital parameters of ZACube-2...63
Table 5:2: General satellite information 63
Table 5:3: Baseline Case study...64
Table 5:4: Case study 1 64
Table 5:5: Case study 2 64
Table 5:6: Case study 3 64
Table 6:1: CubeSat mass variations...73
Table 6:2: Concept 1 advantages and disadvantages...76
Table 6:3: Concept 2 advantages and disadvantages...76
Table 6:4: Concept design requirements...77
Table 6:5: New concept elevation 77
Table 6:6: Mass analysis of the de-orbiting concept..81
Table 6:7: Launch Conditions for finite element analysis 81
Table 6:8: Summary of FEA results for longitudinal launch conditions......................87
Table 6:9: Summary of FEA results for lateral launch conditions 87

Table 6:10: Orbital lifetime predictions for each case study 89
Table 6:11: Estimated Orbital Lifetime Predictions...90
Table 6:12: Ballistic coefficients 91
Table 6:13: Preliminary design specifications...92
Table 6:14: Summary of Soyuz longitudinal loading FEA results 93
Table 6:15: Summary of Soyuz lateral Load FEA results 93
Table 6:16: Summary of worst-case longitudinal load FEA results............................93
Table 6:17: Summary Worst case lateral FEA results 93
Table 6:18: Summary of maximum and minimum natural frequencies......................94

LIST OF ABBREVIATIONS

ADR Active Debris Removal

BET Bare Electrodynamic Tethers

BNSC British National Space Centre British National Space Centre

CDS CubeSat Design Specification

CPUT Cape Peninsula University of Technology

DAD Drag Augmentation Devices

DAS Debris Assessment Software

ESA European Space Agency

FSATI French South African Institute of technology

FSOA French Space Operations Act
GEO Geostationary Orbit

GMAT General mission analysis tool

GTO Geosynchronous Transfer Orbit

IADC Inter-Agency Space Debris Coordination Committee

LEO Low Earth Orbit

NASA National Aeronautics and Space Administration

NOAA The National Oceanic and Atmospheric Administration

P-POD Poly Picosatellite Orbital Deployer

SSN space surveillance network

STELA Semi-analytic Tool for End of Life Analysis

STK Systems Tool Kit

Chapter one

1 Introduction

1.1 Background

The human fascination with space and space exploration dates back to the 16th century when astronomer, Galileo Galilei completed the first-ever telescopic observation of the night sky (Zanatta et al., 2017). This insatiable fascination led to the development of Sputnik 1 by the Soviet Union, which was successfully launched on the 4th of October 1957 (Kuznetsov, Sinelnikov and Alpert, 2016).

Ever since then, the amount of spacefaring countries and countries capable of launching their own satellites into orbit has increased dramatically. Consequently, the increase in spacecraft launches led to the creation of debris in space, caused by, discarded upper stages of rockets, dead satellites and accidental explosions (Sylvestrea and Ramakrishna Parama, 2017).

The accumulating man-made debris was not given much thought over the years, even though NASA scientists D. J. Kessler and B. G. Cour-Palais predicted that the debris density would be so widespread that accidental satellite collision would develop into a new source of debris generation. (Kessler and Cour-Palais, 1978).

This prediction was ignored until 1995 when the international Academy of Astronautics (IAA) issued the world’s first comprehensive set of orbital debris mitigation guidelines (National Aeronautics and Space Administration, 2012).This was followed by the establishment of the Inter-Agency Space Debris Coordination Committee (IADC) in 2002, which included the space agencies of twelve countries (National Aeronautics and Space Administration, 2012) .

Together they implemented guidelines intended to lessen the growth of the orbital debris (National Aeronautics and Space Administration, 2012). In these guidelines, they demand the removal of any spacecraft in the protected regions known as the Low Earth Orbit (LEO) and Geostationary Earth Orbit (GEO) (IADC, 2007) regions within 25 years after the end of operations (Aerospace Corporation, 2015).

As technology advanced, space exploration became more accessible to private companies and universities. This, in turn, led to the development of nanosatellites , more specifically the

CubeSat (Alanazi and Straub, 2019). Specifications for the CubeSat was developed in 1999 by California Polytechnic State University and Stanford University (Cal Ploy Rev 13, 2017). By creating these standards, it not only allowed students to learn more about space but also unlocked a less expensive way to explore space as well as test and develop new technologies (CubeSat Launch Initiative, 2017). Most nanosatellites are not fitted with a de-orbiting device due to space and weight limitations (Inamori et al., 2015), thus when they become non-operational it results in and increases the space debris.

It is imperative that the nanosatellites that are yet to be launched can be taken out of orbit, once the mission is completed, to reduce the risk of collision and debris generation.

1.2 Research Aims and Objectives

The aim of this research is to simulate and analyse various drag augmentation devices, suitable to deorbit a nanosatellite such as ZACube-2. Therefore, for simplicity reasons the orbital parameters of ZACube-2 will be used during simulations which will be obtained from spacetrack.com. Multiple surveys will be flown by means of software simulations and are thus the primary method of testing and analysing the de-orbiting of a nanosatellite. Parameters such as a change in velocity ($\triangle V$) aerodynamic drag, zonal harmonics, and the earth’s oblateness will be included in the model. Orbital simulation Software such as STK (systems tool kit), GMAT (General mission analysis tool), STELA (Semi-analytic Tool for End of Life Analysis) and Debris Assessment Software (DAS) will be used to perform the simulations.

The research objectives are:

- In-depth and compressive literature review of the current state of technology regarding passive nanosatellite de-orbiting devices.
- The orbital parameters of ZACube-2 will be modelled and simulated in one of the previously mentioned software.
- Execute Orbital decay prediction simulation for ZACube-2 with various de-orbiting devices.
- Evaluate the performance of each de-orbiting device.
- Identify parameters affecting the orbital lifetime.
- Based on data generated from simulations studies and analysis, recommend a concept capable of de-orbiting a nanosatellite within 25 years.

The first objective is crucial since it encompasses an in-depth investigation of the current state of technology, and in doing so creates a foundation of knowledge needed to achieve the remaining objectives. The second and third objective involves applying the knowledge gained from the literature review, to model the orbital parameters for ZACube-2 and execute orbital lifetime predictions. The data generated during these simulations will be recorded and analysed and used to achieve the fourth and fifth objectives. Finally, the sixth objective will be based on the prior objectives and entails the culmination of the knowledge and understanding gained, during the literature review and data produced by the simulations and analysis.

To minimize orbital debris, The Inter-Agency Space Debris Coordination Committee (IADC) proposed a 25-year maximum orbital lifetime limit for orbiting spacecraft and their associated hardware (Aerospace Corporation, 2015). Due to these specified limits, and the projected increase of nanosatellites / CubeSats in space, de-orbiting technology which primarily focuses on de-orbiting of nanosatellites, needs to be investigated.

1.3 Research Assumptions

During this research, the following assumptions will be made.

- Presently ZACube-2 has a final mass of 3.8kg, without a de-orbiting device fitted . The maximum allowable mass according to cube satellites standards is 4kg. Thus, during de-orbiting simulations it will be assumed that the mass will remain constant even if a de-orbiting device is fitted to the 3U satellite . The motivation behind this , is that when the fitment of de-orbiting devices becomes one of the major payloads, it will be prioritized accordingly whilst remaining within the mass limitations.

- The effects of space weather will not affect the mass of ZACube-2. Therefore, it will remain at 3.8kg after launch

1.4 Research Significance

The accumulating space debris has been a developing problem for many years. The urgency of this problem was predicted in 1978 by NASA scientists D. J. Kessler and B. G. Cour-Palais but, was ignored until 1995. To mitigate the debris, build up in LEO and GEO mitigation guidelines were formed by NASA and IADC, which requires the removal of satellites from these regions within 25 years after end of life operation (Aerospace Corporation, 2015).

Failure to meet these guidelines may not only cause catastrophic collisions such as the 2009 collision between Iridium 33 and Cosmos-2251 satellites (Aerospace Corporation, 2015) but, may make future space travel even more challenging, given that the spacecraft will require the ability to navigate through a blanket of debris. Technological advances allowed for the creation of nanosatellites , and since the number of launches is rapidly increasing

(Aerospace Corporation, 2015), it may increase the debris in the protected areas. With this influx comes a greater chance of collision between satellites.

Therefore, this research will make a significant contribution towards the mitigation of space debris by focusing on the end of life operation of nanosatellites, and in doing so aims to lower the collision probability in low earth orbit. Furthermore, it will also initiate and encourage further investigation regarding space debris mitigation methods.

1.5 Thesis Outline Structure

In this chapter, the outline structure of the thesis is briefly discussed under the chapter headings

Chapter1 – Introduction

This chapter provides the reader with background information pertaining to the accumulation of space debris. It also discusses the research aims and objectives. The assumptions made during this research are also included as well as the research significance.

Chapter 2 - Literature review

This chapter begins by giving the reader a brief overview of cube satellites. To create a broader perspective, historical aspects relating to the development of satellites is also discussed. This is followed by a discussion of the space debris problem and mitigation guidelines. The harsh space environment and the effects it has on the satellite systems are also included in this chapter. Lastly, having gained the perspective and knowledge required to mindfully discuss the state of technology regarding passive de-orbiting devices, an in-depth literature review is discussed. Primarily focusing on how de-orbiting was achieved, and the methods and tools used to model the decaying orbit of nanosatellites.

Chapter 3 – Orbital mechanics

This chapter extensively covers the theoretical background needed to understand orbital mechanics. Amongst others, Newtonian laws and Kepler's laws of planetary motion are discussed in this chapter.

Chapter 4 - Orbital perturbations

The perturbation forces experienced by the CubeSats are presented in this chapter. The distinction is made between gravitational forces and non-gravitational forces. This is followed by a discussion relating to the effects these forces have on the orbital decay rate of the satellite.

Chapter 5 - Software simulation environment

This chapter familiarises the reader with the DAS 2.0 software and simulation environment. An overview of the software and why it was selected is explained. This is followed by an explanation regarding the graphical user interface (GUI) of the software and the input files required from the user. Furthermore, the data preparation for each case study is also discussed and presented in this chapter.

Chapter 6 - Results and discussion

The data generated regarding the orbital lifetime estimation for ZACube-2 are presented and discussed in this chapter. Four different scenarios were simulated. The baseline case study presents the orbital lifetime of ZACube-2, without any drag enhancement devices. While Case studies 1,2 and 3 represents ZACube-2 when fitted with three different drag enhancement devices. Two new concepts were discussed and compared, and the best concept was identified using a concept evaluation tool. Finite element, natural frequency and harmonic analysis was performed on the best suited concept.

Chapter 7 - Conclusions and recommendations

The final conclusions regarding the orbital lifetime predictions for ZACube-2 with and without a drag device are elaborated on in this chapter. Conclusions regarding the finite element analysis and modal analysis are also presented in this chapter. This is followed by recommendations and further work

.

Chapter 2

2 Literature Review and Problem Definition

2.1 Introduction

Having established in the previous section that, the launch of nanosatellites is set to increase and given the fact that the IADC requires a de-orbiting strategy. Various technologies for Nanosatellite de-orbiting have already been researched. These technologies can be categorized into two groups, passive, and active technologies. Passive technologies such as drag augmentation devices (DADs) increases the aerodynamic drag experienced by the satellite to achieve de-orbiting. Electrodynamic tethers (EDT) are a second form of passive de-orbiting. It encompasses the tethering of a charged wire or tape that generates electrodynamic drag forces upon interaction with flowing plasma found in earth's atmosphere and simultaneously increases aerodynamic drag. Whereas, active technologies use high velocity chemical expulsion to achieve de-orbiting.

Active technologies fall out of the scope of this study; thus, the literature review will only cover the research done regarding passive de-orbiting technologies. The primary focus will be on how de-orbiting was achieved, the methods and tools used to simulate de-orbiting and the advantages and disadvantages of each concept. In order to gain the knowledge required to mindfully discuss the literature review, a brief overview of the historical aspects relating to the creation of satellites will be discussed. Furthermore, CubeSats will be discussed as well as, the current space debris problem and its associated mitigation guidelines will be introduced.

2.2 CubeSats

2.2.1 CubeSat Overview

For a long period of time, space exploration has always been associated with extremely high risk and high costs, consequently, the only entities that were able to successfully explore space, were government space agencies such as Roscosmos and NASA. Roscosmos, successfully launched the world's first satellite known as, Sputnik 1, which was followed by NASA's Explorer 1. Satellites are typically imagined to be massive structures that take millions of dollars to produce and maintain. However, as time advanced, so did the space technology, which many years later, led to the development of nanosatellites. This new way of thinking in terms of satellite design gave way to a more accessible, affordable and more sustainable way of building satellites. This in turn led to the creation of the CubeSat, which falls in the class of nanosatellites. CubeSats are available in various sizes. Each size is based on the standard CubeSat "Unit" referred to as a 1U.

The decreased costs associated, with CubeSats, are due to the standardization of the dimensions. A 1U CubeSat was standardized as a 10cm cube with the approximate mass of 1 to 1.33kg, by California Polytechnic State University and Stanford University (Cal Poly, 2009). Thus, by standardizing the dimensions and weight of the CubeSat, it allowed the satellites to be launched as a secondary payload on launch vehicles. In addition to this, it also led to the establishment of the CubeSat program, which allows private companies and educational institutions to design, develop, launch and operate satellites with a significantly smaller budget, in comparison to that of massive and complex satellites. This standardization had such a ripple effect on universities worldwide that, on the 21st of November 2013, F'SATI together with CPUT became the first to launch and operate Africa's first nanosatellite seen on the right of figure 1 below. Following the success of ZACube-1, FSATI continued their success by developing a 3U CubeSat, which was launched on the 27th of December 2018. ZACube-2 can be seen on the left of Figure 2.1

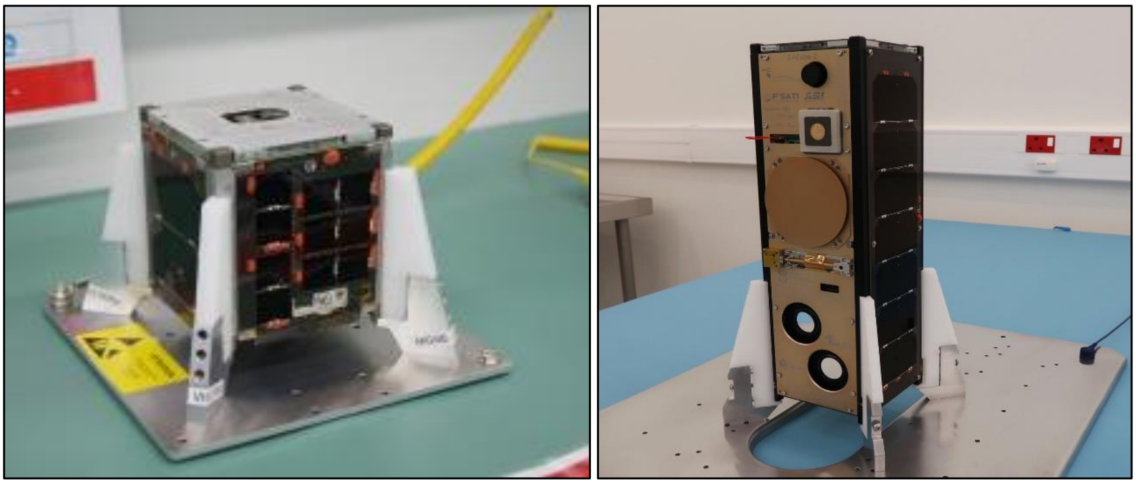

Figure 2.1: ZACube-1 on the left and ZACube-2 on the right
(Adapted from De Villiers and Van Zyl, 2015)

2.2.2 CubeSat General Requirements

The general requirements regarding the design of cube satellites are stipulated in the CubeSat Design Specification (CDS) document. It addresses various aspect of the design requirements, which includes mechanical requirements, electrical requirements and operational requirements. Additionally, it also includes testing requirements. For a more in-depth discussion regarding all the requirements for a CubeSat, the CDS document should be consulted.

2.2.3 CubeSat Dispenser System

The Poly Picosatellite Orbital Deployer (P-POD) shown in Figure 2.2 is Cal Poly's standardized CubeSat deployment system. This was designed in conjunction with the CubeSat and can hold three 1U CubeSats. It also serves as an interface between the launch vehicle and CubeSats. The P-POD has a rectangular shape with a door and spring mechanism. The CubeSats are deployed when the release mechanism is activated via a signal sent from the launch vehicle. A set of torsion springs at the door hinge, forces the door open, followed by the deployment of the CubeSats. When designing a CubeSat, the CDS document should constantly be consulted. This should especially be focused on when designing new components for a CubeSat.

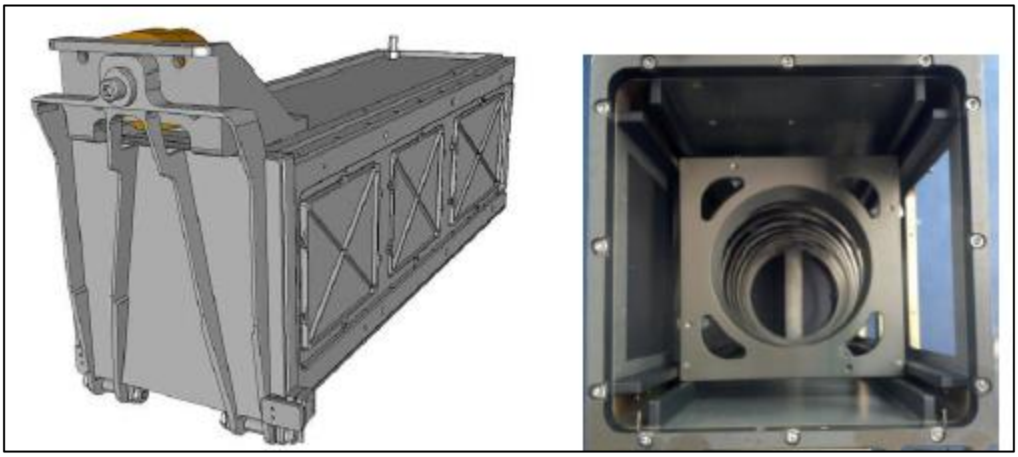

Figure 2.2: P-POD CubeSat Dispenser

(Adapted from Cal Poly Rev 13, 2017)

2.3 Historical Perspective

Since the beginning of time, mankind has consistently been fascinated with understanding the unknown. To better understand our place in the vast universe, we have looked to the night sky, seeking answers to questions like, where do we come from? Where do we fit in? And are we alone? (National Aeronautics and Space Administration, 2004).

History shows us, that efforts to answer these questions date back to an ancient Greek mathematician and astronomer, Claudius Ptolemy (90-168 AD) who led the world to believe that the earth is motionless and is the centre of the universe. This model was known as the geocentric model. Although his model was incorrect, it aided fellow astronomer Nicolaus Copernicus with his proposed theory in the 16th century, that the earth is in fact not the centre of the universe, but rather the sun, and that the planets orbits around the sun in a circular manner (Coyne, 2006).

Even though Copernicus's theory was not fully correct, it ultimately changed the way the science community perceived the solar system. This change in perception was the stepping stones for Tycho Brahe, Johannes Kepler, Galileo Galilei, and Isaac Newton. These astronomers saw the significance of the work done by their predecessors and used it to form new theories to describe the motion of the planets. An in-depth discussion regarding these laws will be covered in chapter 3 under the heading theoretical background.

2.3.1 Kepler and Newton's Revolutionary Theories

Johannes Kepler (1571-1630) is known amongst the scientific community as the founder of celestial mechanics. In a time that was reluctant to change, he fortified and altered the Copernican view of the solar system. Kepler worked on the orbit of Mars, which at the time was known as the Martian problem.

Astronomers had been struggling to explain why Mars appears to move backward in the night sky. Using observations done by Brahe, Kepler deduced that the planets move in an elliptically shaped orbit, with the sun at one of the foci. This discovery is known as Kepler's first law (Horvathy, 2014).

Kepler continued his quest to better understand the motion of the planets and struggled with the change in velocities of the planets. However, he realized that the planets experience an increase in velocity when it is closer to the sun and decrease velocity when it is further from the sun. This together with the realization that the planets travel in an ellipsis, he concluded that a line from the sun to the planet sweeps out equal areas in equal times (Horvathy, 2014). This is known as Kepler's second law, which he published together with his first law in

1609 Kepler’s third law was published a decade later in 1619. With this law, he determined that “The squares of the periodic times are to each other as the cubes of the mean distances.” (Horvathy, 2014) .More simply put, he recognized the relationship between the periods of two planets and the time they needed to orbit the sun, are related to their distance from the sun.

Kepler had made astonishing breakthroughs regarding the motions of the planets; however, his laws were merely a description of the planetary motion and did not explain the forces causing the motion. This posed a new problem, which was finding and quantifying the forces causing the motion.

Isaac Newton (1642-1727) solved this problem by developing his three laws of motion and the Universal law of gravitation. Newton’s first law states that “A body at rest will remain at rest, and a body in motion will remain in motion unless it is acted upon by an external force." In other words, a body cannot stop, move or change direction without an external force acting on it. The second law states that “The force acting on an object is equal to the mass of that object times its acceleration.”

This law describes what happens to an object when an external force is acting on it. Lastly, the third law of motions states that “For every action, there is an equal and opposite reaction.” This law describes what happens to an object when it exerts a force on another object.

Using these laws, Newton derived the universal law of gravity. He found that as two bodies move farther away from one another, the gravitational force between them decreases by the inverse of the square of the distance.

These laws were published in 1987 in “Mathematical Principles of Natural Philosophy” more commonly known as Principia (Peter Dourmashkin, 2012). They have stood the test of time and have been tested multiple times over the past three centuries and is the bedrock of classical mechanics

2.3.2 Space Age

As time advanced, so did the humans view of the universe. Centuries after the discoveries by iconic scientists such as Kepler and Newton, the human curiosity regarding space and space exploration reached new heights. On October 4th, 1957, the Soviet Union successfully launched the world's first satellite, famously known as, Sputnik 1. This monumental event marked the beginning of the space age and the race to space (NASA, 2015).

On January 31st, 1958, America retaliated by launching Explorer 1. In contrast to Sputnik 1, which only had a radio transmitter on board, Explorer 1 was fitted with a cosmic ray and Micrometeorite detector, which led to the discovery of the Van Allen radiation belt (O'Donnell, 2007)

This was then followed by a joint venture between Great Britain and America who launched, the first British satellite known as Arial 1 in 1962 (UK Space Agency, 2012). Canada was the fourth country to join the race with the launch of their Alouette I, which was launched on September 29th, 1962 (Science, 2012).

These were some of the breakthroughs that propelled the space age to such an effect that many nations were able to launch probes and in some cases humans into space. Currently, the biggest satellite orbiting the earth is the International space station (ISS). It is a testament to how far we have come since the beginning of the space age. Advances in telemetry technology allow us to communicate and relay information to and from satellites.

The Minimization of electronic components led to the development of smaller, less expensive satellites such as nanosatellites. These technological advances allowed more nations to design and manufacture complex satellites, and thus led to an increase in satellite launches. Although all these breakthroughs allow us to learn more about ourselves and gets us closer to find answers to question about the vast universe.

It is important to keep in mind that we have been sending objects into earth's atmosphere since 1957. This means that many of the old satellites are not- functional and are creating a debris problem around planet earth, and if left unchecked could cause major problems for future space exploration missions.

2.4 Space Debris Problem

The term “space debris” can be defined as any man-made object orbiting Earth which is no longer operational (Sylvestrea and Ramakrishna Parama, 2017). Since Sputnik 1 was the first satellite to orbit the earth, it is easy to assume that, it also began the generation of the space debris. However, this assumption would be incorrect.

After Sputnik’s launch in 1957, its core launch rocket remained in orbit for 90 days, after which it burnt up on re-entry to earth atmosphere .Similarly, the satellite itself burned up on re-entry a month later (Hall, 2014).

The Momentous problem we now face begun soon after the launch of American satellite Vanguard 1. It was launched into Medium Earth Orbit (MEO) in March 1958 and became non-functional in 1964 (Hall, 2014). This satellite is expected to remain in orbit for almost 200 years, and essentially marks the beginning of the space debris problem.

The space debris problem and effects of it were predicted as early as 1978 by NASA scientist D.J. Kessler and B.G Cour-Palais. They concluded that around the year 2000, the population of the catalogued debris would be so dense that, collisional breakups of satellites would become a new source of additional debris (Kessler and Cour-Palais, 1978).

Sixty years later we find ourselves in the situation exactly as predicted. Increased satellite launches and the lack of de-orbiting strategies, translated in an unregulated debris growth. We have since realized that the problem should urgently be addressed.

Orbital fragments are being tracked and catalogues by the space surveillance network (SSN). Currently, it is estimated that 500,000 pieces of fragmented debris are found in Low Earth Orbit (LEO) (Aerospace Corporation, 2015). The density of the debris in LEO can be seen in Figure 2.3

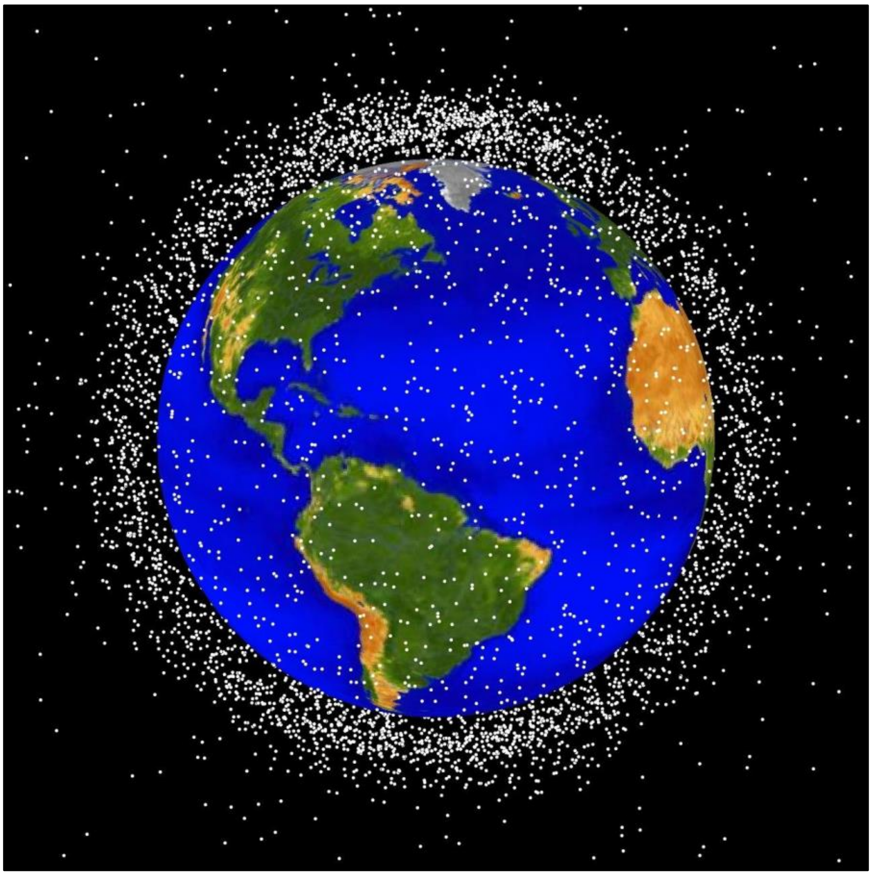

Figure 2.3: Computer generated of orbital debris in LEO

(Adapted from Garcia, 2015)

The problem we face with the orbital debris is indeed a unique one. Besides the fact that it has a regenerative component and is thus, set to increase even if we stop all launches. It is a problem that directly affects all space fairing countries. Because the debris comes in various shape and sizes the damage, they can cause, can be catastrophic. Some fragments in LEO can have a velocity of up to 14 kilometres per second, which translates into 50400 kilometres per hour (Aerospace Corporation, 2015). At these kinds of velocities, the dangers to the satellite systems are clear. Since we are an ever-evolving species it is safe to assume that we will not decrease our satellite launch rate.

Apart from the fact, that satellites now form such an integral part of society, it also enables us to answer the age-old questions through space-based research. Thus, if we do nothing to fix the growing debris future space travel will become even more challenging. In the past satellite designs were more focused on how to withstand the space environment, such as extreme temperature change, and in retrospect this now seems simple. Now, however, we will need to design space systems able to navigate through the cloud of debris and to be able to withstand multiple collisions at momentous speeds. Thus, leaving the space debris unchecked will make future space travel and even higher mountain to conquer. A study conducted by the National Aeronautics Space Administration (NASA) LEGEND (LEO-to-GEO Environmental Debris model) predicted a non-linear growth of objects for the LEO region with no mitigation measures (NASA, 2007). This can be seen in Figure 2.4. It was concluded that, to stabilise the growth, mitigation guidelines must be followed and active debris removal (ADR) will be required.

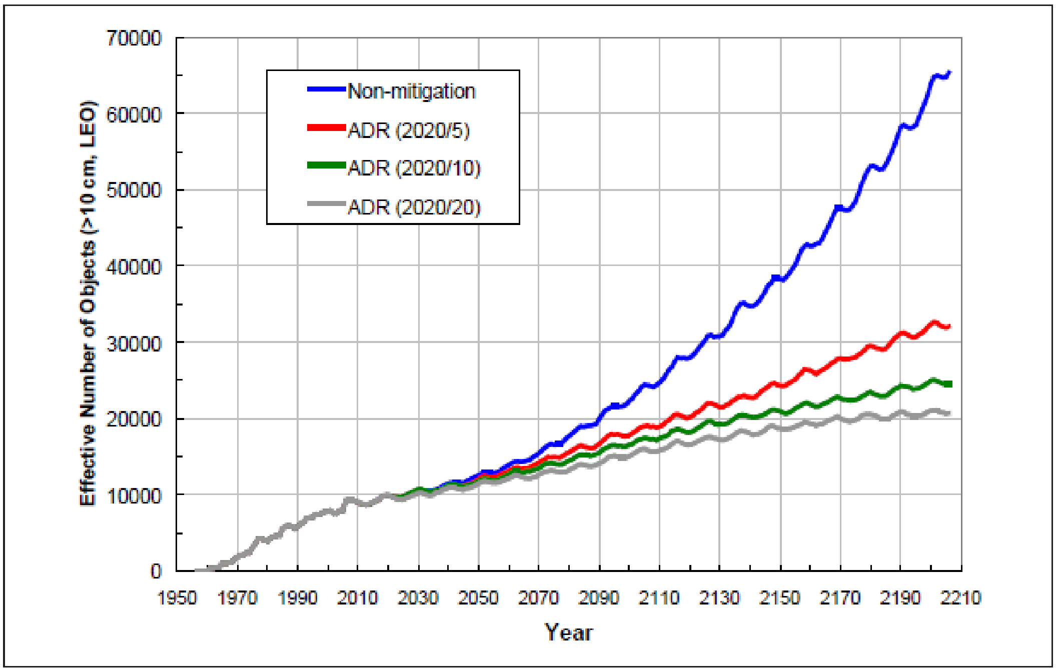

Figure 2.4: LEO environment projection

(Adapted from NASA, 2007)

2.4.1 Concerns and Dangers due to Space Debris

The greatest contribution to the debris is due to collisions and explosions of rockets and satellites (Aerospace Corporation, 2015). In some cases, these events are deliberate and in other cases accidental. An example of intentional satellite destruction is the Fengyun-1C weather satellite on January 11, 2007. As part of the anti-satellite test, the Chinese launched an anti-satellite device (ASAT) to destroy a weather satellite that has been in orbit since May 10th, 1999.

This single event added 3300 fragments (Aerospace Corporation, 2015) to the cloud of debris around the earth. Furthermore, the anti-satellite test numerically speaking, increased the number of catalogued orbital debris by an amount equivalent to the previous 14 years of space activity (Pardini and Anselmo, 2007).

In addition, an accidental collision between Iridium 33 and Cosmos 2251 on February 10th, 2009, added another 2200 fragments of debris. Destruction of rockets and satellites creates fragmentation in various sizes which moves at various velocities. Some of these fragments are catalogued by the Space Surveillance Network (SSN) seen in Figure 2.5 below.

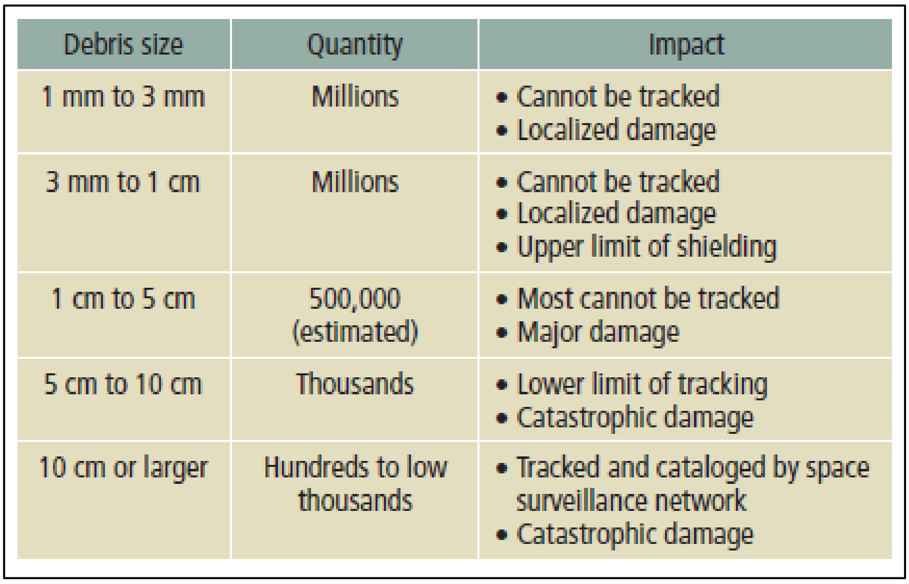

Debris size	Quantity	Impact
1 mm to 3 mm	Millions	• Cannot be tracked • Localized damage
3 mm to 1 cm	Millions	• Cannot be tracked • Localized damage • Upper limit of shielding
1 cm to 5 cm	500,000 (estimated)	• Most cannot be tracked • Major damage
5 cm to 10 cm	Thousands	• Lower limit of tracking • Catastrophic damage
10 cm or larger	Hundreds to low thousands	• Tracked and cataloged by space surveillance network • Catastrophic damage

Figure 2.5: Size of fragments and potential effects of space systems

(Adapted from Aerospace Corporation, 2015)

Unregulated practices, such as the relinquishment of spent rockets and defunct satellites after their operational lifetime, are also a major contributor to the debris. Technological advances allow for an increased number of launches.

Failure to have a safe de-orbiting strategy that does not produce more fragments will result in the dramatic growth of the already growing debris. The growth trend can be seen in Figure 2.6. From this, it is obvious that fragments will increase with time.

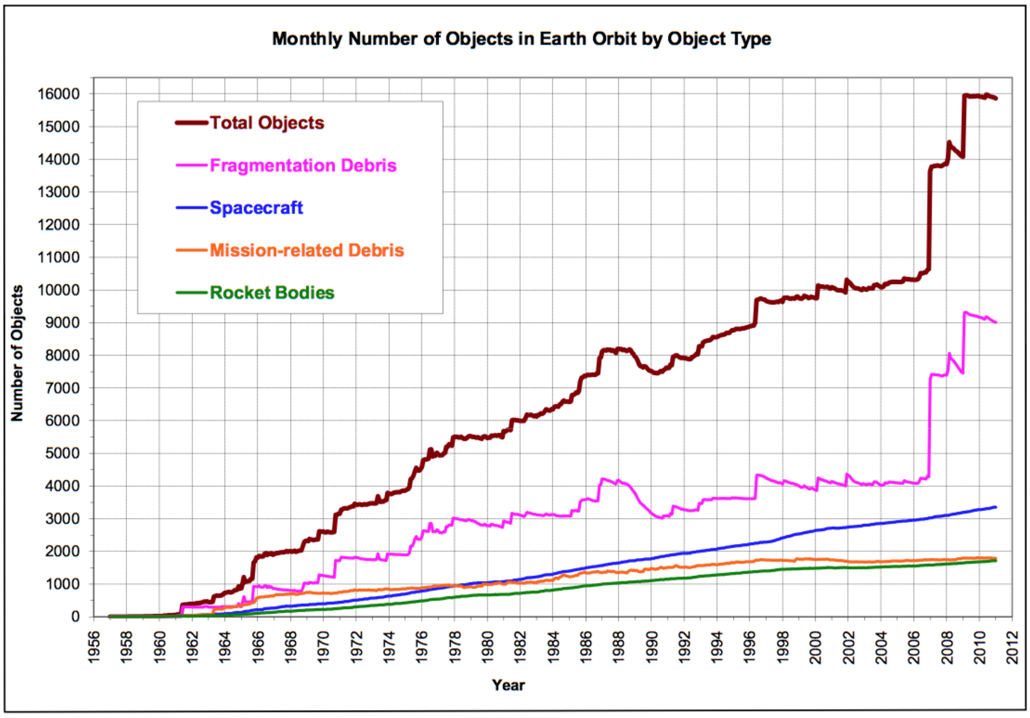

Figure 2.6: Growth of fragments in earth's environment

(Adapted from William Salter, 2015)

If we fail to recognize the urgency of this problem and continue to launch satellites at the current rate, collisions will become a regular occurrence. This poses a direct threat to the ISS and the astronauts on board. It makes spacewalk even more hazardous since the space suites must be able to withstand collisions with fragments.

Furthermore, if the number of fragments is doubled, it will increase collision risk by nearly four times. If no serious action is taken, then in the end, the existing debris will collide with other fragments, and may result in a blanket if small debris fragments orbiting earth.

This self--sustained process, which is particularly critical for the LEO region, is known as the 'Kessler syndrome' (Kessler, Johnson and Matney, 2000). It must be avoided by way of mitigation and remediation measures on an international scale.

2.4.2 Mitigation Guidelines

International space law governs human activities in space. This was established by the united nation outer space treaty in 1967 (Parliament office of science and technology, 2010). However, the treaty was written long before the aerospace community realized that the debris population would become a problem.

Therefore, it did not contain specific debris mitigation or remediation guidelines. The Treaty states that space exploration shall be conducted to avoid “harmful contamination” and should adopt “appropriate measures” to ensure this, but it does not define these terms.

Decades later, it has been established that the growing debris population is a major concern for all space-faring nations. Currently, low earth orbit is the most density populated orbital band. To control the growing debris, various debris mediation organisations have been established.

The U.S government, National Aeronautics and Space Administration (NASA), the Inter-Agency Space Debris Coordination Committee (IADC), the UN Committee on the Peaceful Uses of Outer Space COPUOS) are a few examples of such organisations. Each of the above-mentioned organisations has set out guidelines to address growing debris. A summary of the guideline can be found the appendices section.

Although some guidelines are more extensive than others, they are all in agreement that the growth of the debris must be stopped, or at the very least slowed down.

Technologies addressing de-orbiting will be investigated in the next section. The primary focus will be on strategies and devices suitable for nanosatellites more specifically 3U CubeSats.

2.5 Space Environment Conditions

The space environment can be defined as the region above the earth’s atmosphere. It is harsh, unforgiving and is nothing like the environment we experience on earth. Earth is covered in a blanket of gasses that not only contains the air that we breathe but also protects us from the harsh elements of space. The space environment can be divided into two sections, near-earth, and deep space environment. The near-earth space environment consists of the earth’s upper atmosphere, ionosphere, radiation belts, and magnetosphere. Deep space includes the heliosphere and small body regions (Wertz, 1999a).

Since CubeSats currently only operate in Low Earth Orbit, the deep space environment will be neglected. The following section will investigate some of the elements that the CubeSat will be exposed to in the near-earth space environment. These include electromagnetic radiation, charged particles, space vacuum, and thermal cycling. These elements also affect the performance of the satellite and should thus be kept in mind when designing new satellite components.

2.5.1 Radiation Environment

Trapped electrons, protons, heavy ions, plasma, and cosmic ray particles are all found in the radiation environment. When these particles hit the sensitive microelectronics, they affect the performance and, in some cases, affect the functionality of the satellite. The radiation environment that may damage the satellite’s electronics are categorized into two groups transient particles and trapped particles (Barth, Isaacs and Poivey, 1999)

The trapped electrons have energies up to 10 Mega-electron volts (MeV) and the trapped protons and heavy ions hundreds of (MEV) (Barth, Isaacs and Poivey, 1999). Galactic cosmic rays (GCR) are also of concern for satellite electronics. Galactic Cosmic Rays (GCR) are high energy particles. GCR consists of 83% hydrogen (protons) 13.72% alpha particles, 2% electrons and 0.98% heavier nuclei with energy ranges from few MeV/nucleon to approximately 1015 MeV/nucleon (Sokeng Ifriky Tadadjeu and Shane Martin, 2017). These particles can pass through or stop in satellite systems, sometimes depositing enough energy which causes errors or damage in spacecraft electronics and systems (Wertz, 1999a)Examples of these errors/damages are deterioration from Total ionizing dose (TID), deterioration from Non-ionizing energy loss (NIEL) and Single event effects (SEE) (Barth, Isaacs and Poivey, 1999). Some of the effects can be lessened and, in some cases, prevented by shielding methods.

2.5.2 Space Vacuum

Space is considered a hard vacuum, meaning that it has extremely low pressure. The vacuum pressure range surrounding earth ranges from $1.3*10^{-7}$ kPa at 200km to as little as $1.3*10^{-12}$ kPa at 6500Km (Boudjemai, Hocine, and Guerionne, 2015). This environment creates potential problems for satellites such as out-gassing and cold welding. Out-gassing occurs when trapped gas in the satellite material begin to escape. This can lead to damaged sensors and components. Thus, this should be considered in the material selection process. The chances of a material out-gassing can be lowered baking it in a thermal vacuum chamber before sending the satellite into space.

Cold welding normally occurs when mechanical parts are too close together. When the satellite is on earth the components are separated by a thin layer of air between them. However, when the satellite is released in space the vacuum effectively removes the layer between the components, causing it to be welled together (Jon Sellers et al., 2004). To undo the welding, the ground controllers expose some part of the satellite to the sun while keeping the rest in shade. This causes the materials to expand and contract and may undo the welding.

2.5.3 Thermal Environment

In the absence of atmosphere in space, thermal energy can only be transferred through conduction and radiation with temperatures ranging, from -160ºC to +180ºC (Boudjemai, Hocine, and Guerionne, 2015). It is also possible that heat may be conducted by the on-board components of the satellite. Thermal energy from the sun comes in the form of radiation. The radiation from the sun is the main source of heating that the satellite experiences. The intensity of the radiation also depends on the satellites distance from the sun and seasonal changes such as winter and summer solstice. Thermal changes affect the structural integrity of CubeSats and should be considered during the design process.

2.6 Nanosatellite De-orbiting Technologies and Strategies

The establishment of debris mitigation guidelines and remediation strategies increased the awareness of the space-faring nations and thus resulted in the design and in some cases the development of de-orbiting devices. Nanosatellites are designed and build on a small budget in comparison to the bigger more complex satellites. Thus, the focus of this study will be on passive methods of de-orbiting.

2.6.1 Method 1: Inflatable Drag Augmentation Devices

Inflatable drag augmentation devices utilize aerodynamic drag to achieve de-orbiting. This method does not involve the discharge of propellant into space and is therefore deemed as a passive method of de-orbiting. The first breakthrough regarding inflatable technology occurred in the 1960 when NASA's Project Echo was launch. The original concept began as a 30-inch(0.76m) balloon for the payload of Vanguard to observe atmospheric drag once released into the atmosphere (Campbell, 2015). Since then the concept has been adapted and refined into a concept capable of de-orbiting CubeSats.

The feasibility for using this method for low earth orbiting CubeSats was investigated by (Lokcu and Ash, 2011). During their research they proposed an inflatable structure which is fitted into a container with the dimensions of 9 cm x 9 cm by 2 cm deep seen in figure 2.7. This container is smaller than the overall CubeSat dimensions and can thus be integrated into the structure of the CubeSat. . It was proposed that the structure be inflated with SUVA-236fa refrigerant produced by DuPont.

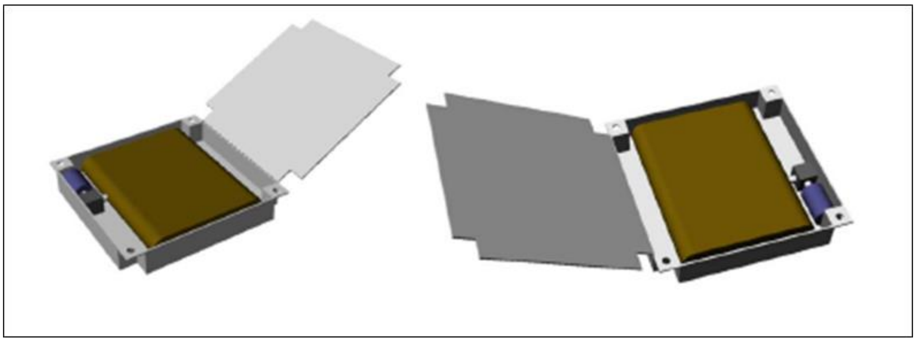

Figure 2.7 Inflatable device container

(Adapted from Lokcu and Ash, 2011)

The criteria used to determine the most suitable geometry of the inflatable structure was the estimated material mass, reliability, and ease of construction. The geometry that satisfied all the listed criteria was a pillows shaped structure seen in Figure 2.8.

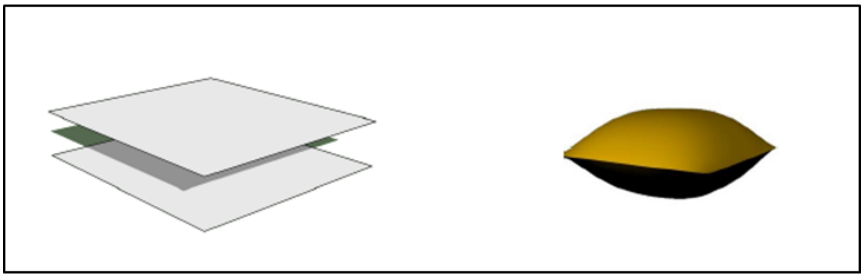

Figure 2.8: Pillow geometry

(Adapted from Lokcu and Ash, 2011)

Simulation results indicated that an inflatable device with a cross-sectional area of 0.5625 m^2, together with a drag coefficient of $C_D = 2$ can meet the 25-year operational lifetime restriction. The overall mass of the deployment system was 150grams and 0.05% of the CubeSats battery power was required for deployment. Given that CubeSats operate of a limited mass and power budget, this method could offer an uncomplicated solution to the CubeSats de-orbiting problem.

The same principle was followed by Aerospace Corporation that build and operated the Areocube-3 CubeSat (Konstantinidis and Förstner, 2013) . The CubeSat had several payloads including a balloon deorbiting device which consisted of a tank, a fill tube, a balloon structure and enclosure. The balloon had a diameter of 0.6m which consisted of four balloon panels.

The balloon subsystem had a volume of $155cm^3$ and was made of aluminized Mylar with 1 mm thickness as seen on the right of in figure 2.9.

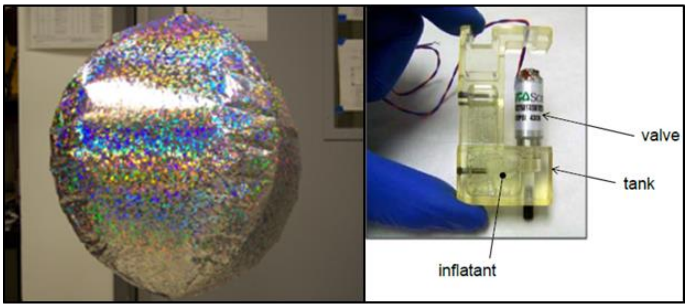

Figure 2.9: Inflated areocube-3 balloon on the left and inflation system on the right

(Adapted from Fuller, Hinkley and Janson, 2010)

The balloon had an average cross-sectional area of $0.28m^2$ and a ballistic coefficient of $0.5m^2/kg$. Similar to the research done by (Lokcu and Ash, 2011) a small inflation system containing SUVA 236fa was used to inflate the balloon(Fuller, Hinkley and Janson, 2010). During the mission the balloon was successfully deployed but did not inflate.

The Gossamer Orbit Lowering Device (GOLD) was developed by the Global Aerospace Corporation (Nock et al., 2010). This device differs from the aforementioned devices in the sense that the geometry of the inflatable structure is a sphere seen in figure 2.10. The objective of GOLD is the same as the previously discussed concepts in the sense that its designed to increase drag and decrease the ballistic coefficient. Although the original concept is relatively large the sphere size is scalable and can thus be adjusted to fit the dimensions of a CubeSat. The GOLD system concept also does not require an operating satellite and functions autonomously. The advantages of these kind of devices outweigh the disadvantages and is seen in table 2:1.

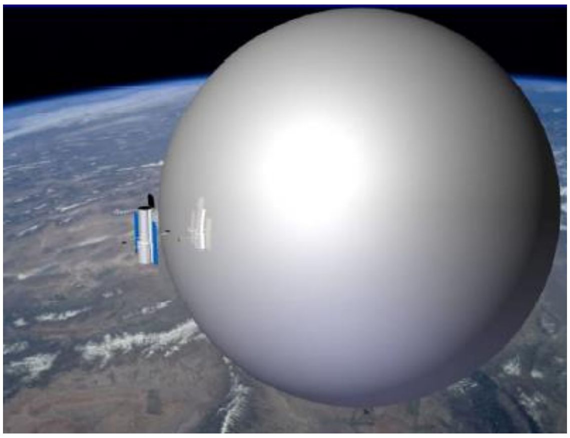

Figure 2.10: GOLD system concept

(Adapted from Nock et al., 2010)

Table 2:1 Advantages and disadvantages of method 1

Advantages	**Disadvantages**
Lightweight	Involves the use of Gas
Scalable	Some requires battery power to deploy
Simplistic design	
Easy to integrate	
Achieves de-orbiting within 25 years	

2.6.2 Method 2: De-orbiting Sail System

Like inflatable devices, de-orbiting sail systems take advantage of the increased aerodynamic drag generated after deployment. The primary objective of a de-orbiting sail is to deorbit a CubeSat, from low earth orbit using drag and solar radiation pressure. It does not require any propellant or any gas for inflation unlike the inflatable devices. Research regarding the design and development of de-orbiting sails was conducted by (Fernandez et al., 2014) and was shown to be advantageous in achieving de-orbiting for nanosatellites from a low earth orbit.

The de-orbiter system seen in figure 2.11 was originally designed to be between 3-4kg and has a sail size of 5 by 5 m^2. To prevent any interference or entanglement between the sail and the satellite, a telescopic enclosure system is used to distance the sail from the satellite before deployment. Deployment is achieved by three compression springs. The original concept exceeds the mass limitations of a 3U CubeSat. However, the feasibility of a scaled down version of the de-orbiter system could be investigated. A 3U CubeSat would require a smaller sail area and therefore the system could be scaled down to fit the CubeSat's requirements and in doing so reduce the overall weight of the system.

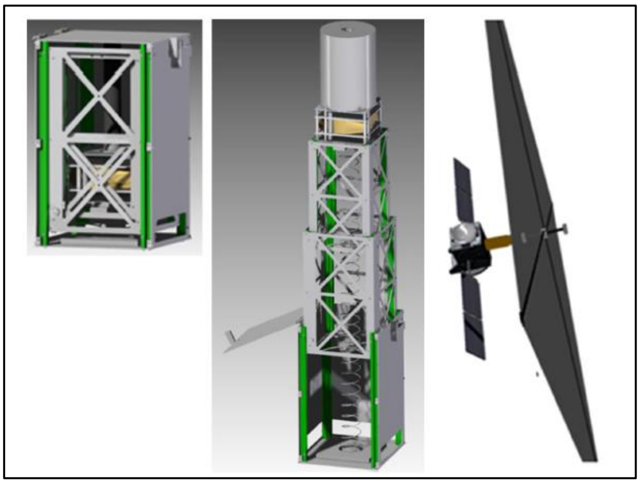

Figure 2.11: Deployment sequence of the gossamer de-orbiting sail system

(Adapted from Fernandez et al., 2014)

Research into the feasibility and development of drag sail devices was investigated by the University of Toronto's Space Flight Laboratory. During their research they proposed a lightweight, modular deployable drag sail suitable for the CubeSat platform (Bonin et al., 2013). The drag sail system was set to be fitted on a 3U CubeSat named CanX-7 (Canadian Advanced Nanosatellite Experiment -7).

The aim of this mission/experiment was to successfully demonstrate the drag sail as a passive deorbiting device. The device consists of four wedge shaped modules seen Figure 2.12 on the right. Each module houses a trapezoidal sail which is supported at its corners. Following successful sail deployments of all four units, a sail area of approximately 5m^2 is achieved as seen in figure 2.10 below.

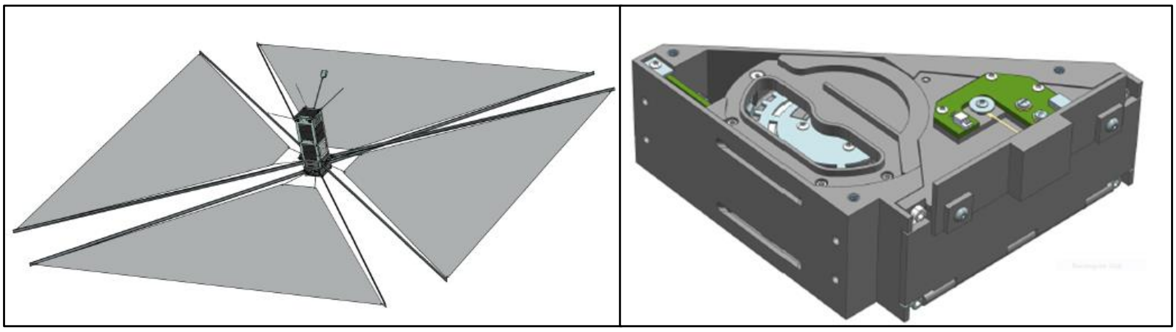

Figure 2.12: CanX-7 de-orbiting device

(Adapted from Bonin et al., 2013)

Sail deployment is archived, by utilizing the stored energy of a coiled steel tape spring booms, which is held in place by a closed door that is tied to the unit structure via a Vectran cord. When deployment is required, a heater is used to cut the cord. Once the cord is cut the boom pushes the door open and release the sail. The deployment process is controlled by the sail module electronics which is responsible for proceeding commands sent from the ground station to the satellite. It also collects and relays information regarding deployment confirmation. De-orbiting analysis was done using STK during which the altitude of the 3U CubeSat was varied between 400km to 1000kms.When no drag sail is fitted the results indicated an expected lifetime of 50 years as the altitude approached 600kms.However, when the drag sail is deployed the predicted lifetime reduces to just above 10 years at an altitude of 1000kms.Although this device is scalable and shows promising simulation results, it requires an substantial addition of electronics to achieve sail deployment and thereby increasing the level of complexity.

Table 2:2: Advantages and disadvantages of de-orbiting method 2

Advantages	**Disadvantages**
Both devices are Scalable	Both have Complex mechanical Designs
Both achieves de-orbiting within 25 years	gossamer de-orbiting sail system Mass (between 3-4kg)
	CanX-7 Requires additional complex electronics to control deployment

2.6.3 Method 3: Electrodynamic tethers (EDT)

The last method of de-orbiting is by means of an electrodynamic tether system. The electrodynamic drag required for de-orbiting is obtained by utilizing the Lorentz force created due to the interaction between an electrical current flowing in a conducting tether in earth's geomagnetic field.

The application of electrodynamic tethers for de-orbiting CubeSats was investigated by (Hoyt, 2009) and resulted in the design of the terminator tape module. The module is a box-shaped seen in Figure 2.13 and houses a thin conductive tape. The length, width, and conductivity of the tape are determined by the size and mass of the satellite and can be adjusted accordingly. This device is highly scalable and can be fitted to CubeSats, Pico, and nanosatellites. The "Nanoterminator Tape" complies with the CubeSat standards and is sized to be mounted on to one face of the CubeSat as seen in Figure 2.14.

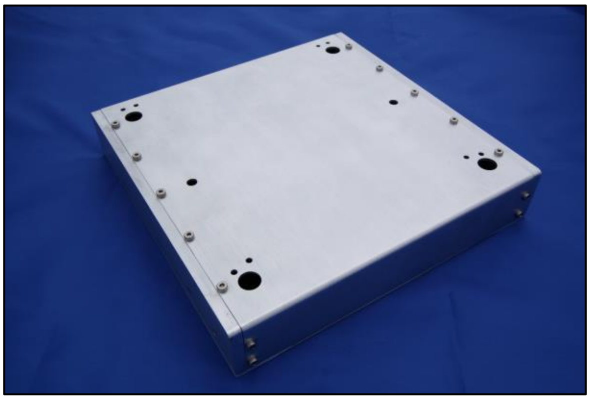

Figure 2.13: Engineering model prototype of the Terminator Tape module

(Adapted from Hoyt, 2009)

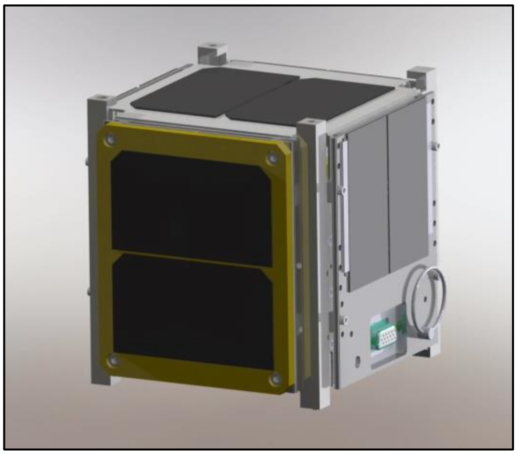

Figure 2.14: Nanoterminator tape module fitted on a 1U CubeSat.

(Adapted from Hoyt, 2009)

The module contains a 30m long tape, the tether is deployed via a burn wire, which is activated by a small circuit integrated into the CubeSat. The module design includes electrical feedthroughs so that solar cells can be mounted on the face of the module. The weight of the module is 80gram excluding the batteries. In addition to being lightweight, this module does not require any propellant and will remain inactive until the tether is deployed at the end of the mission. Performance predictions shown in Figure 2.15 indicates that a 3U fitted with a Nanoterminator will successfully deorbit within 25 years in orbits below 1000km.

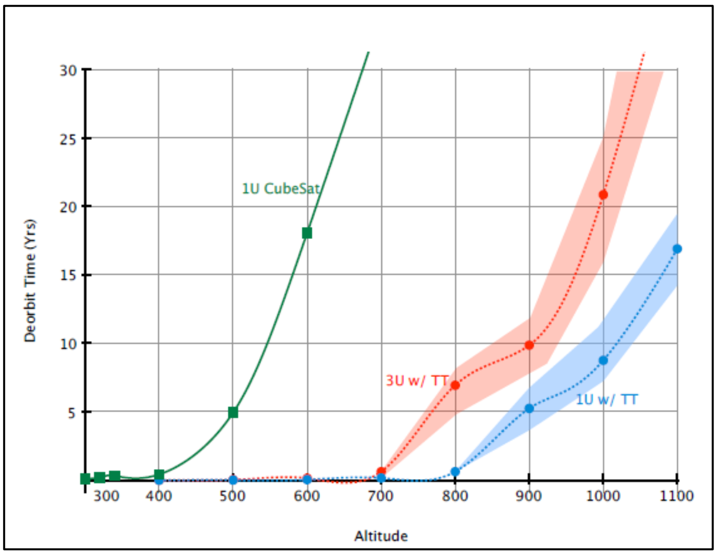

Figure 2.15: Performance predictions for Nanoterminator

(Adapted from Hoyt, 2009)

An alternative to the electrodynamic tether was proposed by (Janhunen, 2010) in the form of an electrostatic plasma brake device. The device is based on the coulomb drag interaction between the ionospheric plasma and a negatively charged thin tether. Although this method bears a resemblance to that of electrodynamic tether in the sense that a thin tape-like tether is deployed the physical mechanisms is different. A detailed discussion regarding the physics of coulomb drag was covered by (Janhunen, 2014). The concept which is theoretically able to de-orbit a 3kg - 100kg satellite from a polar orbit of 900km, comprises of the gravity stabilized tether, the tip ballast mass, and the voltage source seen in the figure 2.16.

Unlike electrodynamic tether, the electrostatic plasma brake does not require a current to flow in the tether and therefore the mass and power consumption are much less than that of the electrodynamic tether of matching performance. Preliminary performance estimations indicated that, a 3U with area of 0.12m^2 fitted with a tether mass of 16g, tip mass of 30g on a tether of 700m, charged with 150V could de-orbit in 93 days from a 600km polar orbit.

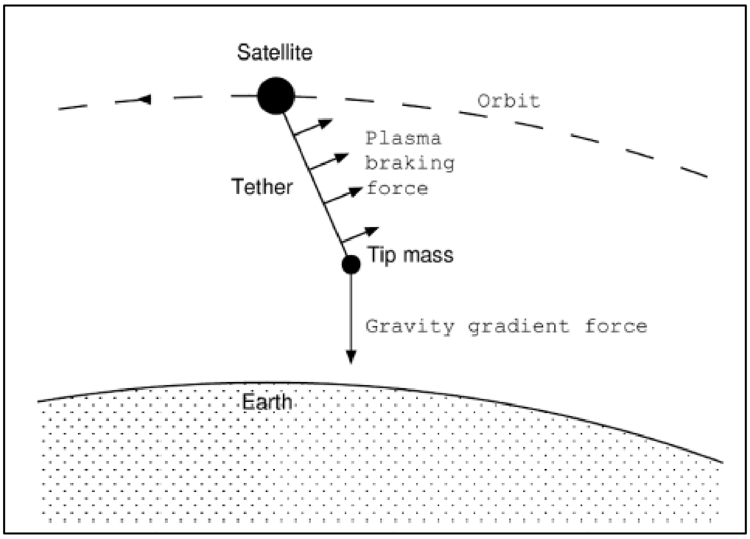

Figure 2.16:Plasma brake concept

(Adapted from Janhunen, 2010)

This concept was included in the ESTCube-1 test mission developed by University of Tartu (Lätt et al., 2014). In an effort to measure the electrostatic plasma braking effects at low Earth orbit, the 1U CubeSat was to deploy a 10m conducting tether, charged to approximately 200V (Janhunen, 2010). Unfortunately, the tether deployment was unsuccessful, and therefore the experiment could not be completed (Slavinskis et al., 2015). The advantages and disadvantages of the method 3 are listed in table 2:3

Table 2:3: Advantages and disadvantages of method 3

Advantages	Disadvantages
Both devices are scalable	The nano tape is activated via burn wire and thus requires additional circuitry to be activated. The plasma brake is stored motorized reel and has complex motor drive electronics.
Both achieves de-orbiting within 25 years	Both devises relies on a lengthy tape may cause accidental collisions with other satellites
Both devices are relatively small and can be integrated into the CubeSat.	
Both are relatively lightweight.	

2.6.4 Deorbiting method Evaluation Tool

The literature review regarding passive deorbiting methods covered various deorbiting strategies, each of which has its advantages and disadvantages. The following section uses an evaluation tool to critically evaluate each of the methods discussed in the literature review. The tool will assign a numeric value to each concept consideration, where one is the most important rating and three is the least important. Table 2.4 below list the importance level of each consideration.

Table 2:4: Concept considerations

Consideration:	Level of importance:
Mass of Concept	1
Size	1
Deorbiting Time/ Functionality	1
Scalability	2
Design Simplicity	2
Activation Method	2
Satellite Operation Interference	2
Aesthetics	3

In table 2.5 each concept is evaluated against the considerations listed in table 2.4 and rated between 1 and 3, where 1 is the best and 3 is the worst. The total score provided by each concept will differentiate which concept is the most suitable. The concept with the lowest score will be the best suited concept.

Table 2:5: Concept evaluation

Deorbiting Method		Method 1	Method 2	Method 3
Design Considerations	Mass of Concept	1*1	1*3	1*1
	Size	1*1	1*3	1*1
	Deorbiting Time/Functionality	1*1	1*1	1*2
	Scalability	2*2	2*2	2*2
	Design Simplicity	2*1	2*2	2*2
	Activation Method	2*2	2*2	2*2
	Satellite operation interference	2*2	2*3	2*2
	Aesthetics	3*2	3*2	3*2
Total score of concepts		23	31	26

The results indicate that method 1: the inflatable structure is a good method to achieve deorbiting. Thus, the new concept will be based on method 1, which takes advantage of the aerodynamic drag exercised by the satellite. The new concept will be introduced and discussed in chapter 6.

2.7 Overview of DAS and STELA de-orbiting software packages

This section covers the comparison and evaluation of DAS and STELA de-orbiting software packages. Although both packages are used to predict the orbital lifetime of a satellite, each of them employs different assumptions such as atmospheric density model selection and drag coefficients that affect the orbital lifetime estimation of the satellite. A brief overview of each software package and their assumptions will be presented below.

2.7.1 Debris Assessment Software (DAS 2.0)

This software was developed by NASA to assist with orbital debris assessment as described in the NASA technical Standard 8719.14 document. This standard provides specific technical requirements for limiting orbital debris and orbital debris generation. This software offers various efficient functions such as, compliance with the NASA debris requirements, on-orbit collisions and orbit evolution analysis. The orbit evolution analysis function brunches out into an Orbital lifetime/ dwell time function, which allows the user to calculate the orbital lifetime of a satellite. To do this, the software requires the user to input the start date (in decimal time), orbital parameters and an area to mass ratio. During this calculation the software assumes a drag coefficient value of 2.2 , along with a reflectivity coefficient of 1.25.

Furthermore, the software does not allow the user to select an atmospheric model or solar flux values, but rather askes the user enter the mission start date. Appropriate solar flux values (F10.7) are then retrieved from environmental models in the tool based on NOAA short-term and NASA long-term predictions. The F10.7 values along with the Jacchia 1976 Standard atmospheric model are then used to calculate the temperature and density of Earth’s upper atmosphere. The propagators used to perform these complex calculations are PROP3D” and “GEOPROP . These propagators are part of the LEGEND three-dimensional, debris evolutionary model that is used by NASA to study the long-term debris projection in LEO, MEO and GEO. Both propagators accounts for various perturbation forces however, PROP3D is the only one out of the two that accounts for atmospheric drag.

2.7.2 The Semi-analytic Tool for End of Life Analysis software (STELA)

STELA was developed by the French space agency (CNES) to support the French Space Operations Act (FSOA). This act’s objective is to better regulate French space operations, which includes limiting and reducing space debris in the protected regions LEO and GEO. Therefore, this tool allows the user to evaluate the level of compliance with the requirements stipulated in the FSOA. STELA offers the user three dynamic orbital models, LEO , GEO and GTO. Once the desired model is selected, the software requires the user to input, the object characteristics, atmospheric model, initial state and orbital parameters. Object characteristics branches out into, mass, reflective area which is by default set to 1.5 and drag coefficient. Under drag coefficient the user can select a constant value which has a default setting of 2.2 but can also be defined by the user, or the user can select variable which extracts values from a drag coefficient file based on the satellites altitude, and lastly Cook, which uses the cook formula to account for random tumbling.

The last two drag coefficient options require no input from the user, these values are automatically selected by the software. The software offers three atmospheric models to choose from, "NRLMSISE-00" which is the recommend default setting, "US-76" model and the Jacchia 77 model. It is important to note that from the three models listed, the US-76 does not account for variation in solar activity. The solar activity for NRLMSISE-00", and Jacchia 77 model can be set by the user or the variable solar flux value can be used, which is extracted from the solar activity file provided by STELA.

An option to select a mean solar value is also available however, the solar flux value is computed by STELA using the daily values in line with what is expected by the atmospheric model. In other words, the mean values change according to the model selected. The propagation model used is based on a semi-analytic extrapolator method. Orbital parameters are integrated using a numerical integrator which is by default set to sixth order Runge-Kutta method. A detailed discussion regarding this method fall out of the scope of this study but can be found by referring to the literature covered by (Butcher, 1996) and (Ismail, 2015).

2.7.3 Comparison and evaluation of DAS and STELA

In terms of satellite de-orbiting simulation capabilities, both software packers offer comprehensive assessments. A few key differences that may affect orbital estimation are listed in table 2.6.

Table 2:6: Key differences between DAS and STELA

Software Package	**DAS**	**STELA**
Atmospheric model selection capabilities.	No model selection available but, Jacchia 1976 Standard atmospheric model is utilized by DAS along with the most recent F10.7 values used to calculate atmospheric density.	Allows user to select one of three atmospheric models.
Solar flux values	Required periodically updated solar flux tables.	Gives various options for the solar activity values.
Drag coefficient	Assumes drag coefficient of 2.2	Allows user to enter: • Constant value defined by the user • Variable, which extracts values from a drag coefficient file and is the default setting • Cook, which uses the cook formula to account for random tumbling.
Reflectivity coefficient	Assumed 1.25	1.5 is the default setting, but user can enter different value.

It is known that atmospheric drag is a primary factor in the orbital lifetime estimation of the satellite, and that atmospheric drag is depended on atmospheric density and the form factor of the satellite. Thus, the selection of an appropriate atmospheric density model will affect the orbital lifetime estimation results.

A major difference between the software packages presented is, that STELA allows the user to select the atmospheric model and gives various options for the solar activity value. Research conducted by (Qiao, Rizos and Dempster, 2013) on the effects on orbital lifetime relating to the selection of the atmospheric density model, found that the orbital predictions of a 3U satellite can vary with as much as 20 years, depending on the model selected. This is not viewed as a negative aspect since certain application would require this option, but in this case, it could be argued that allowing the user to select between multiple atmospheric model increases the human error factor and could result in unreliable results.

Although STELA allows the user to select the drag coefficient, the default value is 2.2, which is the same as the drag coefficient values used in DAS. Furthermore, when variable is selected in STELA the software selects the value according to the altitude of the satellite, and upon further inspection of the drag file used in STELA, showed that between 570km and 600km the values ranges between 2.21 - 2.24, which is not a big difference from the 2.2 assumed in DAS.

Contrastingly to STELA, DAS does not allow the user to select and Atmospheric model or to select solar flux values. Rather, it informs the user when the solar flux table is outdated and requires an updated table. Once the updated table is uploaded, the software proceeds to use the updated F10.7 values to update the atmospheric density model, which then calculates the atmospheric drag. For this reason, DAS was selected as the best suited software for the purpose of this research.

Chapter 3

3 Orbital Mechanics

3.1 Introduction

Orbital mechanics can generally be defined as the study of the motions of artificial satellites moving under the influence of forces such as gravity, atmospheric drag, thrust. Orbital mechanics enable us to understand the motion of a body in space. Thus, a clear understanding of these concepts is fundamental to orbit propagation and determination. This chapter discusses the theory and concepts of orbital mechanics by means of the equation of motion and two-body problem.

3.2 Newton's Laws of Motion and Gravitation (Equation of motion)

Newton's law of motion describes the relationship between the motion of an object and the forces acting on it. In many ways, these laws are viewed as the root of celestial mechanics because together they created the foundation of what we now referred to as orbital mechanics.

These laws are presently still being applied to current aerospace problems and form an intricate part of satellite orbital analysis. The law is listed below, an in-depth discussion regarding Newton's laws can be found in (Peter Dourmashkin, 2012).

- **Newton's First Law (Inertia)** - *A body at rest, will remain at rest and a body in motion at a constant velocity will continue in motion at that constant velocity, unless acted on by some unbalanced external force.* What this means is that if there is no net force acting on the object, the object will remain at constant velocity.

- **Newton's Second Law (Momentum)** - *The rate of change of momentum of a body is directly proportional to the applied force and takes place in the direction in which the force acts.* This law is mathematically expressed by*:*

$$F = m * a \tag{3.1}$$

- **Newton's Third Law (Action-Reaction)** - *For every action, there is an equal and opposite reaction. More simply put if you have two interacting objects A and B then object A exerts a force on object B, and object B also exerts an equal force on object A.*

- **Newton's law of universal gravitation** - *Every object in the universe attracts every other object with a force directed along the line of centres for the two objects that is proportional to the product of their masses and inversely proportional to the square of the distance between the two objects. This law is expressed in equation 3.2*

$$F = G\left(\frac{m_1 m_2}{r^2}\right) \tag{3.2}$$

3.3 Kepler laws of planetary motion

Throughout his life, Kepler studied the motion of the solar system, he used Newton's laws and the knowledge gained from Tycho Brahe to formulate the three laws of planetary motion. These laws are listed below with the first and second law illustrated in Figure 3.1 and Figure 3.2 respectively

1) All planets move in elliptical orbits with the sun at one focus.

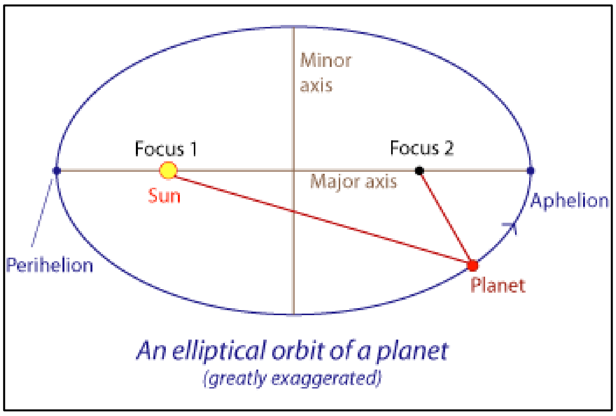

Figure 3.1: Kepler's first Law

(Adapted from Brian Ventrudo, 2013)

2) A line joining any planet to the sun sweeps out equal areas in equal time.

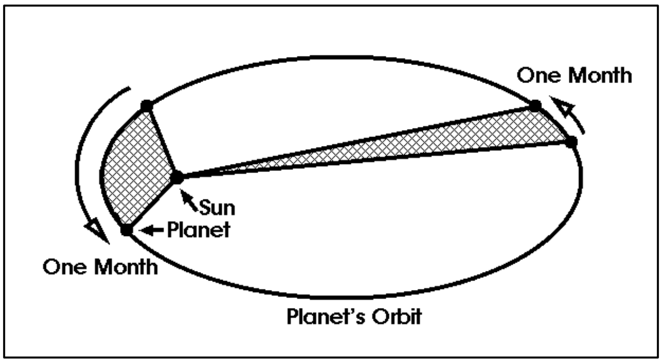

Figure 3.2: Kepler's Second Law

(Adapted from Brian Ventrudo, 2013)

3) The square of the period of any planet about the sun is proportional to the cube of the planet's mean distance from the sun.

3.4 Two-Body Problem

The two-body equation is required to solve the two-body problem. To do this, these three assumptions are made (Chobotov, 2002).

3.4.1 Two-body equation assumptions.

- The inertial frame of reference will be the coordinate system used to solve the two-body-problem.
- No external forces act on the bodies, except that of the mutual gravitational forces that act along the centre line joining the two bodies.
- Both bodies are spherically symmetrical with uniform density and are thus considered to be point masses.

3.4.2 Equations of motion in an inertial frame

Mutual gravitational force is the only force exerted on the two masses shown in Figure 3.3(a) and (b) .The position of their centre of mass is shown relative to an inertial reference frame known as XYZ. The axes do not rotate, even though the origin *O,* of the frame, may move with constant velocity relative to fixed stars. Each body experiences the gravitational attraction of the other. Thus, $\mathbf{F}_{12}$ is the force exerted on $\mathbf{m}_1$ by $\mathbf{m}_2$, and $\mathbf{F}_{21}$ is the force exerted on m_2 by m_1. The position vector $\mathbf{R}_G$ of the centre of mass **G** of the two-mass system is mathematically expressed in equation 3.3 (Curtis, 2005)

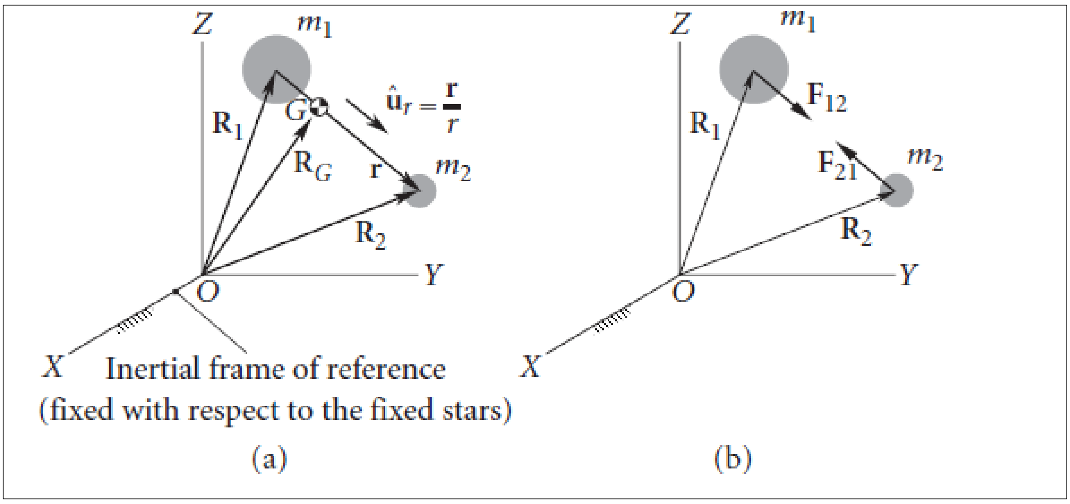

Figure 3.3:(a) Two masses in an inertial frame (b) Free-body diagram of the masses

(Adapted from Curtis, 2005)

$$R_G = \frac{m_1 R_1 + m_2 R_2}{m_1 + m_2} \quad \textbf{(3.3)}$$

Considering Figure 3.4, which represents two bodies of masses m and M with position vectors R_m and R_M. To determine the motion of m relative to M, Newton's gravitational law is applied and yields equation (3.4)

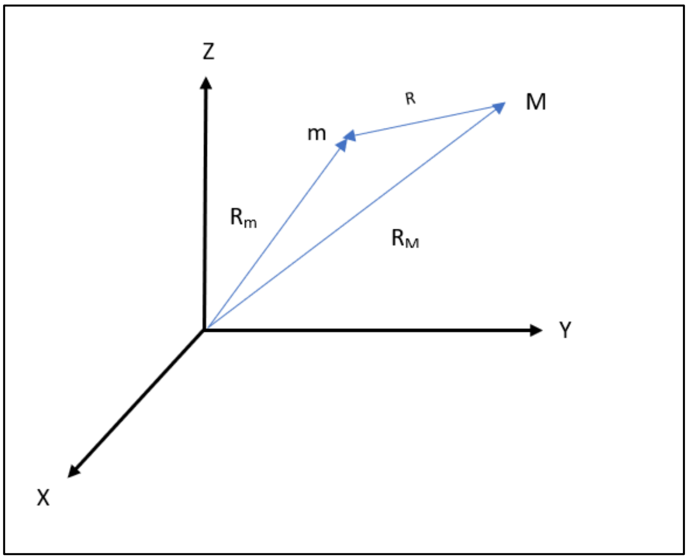

Figure 3.4: Two body system representation

(Adopted from Chobotov, 2002)

$$\ddot{\mathbf{R}} = -\frac{\mathbf{G(M+m)}}{\mathbf{R^3}}\mathbf{R} \tag{3.4}$$

Where,

R = $R_m - R_M$ with the position of body m relative to M

G = Gravitational constant 6.67408 × 10-11 $m^3\ kg^{-1}\ s^{-2}$

M = Mass of the earth 5,972 × 10^{24} kg

m = Mass of satellite

R = Magnitude of position vector **R**

Equation (3.4) can be simplified by inserting the standard gravitational parameter (μ). This parameter is defined as μ = G(M+m) ≈GM. With the assumption that the principal mass M is in inertial space, and m<<M (Chobotov, 2002) equation (3.4) is reduced and becomes the two-body equation of motion seen as equation (3.5). This equation gives the satellite (m) position as it orbits the earth.

$$\ddot{\boldsymbol{R}} + \frac{\boldsymbol{\mu}}{\boldsymbol{R^3}}\boldsymbol{R} = \mathbf{0} \tag{3.5}$$

Equation (3.5) will be elaborated on in section titled ‘Position in an elliptical orbit’

3.5 Kepler's Equation

Having discussed the two-body equation, the next step is to investigate how to calculate a position in an orbit after a certain period. Kepler was able to solve this problem by introducing three anomalies. The term 'anomaly' means, irregularity and is used by astronomers to describe the planetary positions. This term stems from the fact that the observed location of planets often deviated from the predicted locations.

- Eccentric Anomaly (E): This is the auxiliary angle used in the integration of Newton's equation for elliptical motion (Curiel, 2000). This can be seen in Figure 3.5 where (E) is the angle between the main axis to the point Q on the circle which contains the eclipse. This anomaly is mathematically expressed in equation (3.6)

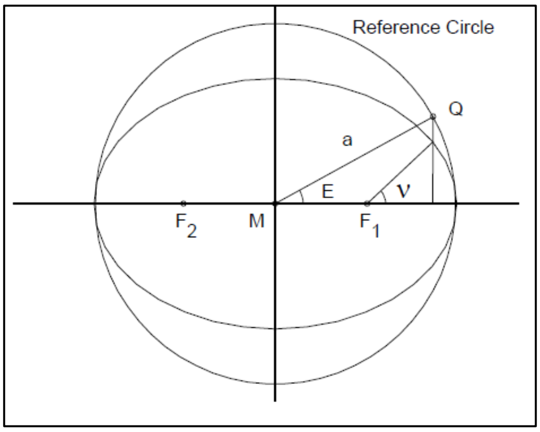

Figure 3.5: Eccentric anomaly

(Adopted from Curiel, 2000)

$$\cos E = \frac{e + \cos\nu}{1 + e\cos\nu} \tag{3.6}$$

- Mean Anomaly (M): The Mean anomaly is a quantity that relates position to time. This quantity is defined as the 'angle measured from the periapsis in the direction of the satellite's motion would sweep out if it moved at a constant angular speed' (Curiel, 2000). Expressed by the following equation (3.7), where T is the time it takes for the satellite to complete one revolution around the earth.

$$M = 2 * \pi * t / T \tag{3.7}$$

- True anomaly (V): This is the angle between the point of perigee and the spacecraft position. This is expressed in equation (3.8)

$$v = M + 2e\sin M \tag{3.8}$$

- Equation (3.9) relates the Mean anomaly (M), Eccentric Anomaly (E) and Eccentricity (e) and is known as the Kepler's equation.

$$M = E - e * \sin(E) \tag{3.9}$$

3.6 A solution to The Two-Body Equation of Motion

In section 3.4 the two-body equation was introduced, by explanations regarding conic section and Kepler's equation. This was done to create a better understanding of how to find positions in orbit. Equation (3.5) is the two-body equation of motion. It describes the motion of the satellite as it orbits the earth.

A solution to equation (3.5) is the polar equation of a conic section, shown as equation (3.10). This equation is special it enables the user to calculate the distance from the primary body and its flight path angle.

$$R = \frac{a(1-e^2)}{1+e\cos v} \tag{3.10}$$

Where,

R = magnitude of the spacecraft's position vector(km)

a = semi major axis

V = True anomaly

e = Eccentricity

Furthermore, the satellite's velocity (V) can be found by equation (3.11)

$$V = \sqrt{GM\left(\frac{2}{r} - \frac{1}{a}\right)} \tag{3.11}$$

It is important to keep in mind that the two-body equation of motion is a special case of the *N-body* problem. It neglects other external forces acting on the celestial body, such as atmospheric drag, solar radiation pressure, and other planetary gravitational forces. Thus, if accurate orbital motion is desired, these forces must be considered.

3.7 Position in Orbit

Relating position in orbit to a given elapsed time, t – t_0 was solved by Kepler. He did this by using the Mean anomaly quantity (M). The mean anomaly equates to the true anomaly for a circular orbit and is mathematically defined by equation (3.12).

$$M - M_0 = n\left(t - t_0\right) \tag{3.12}$$

Where M_0 = Mean anomaly when time is t_0

n = Rate of change of the mean anomaly

Solving the value of (n) can be done by means of the semi-major axis of the orbit in question. Equation (3.13) expresses the rate of change of the mean anomaly.

$$n = \sqrt{\frac{GM}{a^3}} \tag{3.13}$$

3.7.1 Maximum and Minimum Velocities in an Elliptical Orbit

During orbit, a satellite reaches a point where it is closet to earth(perigee) and a point where it furthers from earth (apogee). The velocity of the satellite at perigee and apogee differ.

The satellite travels faster when it reaches perigee than when it is at apogee. To find velocities of the satellite at each point the equations 3.14 and 3.15 are used.

$$V^2{}_{perigee} = \mu\left(\frac{2}{r_p} - \frac{1}{a}\right) \tag{3.14}$$

$$V^2{}_{Apogee} = \mu\left(\frac{2}{r_a} - \frac{1}{a}\right) \tag{3.15}$$

Where:

$\mu =$ Standard gravitational constant $(3.9 * 10^{14} m^3 / s^2)$

r_p = Radius of earth + perigee height (km)

r_a = Radius of the earth + apogee height (km)

a = Semi-major axis (km)

3.8 Laws of Conservation

Mechanical energy and angular momentum of a satellite are conserved, during orbital motion since it occurs in a conservative gravitational field. Thus, the total energy remains constant.

3.8.1 Mechanical Energy

Total Mechanical energy (E) is an important element in understanding satellites orbital motion. It consists of the satellites potential energy (PE) and kinetic energy (KE), The total mechanical energy is the sum of potential and kinetic energy which is expressed in equation (3.14)

$$E = PE + KE \tag{3.16}$$

Where,
E = Total mechanical energy (kg m^2/s^2)
PE = potential energy (kg m^2/s^2)
KE = Kinetic energy (kg m^2/s^2)

3.8.1.1 Potential Energy

To find a satellite potential energy (PE) that is in orbit high above the earth, it should be noted that gravitational acceleration varies depending on the distance of the satellite from the centre of the earth. The (PE) of a satellite can be found by equation (3.17)

$$PE = -\frac{m\mu}{R} \tag{3.17}$$

Where,
m = Mass of the spacecraft (kg)
μ = Gravitational parameter ($3.986 * 10^{14}$ m^3/s^2)
R = Satellite's distance from the centre of the earth (km)

3.8.1.2 Kinetic Energy

Kinetic energy can be defined as a function the satellites mass(*m*) and velocity(*V*). This is expressed by equation (3.18). Relating both equation (3.17) and equation (3.17) yields equation (3.19), which is the total mechanical energy equation.

$$KE = \frac{1}{2} m V^2 \tag{3.18}$$

$$E = -\frac{m\mu}{R} + \frac{1}{2} m V^2 \tag{3.19}$$

Orbital motion happens in a conservative field, which means that the total mechanical energy remains constant irrespective of the satellite is at apogee or perigee. This is achieved by a constant trade-off between an increase in potential and a decrease in kinetic energy and vice versa. This is also the reason why at apogee, the satellite moves slower than at perigee because it has an increase in potential energy by a decrease in kinetic energy. Hence this constant trade-off between the two keeps the total mechanical energy constant.

3.8.1.3 Specific Mechanical Energy

Specific mechanical energy (ϵ) is derived from that mechanical equation, with the exception that it does not consider the mass in question. In doing so, it results in a more generalized equation which can be applied to any object in orbit regardless of its mass. Shown in equation (3.20).

$$\varepsilon = \frac{-\mu}{R} + \frac{V^2}{2} \tag{3.20}$$

Equation (3.20) is also useful in finding the velocity of the satellite. If the specific mechanical energy(ϵ) and the satellite's distance from the centre of the earth(R) are known, then it follows that the velocity at any point in orbit can be calculated. manipulation of equation (3.20), yielded equation (3.21).

$$V = \sqrt{2\left(\frac{\mu}{R} + \varepsilon\right)} \tag{3.21}$$

3.8.2 Angular Momentum

Angular momentum ($\vec{H}$) is defined as the amount of resistance that a spinning object has to change in spin rate or direction of spin (Wertz, 1999b). This is expressed in equation (3.22). Notice that it contains mass. The specific angular moment $\vec{h}$ is derived from equation (3.22) and is defined as the cross product of the position ($\vec{R}$) and velocity ($\vec{V}$) vectors shown in equation (3.23) and does not include the mass of the object.

$$\vec{\boldsymbol{H}} = \vec{\boldsymbol{R}}\, \chi\, \boldsymbol{m}\vec{\boldsymbol{V}} \tag{3.22}$$

$$\vec{\boldsymbol{h}} = \vec{\boldsymbol{R}}\, \boldsymbol{x}\, \vec{\boldsymbol{V}} \tag{3.23}$$

Where,

$\vec{H}$ = Satellite’s angular momentum vector (kg · m^2/s)

$\vec{R}$ = Satellite’s position vector (km)

$\vec{V}$ = Satellite’s velocity vector (km/s)

m = Mass of the satellite (kg)

$\vec{h}$ = Satellite’s specific angular moment (km^2/s)

The plane that contains the position ($\vec{R}$) and velocity ($\vec{V}$) vectors are known as the orbital plane, seen in Figure 3.6. The specific angular momentum is always perpendicular to the position and velocity vectors.

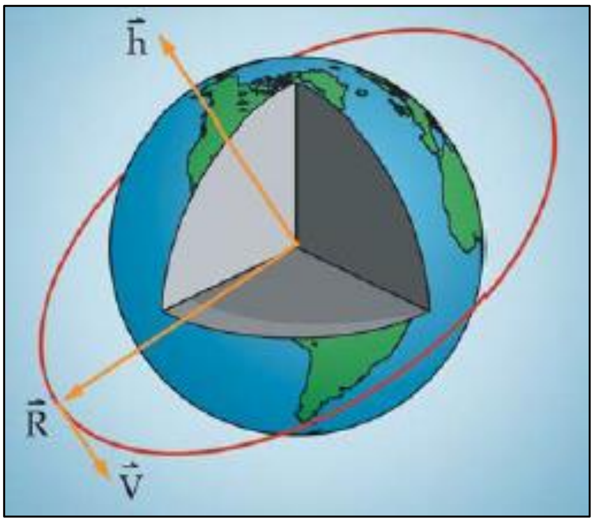

Figure 3.6: Orbital plane containing position and velocity vectors

(Adapted from Jon Sellers et al., 2004)

3.9 Classical Orbital Elements

In the previous section, the movement of the satellite as it orbits the earth relative to the inertial reference frame was investigated. In this section, the movement of the satellite with respect to earth will be investigated. This is achieved by looking at the elements that define the shape, size, and orientation of the orbit known as the Keplerian orbital elements.

Kepler defined six orbital elements. These elements are categorized into two groups, dimensional elements and orientation elements. The first category describes the size and shape of the orbit and relate the position in the orbit to time, while the second category specify the position of the orbit in inertial space (Chobotov, 2002).

3.9.1 Semi-Major Axis

The semi-major axis describes the size of the orbit, and the size of the orbit is related to the specific mechanical energy (ϵ) which is shown in equation (3.24). A visual perspective of the semi-major axis is seen in Figure 3.7. It is one half the distance across the long axis of an ellipse. The distance between the foci (F and F') of the ellipse is 2c.

$$\varepsilon = -\frac{\mu}{2a} \qquad \textbf{(3.24)}$$

Where, ϵ =Specific mechanical energy in (km^2/s^2)
μ = Gravitational parameter of central body in (km^3/s^2)
a = semimajor axis in (km)

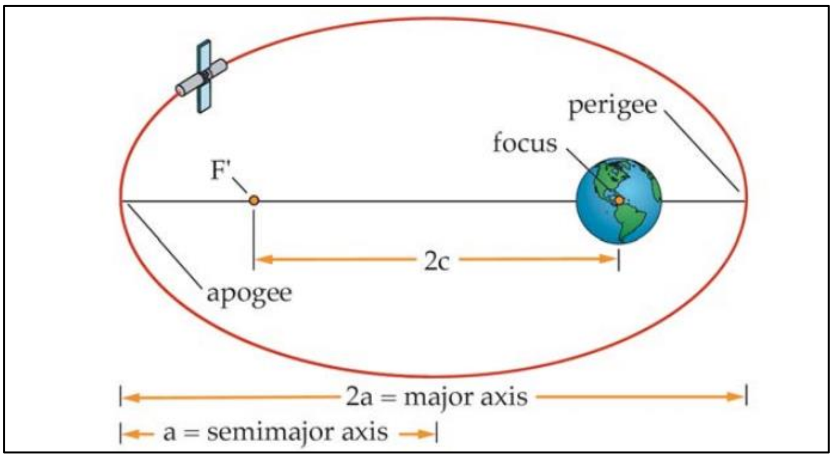

Figure 3.7: Semi-Major Axis

(Adapted from Jon Sellers et al., 2004)

3.9.2 Eccentricity

The eccentricity (e) of an orbit describes the shape or oddness of the conic section in terms of its eccentricity. It specifies the shape of an orbit by looking at the ratio of the distance between the two foci and the length of the major axis.

The ratio ranges between zero and one. An eccentricity value of zero corresponds to a circular orbit and a value of one corresponds to a parabolic orbit. Eccentricity value bigger than zero but smaller than one, it is indicative of an elliptical orbit. Equation (3.25) is used mathematically express the eccentricity value.

$$e = \frac{2c}{2a} \qquad \textbf{(3.25)}$$

3.9.3 Inclination

Inclination (i) of an orbit is the angular distance between a satellites orbital plane and the equator of the earth as seen in Figure 3.8. It can also be described as the tilt angle between two planes. This element is used to define different kinds of orbits. For instance, when an orbit has an inclination value of 0º or 180º then it would be known as an equatorial orbit because it remains over the equator. An inclination value of i = 90º would be called a polar orbit because it crosses over the north and south poles.

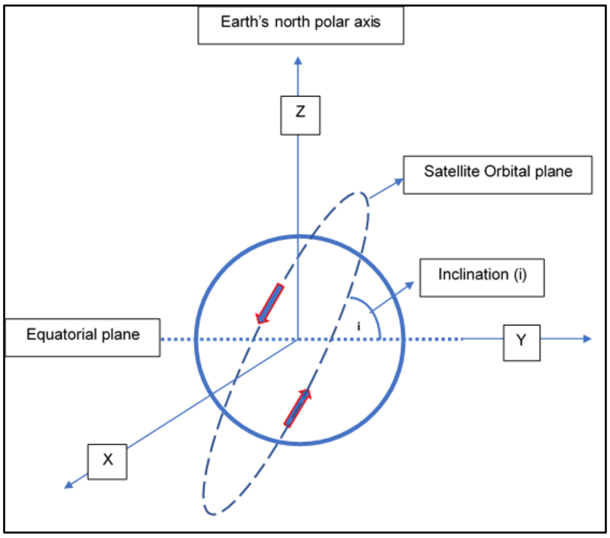

Figure 3.8: Inclination

3.9.4 Right Ascension of the Ascending Node

The right ascension of the ascending node (RAAN), is the point in an orbit when the orbital plane intersects the equatorial plane moving from south to north (in an upward direction). This can be seen in Figure 3.9, which indicates the RAAN with a red dot**.**

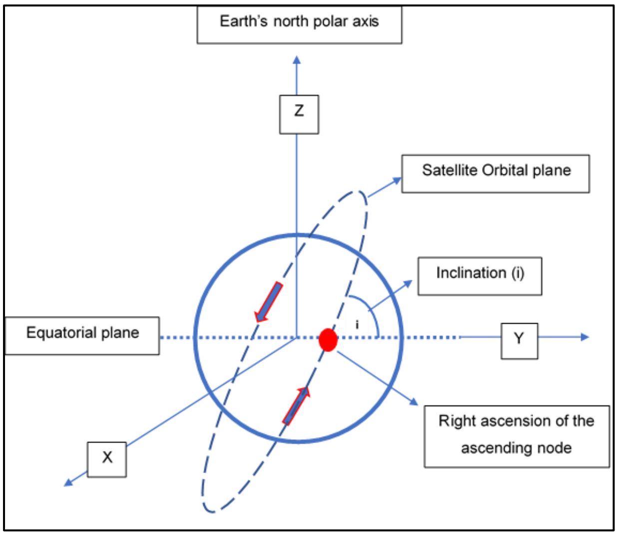

Figure 3.9: Right ascending node

3.9.5 Argument of Perigee

This is defined as the angle between the ascending node and perigee which is shown in Figure 3.10 and can be identified by the black arc. This angle is always measured along the satellites orbital path and motion. Also note, perigee is the point in the orbit when the satellite is closest to the earth.

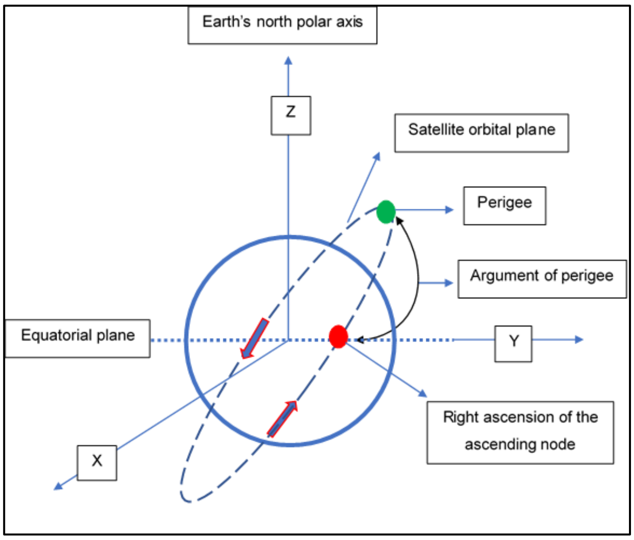

Figure 3.10: Argument of perigee

3.9.6 True Anomaly

True anomaly (*v*), is the angle along the orbital path from the perigee to the satellites position vector(**R**) shown in Figure 3.11. Just like the argument of perigee, true anomaly is measured in the direction of the satellite's motion.

This orbital element provides location information of the satellite during its orbit. Hence it varies with time which makes sense since it generates location information and the satellite is continuously moving.

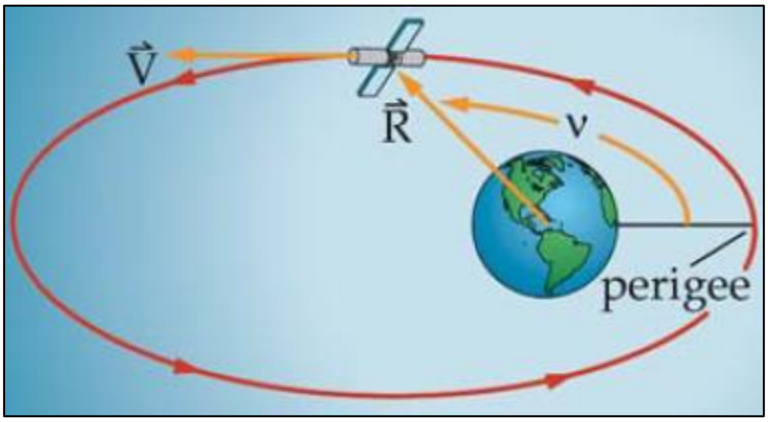

Figure 3.11: True anomaly

(Adapted From: Jon Sellers et al., 2004)

3.10 Orbit Types

The type of orbit selected for a satellite is mission-specific, thus the selected orbit is based on the purpose of the mission. This can include (but not limited to) remote sensing, communication weather, and navigation. Furthermore, the orbital speed of the satellite is determined by the orbit type and is linked to the orbital altitude. More simply put, low orbiting satellites orbit at significantly higher speeds than high orbiting satellites. Nanosatellites are small, which means they have very small weight and energy budgets. For this reason, nanosatellites are primarily launched into low earth orbit.

3.10.1 Low Earth Orbit (LEO)

This orbit ranges from approximately 500-1200kms from the surface of the earth. At these altitudes, on-board sensors have the best resolution, communication systems require the least power to communicate to the earth, and rockets require the least energy to get them to orbit. Since this orbit is close to earth it is commonly used for remote sensing and earth observation missions. Additionally, because this orbit is near earth it results in a close-up view of the earth at a high resolution. Furthermore, given the fact that this orbit is close to the earth, a high orbital speed of as high as 7.8km/s is needed for the satellite to stay in orbit. In turn, the high orbital speed results in a shorter orbital period of approximately 90 minutes.

3.10.2 Polar Orbit

This is a low earth orbit in which the satellite crosses both the north and south pole during each orbit. Common orbital height of up to 1000kms. This orbit has the advantage of producing high-resolution images and can map the entire globe. Example of a satellite in this orbit is Landsat7 which is used for remote sensing.

3.10.3 Medium Earth Orbit (MEO)

Medium earth orbit ranges from 20,000km - 36,000km and is between low earth orbit and geostationary orbit. However, high radiation, caused by the Van Allen belts, renders some of the MEO regions unusable. This type of orbit is mostly used for navigation purposes and example of this would be the global positioning satellites (GPS). Because this orbit is higher up, launching costs are higher and more power is needed for communication.

3.10.4 Sun-Synchronous (SSO)

This orbit is synchronous with the Sun. This is a specialized orbit and is generally used for weather and earth resources applications. This orbit is near the earth and has an orbital period of approximately 96 to 100 minutes. SSO is especially good for imagery since it offers consistent lighting conditions of the surface over several years which is useful for comparative studies.

3.10.5 Geosynchronous Earth Orbit (GEO)

This orbit has a height of up to 35,786km and matches the rotation speed of earth around its N/S spin axis, with the period of 23 hours 56 minutes 4.1 seconds. A common application for this orbit would be communication satellites and weather satellites.

3.10.6 Geostationary Orbit

The geostationary orbit is like the geosynchronous orbit, in the way that it also matches the rotational speed of the earth, with the exception that it remains above the earth's equator. Because the satellite is stationary relative to the earth, no satellite tracking is required, thus a communication antenna can be permanently positioned in the direction of the satellite without needing to track it.

Figure 3.12 is a summarized list of the various orbit types and the missions associated with each one.

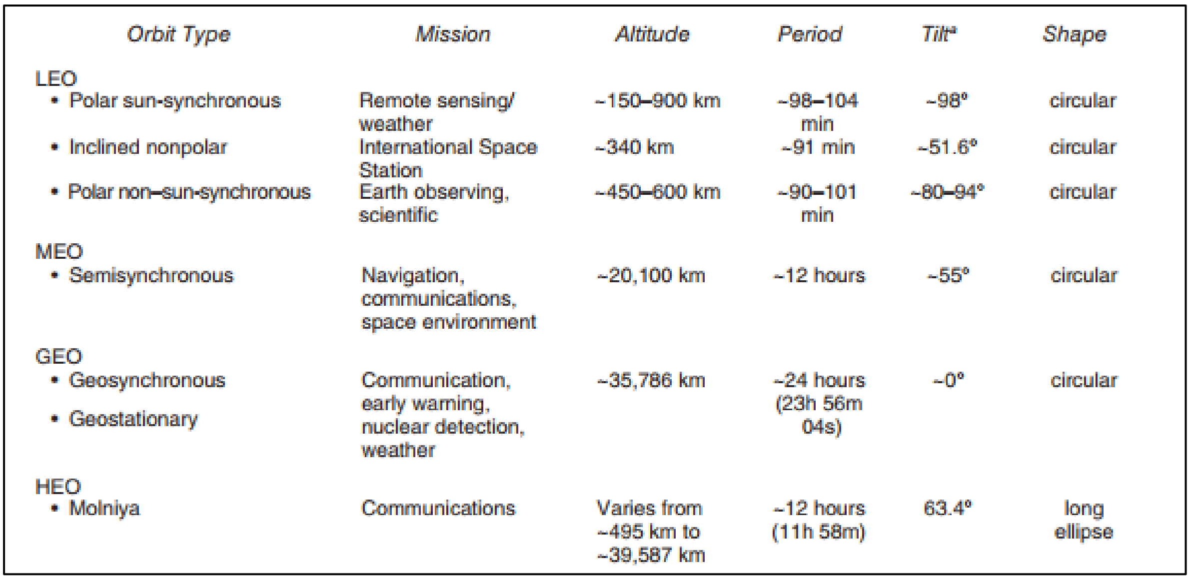

Orbit Type	*Mission*	*Altitude*	*Period*	*Tilt*[a]	*Shape*
LEO					
• Polar sun-synchronous	Remote sensing/ weather	~150–900 km	~98–104 min	~98°	circular
• Inclined nonpolar	International Space Station	~340 km	~91 min	~51.6°	circular
• Polar non–sun-synchronous	Earth observing, scientific	~450–600 km	~90–101 min	~80–94°	circular
MEO					
• Semisynchronous	Navigation, communications, space environment	~20,100 km	~12 hours	~55°	circular
GEO					
• Geosynchronous • Geostationary	Communication, early warning, nuclear detection, weather	~35,786 km	~24 hours (23h 56m 04s)	~0°	circular
HEO					
• Molniya	Communications	Varies from ~495 km to ~39,587 km	~12 hours (11h 58m)	63.4°	long ellipse

Figure 3.12: Orbital types

(Adapted from Roesler, Jaffe, and Henshaw, 2017)

Chapter 4

4 Orbital Perturbations

4.1 Orbital Perturbations

Section 3.4 discussed the principles of motion of two mutually attracting bodies, with the assumptions that both are spherically symmetrical with uniform density and move in an inertial frame of reference.

These assumptions allow both bodies to be treated as point masses, and as a result, it was shown that elliptical conic orbit was a solution to the differential equation of motion of a two-body system.

However, when a satellite is in orbit, the shape of the orbit deviates from that of an ellipse. This deviation is known as an orbital perturbation. Sources that cause this phenomenon can be divided into two categories:

- Gravitational: considers third body interaction and the oblateness of earth.
- Non – gravitational: Solar radiation pressure and atmospheric drag

The equation of motion for a two-body problem with perturbations is given by:

$$\ddot{\boldsymbol{R}} = \frac{\boldsymbol{\mu}}{\boldsymbol{r^3}}\boldsymbol{R} + \boldsymbol{a_p} \tag{4.1}$$

Where, R = the satellite position vector
μ = Earths gravitational parameter
a_p = Perturbative accelerations

These forces affect the orbital elements and results in long and short periodic and secular variation(Robert A. Braeunig, 2013). Long periodic variations are variations with a period greater than the orbital period of the satellite. It is a trigonometric function of the slow varying argument of perigee (ω).

Short periodic variations are periodic elements with a shorter orbital period compared to that of the satellite. It is a trigonometric function of fast varying elements, such as true anomaly(v) mean anomaly(M) and eccentric anomaly(E).

Secular variations are a non-oscillating continuous drift of an element from an adopted epoch value and increase or decrease linearly over time (Opperman, 2003). These variations are shown in Figure 4.1 where ‘c’ represents the general orbital element, the straight-line represents secular variations, and the non-osculating line shows a combination of long-period and secular variations.

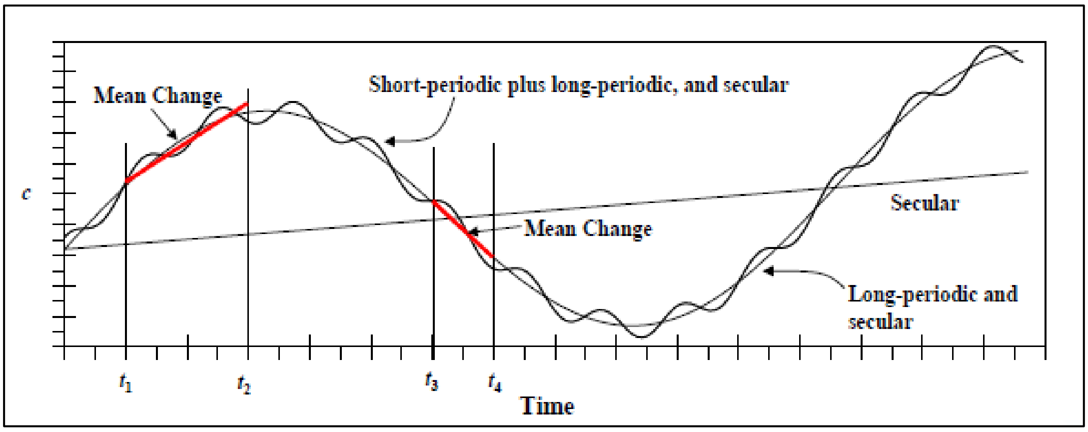

Figure 4.1: Orbital element perturbation

(Adapted from Vallado, 2010)

4.2 Third-Body Perturbation

The gravitational forces of the moon and sun cause periodic variations in all the orbital elements. This is due to the moon and sun applying an external torque to the orbits which cause the angular moment vector to rotate (James Wertz, David Everett, 2011).

This variation is minuscule for satellites in LEO. However, this effect becomes important for satellites in geosynchronous orbits and requires correction for the satellite to remain in a certain position. For nearly circular orbits, the Lagrange planetary equations can be used to find approximate rational rates for the ascending node (Ω) and argument of perigee (ω).

Ascending node:

$$\Omega_{moon} = -0.00338\cos(i)/n \tag{4.2}$$

$$\Omega_{sun} = -0.00154\cos(i)/n \tag{4.3}$$

Argument of perigee:

$$\omega_{moon} = 0.00169(4-5\sin^2 i)/n \tag{4.4}$$

$$\omega_{sun} = 0.00077(4-5\sin^2 i)/n \tag{4.5}$$

Where (*i)* is the orbit inclination, (*n*) is the number of orbits per day and ascending node and argument of perigee in degrees per day.

4.3 Earth's Oblateness

Viewed from space earth appears to be a perfect homogeneous sphere. However, it is not. Due to earth's rotation and centrifugal forces, it bulges at the equator and flattens out towards the poles. This results in a radius variation of 22km at the equator, compared to the poles. The fattening at the poles is termed oblateness, expressed by equation (4.6).

$$oblateness = \frac{equatorial\ radius - polar\ radius}{equatorial\ radius} \tag{4.6}$$

The oblateness of the earth causes variations in the angular distance from the equator or poles (Curtis, 2005). This variation is known as zonal variations. J_2 is the dimensionless parameter that quantifies the major effects that the oblateness has on a satellite in orbit.

The non-spherical shape causes both periodical and secular variations (Robert A. Braeunig, 2013). However, the secular variations are dominant and result in variations in the ascending node(Ω) and argument of perigee(ω).

This is caused by the J_2 zonal harmonic. These variations are the result of the equatorial bulge. The added radius, adds an additional attraction force component which acts towards the equator (Afful, 2013) which thereby affects the Ω and ω elements.

The variation rates can be computed by the following equations.

$$\dot{\Omega} = -\frac{3}{2}\frac{J_2R^2}{P^2}\bar{n}\cos i \tag{4.7}$$

$$\dot{\omega} = \frac{3}{2}\frac{J_2R^2}{P^2}\bar{n}\left(2 - \frac{5}{2}\sin^2 i\right) \tag{4.8}$$

$$\bar{n} = \sqrt{\frac{\mu}{a_0^{\ 3}}}\left[1+\frac{3}{2}\frac{J_2R^2}{P^2}\left(1-\frac{3}{2}\sin^2 i\right)(1-e^2)^{1/2}\right] \quad \textbf{(4.9)}$$

Where,

$\dot{\Omega}$ =Rate of ascending node

$\dot{\omega}$ =Argument of perigee rate

$\bar{n}$ =Orbit mean motion with J_2 correction

$J_2 =$ 0.00108263

$R =$Earths equatorial radius

$i =$ Orbital inclination

$\mu =$Gravitational constant

a_0 =Semi-major axis at epoch

$e =$Orbit eccentricity

$p = (1-e^2)$

4.4 Oscillating and Mean Orbital Elements

Oscillating elements are those elements that vary with time, which includes all periodic and secular effects. These orbital elements are useful when high precision and very accurate simulations are required in a short amount of time.

Mean elements are the average of the orbital elements over a selected period, thus it is not influenced by short-period variations and high-frequency content (Zhong and Gurfil, 2013). For this reason, mean elements are used in long-term satellite behaviour predictions.

Mean element theory is the formal mathematical theory for approximating motion, which separates the effects of the fast motions such as the true anomaly (V) from those that are slowly varying motions such as right ascending node(Ω) (STK, 2019).

Examples of these theories are the Kozai-Izak and Brouwer-Lyddane theorems. The Kozai-Izak theorem only considers the elements that involve averaging of the period of the orbit. Furthermore, the only perturbation considered in this theorem is the oblateness of the earth.

The Brouwer-Lyddane differs from the Kozai by considering both long and short element variations. Additionally, it also considers J_2, J_3 J_4 and J_5 perturbation terms (STK, 2019).The above-mentioned theorems are very similar and should be used cautiously.

4.5 Gravity Potential Theory

Gravity potential theory is introduced for better understanding regarding the gravity harmonics of earth. There are three categories of the normalizes gravitational coefficient known as zonal, sectoral and tesseral harmonics. Figure 4.2 gives a visual representation of the three categories.

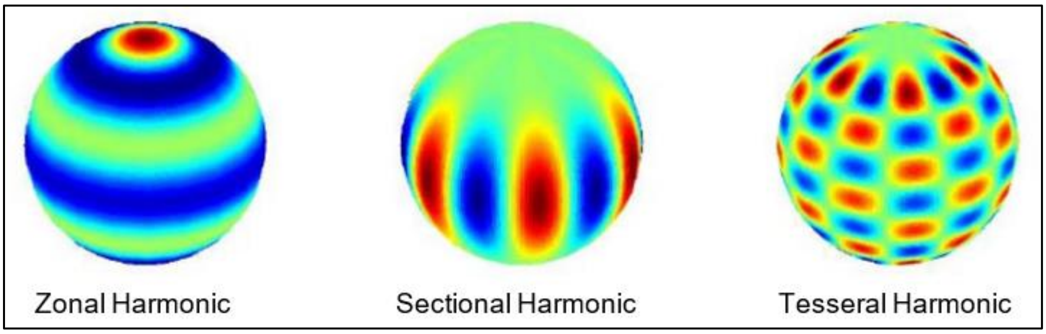

Figure 4.2: Zonal harmonics

(Adapted from Forsberg, 2016)

The gravity potential theory uses a potential function to model the gravitational field of a body with finite mass (Chobotov, 2002). Thus, assuming that a satellite is orbiting a central mass, which is a perfectly spherical, symmetric and homogeneous, it follows that the acceleration experienced by the satellite can be given by equation (4.10) and (4.11) (Opperman, 2003):

$$\ddot{\boldsymbol{r}}_{\boldsymbol{2-body}} = \boldsymbol{\nabla\Phi}_{\boldsymbol{2-body}} \qquad \textbf{(4.10)}$$

Where,

$\Phi_{2-Body} = -\frac{\mu}{R^3}$ R ,the gravitational potential of a ideal spherical body **(4.11)**

∇= Gradient vector operator (del) talking partial derivatives in each respective axes.

From equation (4.11) it can be deduced that the strength of the potential gravity at a point in space is directly proportional to the mass of the body thru the μ = G(M+m) ≈GM and inversely proportional to the cube of the distance to the centre of the body (Chobotov, 2002).

However, it has been established that the earth is non-spherical and asymmetric. It bulges at the equator and flattens out towards the poles. The asymmetric mass distribution causes a variation in the gravitational field, which deviates from the perfect spherical model. This gravitational deviation results in periodic variations in the orbital elements (Afful, 2013). For this reason, equation (4.10) does not accurately represent the gravitational field of earth.

Nevertheless, the potential gravity theory can be used to derive a suitable equation for earths non-spherical shape. The acceleration of the satellite due to the non-spherical shape of earth can be obtained by taking the gradient of the potential function Φ of the earth and substituting it into equation (4.10). Hence, it yields equation (4.12).

$$\ddot{\mathbf{R}} = \boldsymbol{\nabla}\boldsymbol{\Phi}_{\mathbf{Earth}} \tag{4.12}$$

Where, the potential function Φ_{Earth} is defined by (Afful, 2013)

$$\Phi_{Earth} = \frac{\mu}{r}\left[1 - \sum_{n=2}^{\infty}\left(\frac{R_e}{r}\right)^n \left\{J_n P_n \sin\varphi - \sum_{m-1}^{n} J_{nm} P_{nm} \sin\varphi \cos m(\theta - \theta_{nm})\right\}\right] \tag{4.13}$$

Where,

$r =$ Geocentric Distance.

$\varphi =$ Geocentric latitude.

$\theta =$ Geocentric longitude.

$\theta_{nm} =$ Equilibrium longitude for J_{nm}.

$R_e =$ Equatorila raduius of Earth.

$\mathrm{J}_{nm} =$ Harmonic coefficients.

$\mu =$ Gravitational Parameter.

$P_n =$ Legrandre polynomials of degree n and order 0.

$P_{nm} =$ Associated Legendre polynomial of degree n and order m.

A detailed derivation and expansion of equations (4.12) and (4.13) falls out of the scope of this study but can be found in (Chobotov, 2002).

4.6 Solar Radiation Pressure

Solar radiation pressure is defined as the force exerted on the satellite's surface, caused by light energy radiated from the sun and forms part of the non-gravitational perturbation category. It causes variations in all orbital elements but is most prevalent in terms of eccentricity variations (Chobotov, 2002). The magnitude of the force acting on the satellite is proportional to the effective area, surface reflectivity, and solar flux, but inversely proportional to the speed of light. The effects of solar pressure cannot be ignored if a satellite is equipped with large solar arrays. The normal and tangential forces experience by the sunlit areas of the satellite is expressed in equation 4.14 and 4.15 respectively (Curiel, 2000).

$$f_N = \frac{I}{C} A(1+\beta)\cos^2\Phi \tag{4.14}$$

$$f_T = \frac{I}{C} A(1-\beta)\sin\Phi\cos\Phi \tag{4.15}$$

Where,

$I =$ Solar radiation constant at mean sun-earth distance $1.36 * 10^3$ joule/m^2/sec
$C =$ Speed of light
$\beta =$ Optical reflection constantΦ.
$\beta = 1$ for mirror surface (total reflection).
$\beta = 0$ for blackbody (total absorbtion).
$\beta =$ -1 total transmission (transparent).
$A = A$rea of the sunlit part of the satellite in m^2.
$\Phi =$ Angle between the surface area and direction towards the sun

Satellites have complex geometries, with some areas being more reflective or transparent than others. This together with constant sun angle and location changes, makes the modelling of acceleration due to solar radiation pressure very complex. However, assuming that the satellite has a high reflectivity (Curiel, 2000) and that the acceleration will act along the sun-satellite direction, it follows that the acceleration can be expressed as:

$$f = -2\frac{I}{C}\frac{A_e}{m} r_{ss} \tag{4.16}$$

Where,

$A_e =$ Projected total sunlit area on a plane perpendicular to the satellite-sun direction.
$r_{ss} =$ Vector of unit lenght in the satellites-sun direction.

4.7 Atmospheric Drag

Drag can be defined as a force exerted on an object moving through air or liquid. This force acts opposite to the motion of the object and tends to slow the object down. When a satellite is in low earth orbit (600km) it is bombarded by gas molecules. This creates a drag force that acts opposite to the satellites velocity vector and thus removes energy from the orbit. Although atmospheric drag is and non-conservative force it is considered the most dominant force acting on low earth-orbiting satellites. The continuous frictional force will continually remove energy from the orbit until the satellite re-enters the atmosphere at which point it will start to disintegrate or burn up. The magnitude of the force due to atmospheric drag is expressed by equation (4.17)

$$F_{Drag} = -\frac{1}{2}\rho\left(\frac{C_D A}{m}\right)V^2 \tag{4.17}$$

Where,

$\rho =$ Atmospheric density $(\mathrm{kg/m^3})$ D
$C_D =$ Dimensionless drag coefficient assumed as 2.2
$A =$ Cross-sectional area $(\mathrm{m^2})$
$m =$ Satellite mass (kg)
$V =$ Orbital velocity of the satellite (m/s)
$F_{Drag} =$ Drag force (N)

The rate of a satellite's orbital decay largely depends on the atmospheric density (ρ). The value of the atmospheric density depends on the physical properties of the atmosphere. This is a complex parameter to accurately model since it fluctuates with time and geographic position. Thus, for an accurate atmospheric drag prediction, the selection of the appropriate density profile is of critical importance. C_D is a dimensionless drag coefficient and is dependent on the geometric form of the satellite. The drag coefficient for earth-orbiting satellites is generally assumed to be high ranging between 2 and 2.2 for satellite (Qiao, Rizos and Dempster, 2013). A high C_D implies that a satellite moves through the atmosphere with great resistance. The opposite is true for a low C_D value. The ballistic coefficient (BC) equation is given as $\frac{m}{C_D A}$. The ballistic coefficient can be considered a measure of the influence the atmosphere has on the satellites orbital decay. The Ballistic coefficient for satellites is typically in the range of 25 to 100kg/m^2. When the satellite has as low (BC) it responds rapidly to the atmosphere and will thus decay to faster. The opposite is true for satellites with high (BC) values (James Wertz, David Everett, 2011).

4.8 Atmospheric Density

The atmosphere of earth is a layer of gasses surrounding the planet and retained by earth's gravity. It comprises of a mixture of gasses which includes, Nitrogen (N_2), Oxygen (O_2) Argon (Ar), and water (H_2O). Atmospheric density is part of the atmospheric drag equation (equation 4.17), which makes it a critical component when calculating a satellite orbital lifetime.

Accurate atmospheric modelling is extremely complex because it varies with altitude, time, season, geographical latitude and longitude and solar activity. According to (Douglas L.Dowd and B.D.Tapley, 1979) atmospheric density is normally determined by using a priori model based on historical satellite data.

However, since atmospheric density exhibits such complex spatial and temporal variations the computed values will be inaccurate for real-time calculations, due to time lags in updating the parameters which account for solar and geomagnetic activity. For this reason, the atmospheric model selection is the main source of unreliable orbital lifetime predictions (Qiao, Rizos and Dempster, 2013).

4.8.1 Atmospheric Density Models

Atmospheric density models calculate the atmospheric density at three probable solar activity levels. 5%, 50% and 95% over several solar cycles (Afful, 2013). Three classes of atmospheric models are available, each one with focusing on different parameters. Below follows a brief discussion of the three classes.

4.8.2 Jacchia-Roberts Model

This model calculates atmospheric density values for altitudes at 90km and above. This is achieved by sectioning the atmosphere into three altitude groups , 90-100kms, 100-125kms and higher. The final condition in each lower band is the initial condition for the next higher band. This model also takes into account temperature profiles along with assuming certain values for the molecular mass of major atmospheric gasses (Douglas L.Dowd and B.D.Tapley, 1979).

When the attitude is greater than 125km an inverse tangent function for the temperature profiles is used. This model is commonly used in the determination for satellite drag forces. It has an accuracy ranging between 15-20% predicted total densities and 6-10% for the predicted temperatures (Bruinsma, Tamagnan and Biancale, 2004).

4.8.3 Mass Spectrometer and Incoherent Scatter Model

The Mass Spectrometer and Incoherent Scatter model (MSIS) is an empirical model. It describes the neutral temperature and densities in the earth's atmosphere by using data generated from satellites, rockets and incoherent scatter radars (Cox, 1994). The difference between the Jacchia- Roberts model and the MSIS, is that the MSIS accounts for the local density variations and the Jacchia-Roberts does not.

4.8.4 Cosmos Satellite-Derived Density Model

The foundation of this model is built on the data generated by the 145 Cosmos satellites from 1964-1970.This model calculates the atmospheric density by utilizing twenty constants derived by fitting density observations, over a range of altitudes and temperatures encountered by the satellites (Douglas L.Dowd and B.D.Tapley, 1979).

4.8.5 Effects of Atmospheric Density Model on Orbital Lifetime Predictions.

A study done by (Qiao, Rizos and Dempster, 2013) on the effects on orbital lifetime relating to the selection of the atmospheric density model, found that the orbital predictions of a 3U satellite can vary with as much as 20 years, depending on the model selected. The results are shown in Figure 4.3. Thus, selecting the appropriate density model is imperative when calculating orbital lifetime for a satellite.

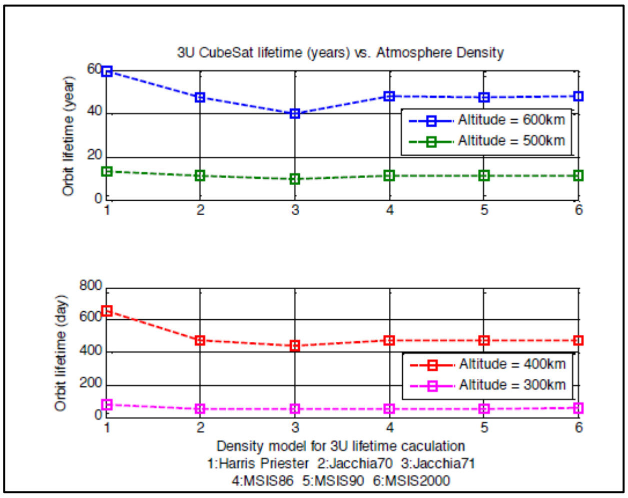

Figure 4.3: Orbital lifetime vs atmospheric model

(Adapted from Qiao, Rizos and Dempster, 2013)

4.9 NORAD Two-Line Elements Set

NORAD two-line element (TLE) set is a data format used to describe the orbital elements of a satellite as it orbits the earth (Croitoru and Oancea, 2016). The TLE’s can be used to compute satellite position at any time. This information is supplied by NASA and is readily and freely available to the public on the Celestrack website.

Figure 4.4 shows an example of all the orbital information contained in a typical two-line element data set.

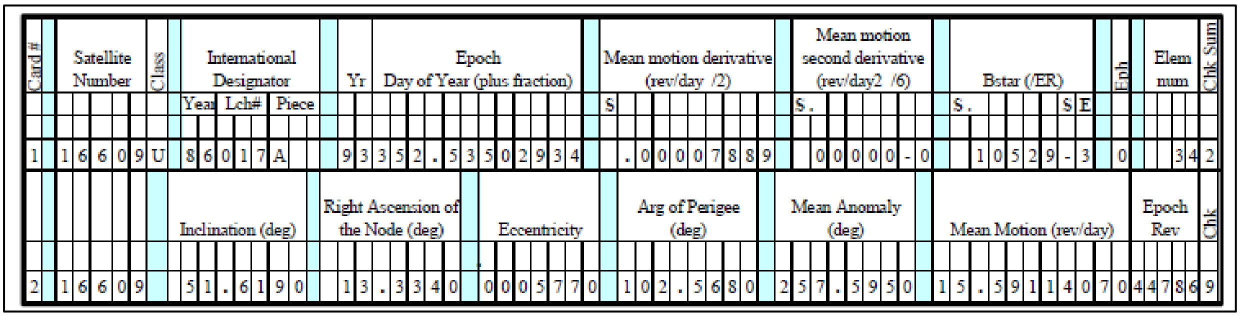

Card #	Satellite Number	Class	International Designator			Epoch		Mean motion derivative (rev/day /2)	Mean motion second derivative (rev/day2 /6)	Bstar (/ER)	Eph	Elem num	Chk Sum
			Year	Lch#	Piece	Yr	Day of Year (plus fraction)	$	$.	$. $ E			
1	16609	U	86	017	A	93	352.53502934	.00007889	00000-0	10529-3	0	34	2

Card #	Satellite Number	Inclination (deg)	Right Ascension of the Node (deg)	Eccentricity	Arg of Perigee (deg)	Mean Anomaly (deg)	Mean Motion (rev/day)	Epoch Rev	Chk
2	16609	51.6190	13.3340	0005770	102.5680	257.5950	15.59114070	44786	9

Figure 4.4: Two-line elements

(Adapted from Vallado and Cefola, 2012)

4.9.1 Two-Line Elements of ZACube-2

Below is the two-line element data set for ZACube-2. It contains all the elements shown in Figure 4.4

```
ZACUBE-2
1 43907U 18111AH  19188.18944290  .00000272  00000-0  13994-4 0  9990
2 43907  97.2890  92.9186 0020077 287.8639  72.0409 15.24199192 29268
```

By using the TLE description the data extracted from the set is as follows:

- Satellite name: ZACube-2
- Inclination(i) : 97.289º
- RAAN(Ω): 92.9186 º
- Eccentricity(e): 0.0020077
- Argument of perigee(ω): 287.8639
- Mean Anomaly(M): 72.0409 º
- Mean Motion(n): 15.24199192 orbits/day
- B* Value : 0.13994e-4

The TLE value does not directly show the apogee and perigee altitudes. Thus, to obtain the apogee and perigee altitudes the TLE file was converted using STELA TLE conversion tool.

- Apogee altitude : 504.07 km
- Perigee altitude : 476.49 km

Chapter 5

5 Software Simulation Environment

5.1 Introduction

This chapter describes the simulation methods and methodology implemented in this study. NASA's Debris Assessment Software 2.0 (DAS 2.0) was used to perform simulations. This software package was selected since its propagators and space environment models are regularly updated. Unlike other software packages, DAS does not require the user to input solar flux values or to select an atmospheric model, instead, the user is asked to input the launch dates and the software selects the most updated and appropriate values. This is an important function because solar flux values are used to calculate atmospheric drag experienced by the satellite. Thus, if outdated values are used it will result in inaccurate results. Consequently, by not allowing the user to select different atmospheric models, it creates less room for human error and outputs more reliable results.

5.2 DAS 2.0 Simulation Environment

The graphical user interface (GUI) of DAS consists of three main tabs known as mission editor, requirement assessments and science and engineering. Each of these tabs branches out to various operations that can be performed by the software. The Science and engineering tab were selected to utilize the orbit evolution analysis tool seen in Figure 5.1. The user simply enters the orbital elements of the satellite and clicks run. The program will show the results in the output section.

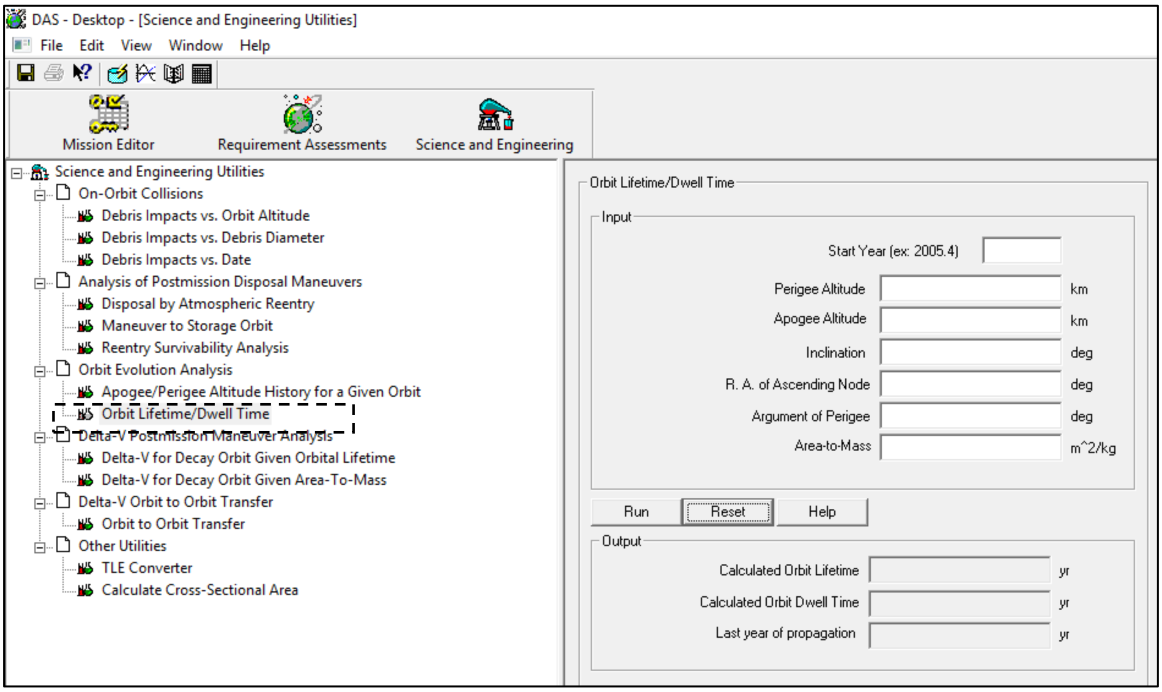

Figure 5.1:DAS main window

5.3 Propagators used in DAS 2.0

NASA’s “PROP3D” and “GEOPROP” propagators are used by DAS to perform complex orbital calculations. GEOPROP is used to calculate the motion of satellites in geosynchronous orbits, while PROP3D is used to calculate the orbits for all other objects. Both are designed to maintain accuracy over long propagation periods with reasonable computational speeds. Additionally, both accounts for all significant perturbing forces, which influences the orbital lifetime of the satellite. A table listing the propagators and reference models used can be found the appendices section.

5.4 Scientific Decimal time

The scientific decimal time format has been used by astronomers to calculate the time elapsed between two events during a study. In this time format the years, days, hours, minutes and seconds as we know it, are divided into 10 equal parts. This makes plotting a graph of elapsed time much easier.

The scientific decimal time format is used in the DAS software package to predict the orbital lifetime of a satellite. Decimal time is identified using a decimal e.g. 5.508 years. However, in general, this time format does not really give the user any useful information and thus needs to be converted to UTC Time in other words, years, days hours and, minutes. The algorithm behind the conversion of the decimal time falls out of the scope of this study, therefore an online converter was used to convert the decimal time to Coordinated Universal Time (UTC) time format.

5.5 Data Preparation for Orbital Lifetime Analysis Baseline Case

To perform orbital lifetime analysis on ZACube-2, the orbital parameters and general information such as satellite launch date, final mass, and final cross-sectional area were needed. The Orbital parameters were extracted from the satellites TLE file discussed in chapter 4.9. In addition, the general satellite information was provided by FSATI. The data seen in table 5.1and table 5.2 summarises the orbital parameters and general information for ZACube-2.

Table 5:1: Orbital parameters of ZACube-2

Apogee(km)	Perigee(km)	Inclination(deg)	RAAN(deg)	Argument of perigee(deg)
504.01	476.49	97.289	92.918	287.863

Table 5:2: General satellite information

Launch Date	Launch date (decimal years)	Final Mass(kg)	Cross-sectional Area (m^2)	Area/mass(m^2/kg)	Ballistic Coefficient (kg/m^2)
27/12/2018	2018.9877	3.8	0.03	0.0079	57.57

The values seen in table 5.1 and table 5.2 were used as the baseline values during the orbital lifetime analysis because it does not include any drag enhancement devices, thus, the results obtained using these values were used as the point of reference to which the rest of the simulation results were compared to. It should also be noted that the ballistic coefficient was calculated using $\beta = \frac{m}{C_D A}$. The C_D value is a dimensionless drag coefficient and is dependent on the geometric form of the satellite. For earth-orbiting satellites, the C_D values range between 2 and 4. However, from literature, we know that a value of 2.2 is used when calculating the ballistic coefficient for cube satellites. This value is also used in DAS software. Since the C_D is a constant in the ballistic coefficient formula, the only other parameters that can affect the orbital decay rate during simulation is the area/mass value. Consequently, these parameters were varied during simulations by adding drag enhancement devices. The results of these simulations are illustrated and analysed in chapter 6.

5.5.1 Data Preparation for ZACube-2 with no Drag Enhancement Device.

The values seen in Table 5:3, were used to predict the orbital lifetime of ZACube-2 as is. In other words, these values and results generated after simulation are used as the standard orbital lifetime expected for ZACube-2 without any de-orbiting device.

Table 5:3: Baseline Case study

Final Mass (kg)	Cross-sectional Area (m^2)	Area/mass(m^2/kg)	Ballistic Coefficient (kg/m^2)
3.8	0.03	0.0079	57.57

5.5.2 Data Preparation for Case Study 1: Inflatable Pillow Device

This case was based on the research conducted by (Lokcu and Ash, 2011) in which the cross-sectional area was increased by 0.37m^2, thus increasing the overall cross-sectional area from 0.03m^2 to 0.4m^2. Consequently, the area/mass parameter and ballistic coefficient decreases to 0.11m^2/kg and 4.31 kg/m^2 respectively. Table 5:4 summarises these parameters.

Table 5:4: Case study 1

Final Mass (kg)	Cross-sectional Area (m^2)	Area/mass(m^2/kg)	Ballistic Coefficient (kg/m^2)
3.8	0.4	0.11	4.31

5.5.3 Data Preparation for Case 2 Solar Sail

Case study 2 was based on the solar sail concept. An additional 10m^2 was added to the original cross-sectional area which increased to 10.03m^2. The additional cross-sectional area was based on the study of the Nanosail-D2 done by NASA and is discussed in the literature review. Table 5.5 is a summary of the parameters used during simulations.

Table 5:5: Case study 2

Final Mass (kg)	Cross-sectional Area(m^2)	Area/mass(m^2/kg)	Ballistic Coefficient(kg/m^2)
3.8	10.03	2.6	0.092

5.5.4 Data Preparation of Case Study 3: New Inflatable Cube Design Concept

This case study was based on a new concept that was created as a result of this research. The addition of this device increased the overall cross-sectional area to 0.52m^2.Table 5:6 summarises the parameters for the case study in question.

Table 5:6: Case study 3

Final Mass (kg)	Cross-sectional Area (m^2)	Area/mass(m^2/kg)	Ballistic coefficient(kg/m^2)
3.8	0.52	0.14	3.32

Chapter 6

6 Results and Discussion

6.1 Introduction

This chapter displays the results generated from the simulations performed in the DAS 2.0 software package. During this study, the effects of drag enhancement devices on ZACube-2's orbital lifetime predictions was investigated. A comparisons study related to the predicted orbital lifetime of the CubeSat was conducted using various drag enhancement devices. These included an inflatable pillow structure, a drag sail, and a new inflatable cube de-orbiting device (ICDD) concept. Two deployment concepts were presented. The most suitable concept was identified using a concept evaluation tool. The best concept was modelled in Solidworks followed by finite element analysis. Additionally, the effects of other parameters, such as mass variation affecting the orbital lifetime predictions of ZACube-2 were also investigated in the form of a mass sensitivity study.

6.2 Orbital Lifetime Assessment Process

To ensure the results obtained from the simulations are reliable and true, the same procedures and processes needed to be followed for each simulation. The components affecting these processes are seen in figure 6.1 below. This step by step process was followed each time simulation was performed. Thus, by following these steps the results obtained maintained their integrity.

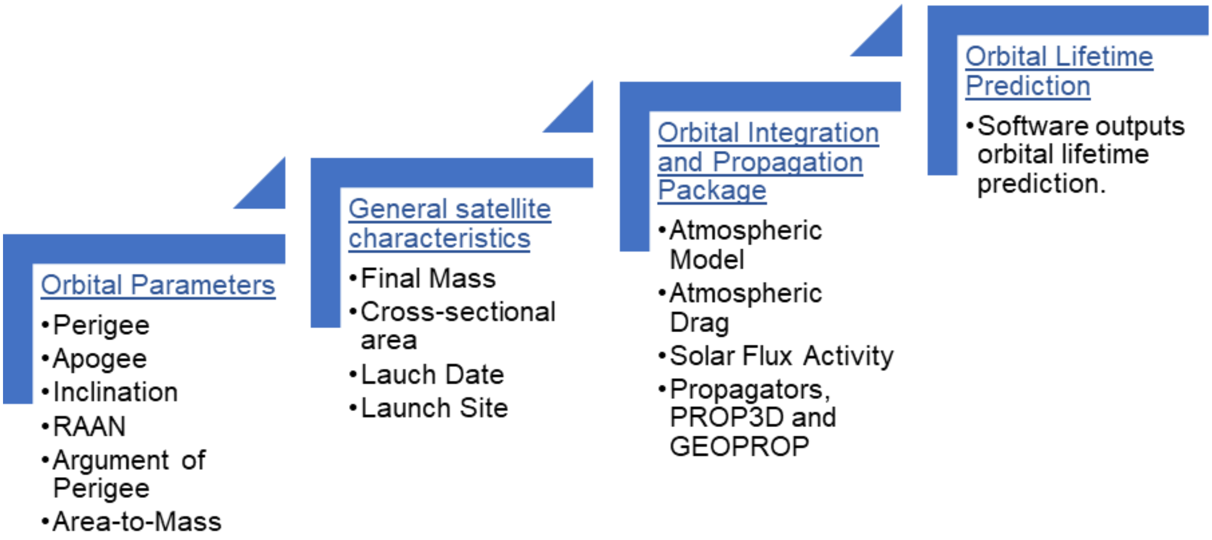

Figure 6.1: Orbital lifetime assessment process

6.3 Simulation Results

This section displays the results generated during the de-orbiting simulations for ZACube-2. Four missions were simulated, each with different area-to-mass values, while the initial orbital parameters were kept constant.

6.3.1 Baseline Case: Orbital Lifetime Predictions for ZACube-2 with no Drag Enhancement Device.

To be able to compare the changes in the orbital lifetime of ZACube-2, a baseline case was created. In the first case study, no parameters were changed or varied. The results showed that ZACube-2 has a predicted orbital lifetime of 4.047 decimal years.

This translates into an orbital lifetime of 4 years,17 days (1477Days). Natural re-entry will occur in the year 2023. This can be seen in Figure 6.2 and Figure 6.3 respectively. Furthermore, figure 6.2 shows the input files needed to predict the orbital lifetime as well as the year of re-entry.

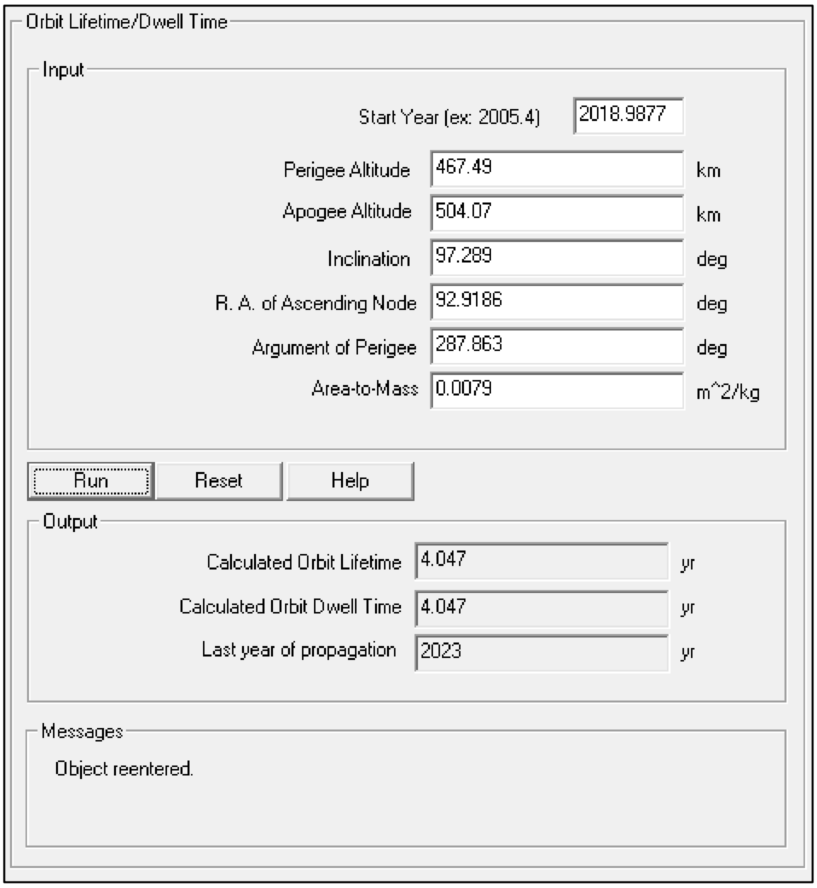

Start Year (ex: 2005.4) 2018.9877
Perigee Altitude 467.49 km
Apogee Altitude 504.07 km
Inclination 97.289 deg
R. A. of Ascending Node 92.9186 deg
Argument of Perigee 287.863 deg
Area-to-Mass 0.0079 m^2/kg

Calculated Orbit Lifetime 4.047 yr
Calculated Orbit Dwell Time 4.047 yr
Last year of propagation 2023 yr

Object reentered.

Figure 6.2: ZACube-2 orbital lifetime prediction when fitted with no drag enhancement device

Figure 6.3 depicts the natural de-orbiting prediction and shows the fluctuations in the apogee and perigee altitudes. The top line marked by the upward-facing triangles represents the apogee altitude. The second line marked with crosses represents the perigee altitude. From the graph variations in both apogee and perigee heights can be seen. This is due to space weather and to secular changes in the semi-major axis and orbit eccentricity, which is a result of the perturbation forces of atmospheric drag and solar radiation pressure. Since ZACube-2 is in a LEO, these forces predominantly affect the orbital decay of the CubeSat.

Along with the noticeable fluctuations of both apogee and perigee, it is also evident that the lines converge at an approximate height of 250Km. A bigger scaled image of Figure 6.3 can be found in the appendix section D-2.

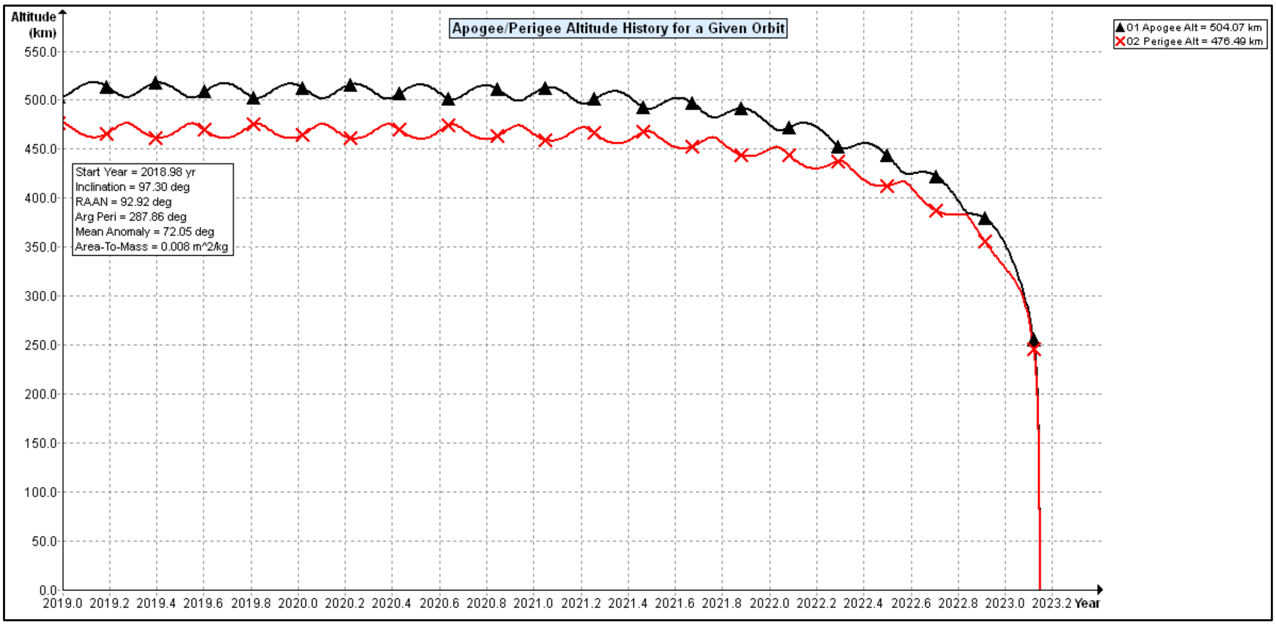

Figure 6.3: Graphical output for ZACube-2 orbital lifetime prediction with no drag enhancement device

The change in velocity required for ZACube-2 to deorbit from LEO with an orbital lifetime of 4 years and 17 days and the area-to-mass ratio of 0.008m^2 is 12.5m/s. This can be seen in Figure 6.4 and is identified by the line marked with a cross. The 2 remaining lines identified by the square and circle show the change in velocity (△V) if the orbital lifetime of ZACube-2 of 3 and 5 years were. It shows a (△V) of 7.5m/s and 11.2m/s respectively.

Furthermore, it can also be noticed that the higher the altitude is the bigger the change in velocity required to move into a decaying orbit. This makes sense because if the satellite is closer to earth, the orbital speed is much higher and requires a smaller change in velocity.

However, if the satellite is further from earth it has a slower orbital speed and thus needs a bigger change in velocity to reach a decaying orbit. A bigger scaled graph of Figure 6.4 can be found in the appendix section C.

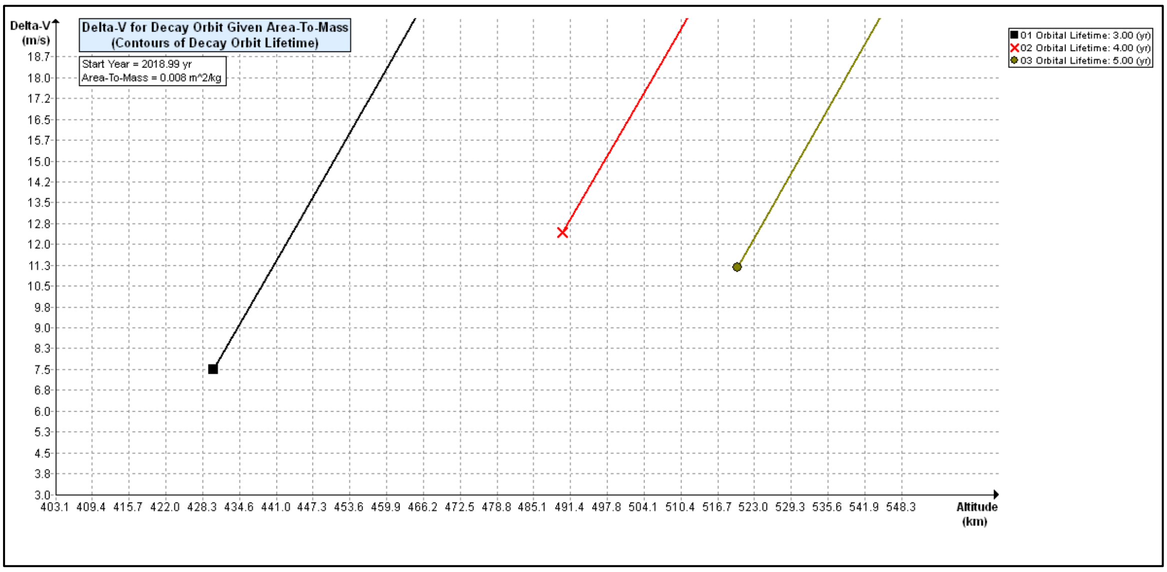

Figure 6.4: Delta-V required for decaying orbit with area-to-mass of 0.008m^2

6.3.2 Case Study 1: Orbital lifetime Prediction for ZACube-2 with Inflatable Pillow Structure.

In the second case study, ZACube-2 was hypothetically fitted with an inflatable pillow structure, which is based on the research conducted by (Lokcu and Ash, 2011). The results showed that when the device is deployed, the orbital lifetime prediction decreased to 1.889 decimal years. This translates into an orbital lifetime of 1 year and 10 months (689 days) after deployment of the device and is thus a 53% reduction in the orbital lifetime estimation.

During this case study, the cross-sectional area of the satellite was increased to 0.4m^2. This increase was due to the additional cross-sectional area provided by the inflatable pillow structure. Since the effective cross-sectional area was increased while the mass was kept constant the area-to-mass value increased from 0.0079m^2 to 0.11m^2.

The increase in the area-to-mass parameter resulted in an increased drag force, which increased the satellites orbital decay rate with such an effect that it is predicted to deorbit within less than two years. The predicted re-entry is early 2021 and can be seen in Figure 6.6 .Figure 6.5 shows the input data used during the simulation.

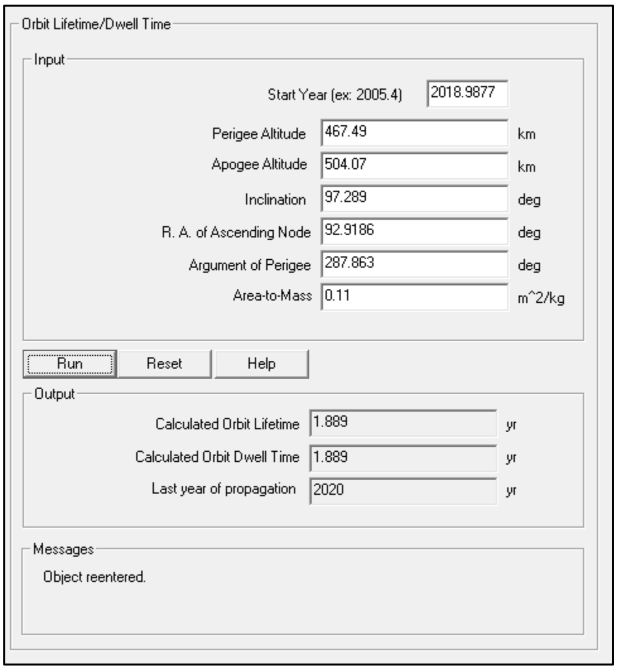

Start Year (ex: 2005.4) 2018.9877

Perigee Altitude 467.49 km

Apogee Altitude 504.07 km

Inclination 97.289 deg

R. A. of Ascending Node 92.9186 deg

Argument of Perigee 287.863 deg

Area-to-Mass 0.11 m^2/kg

Calculated Orbit Lifetime 1.889 yr

Calculated Orbit Dwell Time 1.889 yr

Last year of propagation 2020 yr

Object reentered.

Figure 6.5: ZACube-2's orbital lifetime prediction when fitted with inflatable pillow structure

Figure 6.6 is a graphical representation of the predicted de-orbiting of ZACube-2 when fitted with the drag enhancement device. The graph also shows the fluctuations of the apogee and perigee heights as well as the line convergence at 250km. When comparing the point of convergence to the baseline case, the point of convergence of case study 1 is at a higher altitude. Therefore it can be deduced that, the decaying orbit commenced sooner and resulted in a shorter de-orbiting time.

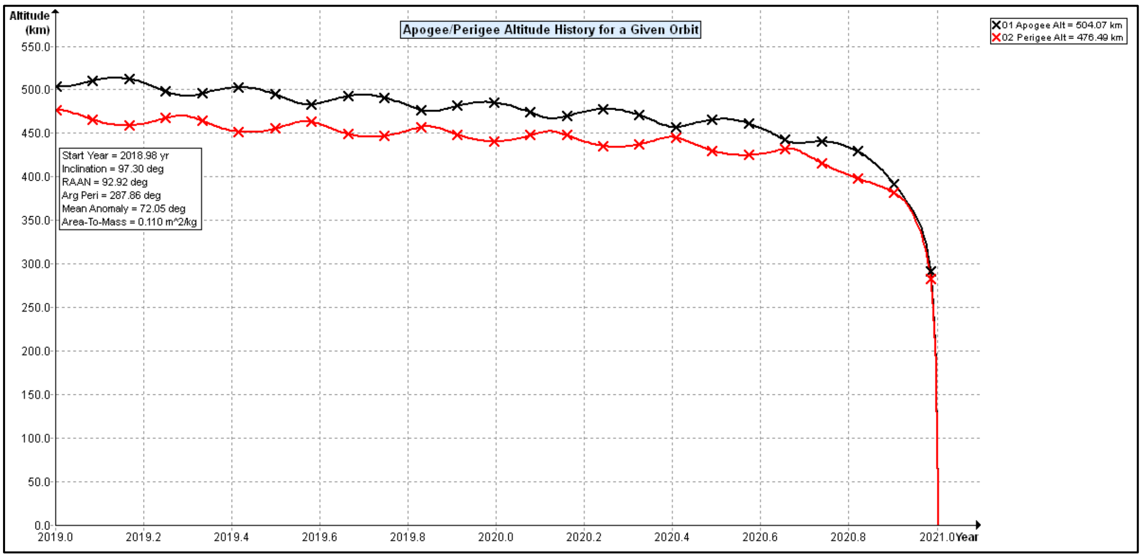

Figure 6.6: Graphical output of the orbital lifetime prediction of ZACube-2 with inflatable pillow structure

6.3.3 Case Study 2: Orbital Lifetime Predictions of ZACube-2 Fitted with a Drag Sail

In the third case study, the effects of the addition of a drag sail with a cross-sectional area of $10m^2$ were simulated. The results showed a massive orbital life reduction from 4 years to 28 days, which is a reduction of 98%.

This is mainly due to the significant increase in the area-to-mass ratio from $0.0079m^2$ to $2.6m^2$. The satellite is expected to re-enter in January 2019, which is less than a month after launch. Figure 6.7 shows the input data used during the simulations as well as the year of re-entry.

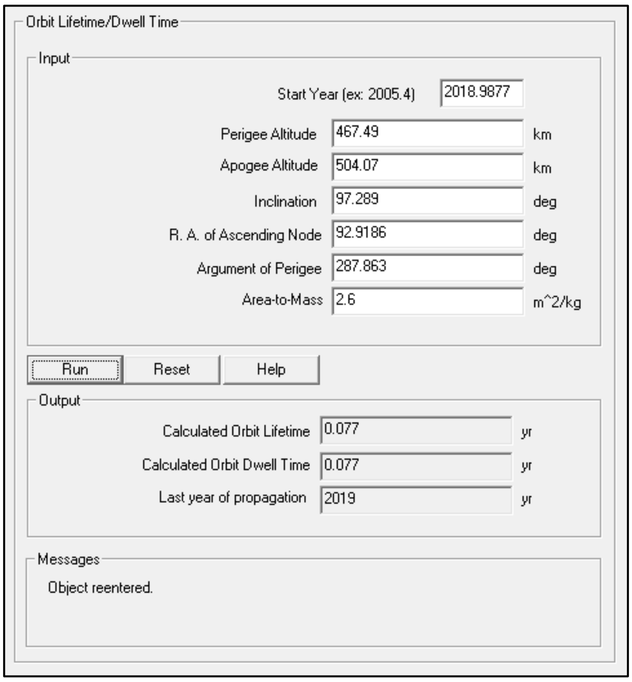

Orbit Lifetime/Dwell Time

Input

Start Year (ex: 2005.4) 2018.9877
Perigee Altitude 467.49 km
Apogee Altitude 504.07 km
Inclination 97.289 deg
R. A. of Ascending Node 92.9186 deg
Argument of Perigee 287.863 deg
Area-to-Mass 2.6 m^2/kg

Output

Calculated Orbit Lifetime 0.077 yr
Calculated Orbit Dwell Time 0.077 yr
Last year of propagation 2019 yr

Messages

Object reentered.

Figure 6.7: ZACube-2 orbital lifetime prediction when fitted with $10m^2$ drag sail

Figure 6.8 is a graphical representation of the predicted orbital lifetime when ZACube-2 is fitted with the $10m^2$ drag sail. This graph shows a much steadier decrease in both apogee and perigee heights when compared to the previous cases. This is due to the significantly larger cross-sectional area.

Furthermore, since the predicted orbital lifetime was only 28 days, the lack of apogee and perigee altitude variations also speaks to how solar activity levels affects the satellites orbital lifetime predictions. From Figure 6.8 the point of convergence can be approximated to just below 300km which is higher than the baseline case of 250km, which could indicate that the decaying orbit began sooner.

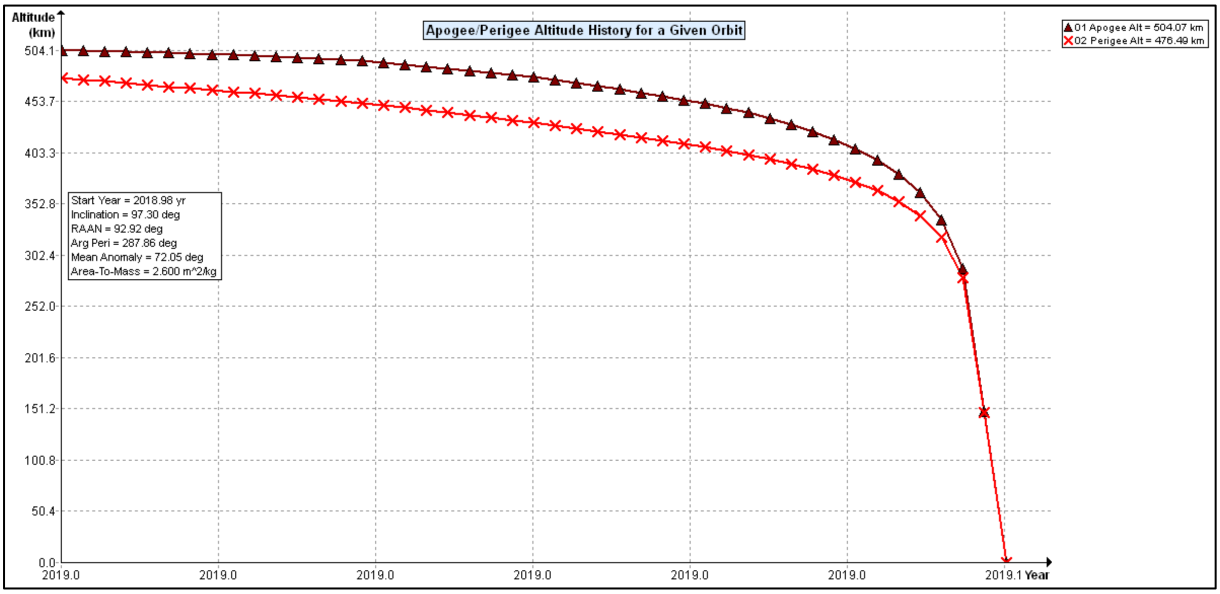

Figure 6.8: Graphical output of the Orbital Lifetime Prediction of Zacube-2 when fitted with $10m^2$ drag sail

6.3.4 Case Study 3: Orbital Lifetime Predictions of ZACube-2 Fitted with a $0.49m^2$ cube concept

The last case study is based on the addition of an inflatable cube concept. The idea behind the concept was inspired by the research done by (Lokcu and Ash, 2011). This concept involves the deployment of an inflatable cube structure, with a cross-sectional area of $0.49m^2$. The implications on the predicted orbital lifetime when fitted with this mechanism is seen in Figure 6.9 and Figure 6.10 respectively.

The predicted orbital lifetime after the mechanism is deployed is 1.654 decimal years. This translates to 1 year and 7 months (603 Days). The orbital lifetime was therefore reduced from 4 years to 1 year and 7 months after the deployment of the mechanism indicating a deduction of 59%

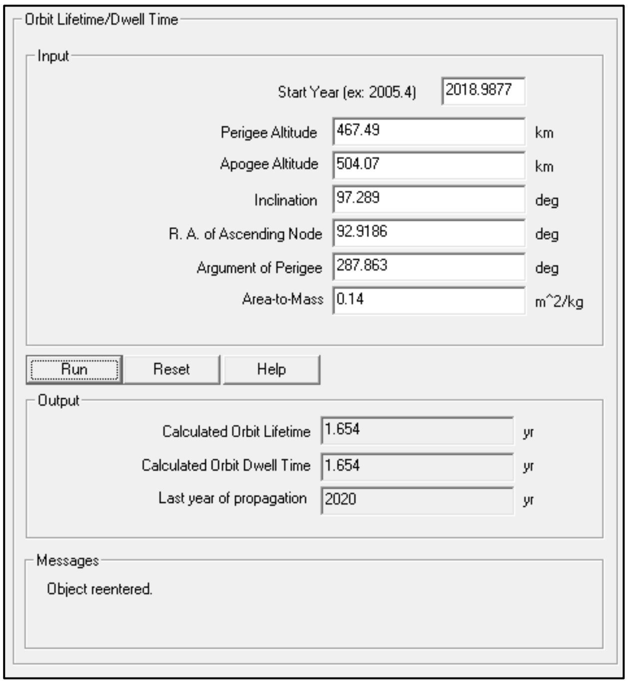

Start Year (ex: 2005.4) 2018.9877

Perigee Altitude 467.49 km

Apogee Altitude 504.07 km

Inclination 97.289 deg

R. A. of Ascending Node 92.9186 deg

Argument of Perigee 287.863 deg

Area-to-Mass 0.14 m^2/kg

Calculated Orbit Lifetime 1.654 yr

Calculated Orbit Dwell Time 1.654 yr

Last year of propagation 2020 yr

Object reentered.

Figure 6.9: ZACube-2 Orbital Lifetime Prediction when fitted with 0.49m^2 inflatable cube structure.

Figure 6.10 graphically shows the implementations on the predicted orbital lifetime of ZACube-2 when fitted with the cube mechanism. The upper line marked with the triangle-shaped shows the fluctuation in the apogee altitude. This is followed by the lower line indicating the fluctuations of the perigee altitude. Both lines exhibit fluctuations, due to changes in solar activity. The point at which the lines converge can be approximated to just below 300km.

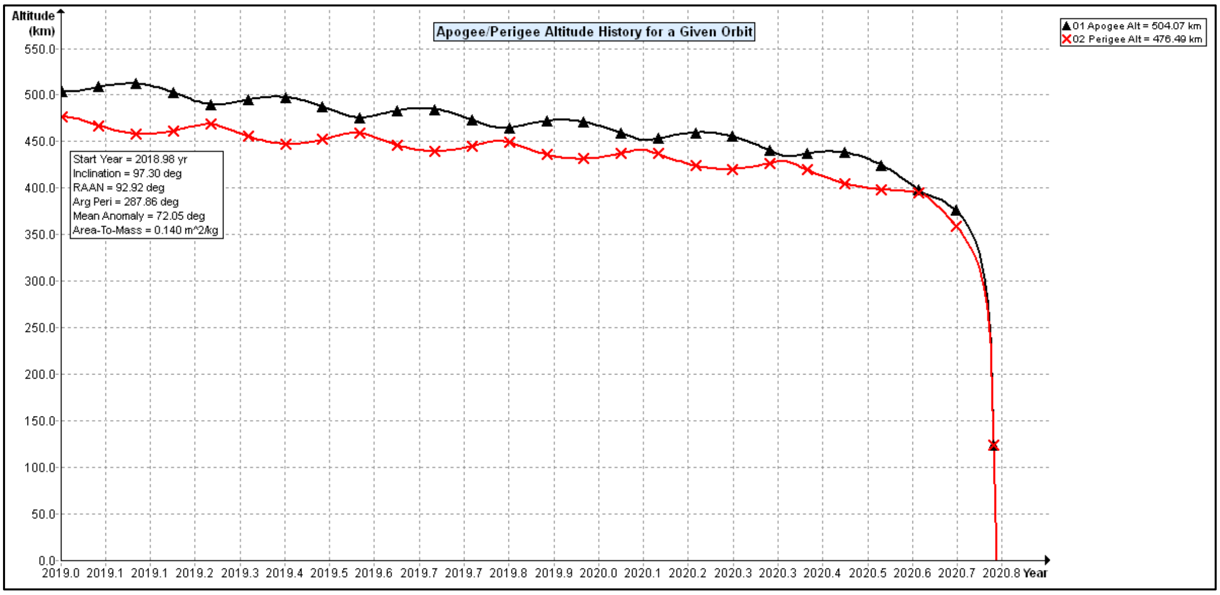

Start Year = 2018.98 yr
Inclination = 97.30 deg
RAAN = 92.92 deg
Arg Peri = 287.86 deg
Mean Anomaly = 72.05 deg
Area-To-Mass = 0.140 m^2/kg

Figure 6.10: Graphical output of the Orbital Lifetime Prediction of ZACube-2 when fitted with the new inflatable cube concept 0.49m^2

6.4 Mass Sensitivity Study

CubeSats should conform to the standardised geometry and mass specifications as set out in the CubeSat Design Specifications (CDS) documents published by California Polytechnic State University (Cal Poly). Version 13 of this document is currently the most updated version and gives the following mass restrictions.

Table 6:1: CubeSat mass variations

Mass for 1U	Mass for 2U	Mass for 3U
1.0kg - 1.33 kg	2.0kg - 2.66kg	3.0kg - 4.0kg

Ideally a 1U would have a mass of 1kg, 2U mass of 2kg and a 3U mass of 3kg, however, due to different manufacturing methods, the mass of these satellites varies which can be seen in Table 6:1. Satellite mass is related to the total mechanical energy of the orbit (equation3.19) and to aerodynamic drag (equation 4.17). Consequently, changes in the mass parameter will influence the orbital lifetime prediction of ZACube-2. Figure 6.11 shows a steady increase of orbital life over mass increments of 200grams. It indicates that with every 200grams of mass added, the orbital life will increase by an average of 28 days.

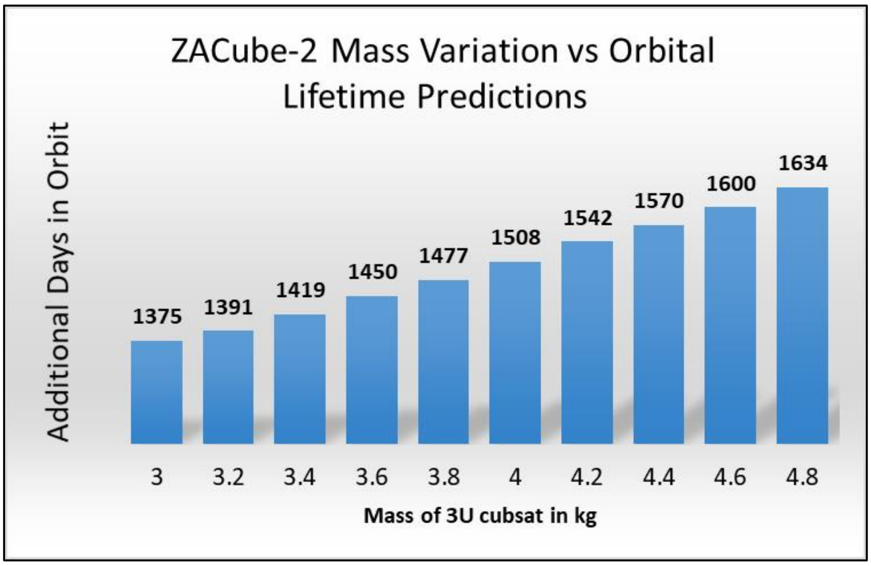

Figure 6.11: CubeSat Mass Variation study for ZACube-2

6.5 Cross-Sectional Area Analysis

Aerodynamic drag is one of the predominant forces that the CubeSat will experience and is directly related to the cross-section of the CubeSat. Figure 6.12 illustrates the results generated when the cross-sectional area was increased by increments of 0.2m^2. It indicated that an increase of 0.2m^2 reduced the orbital lifetime of ZACube-2 by an average of 21 days. This may seem like and negligible amount, however, if combined with mass reducing manufacturing methods such as additive manufacturing de-orbiting can be achieved.

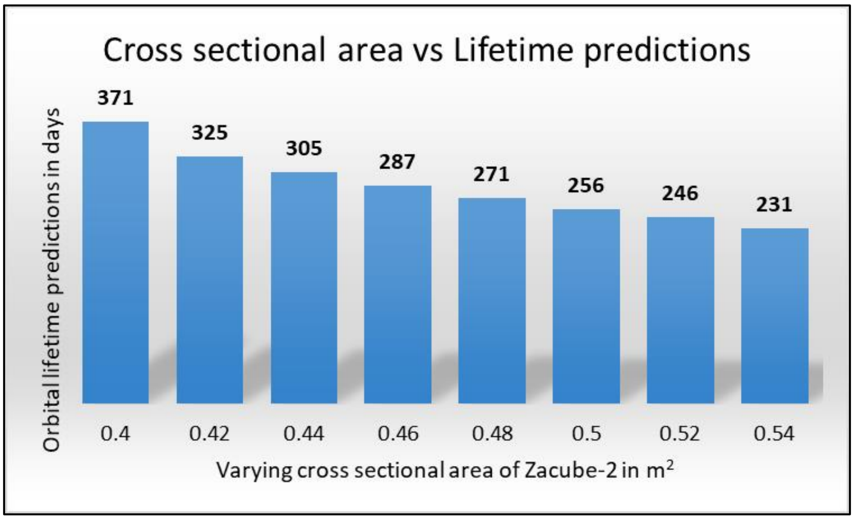

Figure 6.12: Cross-Sectional Variation Study

6.6 Ballistic Coefficient vs Orbital Lifetime

Results showing the changes in orbital lifetime predictions for ZACube-2 with different ballistic coefficients are presented in Figure 6.13. It is evident this value influences the predicted orbital lifetime.

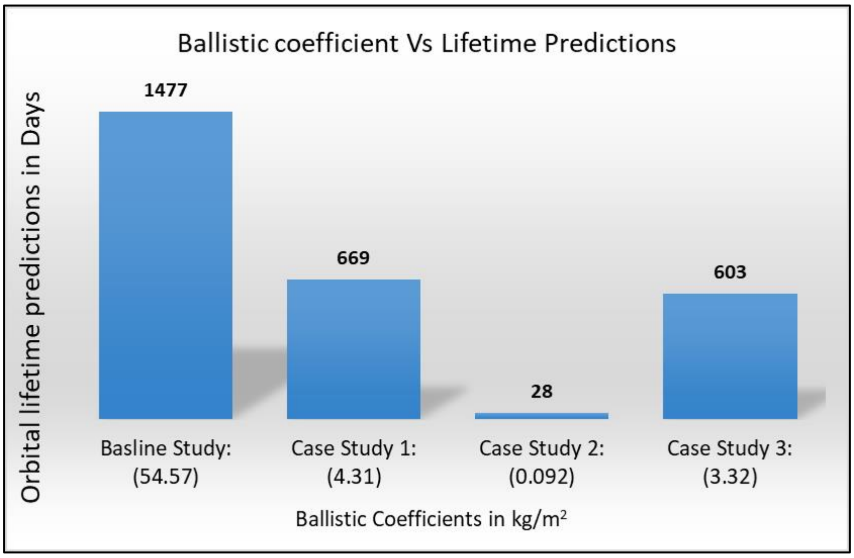

Figure 6.13: Ballistic Coefficient vs Orbital Lifetime Predictions for Zacube-2

6.7 Deployment Mechanism Concept Design

The evaluation of the passive de-orbiting methods completed in the literature review indicated that inflatable structures are a good and inexpensive method to achieve de-orbiting. Based on this evaluation and the simulations results, two concepts were created and evaluated. The design requirements and limitations are listed below.

Design requirements

- Comply with CubeSat standards
- Be able to cause de-orbiting within 25 years
- Must be easy to integrate into the CubeSat
- Not affect the performance of the CubeSat
- Be scalable
- Have a simplistic design for easier manufacturing purposes
- Must be lightweight

Design limitations

- Size
- Cost
- Mass

6.7.1 Concept 1: Deployment Using the mini frangibolts Actuator

This concept involves using two mini frangibolt actuators to keep the lid in place and remove the lid when deployment is needed. The frangibolts has a mass of 8 grams each and has an operational voltage of 6Volts. The diameter of the actuator is 12.7 mm. This actuator has been successfully used in previous space applications and is thus space proof. In this concept, the lid is completely removed from the structure, and thus as the advantage of not damage in the thin inflatable cube. However, it also has the disadvantage of adding extra debris to space in the form of discarding the lid in space.

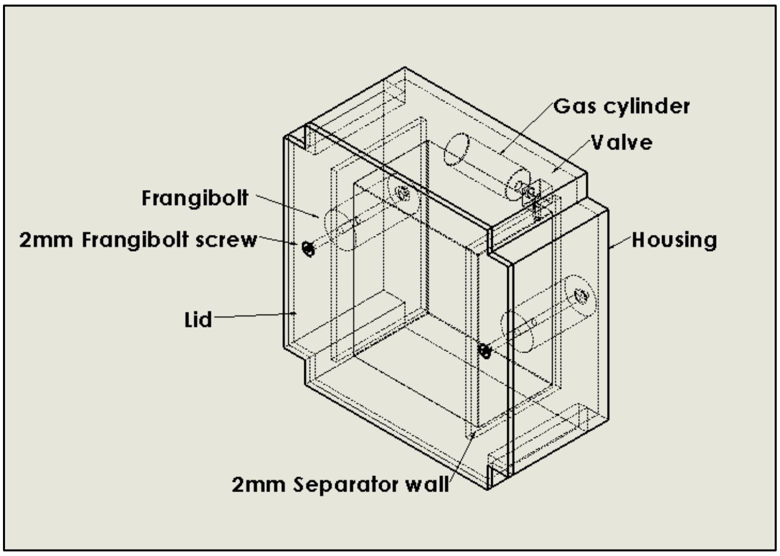

Figure 6.14: Concept 1

Table 6:2: Concept 1 advantages and disadvantages

Concept 1 Advantages
Actuator is relatively lightweight
The actuator is relatively small in diameter
No hinge to keep the door open, thus no extra weight
No interference of the door when the cube is being inflated
Remains inactive until deployment, therefore it does not affect the normal satellite operations
Concept 1 Disadvantages
The discard of the lid in space adds to the debris

6.7.2 Concept 2: Deployment Using Micro Latching Actuator

This concept involves using a micro latching actuator to open the door, this actuator has a mass of 15 grams each and require 14 volts to operate. The nominal diameter is 25.4mm. Once the lid has been opened, a self-locking hinge is required to keep the lid from closing again so that the inflate structure can be activated.

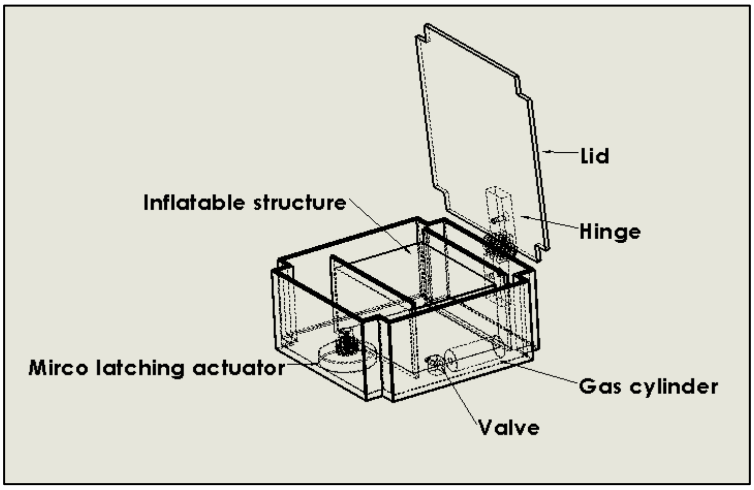

Figure 6.15: Concept 2

Table 6:3: Concept 2 advantages and disadvantages

Concept 2 Advantages:
Does not add to the growing debris
Remains inactive until deployment, therefore it does not affect the normal satellite operations
Concept 2 Disadvantages:
Self-locking hinge adds weight to the CubeSat
Big actuator diameter
Mass of the actuator
Requires high operational voltage

6.7.3 New Concept Evaluation

The two concepts presented were evaluated using evaluations tool which assigns a numeric value to each concept design requirements, where one is the most important and in three least important. During the evaluations the all the design requirements and their corresponding level of importance are weighed against both concepts. Each concept is then scored out of three. Where 1 is the best and 3 is the worst. The total score provided by each concept will differentiate which concept is the most suitable for de-orbiting a CubeSat.

Table 6:4: Concept design requirements

Design Requirements:	**Level of importance:**
Mass of Concept	1
Must comply with CubeSat standards	1
Must be able to cause de-orbiting within 25 years	1
Must not affect the performance of the CubeSat	1
Must be easy to integrate into the CubeSat	1
Satellite Operation Interference	2
Design Simplicity	2
Scalability	3

From table 6.5 concept 1 achieved the lowest score and is thus recommended concept.

Table 6:5: New concept elevation

Design Requirements:	**Concept 1**	**Concept 2**
Mass of Concept	1*1	1*3
Must comply with CubeSat standards	1*1	1*1
Must be able to cause de-orbiting within 25 years	1*1	1*1
Must not affect the performance of the CubeSat	1*1	1*2
Must be easy to integrate into the CubeSat	1*2	1*2
Satellite Operation Interference	2*2	2*2
Design Simplicity	2*2	2*3
Scalability	3*2	3*2
Total score	**20**	**25**

6.8 Overview of the New Inflatable Cube De-Orbiting Device (ICDD) Concept

Figure 6.16 gives an overview of the de-orbiting device. It consists of two mini frangibolt actuators situated at the right and left side of the housing. These actuators are used to hold the lid in place as well as release the lid of the housing when activated.

It also includes a gas cylinder, which houses the gas needed to inflate the folded cube structure. The folded structure is separated from the actuators by two separator walls and act as a protection barrier between the folded material and actuator when it is activated. The use of Aluminium 7075 or 6061-T6 is encouraged in the CDS document. Thus, the elements are housed in aluminium 6061 casing with dimensions, 90 by 90 and 40mm deep and a wall thickness of 2mm.

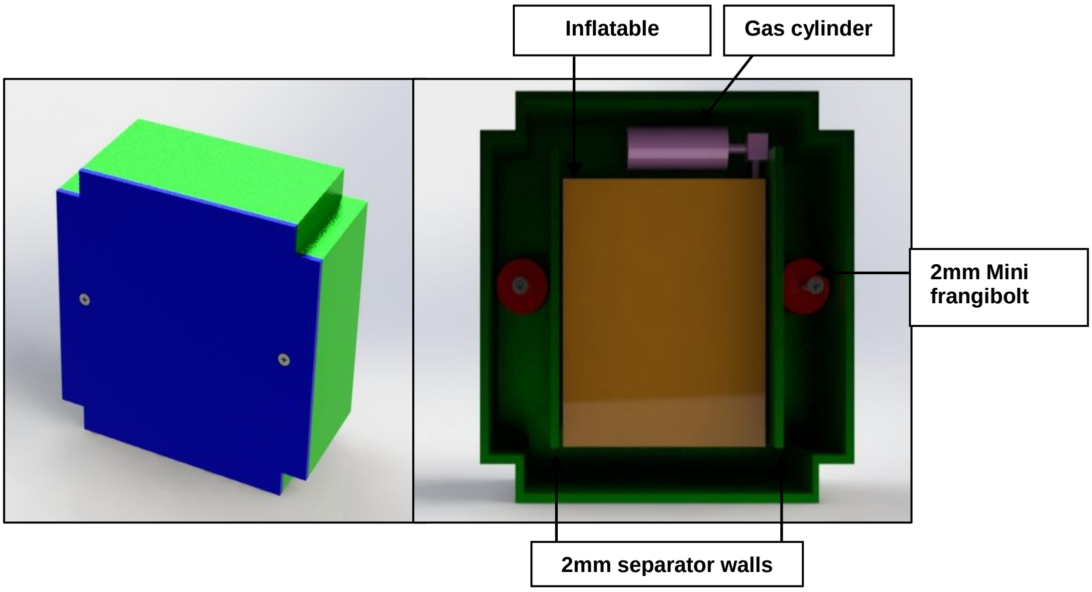

Figure 6.16: New concept design

6.8.1 Inflatable Cube Structure

The proposed device is a drag enhancement device and operates on the principle of increasing aerodynamic drag. The new concept is based on the same principle as that of (Lokcu and Ash, 2011) in the sense that it investigates the effectiveness of an inflatable drag enhancement device. However, having studied, the principles of aerodynamic drag, it came to light that the projected area of the inflatable structure majorly affects the effectiveness of the device. Therefore, it follows that the geometry of the inflatable structure should be of such a nature that creates the highest amount of drag possible.

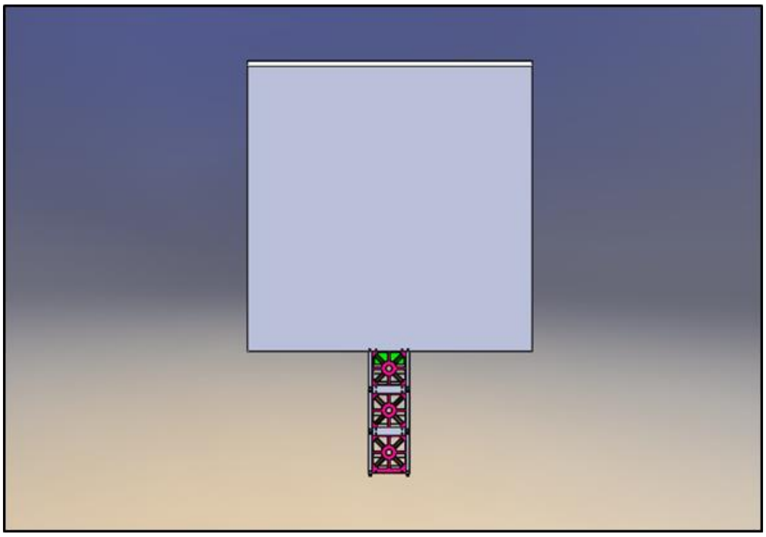

Figure 6.17: Inflatable cube concept deployed

Drag coefficients are used to describe how much resistance /drag an object or shape has when it moves through a fluid or air. If an object has a low drag coefficient it means that the body experiences low drag when moving through the air. Oppositely, if an object has a high drag coefficient it means that he objects experiences a high amount of drag when moving through the air. According to literature, the drag coefficient of a cube in space vacuum varies between 2 and 4, depending on depending on the attitude to the velocity vector (orientation), absorption and specular reflection (James Wertz, David Everett, 2011).It can therefore be reasoned that the cube geometry is suitably shaped for the inflatable structure as seen in figure 6.17. The proposed dimensions of the inflatable cube are 0.7 x 0.7 x 0.7m, this translates into a minimum projected area of 0.49m^2.

A minimum projected area of 0.49m^2 cube was assumed during simulations. Thus it translates to a single face of the cube being normal to the velocity. Although in practice this would require and active attitude control, the assumption served as conservative measure in the sense that the minimum projected area was used during lifetime estimations. However, if the cube rotates at 45º around one axis, the projected area increases to 0.69m^2.

Simulation results in case study 3, indicated that the combination of the cube's high drag coefficient and the additional cross-sectional area 0.49m^2 will add to the drag experienced by ZAacube-2 and cause it to deorbit within 603 days.

6.8.2 Inflatable Cube Material Selection

The space environment is harsh and unforgiving. One aspect of the environment is the extreme temperature changes which affect the structural integrity of materials. For this reason, the material selected for the inflatable cube is Upilex-Ca polyimide film. It offers a unique combination of electrical, thermal, chemical and mechanical properties that can withstand the harsh space environment.

Additionally, it offers a superior adhesive property which is an important factor during the assembly of the cube. It also has a low stiffness factor that will be advantages when folding the film into the desired shape. Lastly. It has a mass density of 1.49e3 kg/m^3 which gives an estimated mass for the cube to be 55 grams. A detailed material properties sheet can be found in the appendix section L.

6.8.3 Mass Analysis of the Inflatable Cube De-Orbiting Device Concept

Mass estimation analysis was completed which include, the housing, lid, inflatable structure, and mini frangibolts. The total mass of the concept excluding the gas cylinder is 0.69 kg. as seen in Table 6.6 below.

Table 6:6: Mass analysis of the de-orbiting concept

Component	**Mass (kg)**
Housing	0.13579
Lid	0.04211
Mini Frangibolts	0.016
Inflatable cube structure	0.055
Total	**0.2489**

6.8.4 Finite Element Analysis of the Housing

During launch CubeSats and their subsystems are exposed to various mechanical, thermal and electromagnetic environments. The three main types of mechanical loading are quasi-static, static and dynamic loading. Each of these loading conditions varies depending on the launch vehicle selected. These loads can cause plastic deformation and complete component failure. Therefore, to ensure the launch survivability of the structure containing the sub-elements of the de-orbiting device, finite element analysis was performed.

The Russian Soyuz rocket was used to launch ZACube-2 into orbit and is frequently used for CubeSat launches. Thus, the loading condition of the Soyuz rocket was used to perform the stress and deformation analysis followed by a worst-case scenario study in which the loads were increased. The table below shows the loading condition used during the finite element analysis.

Table 6:7: Launch Conditions for finite element analysis

	Longitudinal static acceleration (g)	**lateral static acceleration (g)**
Soyuz user's manual	4.3	0.4
Worst case scenario	15	5

6.8.5 FEA Results Using Soyuz Rocket Longitudinal Static Load on the Housing

Solidworks was used to model the forces that the housing of the de-orbiting mechanism will be exposed to. The magnitude of the applied force to the housing was 4.3g. The results are shown in figure 6.18 below. It indicates that the von Mises stress varies from a minimum of 120.404N/m^2 to a maximum of 1.16597e+006 N/m^2. The yield strength of aluminium 6061 is 5.51485e+007 N/m^2, which is higher than the maximum stress experienced by the housing. Therefore, it can be deduced that the structure will not fail under these loading conditions.

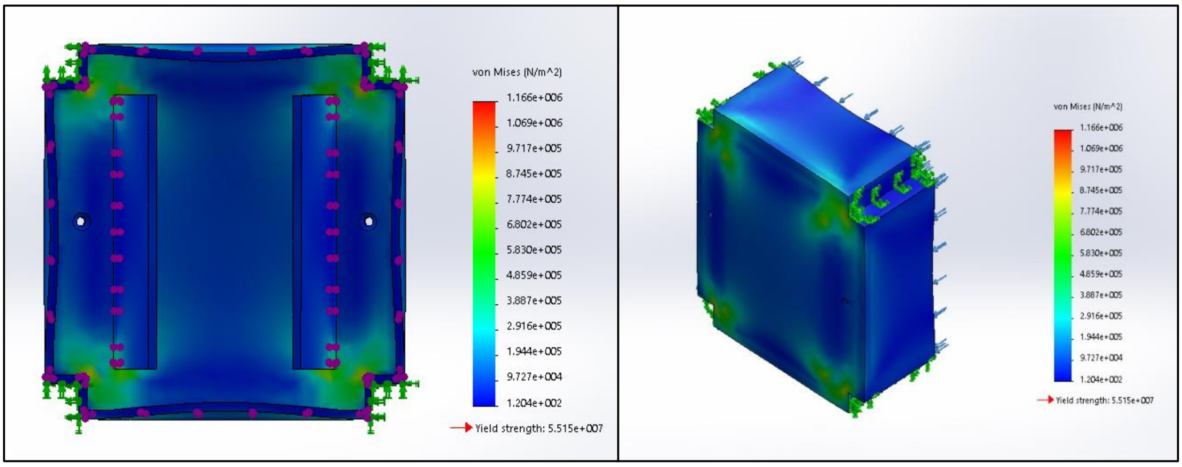

Figure 6.18: von Mises stress on housing under longitudinal Soyuz launch conditions

The maximum displacement was found to be 0.000150634 mm which occurs in the two inner sidewalls seen in figure 6.19. Considering the overall dimensions of the housing, this displacement is small and is within the structural limits of the material.

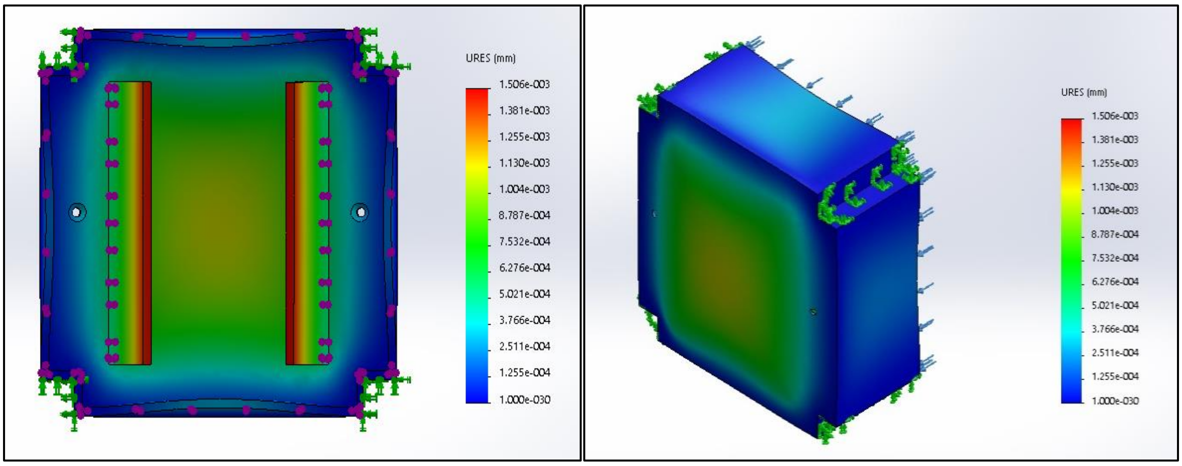

Figure 6.19: Housing displacement under longitudinal Soyuz launch conditions

6.8.6 FEA Results Using Soyuz Rocket Lateral Static Load on the Housing

The lateral stress analysis indicated minimum stress of 0.451514 N/m^2 and a maximum of 9403.9N/m^2. The maximum is well below the yield strength of aluminium 6061, thus the structure will not fail when exposed to the lateral load of 0.4g. Structural integrity is thus maintained.

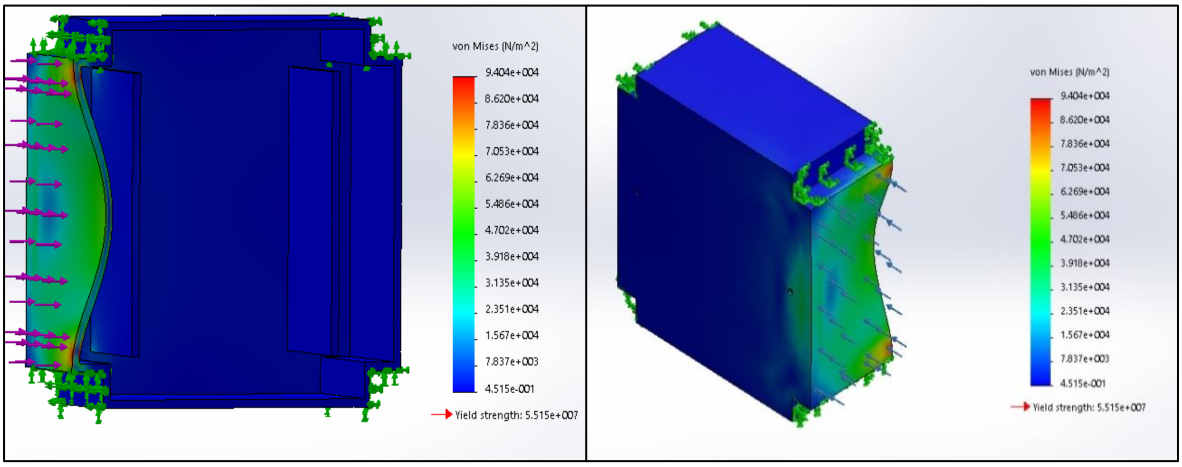

Figure 6.20: von Mises stress of housing under Soyuz lateral launch conditions

The maximum lateral displacement was found to be 0.00027mm which is minuscule when compared to the dimensions of the structure. The displacement is illustrated by the figure below.

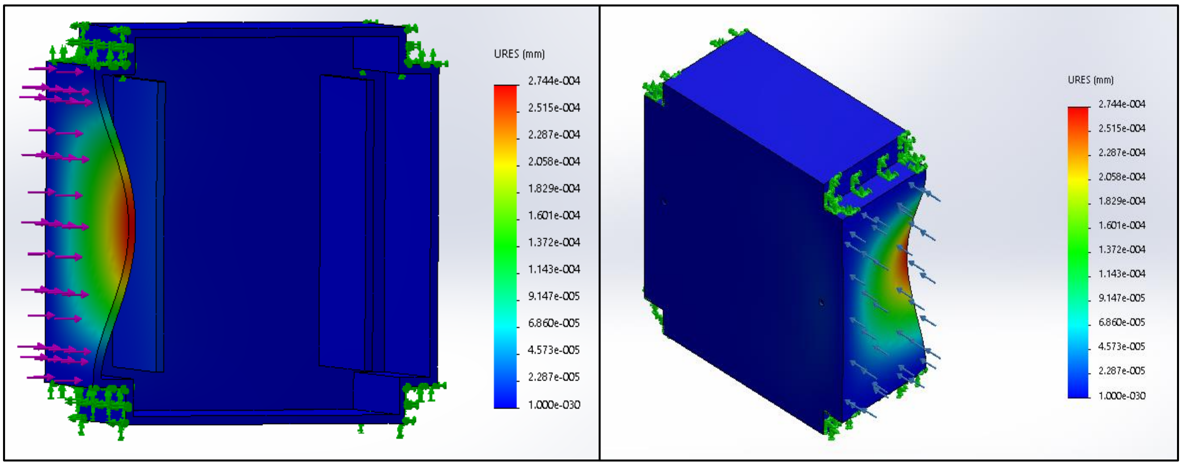

Figure 6.21: Housing displacement under Soyuz lateral launch conditions

6.8.7 FEA Results Using Soyuz Rocket Longitudinal Static Load on the Lid

Finite element analysis indicated a minimum von Mises Stress of 1496.82N/m^2 and maximum and 1.27347e+007 N/m^2 for the lid of the housing. Although the maximum stress is high, it is still less than the yield strength of the aluminium 6061 and thus within the structural limits of the material. The maximum displacement was found to be 0.0216mm, which is slightly higher than the housing displacement but remains within the limits of the structure. The figure below shows the von Mises stress and displacement of the lid when exposed to a 4.3g load.

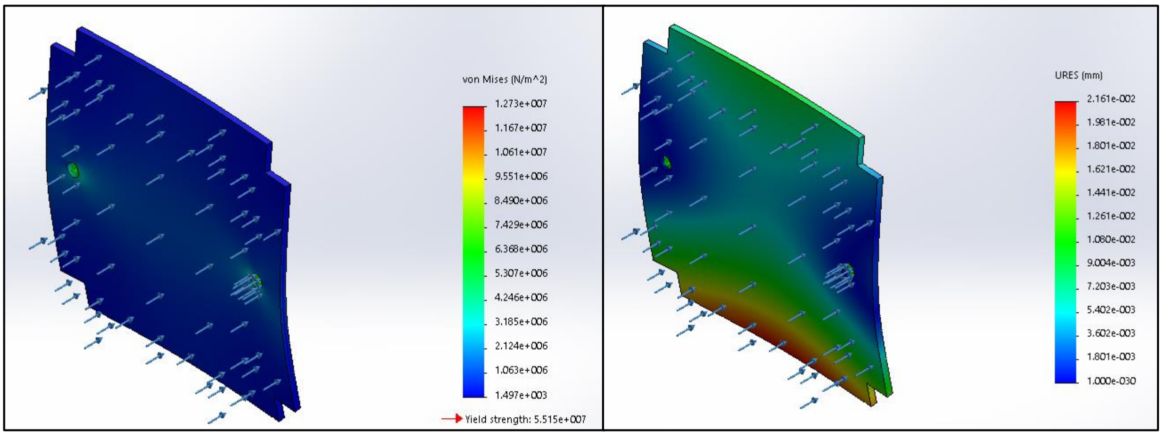

Figure 6.22: von Mises stress on lid (left) and displacement of lid (right) under Soyuz longitudinal launch conditions

6.8.8 FEA Results Using Soyuz Rocket Lateral Static Load on the Lid

Based on finite element analysis the minimum and maximum von Mises stress due to the lateral acceleration was 6.279N/m^2 and 97742.4 N/m^2 respectively. This is well below the yield strength of aluminium 6061 and is thus well within the structural limits of the material. The maximum displacement was 7.22e-006mm. The results of the stress and displacement under lateral loading are shown in the figure below.

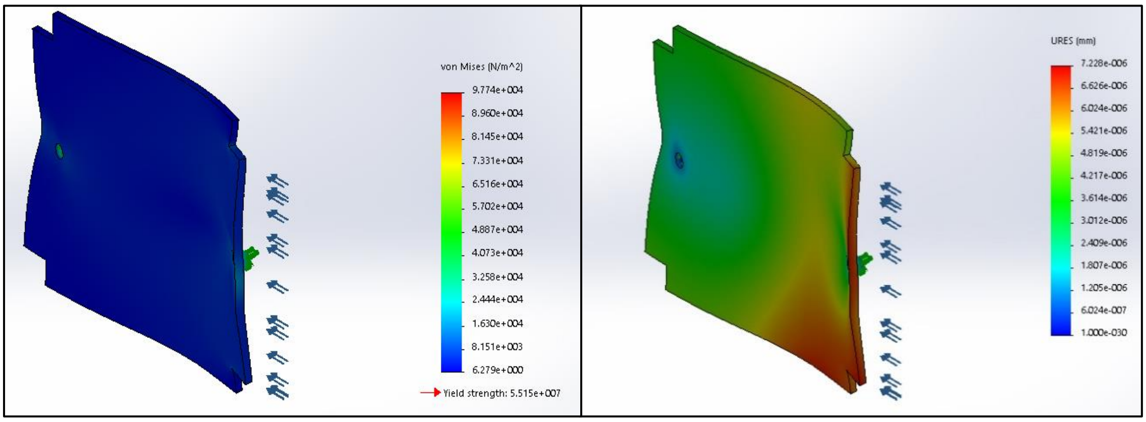

Figure 6.23: von Mises stress on lid (left) and displacement of lid (right) under Soyuz lateral launch conditions

6.8.9 FEA Results Using Worst-Case Scenario Longitudinal Loading on the Housing

Given that loading condition varies with each launch vehicle, a worst-case scenario was also simulated. The figure below shows the minimum and maximum von Mises stressed and displacement when the housing is exposed to a load of 15g. Based on finite element analysis the von Mises varies between 418168 N/m^2 and 4.04949e+006 N/m^2. The maximum stress under the longitudinal launch load of 10g is much higher than that of a normal 4g load, however, it is still within the structural limits of the material. The maximum displacement occurs in the inner sidewalls and was found to be 0.00523159 mm. The stress and displacement results under a longitudinal load of 15g are shown in the figure 6.24.

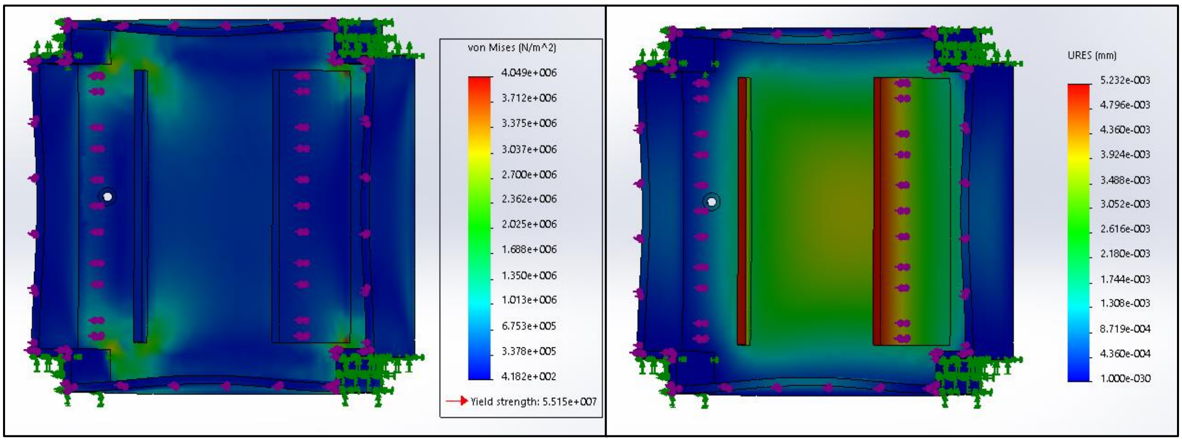

Figure 6.24: von Mises stress (left) and displacement (right) of housing under worst-case launch conditions

6.8.10 FEA Results Using Worst-Case Lateral Loading on the Housing

The von Mises under a lateral load of 5g varied between a minimum of 5.808N/m^2 and a maximum of 1.30189e+006 N/m^2. The maximum displacement was 0.00379793 mm. Although these values are significantly higher than that of the normal condition it is still within the limits of the material. Thus, the structural integrity is maintained under a 5g lateral load.

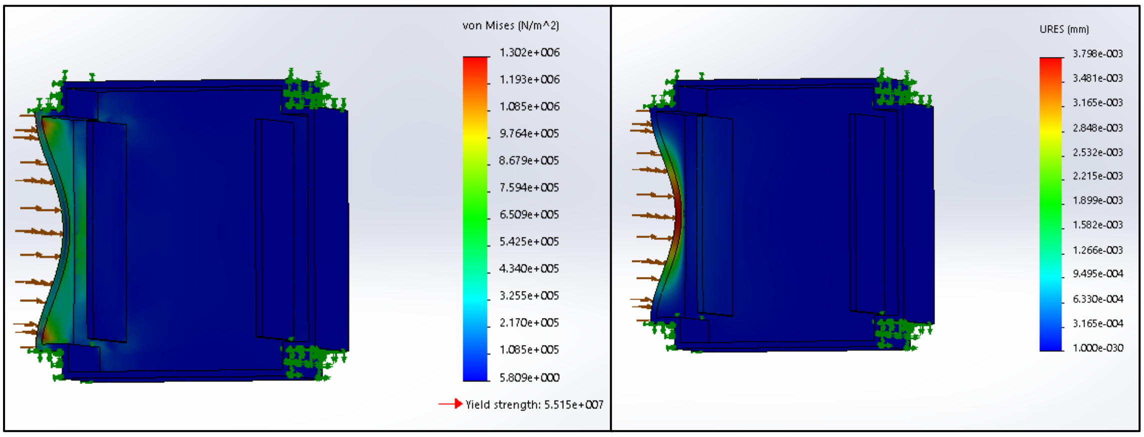

Figure 6.25: von Mises stress (left) and displacement (right) of housing under worst-case lateral launch conditions

6.8.11 FEA Results Using Worst-Case Scenario Longitudinal Loading Conditions on the Lid

Figure 6.26 below illustrated the results found during the worst-case simulation. A load of 15g was applied. Finite element analysis indicated that the minimum and maximum stress was 2012.18 N/m^2 and 1.34828e+007 N/m^2 respectively and is mainly located at the M2 fixture holes. The maximum displacement is 0.0203127mm and is most prevalent at the bottom of the lid.

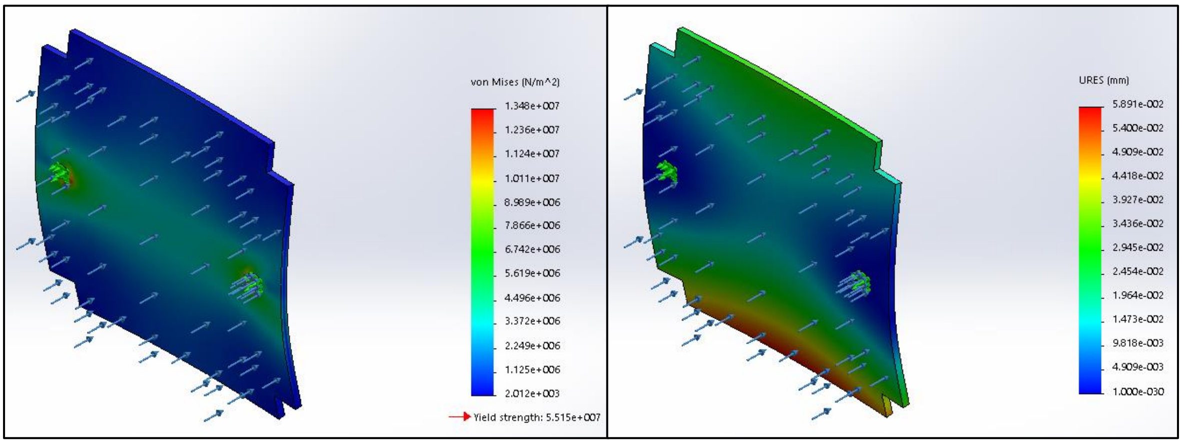

Figure 6.26: von Mises stress (left) and displacement (right) of lid under worst-case longitudinal launch conditions

6.8.12 FEA Results Using Worst-Case Scenario Lateral Loading Conditions on the Lid

Figure 6.27 below shows the von Mises stress and displacement for the lid when it is exposed to a lateral load of 5g. The minimum and maximum stresses are 29.6653 N/m^2 and 499341 N/m^2 respectively, with maximum stress are located around the M2 fixtures. Although displacement occurs over most of the lid, the maximum was found to be 0.058907 mm and is most prevalent at the bottom left corner.

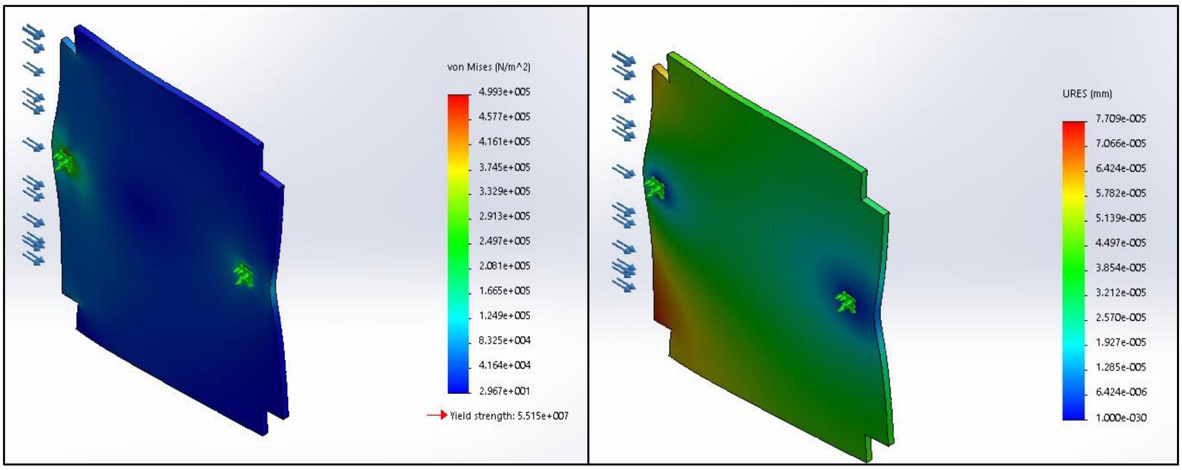

Figure 6.27: von Mises stress (left) and displacement (right) of lid under worst-case lateral launch conditions

6.8.13 Summary of Longitudinal and Lateral FEA results

Table 6.8 and table 6.9 summarize the maximum values produced during the finite element analysis for the housing and the lid of the de-orbiting device under normal and worst-case conditions.

Table 6:8: Summary of FEA results for longitudinal launch conditions

	Soyuz normal conditions		**Worst- case**	
	Housing	Lid	Housing	Lid
Max von Mises Stress	1.16597e+006 N/m^2	1.27347e+007 N/m^2	4.04949e+006 N/m^2	1.34828e+007 N/m^2
Displacement	0.00150634 mm	0.0216098 mm	0.00523159 mm	0.058907 mm

Table 6:9: Summary of FEA results for lateral launch conditions

	Soyuz normal conditions		**Worst- case**	
	Housing	**Lid**	**Housing**	**Lid**
Max von Mises Stress	94036.9 N/m^2	97742.4 N/m^2	1.30189e+006 N/m^2	499341 N/m^2
Displacement	0.0002744 mm	7.22846e-006 mm	0.00379793 mm	7.70886e-005 mm

6.8.14 Location of De-orbiting Device and Fitment

It is recommended that the device be fitted at the top of the CubeSat so that it can still retain solar arrays if needed. Due to the standardized dimensions, the device can be fitted into 1U, 2U or 3U as seen in figure 6.28 below. While the device was specifically designed to deorbit a 3U CubeSat, it can be scaled down to fit a 1U or 2U CubeSat.

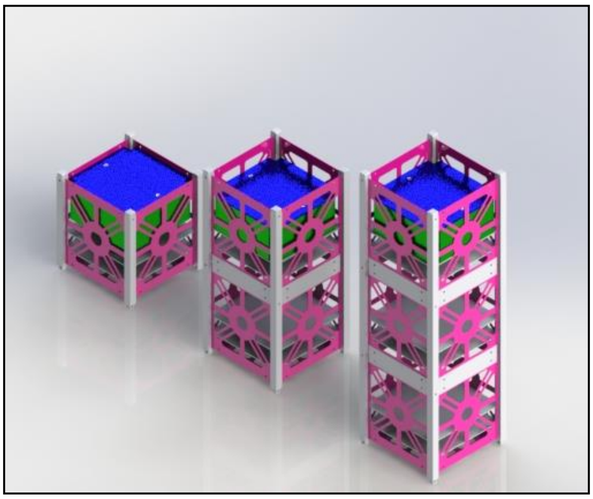

Figure 6.28: Device location

(Adapted from Armin Yousefi Kanani, 2015)

6.8.15 Deployment sequence for De-orbiting Device

The device will remain inactive until activated thereby ensuring that it does not affect the functionality of the satellite. The baseline case study predicted that ZACube-2 will remain in orbit for 4 years,17 days (1477Days) therefore it is recommended that the device be activated close to the end of the 4th year or alternatively when it has completed its primary mission. Figure 6.29 below shows the operational sequence of the de-orbiting mechanism.

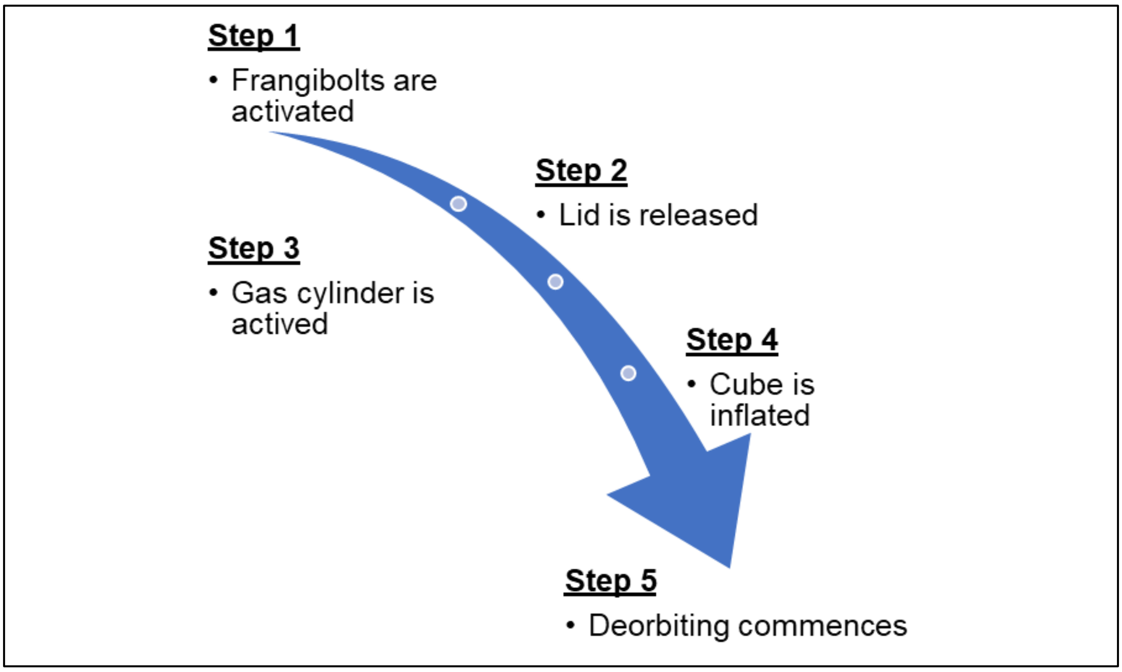

Figure 6.29: Operational sequence of device

6.9 Discussion

Orbital lifetime predictions for ZACube-2 were performed and four scenarios were simulated. The first scenario named the baseline case presented the orbital lifetime with no de-orbiting mechanism fitted. The predicted lifetime for the baseline case was 1477 days, as indicated in Figure 6.2 and Figure 6.3. The baseline case showed that the natural re-entry will occur in March 2023.

This was followed by case study 1, in which ZACube-2 was hypothetically fitted with an inflatable pillow structure which added 0.37m^2 to the original 0.03m^2. Thus, increasing the cross-sectional area to 0.4m^2. The predicted orbital lifetime was reduced from 1477 days to 689 days, indicating a 54% reduction in orbital lifetime seen in Figure 6.5 and Figure 6.6.

In case study 2, ZACube-2 was hypothetically fitted with a 10m^2 drag sail which increased the cross-sectional area from 0.03m^2 to 10.03m^2. This resulted in a massive reduction of 98% in the orbital lifetime prediction shown in Figure 6.7 and Figure 6.8

The 3rd and final case study investigated the implications on the orbital lifetime predictions for ZACube-2 when fitted with a new inflatable cube mechanism. This added an additional cross-sectional area of 0.49m^2 thereby increasing the overall cross-sectional area to 0.52m^2. Following deployment of the mechanism, the orbital lifetime was reduced by 59%, when compared to the baseline case of 1477 days. Table 6:10 shows a summary of the results for each case study.

Table 6:10: Orbital lifetime predictions for each case study

Scenario Name	**Baseline Case**	**Case Study 1: Inflatable pillow structure**	**Case Study 2: Drag Sail**	**Case Study 3: New Cube Concept**
Predicted Orbital Lifetime	1447 Days	689 Days	28 Days	603 Days
% Reduction in Orbital Lifetime		53%	98%	59%

The common thread connecting all the case studies is atmospheric drag given by $F_D = -\frac{1}{2}\rho\left(\frac{C_D A}{m}\right)V^2$ (equation 4.17). This is a non-gravitational perturbation force. Along with the earth's obliqueness, it is the predominant perturbation force acting on low earth-orbiting satellites. The effects of this drag force were presented in Figure 6.3, Figure 6.6, Figure 6.8 and Figure 6.10. This force is greatest at the point of perigee and continuously removes energy from the orbit by gradually lowering the apogee altitude. This continued until the orbit shape has changed from elliptical to a more circular shape. However, due to earth's spheroid shape, the perigee and apogee will never be 100% equal, thus, a perfect circular orbit does not exist in practice. Furthermore, parameters such as, atmospheric density, and the velocity square, are identified as parameters that mainly determine the drag force and orbit rate of decay. The orbital parameters affected by the constant depletion of energy are the semi-major axis and orbit eccentricity.

6.9.1 Parameters Affecting the Orbital Lifetime.

Having shown that aerodynamic drag is the major perturbation force affecting ZACube-2's orbital lifetime, the next was to identify individual parameters. During simulations, area-to-mass was increased to simulate the addition of a drag enhancement device. The implications on the orbital lifetime estimation, for ZACube-2, are shown in Table 6:11. It is clear that increasing the cross-sectional area, will decrease the predicted orbital life of the CubeSat in question. It should also be noted that the projected area values will be influenced by the drag device attitude, which in turn will have an influence on the estimated lifetime predictions.

Table 6:11: Estimated Orbital Lifetime Predictions

Scenario	**Baseline**	**Case Study 1**	**Case Study 2**	**Case Study 3**
Area-to-mass(m^2/kg)	0.0079	0.11	2.6	0.52
Predicted Orbital Lifetime	1477 Days	689 Days	28 Days	603 Days

6.9.2 Effects of Mass and Cross-sectional Sensitivity Study

Given that mass and the cross-sectional area forms part of the aerodynamic drag equation, the effects of varying one of these parameters while keeping the other constant were investigated and the results presented in Figure 6.11 and Figure 6.12. Results indicated that when the mass increased by a margin of 200 grams, the orbital lifetime was increased by an average of 28 days. During the cross-sectional sensitivity study, the cross-sectional area was increased by 0.2m^2. This showed a reduction in orbital lifetime prediction of 21 days. Both results generated from this study indicated that these parameters affect the orbital lifetime of the CubeSat in question.

6.9.3 Ballistic Coefficient (BC)

The ballistic coefficient was calculated using $\frac{m}{C_D A}$. The (BC) value for each case study is seen in Table 6:12. The Ballistic value is an indication of how the satellite in question responds to the atmosphere. A high value is an indication that the satellite will react slower to the atmosphere and thus has a slower decay rate. Oppositely, a satellite with a low (BC) value reacts more rapidly to the atmosphere and this has a higher decay rate. This is evident in all four scenarios simulated, shown in Figure 6.13. It is thus, clear that a lowering the ballistic coefficient for ZACube-2 will result in a faster orbit decay rate.

Table 6:12: Ballistic coefficients

Scenario	Baseline Case	Case Study 1	Case study 2	Case study 3
Ballistic Coefficient:	57.57 kg/m^2	4.3 kg/m^2	0.092 kg/m^2	3.32 kg/m^2
Orbital Lifetime Predictions	1477 Days	689 Days	28 Days	603 Days

The (BC) values for ZACube-2 was calculated using a Drag coefficient value (C_D) value of 2.2 and a maximal cross-sectional area of 0.03m^2. The (C_D) of 2.2 is supposed by literature and is used in the DAS software (James Wertz, David Everett, 2011). The (C_D) value used during Ballistic calculation for the sail (case study: 2) was 4.0.

Atmospheric density(ρ) is renowned for its complexness as it varies with, altitude, time, season and geographical latitude and longitude and solar activity. It is due to this reason that DAS has an updated solar flux file that is updated every 6 months. Thereby ensuring that the lifetime predictions are based on the most recent solar activity. Given that we are currently in the solar minimum part of the solar cycle, the influence on orbital lifetime prediction is minimal when compared to solar maximum. However, it should not be discarded.

6.9.4 Inflatable Cube De-Orbiting Device Discussion

A new inflatable cube device was introduced with preliminary design specifications shown in table 6.13.

Table 6:13: Preliminary design specifications

Material selections	Aluminium 6061
Housing Dimensions	90mm by 90mm, 38mm deep
Lid Dimensions	90mm by 90 mm, 2mm thick
Over All Dimensions	90mm by 90mm, 40mm deep
Inflatable cube material	0.7m by 0.7mUpilex-Ca polyimide film
Total mass	0.6kg
Estimated power required	12v

Solidworks software was used to perform finite element analysis on the housing and lid. Two scenarios were simulated each with different launch conditions. Scenario 1 investigated the stress and displacement of the container and lid when exposed to the launch conditions of the Soyuz rocket. The longitudinal and lateral loads were 4.3 g and 0.4 g respectively as given by the Soyuz user's manual. The results are seen in Figure 6.18 to Figure 6.23. Finite element analysis indicated that the maximum von Mises stress for the housing and lid under a 4.3g load was found to be 1.16597e+006 N/m^2 and 1.27347e+007 N/m^2 respectively. The maximum displacement for the housing and lid under the same load was found to be 0.00150634 mm and 0.0216098 mm. Aluminium 6061 was the material selected for both these components and has a yield strength of 5.51485e+007 N/m^2. This is significantly higher than the maximum stress experienced by both components therefore, it can be concluded that the structural integrity is maintained and that both components will survive these launch conditions.

This was followed by scenario 2 which served as a worst-case scenario. In this scenario, the longitudinal and lateral loads were increased to 15g and 5g respectively. The results are shown in Figure 6.24 to Figure 6.27. Finite element analysis indicated the maximum von Mises stress for the housing and lid under a longitudinal load of 15 g's was found to be 4.04949e+006 N/m^2 and 1.34828e+007 N/m^2 respectively. The maximum displacement under the same load was 0.00523159 mm for the housing and 0.058907 mm for the lid. This scenario served as a factor of a safety study in that it proofed that both components will retain their structural integrity even if the load is unexpectedly increased by a factor of 3.5 (longitudinal load) and a factor of 12.5(lateral load).

A final summary of all the FEA results for both scenarios are shown in table 6.14 to table 6.17.

Table 6:14: Summary of Soyuz longitudinal loading FEA results

	Soyuz normal conditions 4.3g			
	Housing min	**Housing max**	**Lid Min**	**Lid Max**
von Mises Stress	120.404 N/m^2	1.16597e+006 N/m^2	1496.82 N/m^2	1.27347e+007 N/m^2
Displacement	0.00mm	0.00150634 mm	0.00 mm	0.0216098 mm

Table 6:15: Summary of Soyuz lateral Load FEA results

	Soyuz normal conditions 0.4g			
	Housing min	**Housing max**	**Lid Min**	**Lid Max**
von Mises Stress	0.451514 N/m^2	94036.9 N/m^2	6.27928 N/m^2	97742.4 N/m^2
Displacement	0.00mm	0.0002744 mm	0.00 mm	7.22846e-006 mm

Table 6:16: Summary of worst-case longitudinal load FEA results

	Worst-case loading 15gs			
	Housing min	**Housing max**	**Lid Min**	**Lid Max**
von Mises Stress	418.168 N/m^2	4.04949e+006 N/m^2	693.854 N/m^2	4.64926e+006 N/m^2
Displacement	0.00 mm	0.00523159 mm	0.00 mm	0.0203127 mm

Table 6:17: Summary Worst case lateral FEA results

	Worst-case loading 5gs			
	Housing min	**Housing max**	**Lid Min**	**Lid Max**
von Mises Stress	5.80858 N/m^2	1.30189e+006 N/m^2	29.6653 N/m^2	499341 N/m^2
Displacement	0.00 mm	0.00379793 mm	0.00 mm	7.70886e-005 mm

6.9.5 Modal and Harmonic Analysis Discussion

During launch stages, the launch vehicle generates a variety of vibrations. Therefore, modal and natural frequency analysis was performed to extract the natural frequencies and mode shapes of the structure. This was done to ensure that the natural frequencies of the structure do not match the vibrational frequencies generated by the launch vehicle. If the natural frequencies of the structure match the launch vehicle’s vibrational frequency, resonance will occur and may cause catastrophic failure to the structure itself and surrounding components.

Vibrational patterns may vary depending on the selected launch vehicle. It is therefore critical to perform the pre-flight vibration testing as prescribed by the vibration testing criteria of the selected launch vehicle. Soyuz rocket was selected to launch ZACube-2 into orbit and is a commonly used for CubeSat launches, thus the sinusoidal dynamic loading frequency range of 1Hz-100Hz and the corresponding static loads shown in table 6.7 was used during the sinusoidal dynamic load response analysis.

The first six natural frequencies and mode shapes of the lid, housing and assembled structure were extracted using frequency analysis and is shown in appendices section O, sub-sections 1 till 3. A summary of the lowest and highest frequencies is shown in Table 6:18. The results show that the lowest natural frequencies for each individual component and assembled structure are well above the testing range of 1Hz-100Hz.

Table 6:18: Summary of maximum and minimum natural frequencies

Component	Lowest Natural frequency (Hz)	Highest natural frequency (Hz)
Lid	583	2568
Housing	1066	277
Assembled Structure	3140	6104

The natural frequency analysis was followed by harmonic analysis. The response of each component was individually evaluated followed by the response of the assembled structure. The overall evaluation range was 1Hz-100Hz, which was broken down into seven smaller ranges along with the appropriate longitudinal and lateral loading associated with each range. A worst-case scenario was also included to investigate the response of the components and assembled structure if resonance would occur.

The full analysis results of the lid and housing as individual components are shown in appendices section O, sub-sections 4 till 8. Harmonic analysis results regarding the response of the lid indicated that the maximum displacement and stress under both longitudinal and lateral loading conditions were very similar and in the range of 0.017mm and 3.65-+006N/m^2 at 100Hz.

Similarly, the response of the housing under longitudinal and lateral conditions indicated a maximum displacement and von Mises stress occurred at 100Hz and was found to be 0.007mm and 1.98e+006N/m^2.The response of the assembled structure is seen in appendices section O, sub-sections 9 till 10. Harmonic analysis showed that the maximum displacement and von Mises stress under longitudinal and lateral loading conditions both occur at 100Hz and had a magnitude of 0.0008mm and 9.0e+005 N/m^2.

Based on harmonic analysis the worst-case scenario indicated that if the primary frequency of the structure (3140Hz) were to be reached, a displacement of 49mm will occur and would result in complete structural failure. With that said, the primary frequency of the structure is well above the testing requirements. All though the structure will experience a degree of deformation, the scale of it is too small to cause any serious issues during launch. This may be due to the stiffness of the material and to the light weight of the structure. It can therefore be deduced that the structure will not fail during launch.

Chapter 7

7 Conclusions and Recommendations

This chapter summarises the content of the research and highlights the major findings. It also discusses the initial research objective and gives an overview of how each objective was achieved. The chapter is then concluded by recommendations which may be further elaborated on in future work.

7.1 Overall Conclusion

The purpose of this research was to analyse the effects that de-orbiting devices have on the orbital lifetime predictions of ZACube-2 and to present a new de-orbiting concept. As a reference, the initial research objectives formulated in chapter one is listed below. All objectives have been met.

1) In-depth and comprehensive literature review of the current state of technology regarding passive nanosatellite de-orbiting devices.
2) The orbital parameters of ZACube-2 will be modelled and simulated using the appropriate software.
3) Execute Orbital decay prediction simulation for ZACube-2 with various de-orbiting devices.
4) Evaluate the performance of each de-orbiting device.

5) Identify parameters affecting the orbital lifetime.

6) Based on data generated from simulations studies and analysis, recommend a concept capable of de-orbiting a nanosatellite within 25 years.

The first objective was achieved by completing an in-depth literature review regarding the state of technology pertaining to passive nanosatellite de-orbiting mechanisms. The primary focus was on how de-orbiting was achieved, and the methods and tools used to simulate Nanosatellite de-orbiting. The literature review presented many potential de-orbiting mechanisms, some of which showed so much potential that prototypes were created. A de-orbiting method evaluation was performed to isolate the most appropriate de-orbiting method for ZACube-2. The evaluation indicated that an inflatable structure was the best option.

The second objective was to model the orbital parameters for ZACube-2 in the appropriate software. Many software options were available, such as STK (systems tool kit), GMAT (General mission analysis tool) STELA and NASA’s Debris Assessment Software 2.0 (DAS 2.0).
In choosing the appropriate software to model and perform simulations, the major aspect influencing the decision was the selection of atmospheric models and solar flux values. Atmospheric density models calculate the atmospheric density at three probable solar activity levels. 5%, 50% and 95% over several solar cycles, but are very complex and hard to model. Consequently, the atmospheric model selection is the main source of unreliable orbital lifetime predictions.

Considering the above-mentioned factors, it was determined that DAS 2.0 would be best suited for this study. Contrasting to the other software packages, DAS does not require the user to input solar flux values or to select an atmospheric model. The user is asked to input the launch dates and the software selects the most updated and appropriate values. This is an important function because solar flux values are used to calculate atmospheric drag experienced by the satellite therefore if outdated values are used it will result in inaccurate results. Thus, by not allowing the user to select different atmospheric models, it creates less room for human error and outputs more reliable results.

The third and fourth objectives are the major cornerstones of the study. Four scenarios were simulated and are listed below. The Orbital parameters were extracted from the satellites two-line elements (TLE) file. The apogee and perigee were found to be 504.07 km with a satellite velocity of 7589 m/s and 476.49 km with a satellite velocity of 7629 m/s respectively. Each Case study had its own set of input data required which was covered in the data preparation section.

- Baseline Case: Orbital Lifetime Predictions for ZACube-2 with no Drag Enhancement Device.
- Case Study 1: Orbital lifetime Prediction for ZACube-2 with Inflatable Pillow Structure.
- Case study 2 Case Study: Orbital Lifetime Predictions of ZACube-2 Fitted with a Drag Sail.
- Case Study 3: Orbital Lifetime Predictions of ZACube-2 Fitted with a 0.49m^2 cube concept.

The Baseline case study presented the orbital lifetime predictions of ZACube-2 with no drag augmentation device. The results generated during this study were used as the standards referred to which the rest of the case studies were compared. The baseline case simulation results indicated an orbital lifetime prediction of 1477 days (4 years & 17 days) with a cross-sectional area of 0.03m^2.

This was followed by case study 1 in which ZaCube-2's orbital lifetime was estimated when fitted with an additional 0.37m^2 cross-sectional area. The results showed an orbital lifetime prediction of 689 days When compared to the baseline case of 1477 days (4 years & 17 days), it indicated an overall 53% reduction in orbital lifetime.

The second case study simulated the orbital lifetime of ZACube-2 when fitted with a drag sail that adds 10m^2 to the overall cross-sectional area of the CubeSat. The results showed an orbital lifetime prediction of 28 days. Thus, the result showed a massive orbital lifetime reduction of 98 %, when compared to the baseline case. In this specific case the massive reduction is due to a combination of two factors, firstly the sail size to CubeSat size ratio and secondly the fact that the satellite in question is in such a low orbit. The original concept with a sail size of 10m^2 would not be suitable due to its size and mass. However, it would be recommended that the sail size be adjusted according to the CubeSat size and orbital height, in this way the overall weight of the mechanism would also be reduced.

Lastly, in case study 3, the orbital lifetime of ZACube-2 was estimated when fitted with a new inflatable cube structure concept, which added an additional 0.49m^2 to the overall cross-sectional area. The drag coefficient of a cube in space vacuum varies between 2 and 4, depending on the attitude to the velocity vector (orientation), absorption and specular reflection. This high drag coefficient is exactly the reason that makes it possibly a good structure for de-orbiting. The results showed an orbital lifetime estimation of 603 days (1 year & 7months). When compared to the baseline the orbital lifetime was reduced from 1477 days to 603 days after the deployment of the structure, indicating a deduction of 59% in orbital lifetime.

The fifth objective was to Identify parameters affecting the orbital lifetime prediction for ZACube-2. All the devices simulated are drag augmentation devices which operate on the principles of aerodynamic drag. The aerodynamic equation consists of various parameters including satellite mass and cross-sectional area. During simulations, it became apparent that a change in one or both effects the orbital lifetime predictions.

Consequently, a mass sensitivity study and cross-sectional area variation study was performed. The mass sensitivity study investigated the mass variation of the CubeSat. Ideally, ZACube-2 should have a mass of 3kg, and not 3.8kg. The results yielded showed a steady increase of orbital life predictions over mass increments of 200grams. It indicates that with every 200grams of mass added, the orbital life will be prolonged by an average of 28 days. The results generated from the cross-sectional area variation study when the cross-sectional area was increased by increments of 0.2m^2, indicated an average reduction for orbital lifetime prediction of 21 days. The ballistic coefficient was also identified as a parameter affecting the orbital lifetime prediction of ZACube-2.

Finally, the last objective was to use the data generated from the simulations to create a new de-orbiting concept suitable for ZACube-2. This was achieved by introducing an inflatable cube de-orbiting device (ICDD) concept. The inflated cube creates an additional cross-sectional area of 0.49m^2. The effects of the additional cross-sectional area of 0.49m2^2 were showcased in simulation case study 3. The results showed a 59% reduction in the predicted orbital lifetime of ZACube-2.

Initially, two deployment concepts were considered; however, a concept evaluation tool was used to identify the most appropriate concept. The critical evaluation identified concept 1 as the best suited.

All the design requirements listed in chapter 6 were satisfied. Finite element analysis was performed on the housing and lid of the structure to ensure that it is structurally sound and will not fail during launch. Two scenarios were simulated. During the first scenario, the components were exposed to a maximum longitudinal load of 4.3g, which is the expected static load during a Soyuz rocket launch. Finite element analysis results indicated that the maximum von Mises stress for the housing and lid was 1.16597e+006 N/m^2 and 1.27347e+007 N/m^2 respectively. The stress results for both components are well below the yield strength of aluminium 6061 (5.51485e+007 N/m^2) and therefore it was concluded that the components will survive these launch conditions.

This was followed by a worst-case scenario during which the maximum longitudinal load was increased by a factor of 3.5, thus increasing the load to 15g. The finite element analysis results showed a maximum von Mises the stress of 4.04949e+006 N/m^2 for the housing and 4.64926e+006 N/m^2 for the lid. Similarly, to scenario 1, both stresses are significantly less than the yield stress of aluminium 6061. Consequently, it can be concluded that even if the components are exposed to an unexpected increase in static loading during launch, it will retain its structural integrity and will not fail under these conditions.

In addition to static loading, the structure will be exposed to sinusoidal dynamic loading caused by vibrations generated by the rocket engines and flight stages. Subsequently, harmonic analysis was performed according to the prescribed requirements of the Soyuz rocket user’s manual on the individual components and the assembled structure. Natural Frequency analysis was used to extract the natural frequencies of the lid, housing and assembled structure. The lid and housing as individual components had primary natural frequencies of 583 Hz and 1066 Hz respectively. This was followed by the assembled structure which had a primary natural frequency of 3140 Hz. According to the sinusoidal vibrational test requirements stipulated in the Soyuz rocket user’s manual, the testing range of interest is 1 Hz-100 Hz. Based on harmonic analysis the results indicated that the primary frequencies of the structure are well above the testing range of the rocket. The maximum displacement for the lid, housing and assembled structure were found to be 0.017mm, 0.007mm and 0.0008mm at 100 Hz respectively. The displacement that occurred was minuscule and not significant enough to cause plastic deformation and structural failure. Thus, it can therefore be concluded that the structure will not fail under these dynamic loading conditions.

A worst-case scenario for each of the component and assembled structure were also simulated to investigate the magnitude of the displacement and von Mises stress if resonance would occur. Based on harmonic analysis the results indicated 8mm displacement and 1.76301e+009 N/m^2 stress at 583 Hz for the lid, 12.9mm displacement and 2.37588e+009 N/m^2 stress for the housing at 1066 Hz and a 49.5 mm displacement and 2.89811e+010 N/m^2 stress at 3140 Hz for the assembled structure. Therefore ,if resonance would occur, the structure would most certainly fail and may damages the surrounding satellite components

Considering the reduction, the inflatable cube de-orbiting device (ICDD) concept has on the orbital lifetime predictions of ZACube-2 and the survivability of the deployment mechanism, it can be reasoned that the (ICDD) could in future be an effective way to deorbit nanosatellites.

7.1.1 Conclusion Summary

This research investigated the effects on orbital lifetime prediction of ZACube-2 when fitted with various drag augmented devices. Four Missions were simulated and analysed in NASA's Debris assessment software (DAS 2.0). Case studies 1,2 and 3 all showed a reduction in the orbital lifetime prediction for ZACube-2. Therefore, it can be concluded that the addition of a drag enhancement device to ZaCube-2 will increase the drag to such an effect that it will cause rapid de-orbiting.

Additionally, parameters affecting orbital lifetime predictions were also identified. They are Satellite mass, cross-sectional area, and the ballistic coefficient. From the data generated in the process of identifying parameters affecting the orbital lifetime of ZACube-2, it was deduced that when manufacturing future CubeSats the mass should be kept as close to the standard requirements as possible. This can possibly be achieved by using additive manufacturing techniques. With a combination of keeping the mass low, increasing the cross-sectional area and decreasing the ballistic coefficient of the satellite, de-orbiting can be achieved.

Furthermore, a new inflatable cube de-orbiting device (ICDD) concept was also introduced. The effects on ZACube-2's orbital lifetime was presented and indicated a 59% reduction. Finite element analysis investigating the stress and displacement was conducted and found that the selected deployment mechanism will not fail under a longitudinal load of 15g. In addition to the static loading analysis, natural frequency and harmonic analysis was also performed. Frequency analysis results indicated that the structures lowest natural frequency was 3140 Hz, which is well above the required testing range of 1Hz-100Hz. Hence, the structure will not resonate and will survive the dynamic loading conditions of the Soyuz launch vehicle.

7.2 Recommendations and Further work

The new inflatable cube device (ICD) concept should be further explored. There are many design elements of the new concept that needs further investigation and could result in new research areas. The section below briefly covers some of the main elements that require further investigation.

7.2.1 Deployment Mechanism

In the ICDD concept, the inflatable structure is fitted in the middle of the housing. When the mini frangibolts are activated the lid is released. Originally it was assumed that the folded structure would just be inflated and automatically be lifted out of the housing. However, it is recommended that a compression spring be fitted on the bottom of the housing so that when the lid releases the spring expands and in doing so lifts the folded structure out of the housing.

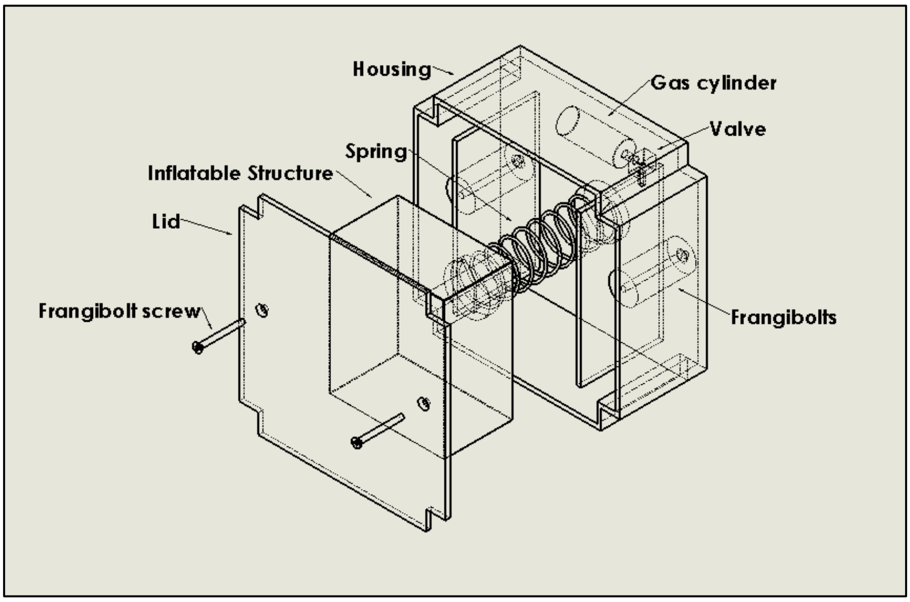

Figure 7.1: Deployment mechanism

7.2.2 Inflatable Gas

The gas used should be of such a nature that it is able to withstand extreme heat changes. Failure to do this may cause unwanted leaks and even explosions. This is a crucial part of the design since selecting inappropriate or ineffective gas will result in the cube not being fully inflated and thus affect the de-orbiting rate. Research done by (Lokcu and Ash, 2011) and (Fuller, Hinkley and Janson, 2010) indicated that SUVA-236fa refrigerant produced by DuPont, could possibly be a plausible option. However, additional experiments should be conducted to find the most appropriate gas for inflation.

7.2.3 Gas Cylinder Design

The gas cylinder design must be of such a nature that it safely shelters the gas from the harsh space environment and violent launch conditions. It will also require a custom valve. It might be a good idea, to explore the use of a normally closed solenoid valve, which will remain closed until activated. The advantage of this is that the cylinder will be airtight and will not accidentally open. However, the solenoid valve will require battery power. Consequently, it will increase the overall power needed to successfully deploy the inflated cube. Moreover, if a custom valve is needed, it will increase the overall cost of the device.

7.2.4 Concept Attitude Variation

During simulation a minimum projected area of 0.49m2 cube was assumed. In practice this would only be possible if the concept had an active attitude control. Therefore it is recommended that the effects of the cube’s attitude variation on the estimated lifetime predictions be further investigated

8 REFERENCES

Aerospace Corporation (2015) 'Understanding Space Debris', *Crosslink*, 16(1), pp. 1–61.

Afful, M. A. (2013) *Orbital Lifetime Predictions of Low Earth Orbit Satellites and the effect of a DeOrbitSail*.

Alanazi, A. and Straub, J. (2019) 'Engineering Methodology for Student-Driven CubeSats', *Aerospace*, 6(5), p. 54.

Armin Yousefi Kanani (2015) *The Cube Sat (satellite) (1U, 2U,3U)| 3D CAD Model*. Available at: https://grabcad.com/library/the-cube-sat-satellite-1u-3u-1 (Accessed: 25 September 2019).

Barth, J. L., Isaacs, J. C. and Poivey, C. (1999) 'The radiation environment for the next generation space telescope', *Research Gate*, pp. 3–28.

Bonin, G., Hiemstra, J., Sears, T. and Zee, R. E. (2013) 'The CanX-7 Drag Sail Demonstration Mission : Enabling Environmental Stewardship for Nano- and Microsatellites', *27th Annual AIAA/USU Conference on Small Satellites*, pp. 1–16.

Boudjemai, A., Hocine, R. and Guerionne, S. (2015) 'Space environment effect on earth observation satellite instruments', *RAST 2015 - Proceedings of 7th International Conference on Recent Advances in Space Technologies*, (June), pp. 627–634.

Brian Ventrudo (2013) *Kepler's Laws – One Minute Astronomer*. Available at: https://oneminuteastronomer.com/8626/keplers-laws/ (Accessed: 5 July 2019).

Bruinsma, S., Tamagnan, D. and Biancale, R. (2004) 'Atmospheric densities derived from CHAMP/STAR accelerometer observations', *Planetary and Space Science*, 52, pp. 297–312.

Butcher, J. C. (1996) 'History of Runge-Kutta methods', 20, pp. 247–260.

Cal Ploy Rev 13 (2017) *CubeSat Design Specification*, *Encyclopedia of Machine Learning and Data Mining*.

Campbell, A. (2015) 'August 1960 - Project Echo Launched'.

Chobotov, V. A. (2002) *Orbital Mechanics Third Edition*.

Cox, C. M. (1994) 'Evaluation of semiempirical atmospheric density models for orbit determination applications', *Research Gate*, (April), pp. 400–401.

Coyne, G. V (2006) 'Discovery in the New Cosmology of Copernicus , Kepler and Galileo', *Acta Sc*, 18, pp. 10–22.

Croitoru, E.-I. and Oancea, G. (2016) 'Satellite Tracking Using Norad Two-Line Element Set Format', *Scientific Research and Education in the Air Force*, 18(1), pp. 423–432.

CubeSat Launch Initiative, N. (2017) *CubeSat 101: Basic Concepts and Processes for First-Time CubeSat Developers*.

Curiel, Al. da S. (2000) *Orbital Motion*.

Curtis, H. D. (2005) *Orbital Mechanics for engineering students*. Elsevier Butterworth-Heinemann.

Douglas L.Dowd and B.D.Tapley (1979) 'Density model for the upper atmosphere', *Celestial Mechanics*, 20, pp. 271–294.

Fernandez, J. M., Visagie, L., Schenk, M., Stohlman, O. R., Aglietti, G. S., Lappas, V. J. and Erb, S. (2014) 'Design and development of a gossamer sail system for deorbiting in low earth orbit', *Acta Astronautica*. Elsevier, 103, pp. 204–225.

Forsberg, R. (2016) *Lectures on gravity field basics and GRACE*.

Fuller, J. K., Hinkley, D. and Janson, S. W. (2010) 'CubeSat Balloon Drag Devices Presentation. The Aerospace Corporation', *Physical Science Laboratories*.

Garcia, M. (2015) 'Space Debris and Human Spacecraft'. Available at: https://www.nasa.gov/mission_pages/station/news/orbital_debris.html (Accessed: 4 July 2019).

Hall, L. (2014) 'The History of Space Debris', in *Space Traffic Management Conference*, p. 13.

Horvathy, P. A. (2014) 'The laws of planetary motion, derived from those of a harmonic oscillator (following Arnold)', *Research Gate*, (January).

Hoyt, R. (2009) 'Terminator Tape: A Cost-Effective De-Orbit Module for End-of-Life Disposal of LEO Satellites', *AIAA SPACE 2009 Conference & Exposition*, (September), pp. 1–9.

IADC (2007) 'IADC-2002-01, IADC Space Debris Guidelines, Revision 1.pdf', (22), pp. 1–10.

Ismail, M. M. (2015) 'Goeken-Johnson Sixth-Order Runge-Kutta Method', (January 2011).

James Wertz, David Everett, J. P. (2011) *James Wertz, David Everett, Jeffery Puschell - Space Mission Engineering - The New SMAD vol 28*.

Janhunen, P. (2010) 'Electrostatic plasma brake for de-orbiting a satellite', *Journal of Propulsion and Power*, 26(2), pp. 370–372.

Janhunen, P. (2014) 'Coulomb drag devices: electric solar wind sail propulsion and ionospheric deorbiting', pp. 1–8.

Jon Sellers, J., Astore, W. J., Giffen, R. B. and Larson, W. J. (2004) 'Understanding Space - An Introduction to Astronautics', p. 772.

Kessler, D. J. and Cour-Palais, B. G. (1978) 'Collision frequency of artificial satellites: The creation of a debris belt', *Journal of Geophysical Research*, 83(A6), p. 2637.

Kessler, D. J., Johnson, N. L. and Matney, M. (2000) 'THE KESSLER SYNDROME : IMPLICATIONS TO FUTURE SPACE', *AAS*, pp. 1–15.

Konstantinidis, K. and Förstner, R. (2013) 'Cuballute: A cubesat mission to deploy an inflatable hypersonic drag body (ballute) in the martian atmosphere', *Proceedings of the International Astronautical Congress, IAC*, 10(October 2013), pp. 7782–7791.

Kuznetsov, V. D., Sinelnikov, V. M. and Alpert, S. (2016) 'Sputnik 1 and the First Satellite Ionospheric Experiment', *Research Gate*, (November), pp. 1–2.

Lätt, S. *et al.* (2014) 'ESTCube-1 nanosatellite for electric solar wind sail in-orbit technology demonstration', *Proceedings of the Estonian Academy of Sciences*, 63(2S), pp. 200–209.

Lokcu, E. and Ash, R. L. (2011) 'A de-orbit system design for CubeSat payloads', *RAST 2011 - Proceedings of 5th International Conference on Recent Advances in Space Technologies*, pp. 470–474.

NASA (2007) *Orbital Debris Quarterly News A publication of The NASA Orbital Debris Program Office*.

NASA (2015) 'Birth of the Space Age'. Available at: https://www.nasa.gov/multimedia/imagegallery/image_feature_1773.html (Accessed: 8 October 2018).

NASA (2017) *NASA Procedural Requirements NPR 8715.6B Subject: NASA Procedural Requirements for Limiting Orbital Debris and Evaluating the Meteoroid and Orbital Debris Environments*.

National Aeronautics and Space Administration (2004) *The Vision for Space Exploration*.

National Aeronautics and Space Administration (2012) 'Orbital Debris Management & Risk Mitigation', p. 24.

Nock, K. T., Gates, K. L., Aaron, K. M. and McRonald, A. D. (2010) 'Gossamer orbit lowering device (GOLD) for safe and efficient de-orbit', *AIAA/AAS Astrodynamics Specialist Conference 2010*, (August), pp. 1–12.

Nola Taylor Redd (2017) *Famous Astronomers | List of Great Scientists in Astronomy*, *Space.com*. Available at: https://www.space.com/16095-famous-astronomers.html (Accessed: 4 September 2018).

O'Donnell, F. (2007) 'Explorer', *JPL*, pp. 1–45.

Opperman, B. D. L. (2003) *Precision Propagation and Orbit Decay Prediction of Low Earth Orbit Satellites*.

P.Chatters, E. and Eberhart, B. (2017) *Orbital mechanics*, *IEEE Spectrum*.

Pardini, C. and Anselmo, L. (2007) *EVOLUTION OF THE DEBRIS CLOUD GENERATED BY THE FENGYUN-1C FRAGMENTATION EVENT*.

Parliament office of science and technology (2010) *SPACE DEBRIS*.

Peter Dourmashkin (2012) *Chapter 7 Newton's Laws of Motion*.

Qiao, L., Rizos, C. and Dempster, A. (2013) ‘Analysis and Comparison of CubeSat Lifetime’, *In Proceedings of the 12th Australian Space Conference*, pp. 249–260.

Robert A. Braeunig (2013) *Basics of Space Flight: Orbital Mechanics*, *Rocket and space technology*. Available at: http://www.braeunig.us/space/orbmech.htm (Accessed: 16 January 2019).

Science, L. talk (2012) ‘BLM X – Backgrounder : Brief History of Space Exploration’, *Lets talk science*, pp. 1–4.

Slavinskis, A. *et al.* (2015) ‘ESTCube-1 in-orbit experience and lessons learned’, *IEEE Aerospace and Electronic Systems Magazine*, 30(8), pp. 12–22.

Sokeng Ifriky Tadadjeu, B. D. N. and Shane Martin, R. R. V. Z. and M. M. (2017) ‘Ion Beams for Space Applications’, in *Intech*, p. 13.

SOLIDWORKS Help Manual, D. S. 2019) (2019) *SOLIDWORKS Help Manual, Dassault Systems 2019*. Available at: https://help.solidworks.com/2018/English/SolidWorks/cworks/c_Harmonic_Analysis.htm.

STK (2019) *STK - Satellites - Mean Elements*. Available at: http://help.agi.com/stk/index.htm#stk/vehSat_meanElements.htm (Accessed: 29 January 2019).

Sylvestrea, H. and Ramakrishna Parama, V. R. (2017) ‘Space Debris: Reasons, types, impacts and management’, *Indian Journal of Radio and Space Physics*, 46(1), pp. 20–26.

UK Space Agency (2012) ‘Space:Uk Space Agency’, *Space:Uk*, (35), p. 17.

Vallado, D. A. (2010) *Tutorial Lectures at the 4 th ICATT*.

Vallado, D. A. and Cefola, P. J. (2012) ‘Two-line element sets - Practice and use’, *Proceedings of the International Astronautical Congress, IAC*, 7(January 2012), pp. 5812–5825.

De Villiers, D. and Van Zyl, R. (2015) ‘ZACube-2: The successor to Africa’s first nanosatellite’, *Amsat SA Space Symposuim*.

Wertz, james R. and W. J. L. (1999a) *Space Mission Analysis and Design*.

Wertz, james R. and W. J. L. (1999b) ‘Understanding Orbits’, in *Space mission analysis and design*.

William Salter, A. (2015) *Space Debris A Law and Economics Analysis of the Orbital Commons*.

Zanatta, A., Zampieri, F., Basso, C. and Thiene, G. (2017) ‘Galileo Galilei: Science vs. faith’, *Global Cardiology Science and Practice*, 2017(2), pp. 1–11.

Zhong, W. and Gurfil, P. (2013) ‘Online Estimation of Mean Orbital Elements with Control Inputs’, in *Proceedings of the EuroGNC 2013, 2nd CEAS Specialist Conference on Guidance, Navigation & Control*, pp. 1044–1062.

APPENDICES

Appendix A Design Specification for a 3U CubeSat

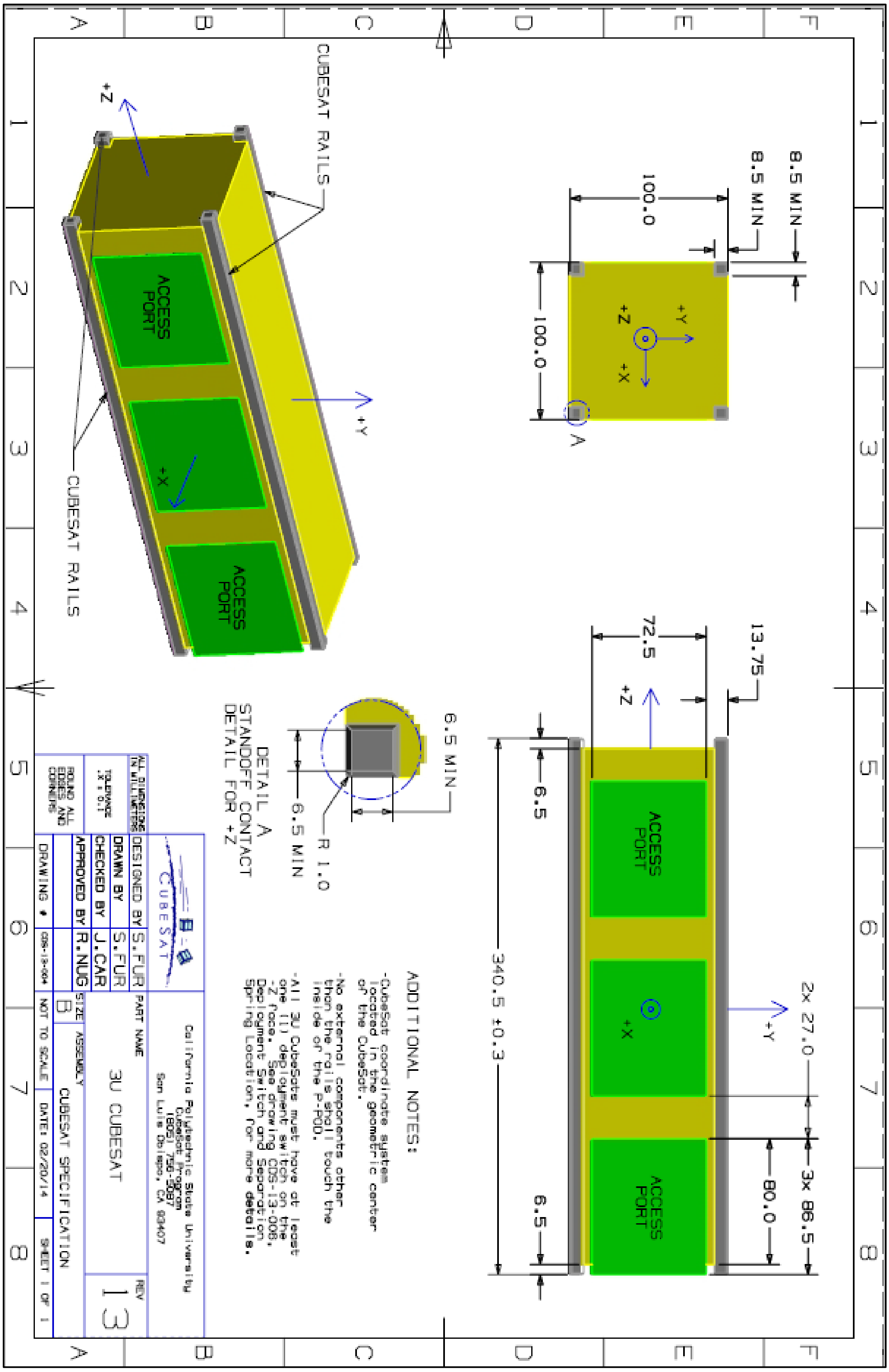

Appendix Figure A-1:3U Specificatons

Appendix B Velocity Calculations at Perigee and Apogee for ZaCube-2

Velocity at Perigee using equation (3.14):

$$
\begin{aligned}
v^2 &= \mu\left(\frac{2}{r_p} - \frac{1}{a}\right) \\
v^2 &= 3.98 * 10^{14}\left(\frac{2}{(6854.49 * 10^3)} - \frac{1}{(6871 * 10^3)}\right) \\
v^2 &= 58.208 km^2 / s^2 \\
v &= \sqrt{58.208} \\
v &= 7629.13 m / s
\end{aligned}
$$

Velocity at Apogee using equation (3.15):

$$
\begin{aligned}
v^2 &= \mu\left(\frac{2}{r_a} - \frac{1}{a}\right) \\
v^2 &= 3.98 * 10^{14}\left(\frac{2}{(6882.07 * 10^3)} - \frac{1}{(6871 * 10^3)}\right) \\
v^2 &= 57.738 km^2 / s^2 \\
v &= \sqrt{57.738} \\
v &= 7598.56 m / s
\end{aligned}
$$

Where:

$\mu =$ Standard gravitational constant $(3.9 * 10^{14} m^3 / s^2)$

$\mathrm{r}_e =$ Equatorial radius of earth (6378 km)

$\mathrm{r}_p =$ Radius of earth + perigee hight (km)

$r_a =$ Radius of the earth + apogee hight (km)

$a =$ Semi-major axis (km)

Appendix C Change in velocity required to induce a decaying orbit for ZaCube-2

Appendix Figure C-1: Change in velocity reuired for decaying orbit

Appendix D Baseline Case Study Input Data

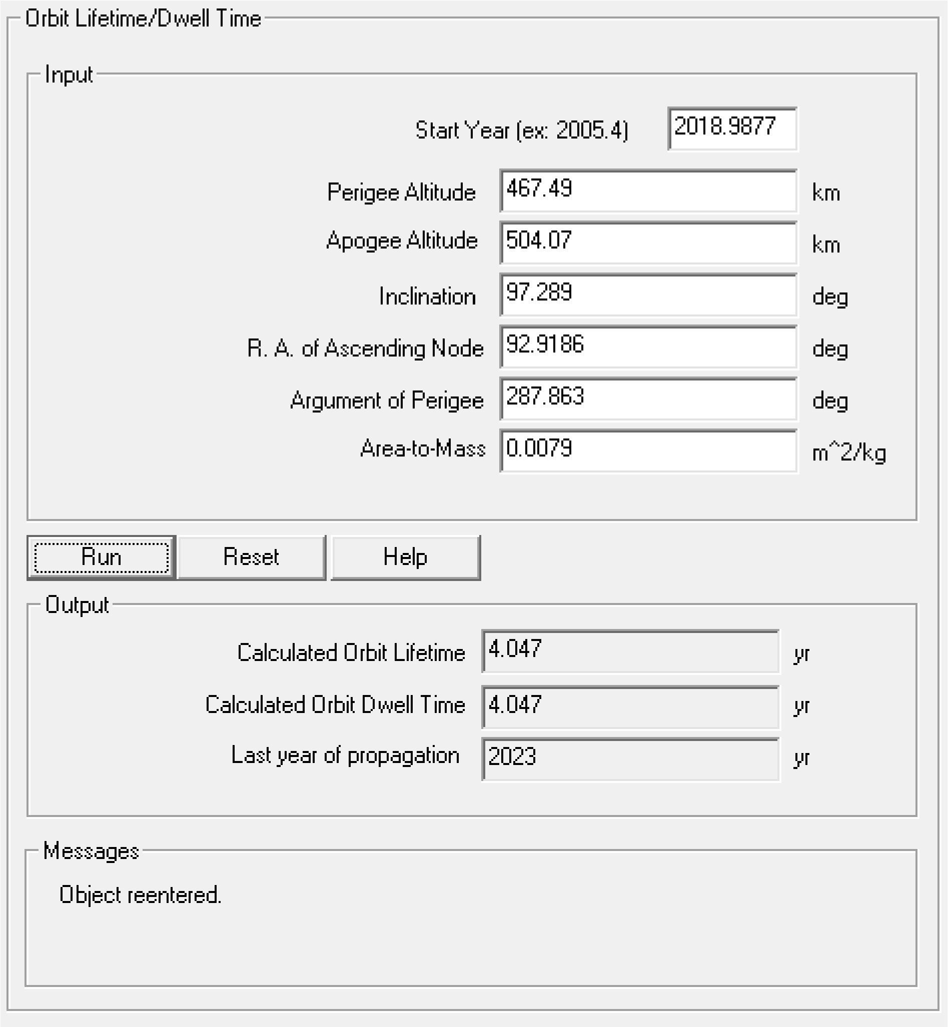

Orbit Lifetime/Dwell Time

Input

Start Year (ex: 2005.4) 2018.9877
Perigee Altitude 467.49 km
Apogee Altitude 504.07 km
Inclination 97.289 deg
R. A. of Ascending Node 92.9186 deg
Argument of Perigee 287.863 deg
Area-to-Mass 0.0079 m^2/kg

Output

Calculated Orbit Lifetime 4.047 yr
Calculated Orbit Dwell Time 4.047 yr
Last year of propagation 2023 yr

Messages

Object reentered.

Appendix Figure D-1: Baseline study input data

Baseline Case Graphical Results

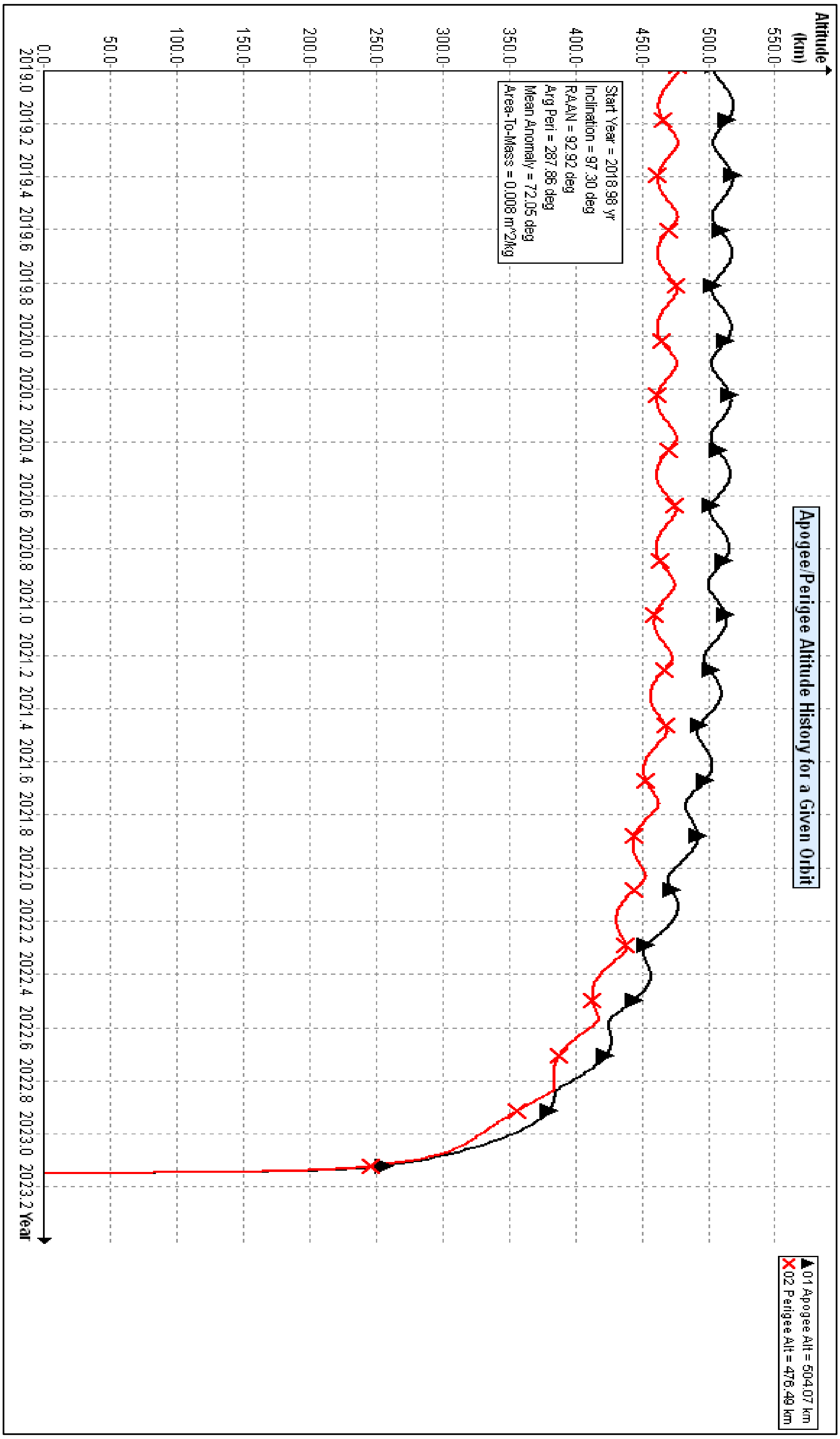

Appendix Figure D-2: Basline graphical results

Appendix E Case Study 1 Input Data

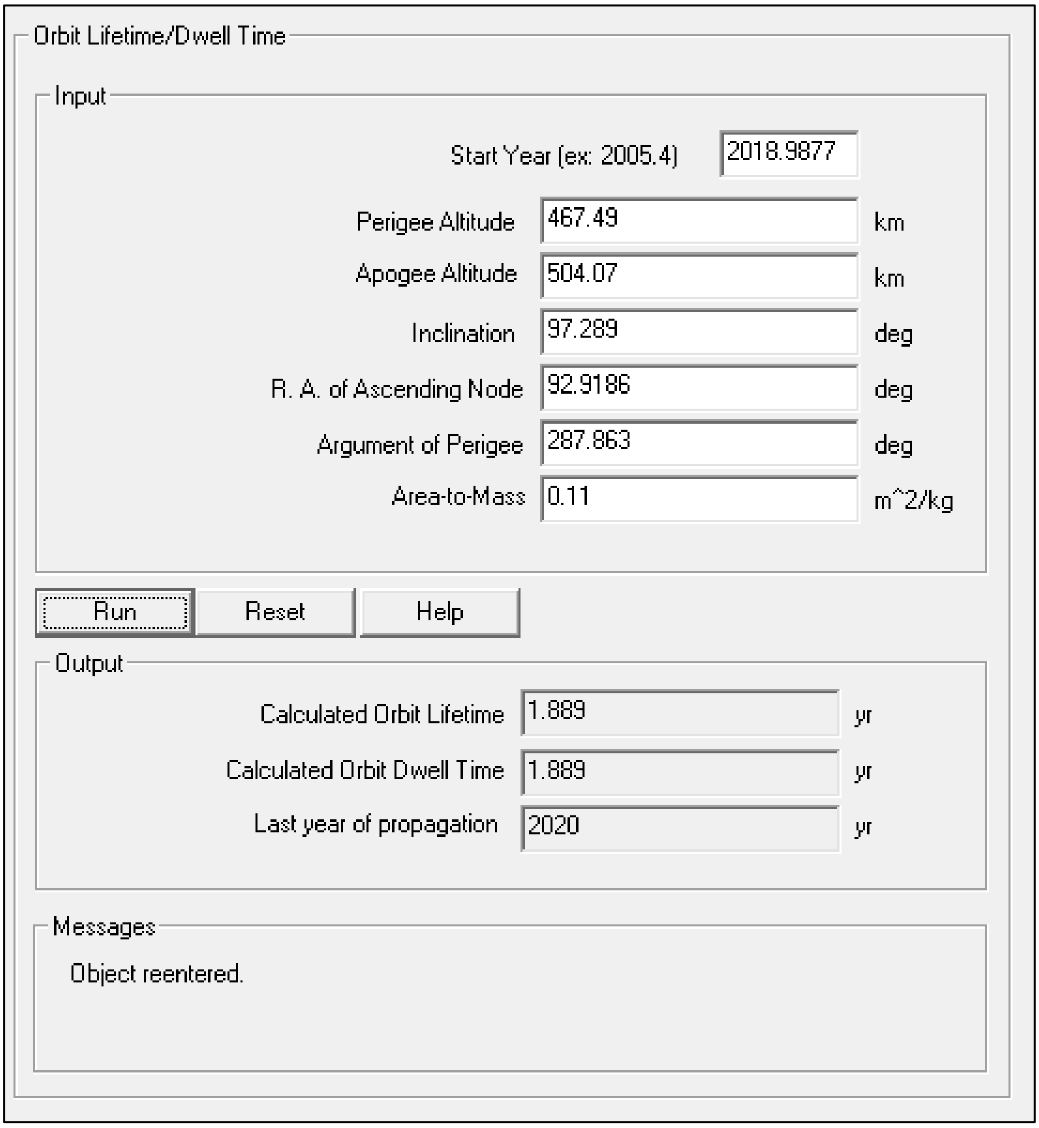

Start Year (ex: 2005.4) 2018.9877

Perigee Altitude 467.49 km

Apogee Altitude 504.07 km

Inclination 97.289 deg

R. A. of Ascending Node 92.9186 deg

Argument of Perigee 287.863 deg

Area-to-Mass 0.11 m^2/kg

Calculated Orbit Lifetime 1.889 yr

Calculated Orbit Dwell Time 1.889 yr

Last year of propagation 2020 yr

Object reentered.

Appendix Figure E-1: Case study 1 input data

Appendix E-2: Case study 1 Graphical Results

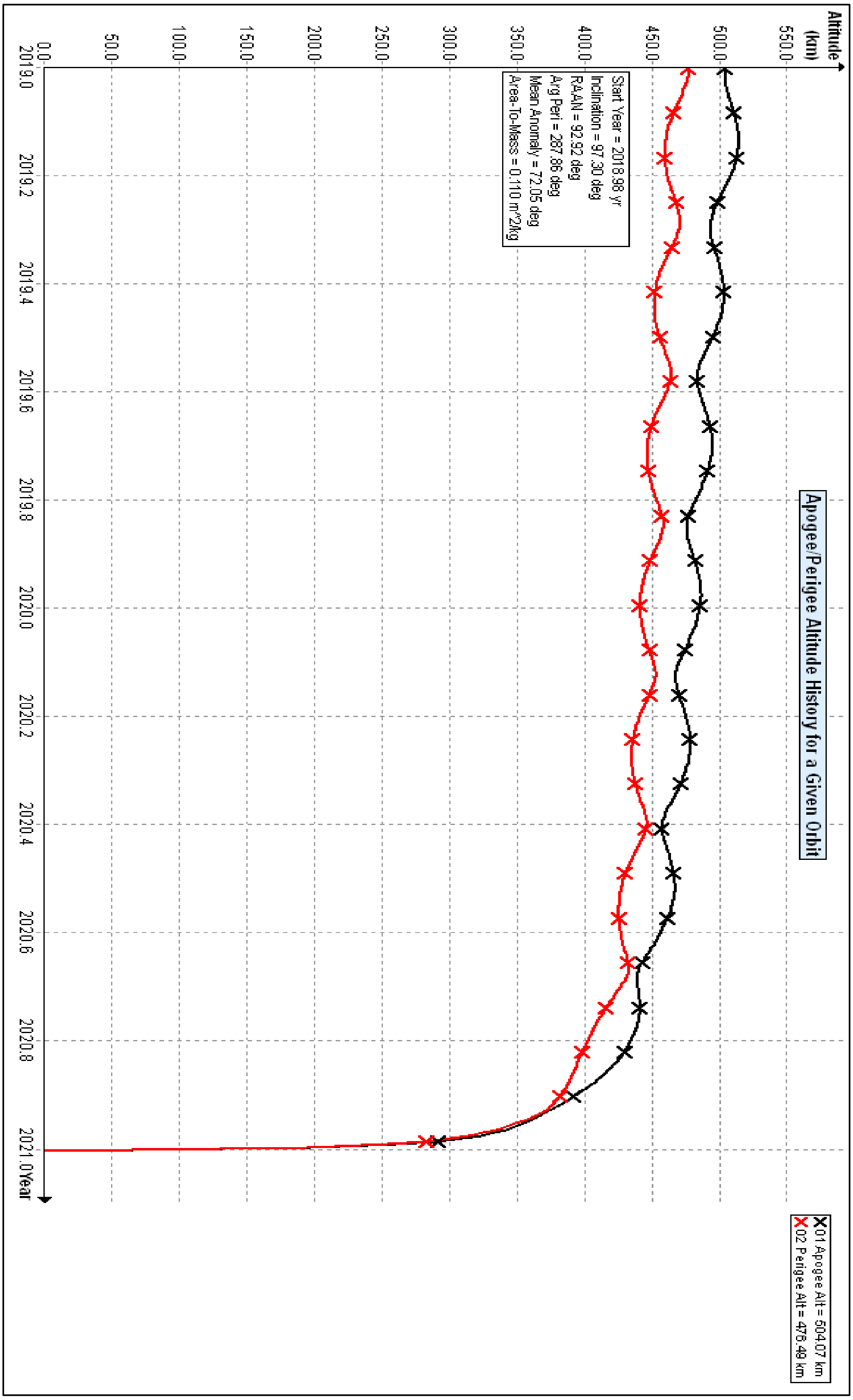

Appendix Figure E-2: Case study 1 graphical results

Appendix F Case Study 2 Input Data

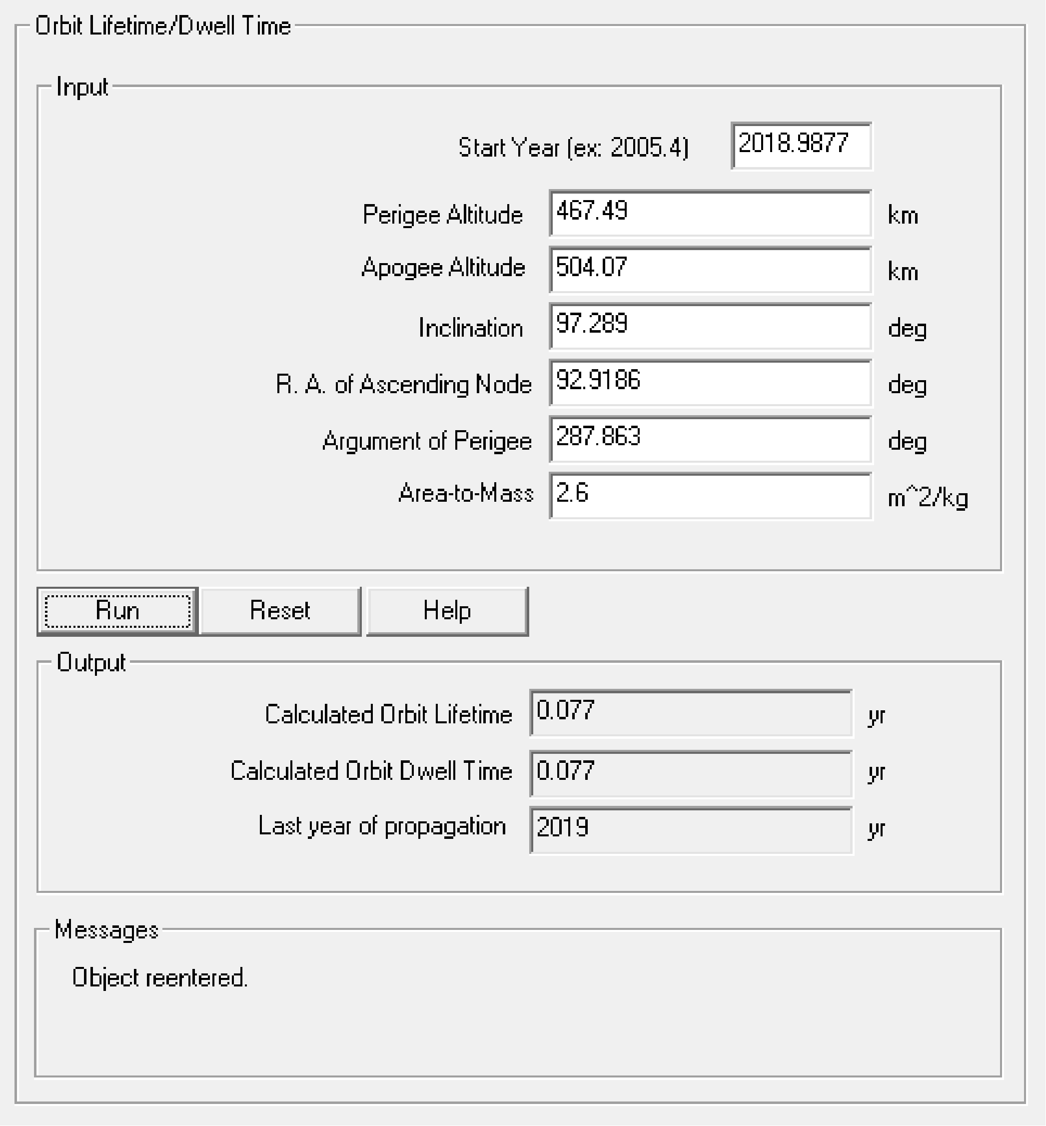

Start Year (ex: 2005.4) 2018.9877

Perigee Altitude 467.49 km

Apogee Altitude 504.07 km

Inclination 97.289 deg

R. A. of Ascending Node 92.9186 deg

Argument of Perigee 287.863 deg

Area-to-Mass 2.6 m^2/kg

Calculated Orbit Lifetime 0.077 yr

Calculated Orbit Dwell Time 0.077 yr

Last year of propagation 2019 yr

Object reentered.

Appendix Figure F-1: Case study 2 input data

Appendix F-2: Case Study 2 Graphical Results

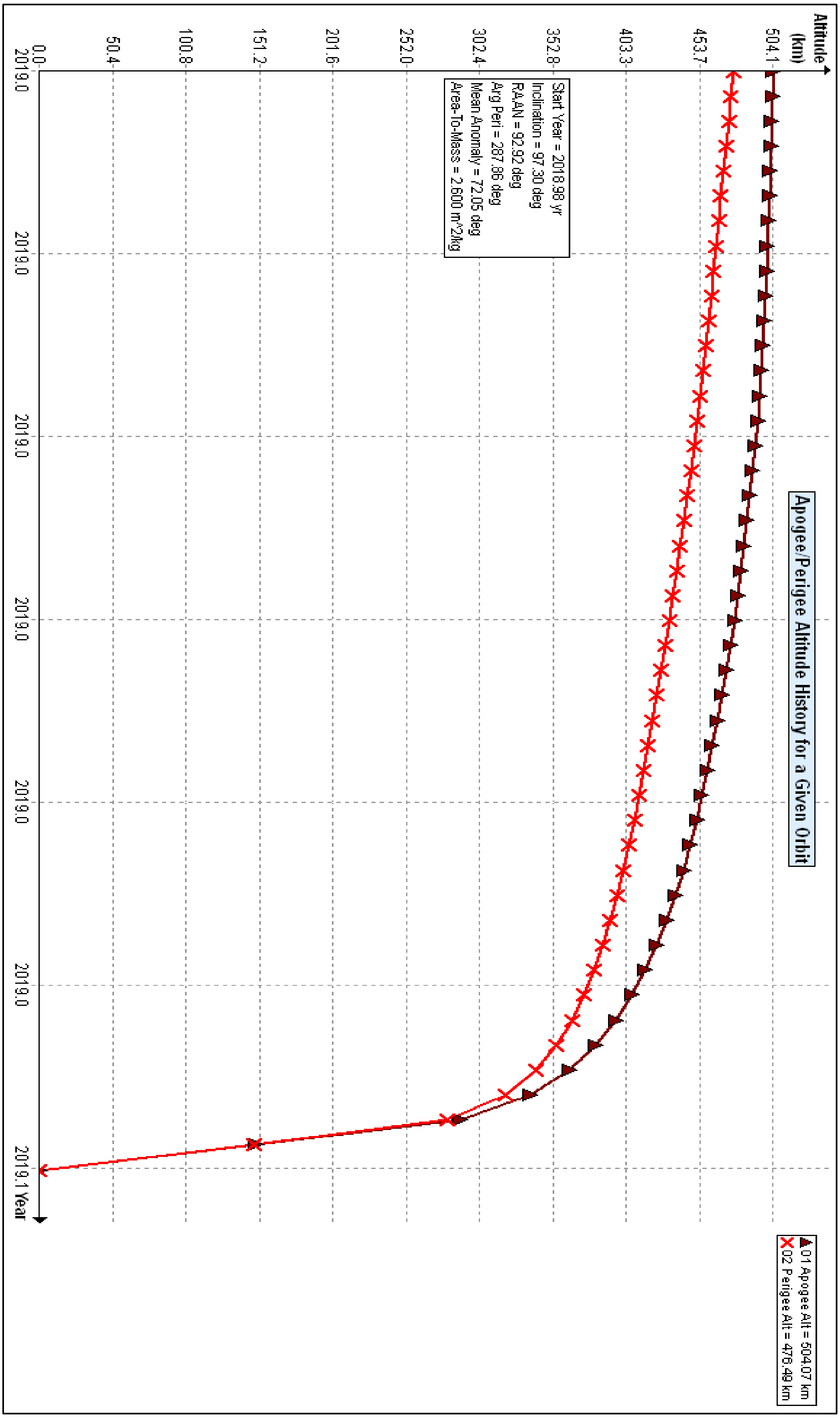

Appendix Figure F-2: Case study 2 graphical data

Appendix G Case Study 3 Input Data

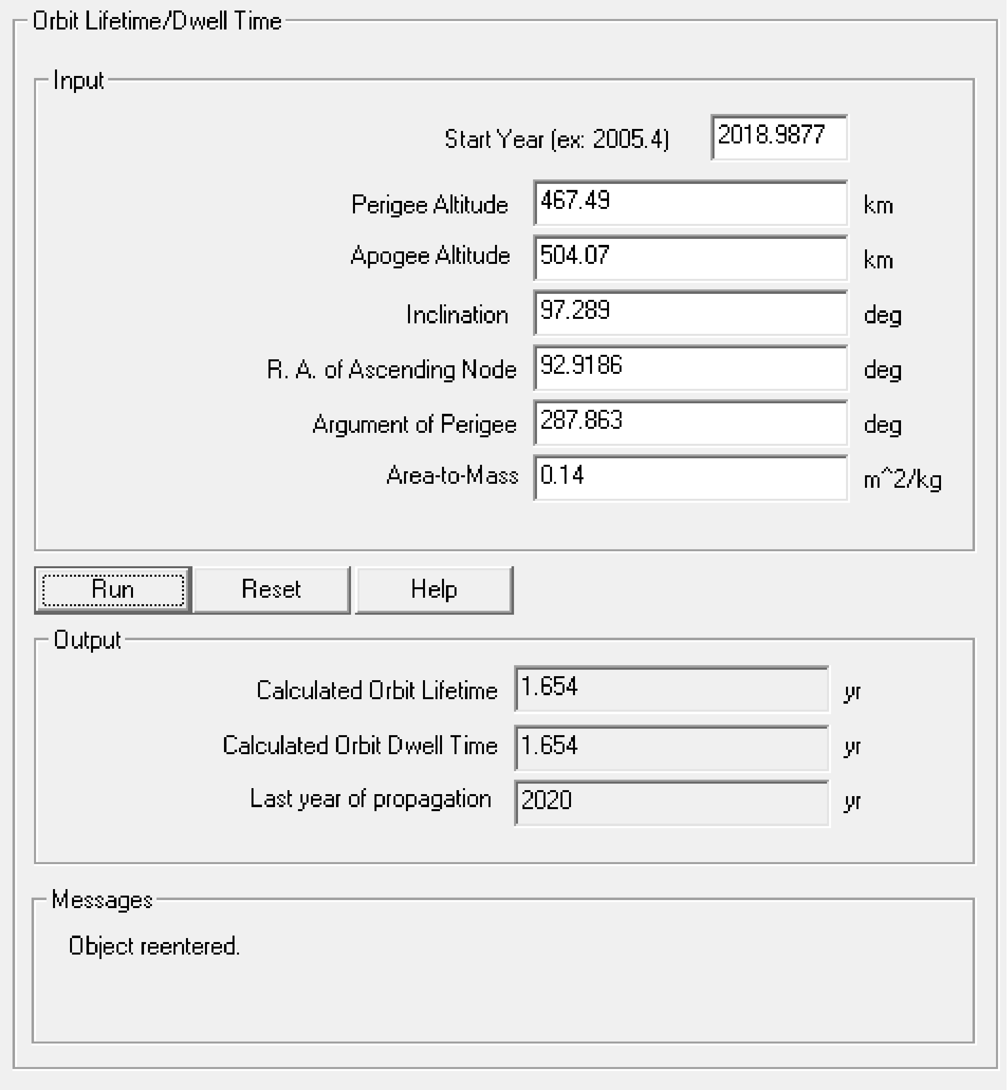

Start Year (ex: 2005.4) 2018.9877

Perigee Altitude 467.49 km

Apogee Altitude 504.07 km

Inclination 97.289 deg

R. A. of Ascending Node 92.9186 deg

Argument of Perigee 287.863 deg

Area-to-Mass 0.14 m^2/kg

Calculated Orbit Lifetime 1.654 yr

Calculated Orbit Dwell Time 1.654 yr

Last year of propagation 2020 yr

Object reentered.

Appendix Figure G-1: Case study 3 input data

Appendix G-2: Case Study 3 Graphical Results

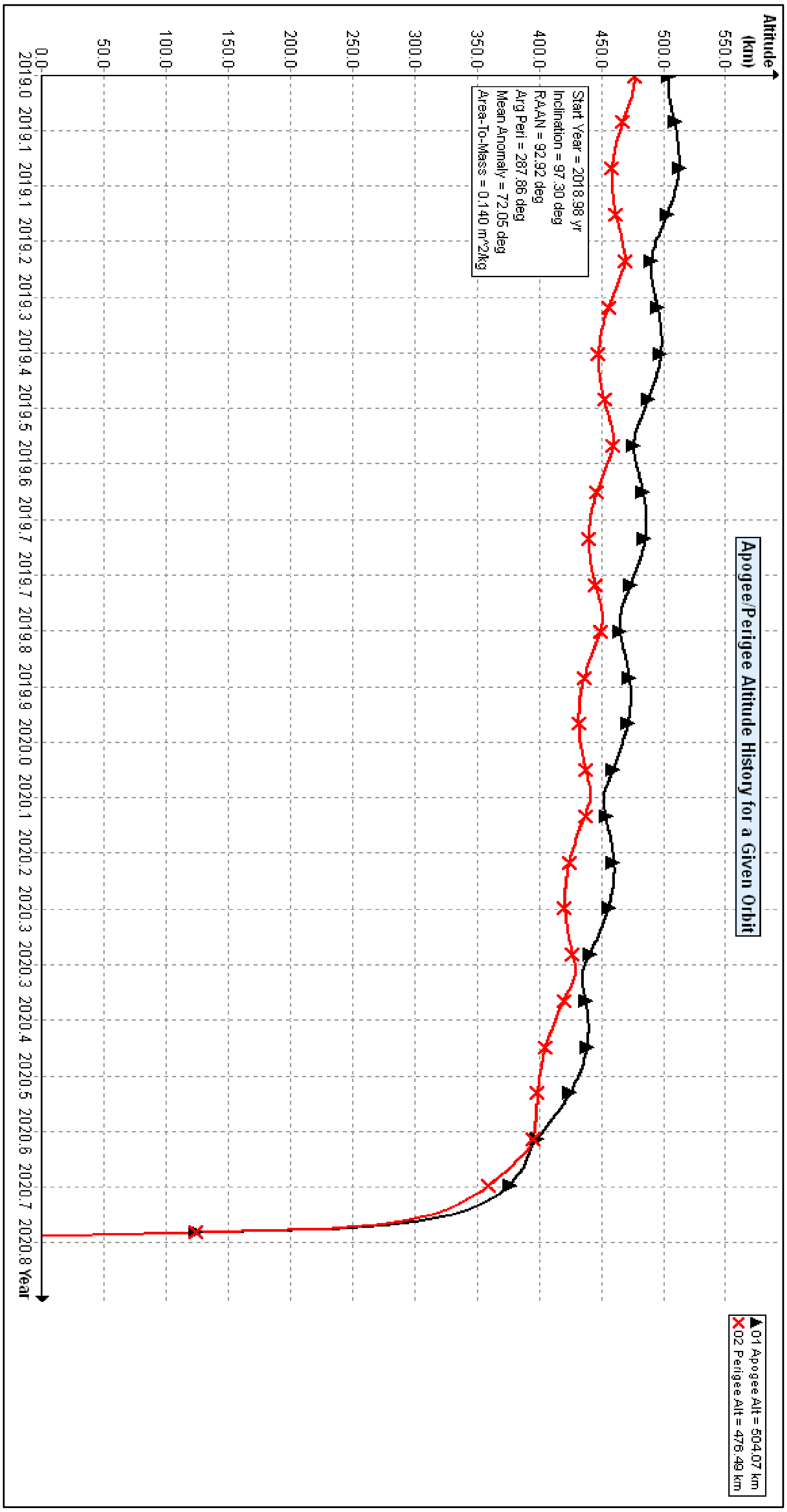

Appendix Figure G-2: Case study 3 graphical results

Appendix H Ballistic Coefficient Calculations

Where:
Satellite of Mass =3.8 kg
Cd Values= 2.2

The ballistic coefficient for the Baseline Case was calculated as follows:

$$BC = \frac{m}{C_D A}$$

$$BC = \frac{3.8}{(2.2)(0.03)}$$

$$BC = 57.57 kg / m^2$$

The ballistic coefficient for case study 1 was calculated as follows:

$$BC = \frac{m}{C_D A}$$

$$BC = \frac{3.8}{(2.2)(0.4)}$$

$$BC = 4.31 kg / m^2$$

The ballistic coefficient for case study 2 was calculated as follows:

$$BC = \frac{m}{C_D A}$$

$$BC = \frac{3.8}{(4.0)(10.3)}$$

$$BC = 0.092 kg / m^2$$

The ballistic coefficient for case study 3 was calculated as follows

$$BC = \frac{m}{C_D A}$$

$$BC = \frac{3.8}{(2.2)(0.52)}$$

$$BC = 3.32 kg / m^2$$

Appendix I Mass Sensitivity Study Data

The table below shows the data used to produce the mass sensitivity graphs discussed in chapter 6.

Area/Mass=m^2/kg	**Orbital Lifetime prediction in days**
(0.03/3) = 0.01	1375
(0.03/3.2) = 0.0093	1391
(0.03/3.4) = 0.0088	1419
(0.03/3.6)= 0.0083	1450
(0.03/3.8) = 0.0079	1477
(0.03/4) = 0.0075	1505
(0.03/4.2) = 0.0071	1542
(0.03/4.4) = 0.0068	1570
(0.03/4.6) = 0.0065	1600
(0.03/4.8) = 0.0062	1634

Appendix J Cross-sectional Area Analysis Data

The table shows data used to produce the cross-sectional area graph discussed in chapter 6.

Area/Mass=m^2/kg	Orbital Lifetime prediction in days
(0.03+0.37)/(3.8) = 0.105	703
(0.03+0.39)/(3.8) = 0.110	689
(0.03+0.41)/(3.8)= 0.115	675
(0.03+0.43)/(3.8) = 0.121	659
(0.03+0.45)/(3.8) = 0.126	645
(0.03+0.47)/(3.8)= 0.131	631
(0.03+0.49)/(3.8)= 0.136	612
(0.03+0.51)/(3.8) = 0.142	597

Appendix K Debris Mitigation Guidelines

The mitigation of orbital debris can be divided into two core categories:

- Protecting satellites from debris by avoiding collisions and shielding
- Reducing the amount of new debris created and, in the long run, removing existing debris.

Each of the above-mentioned organisations has set out guidelines in an effort to address growing debris. Below is a brief outline of some of the guidelines as set by the organizations with the focus mainly on LEO.

U. S Government has four main objectives

- Control of debris released during normal operations
- minimizing debris generated by accidental explosions
- selection of safe flight profile and operational configuration
- Post mission disposal of space structures.

NASA has similar objectives which can be found in NASA Procedural Requirements for Limiting Orbital Debris and Evaluating the Meteoroid and Orbital Debris Environments report(NASA, 2017). The main objectives are:

- Orbital debris released as part of normal operations is minimized.
- The potential for orbital debris generated by accidental explosions is limited.
- The potential for breakup or loss of passivation and disposal capabilities due to on-orbit collisions is limited.
- The number of expended or decommissioned space objects remaining in orbit, and their durations in orbit, are limited.
- The likelihood of collisions with other space objects is minimized

The Inter-Agency Space Debris Co-ordination Committee (IADC) was founded in 1993, comprising 11 national space agencies including NASA, ESA and the British National Space Centre (BNSC). The Guidelines cover the overall environmental impact of the missions with a focus on the following:

- Limitation of debris released during normal operations
- Minimisation of the potential for on-orbit break-ups
- Post-mission disposal within 25 years
- Prevention of on-orbit collisions

Appendix L Upilex-Ca Material Specifications

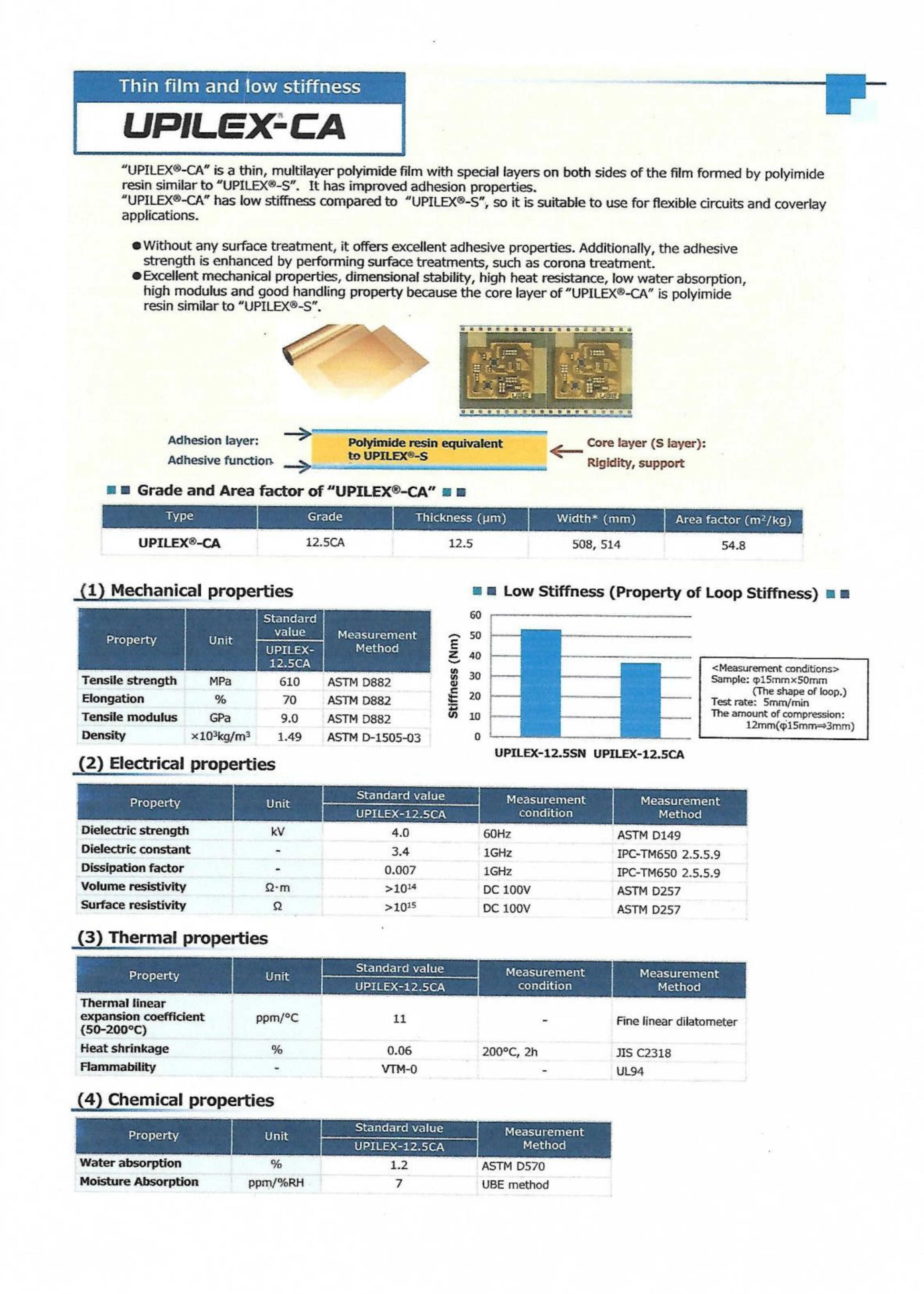

Thin film and low stiffness

UPILEX®-CA

"UPILEX®-CA" is a thin, multilayer polyimide film with special layers on both sides of the film formed by polyimide resin similar to "UPILEX®-S". It has improved adhesion properties.
"UPILEX®-CA" has low stiffness compared to "UPILEX®-S", so it is suitable to use for flexible circuits and coverlay applications.

- Without any surface treatment, it offers excellent adhesive properties. Additionally, the adhesive strength is enhanced by performing surface treatments, such as corona treatment.
- Excellent mechanical properties, dimensional stability, high heat resistance, low water absorption, high modulus and good handling property because the core layer of "UPILEX®-CA" is polyimide resin similar to "UPILEX®-S".

Grade and Area factor of "UPILEX®-CA"

Type	Grade	Thickness (μm)	Width* (mm)	Area factor (m²/kg)
UPILEX®-CA	12.5CA	12.5	508, 514	54.8

(1) Mechanical properties

Property	Unit	Standard value	Measurement Method
		UPILEX-12.5CA	
Tensile strength	MPa	610	ASTM D882
Elongation	%	70	ASTM D882
Tensile modulus	GPa	9.0	ASTM D882
Density	×10³kg/m³	1.49	ASTM D-1505-03

Low Stiffness (Property of Loop Stiffness)

<Measurement conditions>
Sample: φ15mm×50mm
(The shape of loop.)
Test rate: 5mm/min
The amount of compression:
12mm(φ15mm⇒3mm)

(2) Electrical properties

Property	Unit	Standard value	Measurement condition	Measurement Method
		UPILEX-12.5CA		
Dielectric strength	kV	4.0	60Hz	ASTM D149
Dielectric constant	-	3.4	1GHz	IPC-TM650 2.5.5.9
Dissipation factor	-	0.007	1GHz	IPC-TM650 2.5.5.9
Volume resistivity	Ω·m	$>10^{14}$	DC 100V	ASTM D257
Surface resistivity	Ω	$>10^{15}$	DC 100V	ASTM D257

(3) Thermal properties

Property	Unit	Standard value	Measurement condition	Measurement Method
		UPILEX-12.5CA		
Thermal linear expansion coefficient (50-200°C)	ppm/°C	11	-	Fine linear dilatometer
Heat shrinkage	%	0.06	200°C, 2h	JIS C2318
Flammability	-	VTM-0	-	UL94

(4) Chemical properties

Property	Unit	Standard value	Measurement Method
		UPILEX-12.5CA	
Water absorption	%	1.2	ASTM D570
Moisture Absorption	ppm/%RH	7	UBE method

Appendix Figure L-1: Upilex –Ca material specifications

Appendix M Soyuz Rocket Sinusoidal Vibrations and g-loading range

Directions	Frequency Band (Hz)						
	1-5	5-10	10-20	20-30	30-40	40-60	60-100
	Sinusoidal amplitude in (g)						
Longitudinal	0.4	0.5	0.8	0.8	0.5	0.5	0.3
Lateral	0.4	0.6	0.6	0.4	0.4	0.3	0.3

Appendix N Perturbation included in DAS orbit propagators

Perturbation	PROP3D	GEOPROP
Atmospheric drag	Oblate, rotating and atmosphere	None
Solar and Lunar gravity	Yes	Yes
Solar radiation pressure (SPR)	Yes	Yes
Earth's Shadow for SRP	Yes	Neglected
Earth's gravity field	Zonal harmonics: J_2,J_3,J_4,$(J_2)^2$	Zonal harmonics: J_2,J_3,J_4, Tesseral harmonics: $J_{2.2}$,$J_{3.1}$,$J_{3.3}$,$J_{4.2}$,$J_{4.4}$

Appendix O Modal and Harmonic Analysis

During launch the structure will be exposed to complex random vibrations generated by the launch vehicle. If these vibrations are within the structure's resonant frequency, the structure will vibrate and may cause irrefutable damage to the satellite. Therefore, modal analysis was performed to extract the natural frequency of the structure and to ensure that the frequencies are of such a nature that resonance will not occur. The frequency range considered is 1Hz-100Hz as stipulated in the European cooperation for space standardization (ECSS) testing manual.

A modal analysis, on its own, only identifies the natural frequencies and mode shapes. This must be followed by exciting the structure with a sinusoidal load of a given force magnitude in a frequency perturbation analysis to obtain the actual displacements and strains from which the stresses are computed based on a linear elastic constitutive relationship defined through the material properties of Young's modulus and Poisson's ratio. Any dynamic analysis also incorporates the inertial effect that needs to be defined by specifying the material density.

As an alternative to the frequency perturbation step, a harmonic analysis can be performed in SOLIDWORKS which calculates the peak steady state response due to harmonic loads. Harmonic loads for this kind of analysis take the form

$$P = Asin(\omega t + \varphi) \tag{O.1}$$

where: A is the amplitude, ω is the frequency, t is time, and φ is the phase angle.(SOLIDWORKS Help Manual, 2019)

1. Natural Frequencies of Analysis of the Lid

The first six natural frequencies of the lid were extracted and are shown in the figures Appendix figure O-1 to appendix figure O-6 below. Also included is a frequency vs mode number chart seen in appendix figure O-7.During analysis the lid was restrained by the two M2 frangibolt connection points, since it will be the only fixed connection between the housing and the lid. It could be argued that the lid will be supported by the walls of the housing and as a result may increase the stiffness which may result in a higher natural frequency.

However, a more conservative approach was taken and only the two fixed points selected. Based on natural frequency analysis the lowest natural frequency is 583.313 Hz and the highest natural frequency was 2568.12 Hz. Both these are much higher than the 5Hz-100Hz range. Therefore, it can be deduced that the component will not resonate during launch.

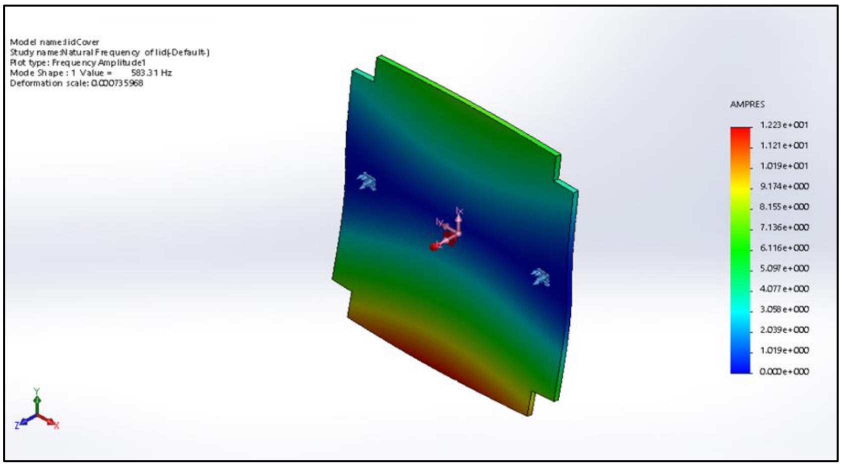

Appendix Figure O-1: Mode Shape 1 of the lid at 583.313 Hz

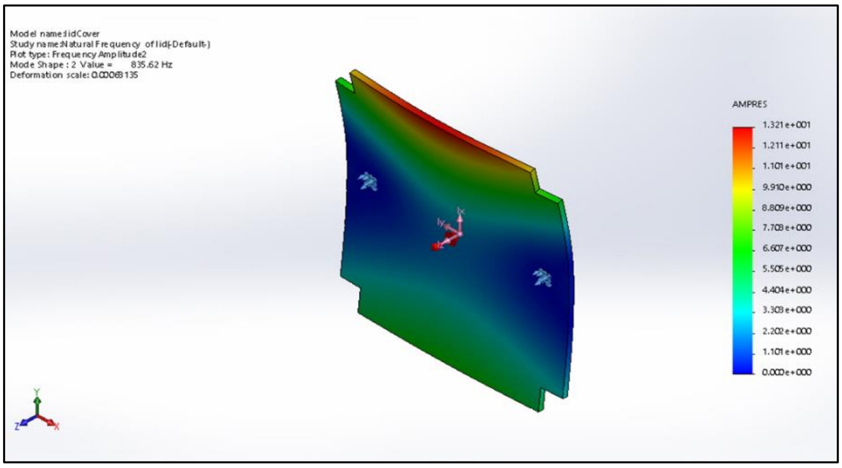

Appendix Figure O-2 Mode shape 2 of the lid at 835.622 Hz

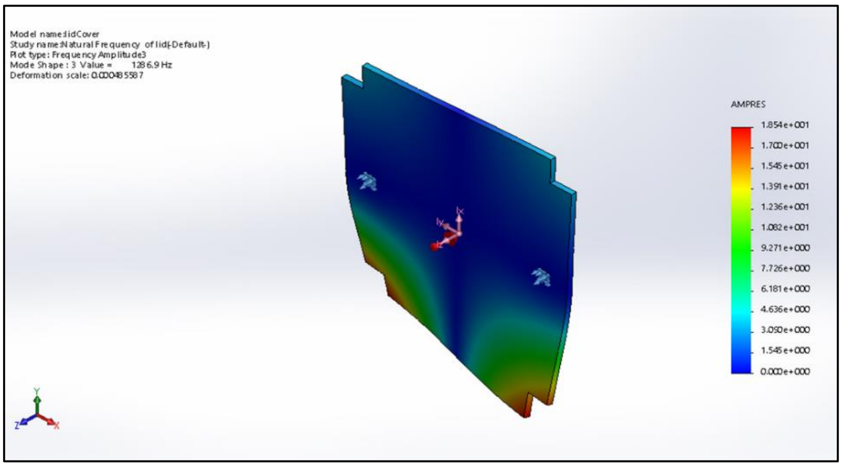

Appendix Figure O-3: Mode shape 3 of the lid at 1286.91 Hz

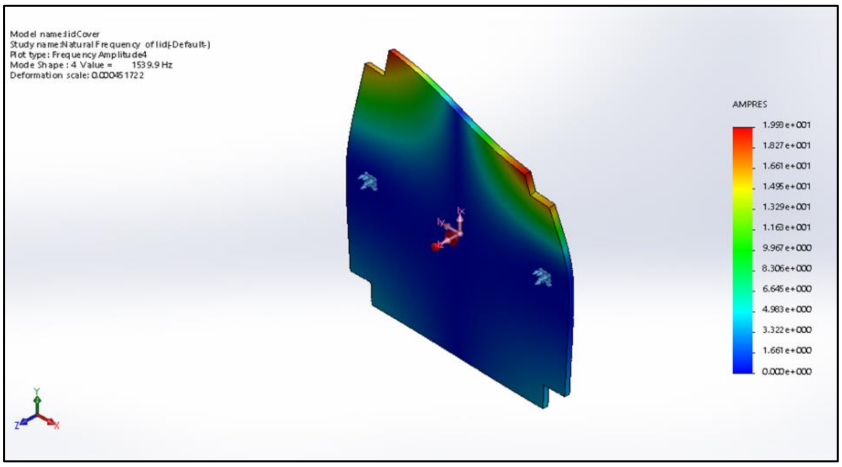

Appendix Figure O-4: Mode shape 4 of the lid at 1539.92 Hz

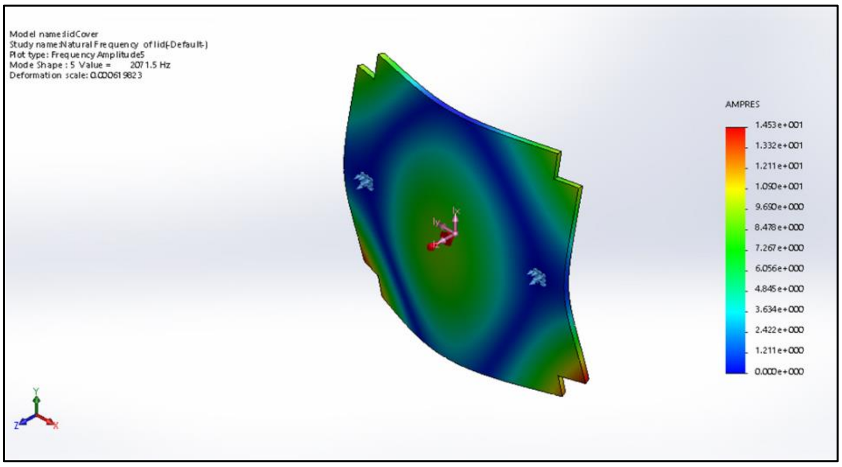

Appendix Figure O-5: Mode shape 5 of the lid at 2071.52 Hz

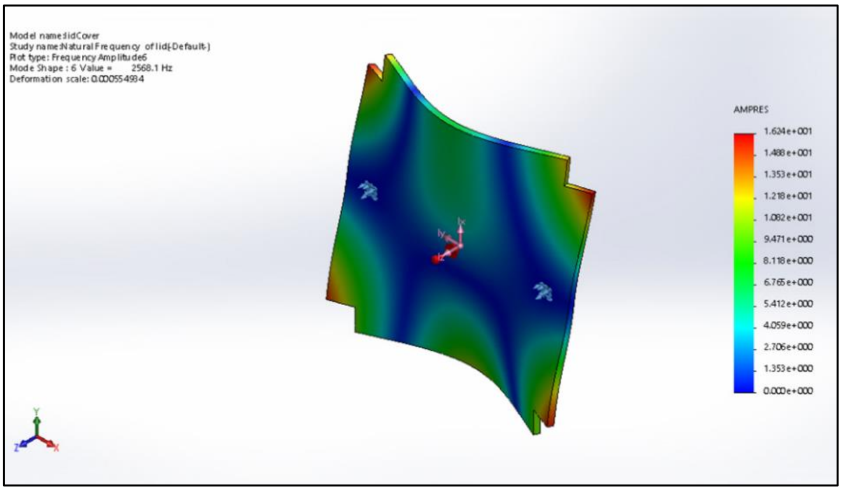

Appendix Figure O-6: Mode shape 6 of the lid at 2568.12 Hz

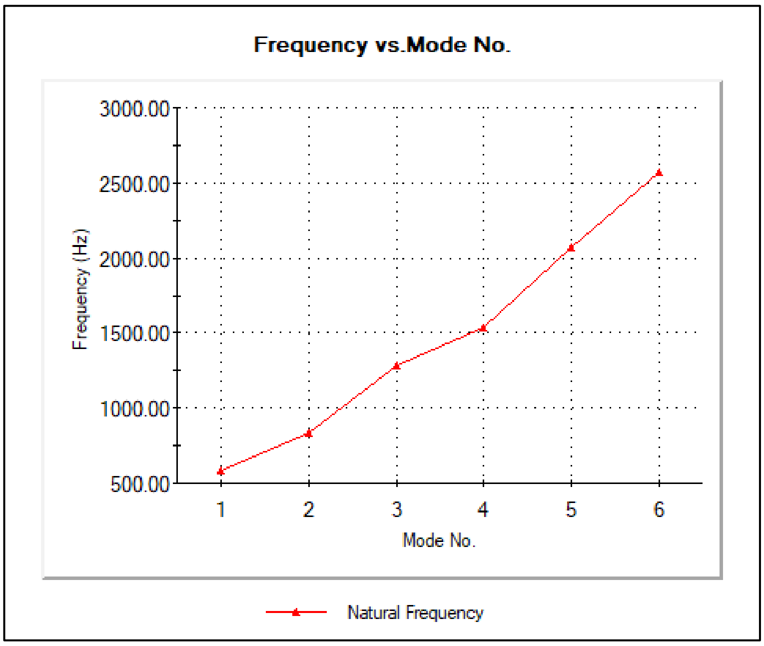

Appendix Figure O-7: Frequency vs Mode Number Chart for lid

2. Natural Frequency Analysis of the Housing

The first six natural frequencies were extracted and is shown in appendix figure O-8 to appendix figure O-13.This is followed by a frequency vs mode shape graph seen inappendix figure O-14.When the structure is assembled and incorporated into a CubeSat structure it will be fixed to the structure by connection points located at all four corners and will be further supported by the CubeSat rails in each corner. Consequently, during natural frequency analyses all four corners were constrained. Based on frequency analysis the results showed that the lowest frequency is 1066.57 Hz and the higher frequency is 2771.6 Hz. These frequencies are well above the 5Hz-100Hz range therefore, resonance will not occur during launch.

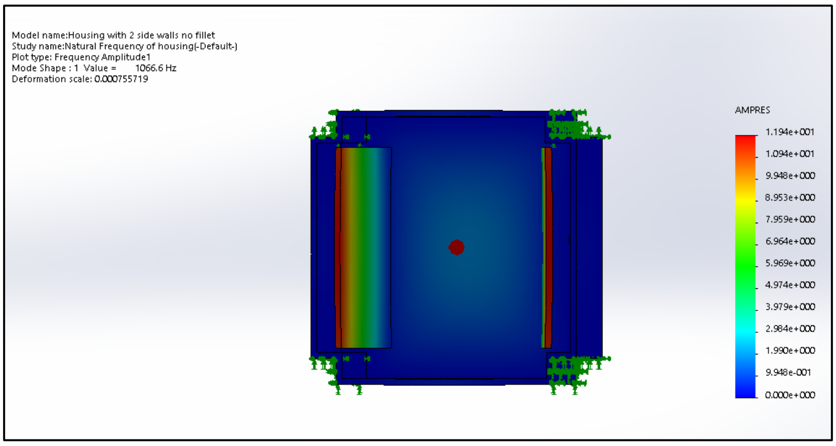

Appendix Figure O-8: Mode shape 1 of the housing at 1066.57 Hz

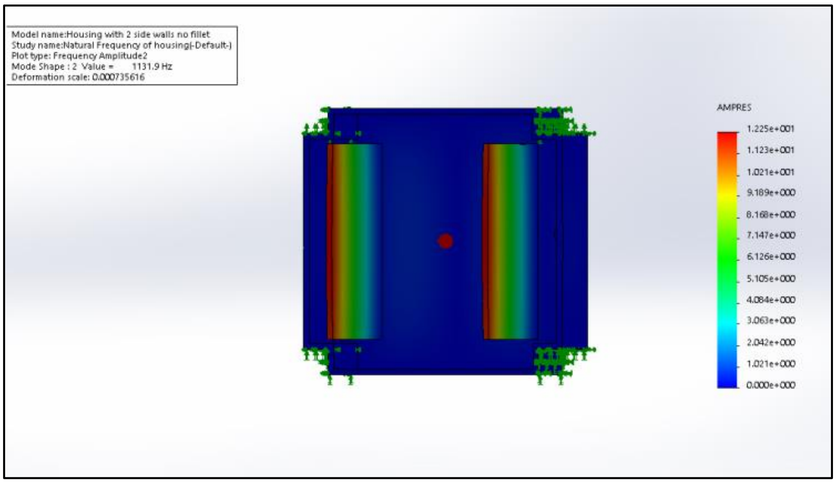

Appendix Figure O-9: Mode shape 2 of the housing at 1131.88 Hz

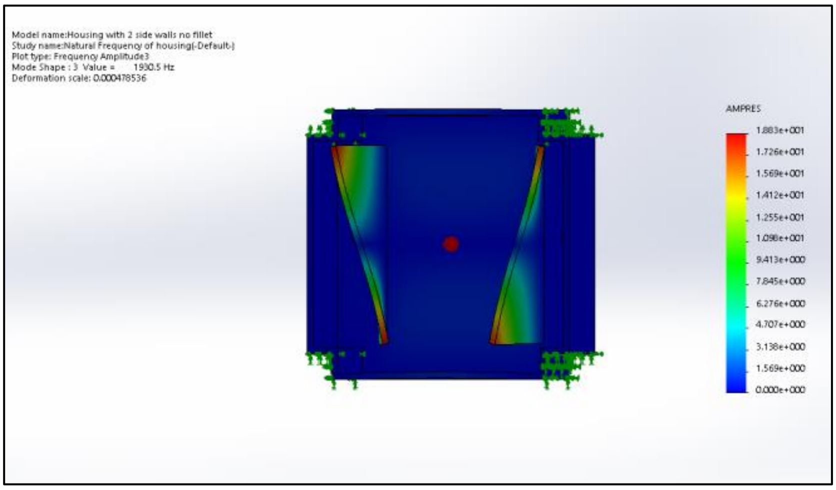

Appendix Figure O-10: Mode shape 3 of the housing at 1930.46 Hz

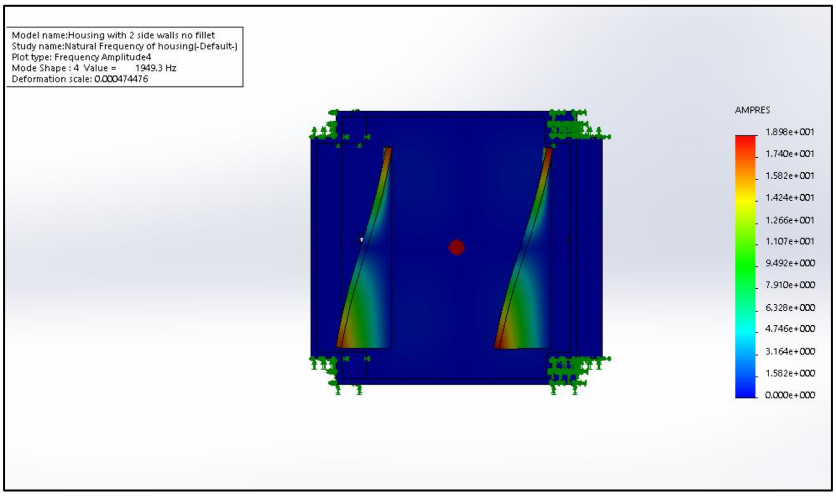

Appendix Figure O-11: Mode shape 4 of the housing at 1949.28 Hz

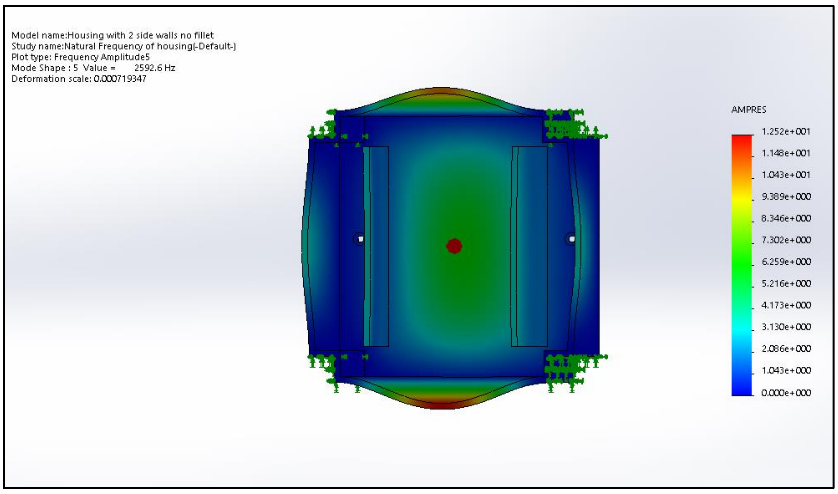

Appendix Figure O-12: Mode shape 5 of the housing at 2592.61 Hz

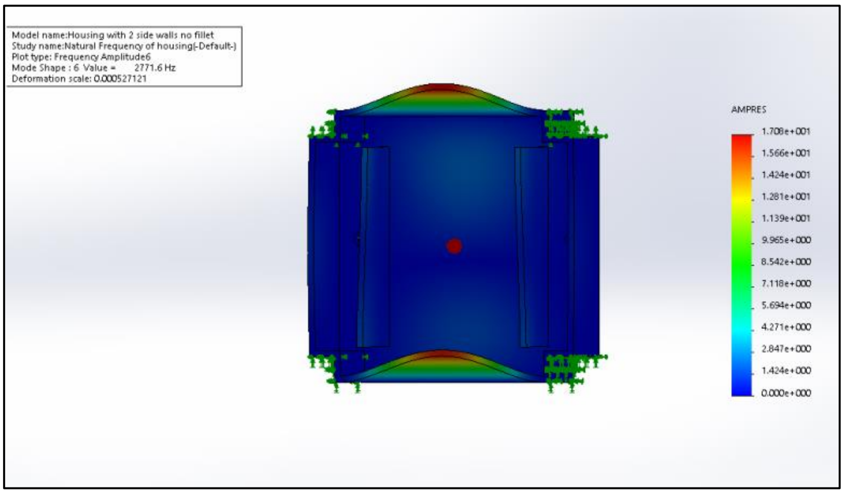

Model name:Housing with 2 side walls no fillet
Study name:Natural Frequency of housing(-Default-)
Plot type: Frequency Amplitude6
Mode Shape : 6 Value = 2771.6 Hz
Deformation scale: 0.000527121

Appendix Figure O-13: Mode shape 6 of the housing at 2771.6 Hz

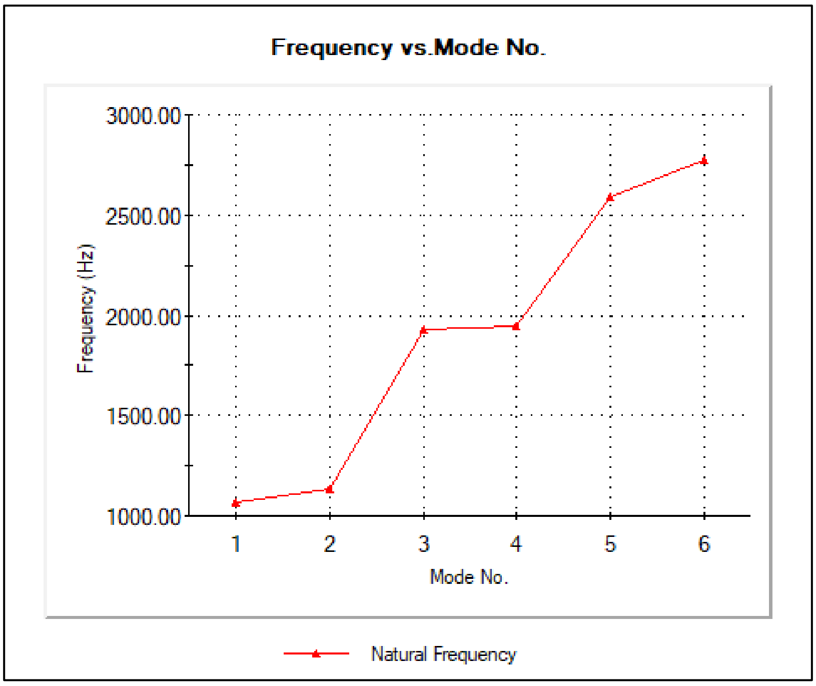

Appendix Figure O-14: Frequency vs Mode shape number of housing

3. Natural Frequency of the Concept

The first six natural frequencies of the assembled structure were extracted and is shown inAppenid figure O-15 to appendix figure O-20. This is followed by appendix figure O-21 which shows the natural frequencies vs mode shape graph. The assembled structure will be affixed to the CubeSat structure by connection points located at all four corners and will be further supported by the CubeSat rails in each corner. Consequently, during natural frequency analysis all four corners were constrained**.** Based on frequency analysis the lowest frequency observed was 3140.7Hz and the highest was 6104.84 Hz.

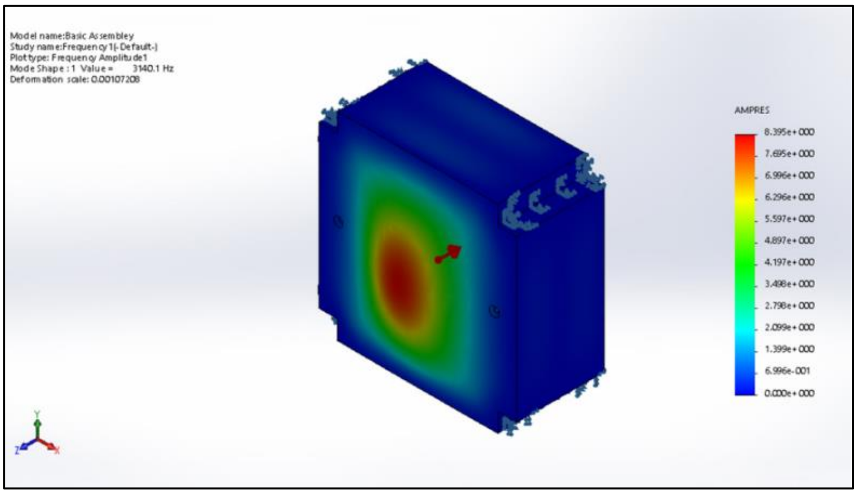

Appendix Figure O-15: Mode shape 1 of the designed structure at 3140.7Hz

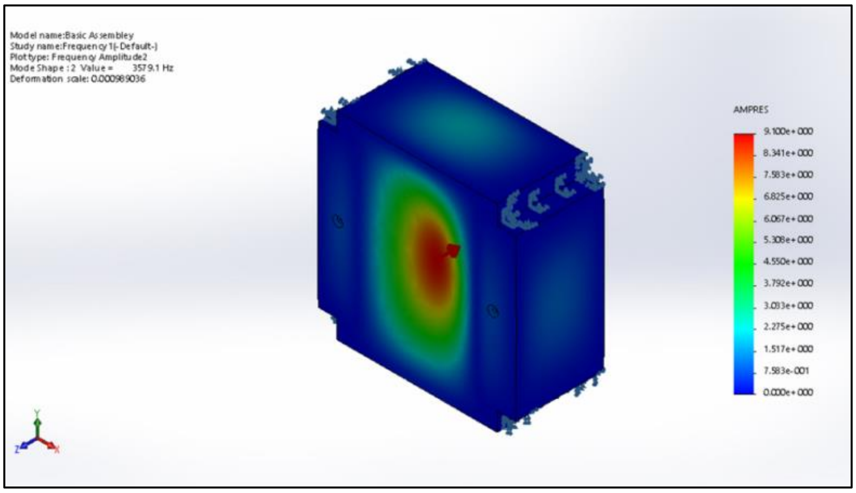

Appendix Figure O-16: Mode shape 2 of the designed structure at 3579.15 Hz

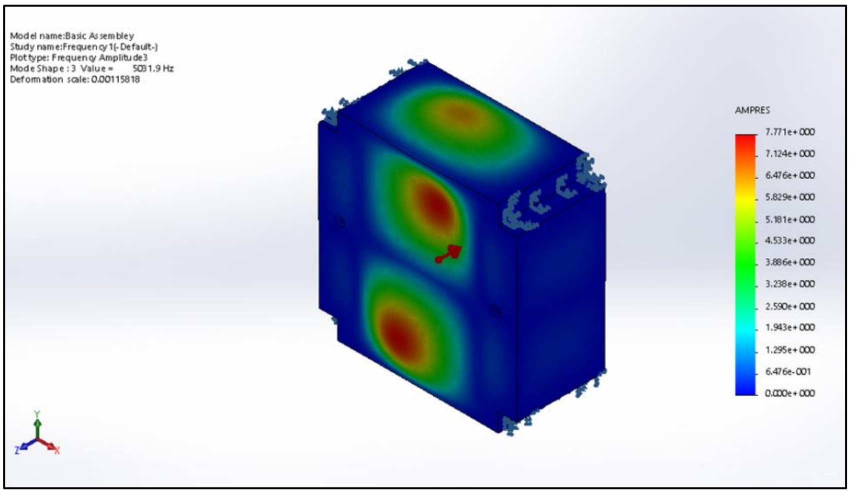

Appendix Figure O-17: Mode shape 3 of the designed structure at 5031.91 Hz

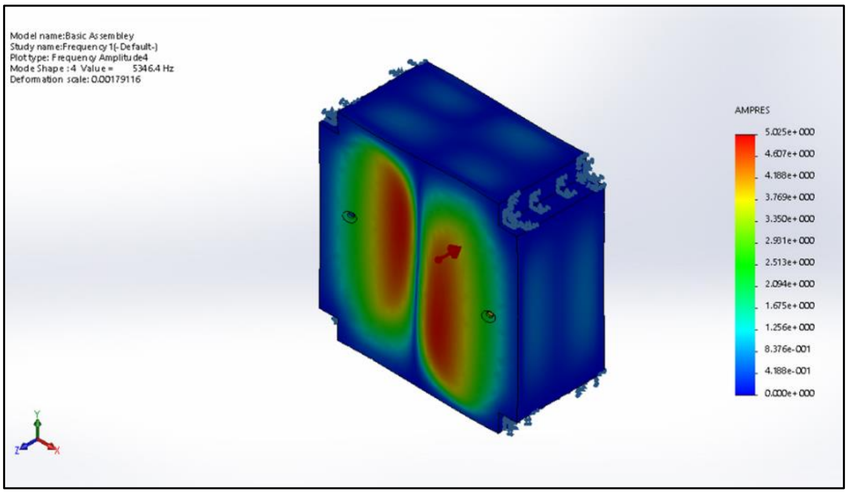

Appendix Figure O-18: Mode shape 4 of the designed structure at 5346.35 Hz

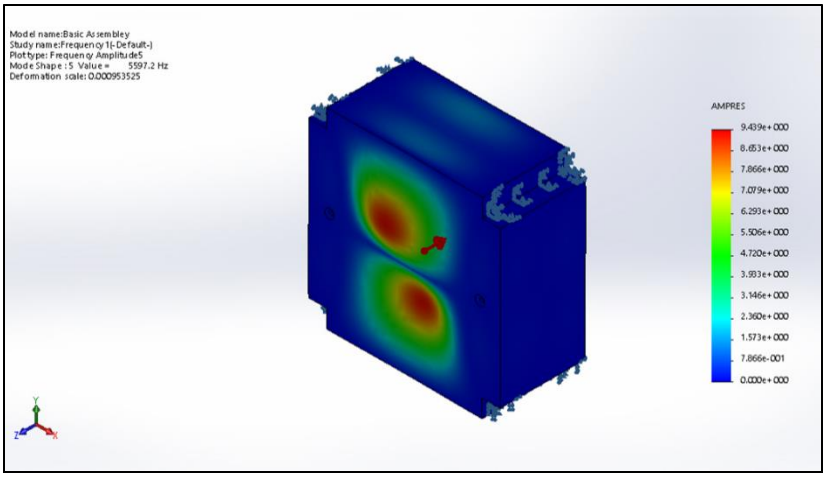

Appendix Figure O-19: Mode shape 5 of the designed structure at 5597.21 Hz

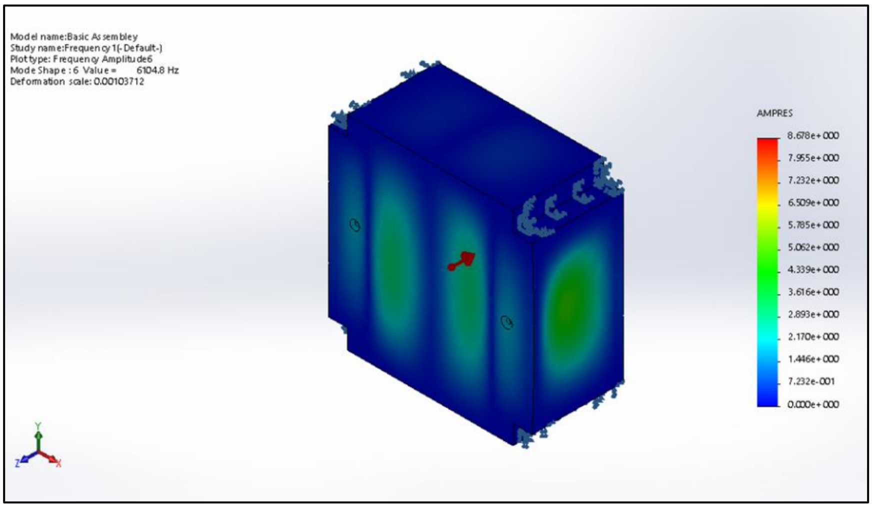
Model name:Basic Assembley
Study name:Frequency1(-Default-)
Plot type: Frequency Amplitude6
Mode Shape : 6 Value = 6104.8 Hz
Deformation scale: 0.00103712

Appendix Figure O-20: Mode Shape 6 of the designed structure at 6104.84 Hz

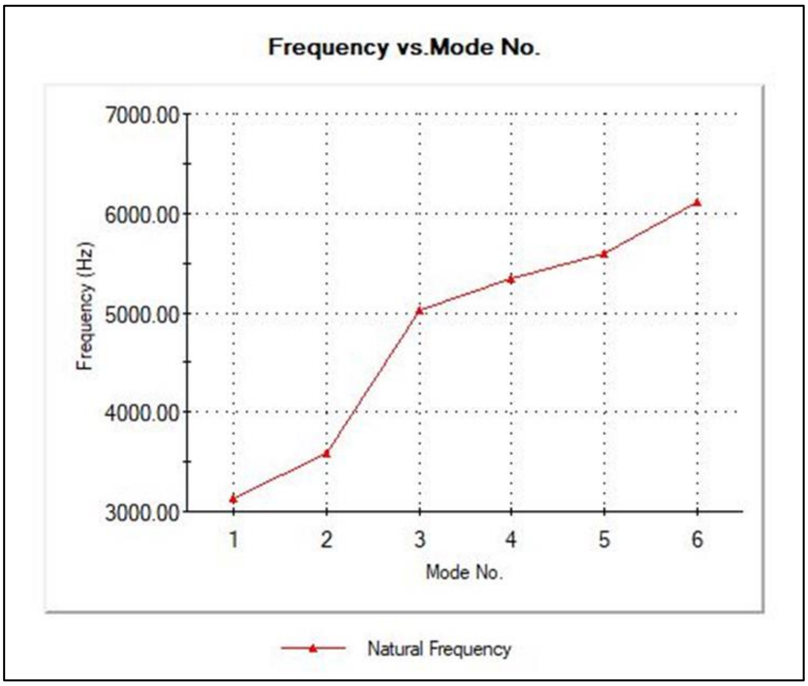

Appendix Figure O-21: Natural frequency vs Mode number graph of the designed structure

4. Sinusoidal Dynamic Load Response Analysis

In addition to the G-force loading, the launch vehicle will exert a combination of vibrations on its payload. Engine vibration during various launch stages creates low frequency sine and random vibrations, which are mechanically transferred to the payload. Similarly, while the launch vehicle travels through the atmosphere acoustic noise and randomised vibrational patterns are generated and transmitted to the payload.

Lastly shock loads which are the result of solid rocket body breaking away from the launch vehicle will also be transmitted to the payload. Due to the complexity of these vibrations, a sinusoidal vibrational pattern is used to analyse the effects it has on the payloads. This is achieved by means of a shaker table or vibrational bed which is set up According to the European cooperation for space standardization (ECSS) testing manual and the sinusoidal vibration profile of the selected launch vehicle. During testing the frequency is increased from 1Hz to 100Hz at a rate of two octaves per minute.

The Soyuz rocket was used to launch ZaCube-2 into orbit and is a commonly used launch vehicle. Thus, the following section shows the results obtained when the structure is exposed to a sinusoidal vibrational pattern ranging from 1Hz -100Hz and their corresponding g-loading as prescribed in the Soyuz rocket manual. The restrain methodology applied during the natural frequency analysis will also be applied during this analysis.

5. Sinusoidal Response of Lid under Longitudinal loading

The following section shows the response of the lid under longitudinal and sinusoidal dynamic loading when constrained only by the M2 frangibolts. Appendix figure O-22 to appendix fifure O23 shows the displacement and von Mises for a sinusoidal frequency range of 1-5Hz and a load of 0.4g. Based on harmonic analysis the maximum displacement was 0.000366665 mm at 5Hz and the maximum von Mises stress was 78372.3 N/m^2 at 5Hz.

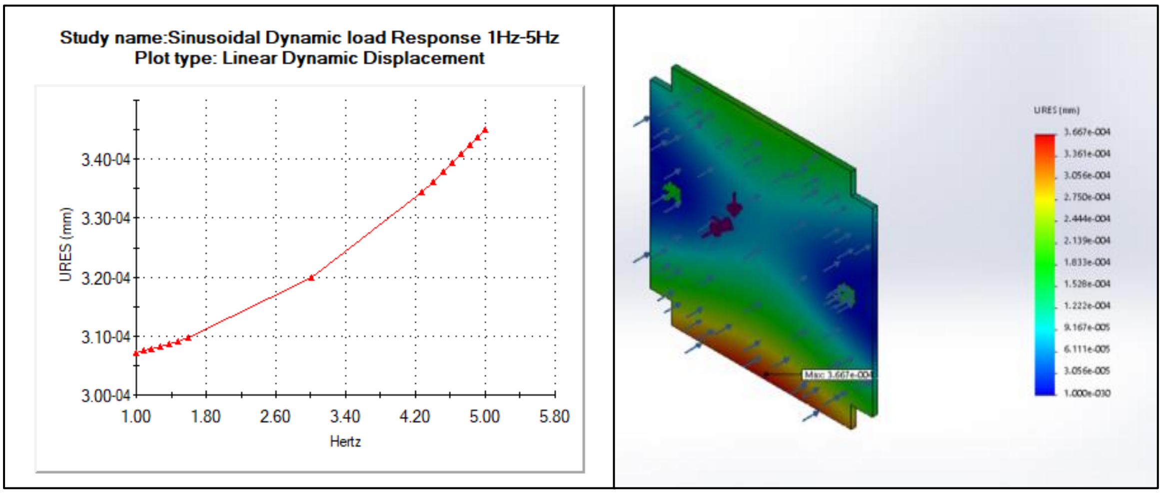

Appendix Figure O-22: Maximum lid displacement under longitudinal loading for frequency range 1Hz-5Hz

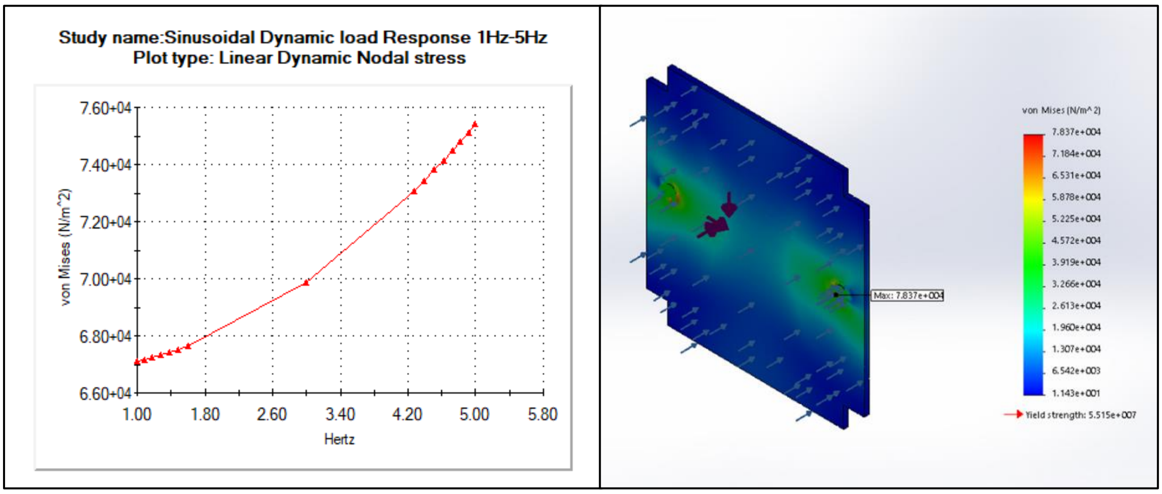

Appendix Figure O-23: von Mises on the lid under longitudinal loading for frequency range 1Hz-5Hz

Appenidx figure O-24 to appendix figure O-25 shows response of the lid when it is exposed to a longitudinal load of 0.5g and a sinusoidal frequency range of 5H-10Hz. Based on harmonic analysis the Maximum displacement and stress were found at 10Hz which was 0.000573647 mm and 122627 N/m^2 respectively.

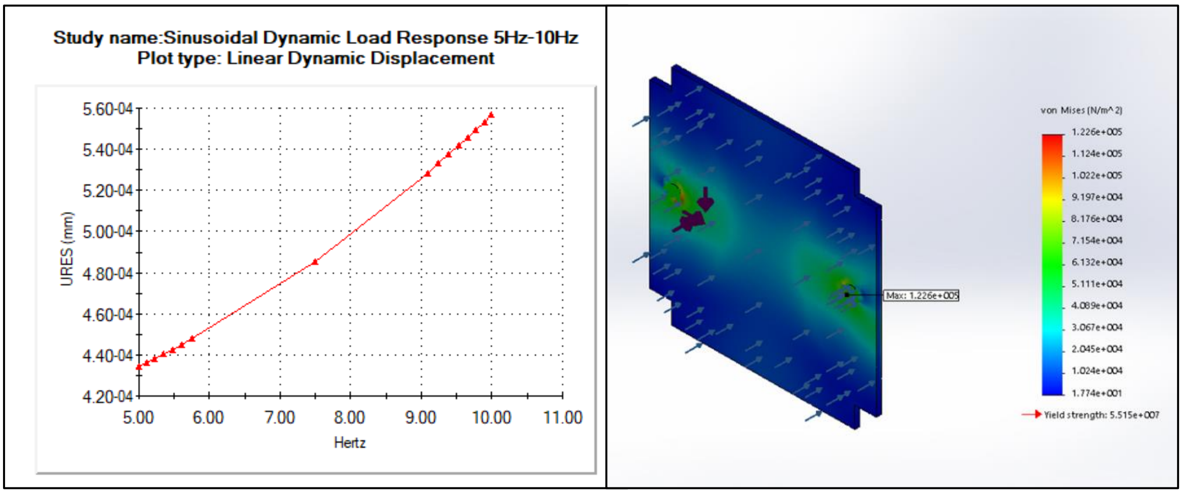

Appendix Figure O-24: Maximum lid displacement under longitudinal loading for frequency range 5Hz-10Hz

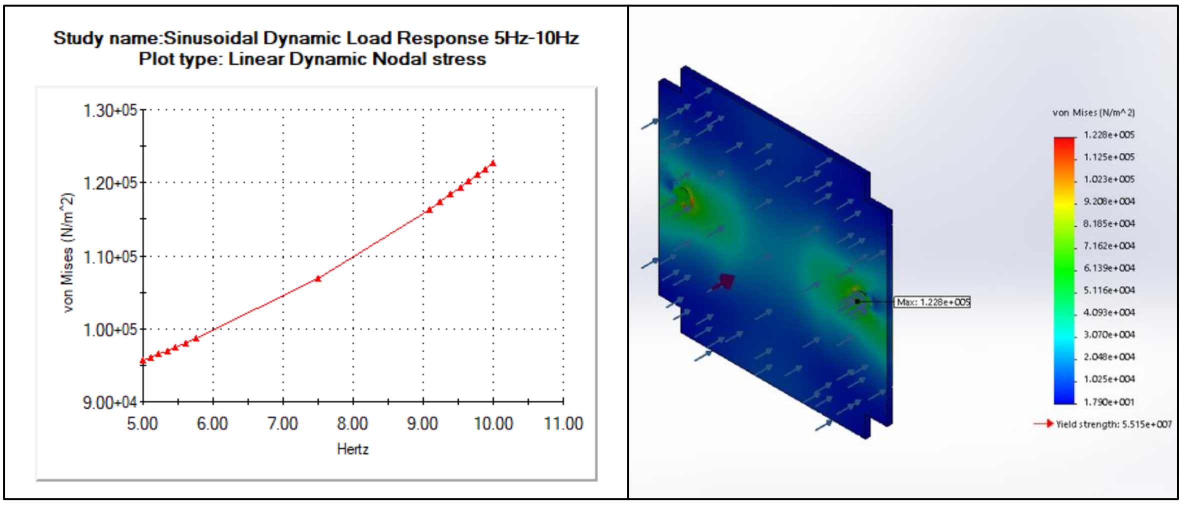

Appendix Figure O-25: von Mises Stress on the lid under longitudinal loading for frequency range 5Hz-10Hz

Appendix figure O-26 to appendix O-27 shows the response of the lid when it is exposed to a sinusoidal dynamic load with frequency range of 10Hz to 20Hz and a longitudinal load of 0.8g. Harmonic analysis indicated that the maximum displacement and von Mises stresses were 0.0012804 mm and 273732 N/m^2 at 20Hz respectively.

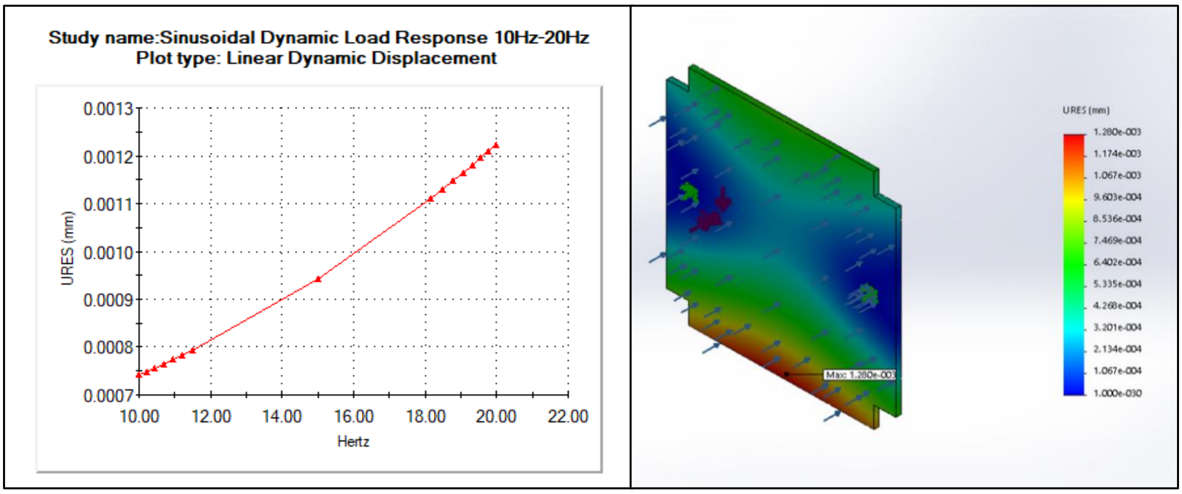

Appendix Figure O-26: Maximum lid displacement under longitudinal loading for frequency range 10Hz-20Hz

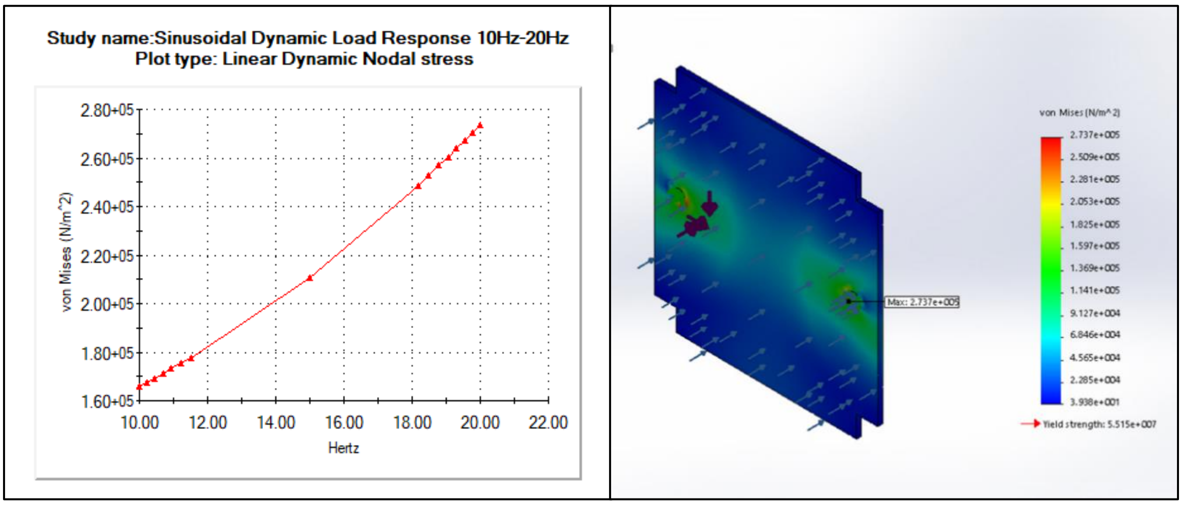

Appendix Figure O-27: von Mises stress on the lid under longitudinal loading for frequency range 10Hz-20Hz

The following figures show the response of the lid when it is exposed to a sinusoidal frequency range 20Hz to 30Hz and a 0.8g longitudinal load. Based on harmonic analysis the maximum displacement was found to be 0.00213668 mm shown in appendix figure O-28. Appendix figure O-29 show the maximum stress at 30Hz and was found to be 458430 N/m^2.

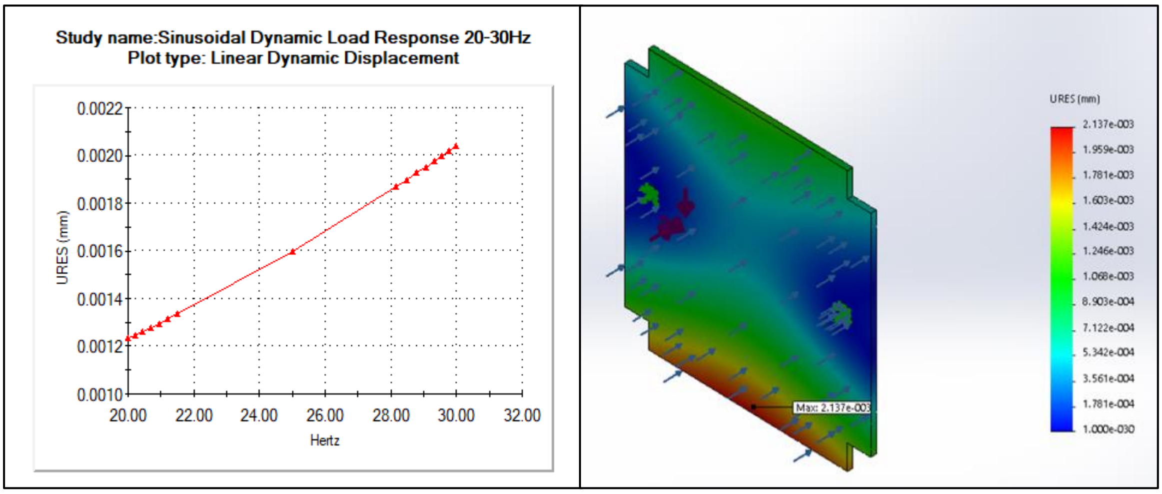

Appendix Figure O-28: Maximum lid displacement under longitudinal loading for frequency range 20Hz-30Hz

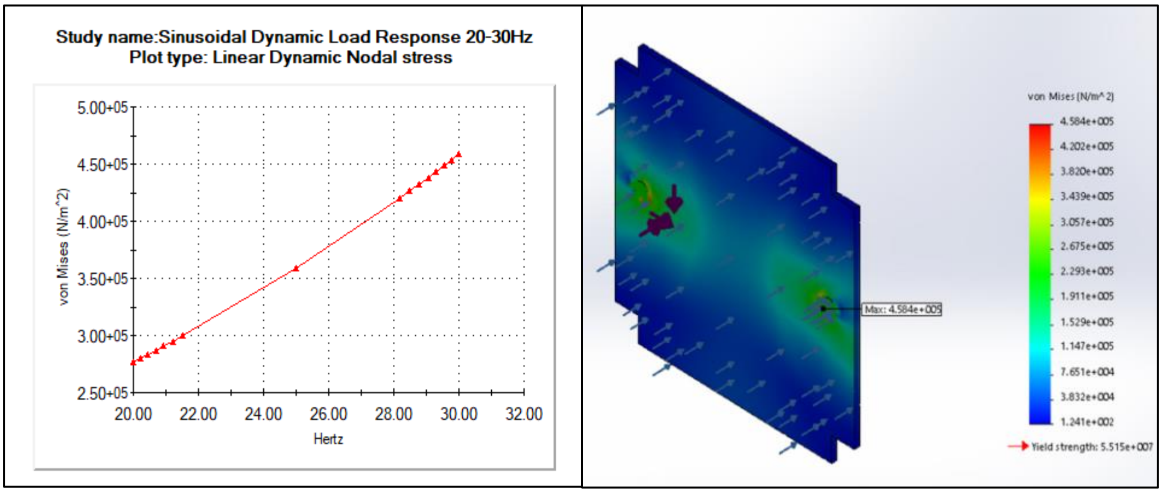

Appendix Figure O-29: von Mises stress on the lid under longitudinal loading for frequency range 20Hz-30Hz

Appendix figure O-30 to appendix figure O-31 shows the response of the lid when it is exposed to a sinusoidal frequency range of 30Hz to 40Hz and a 0.5g longitudinal load. Harmonic analysis indicated a maximum displacement at 40Hz was 0.00312177 mm and the maximum von Mises stress was 647819 N/m^2 at 40Hz.

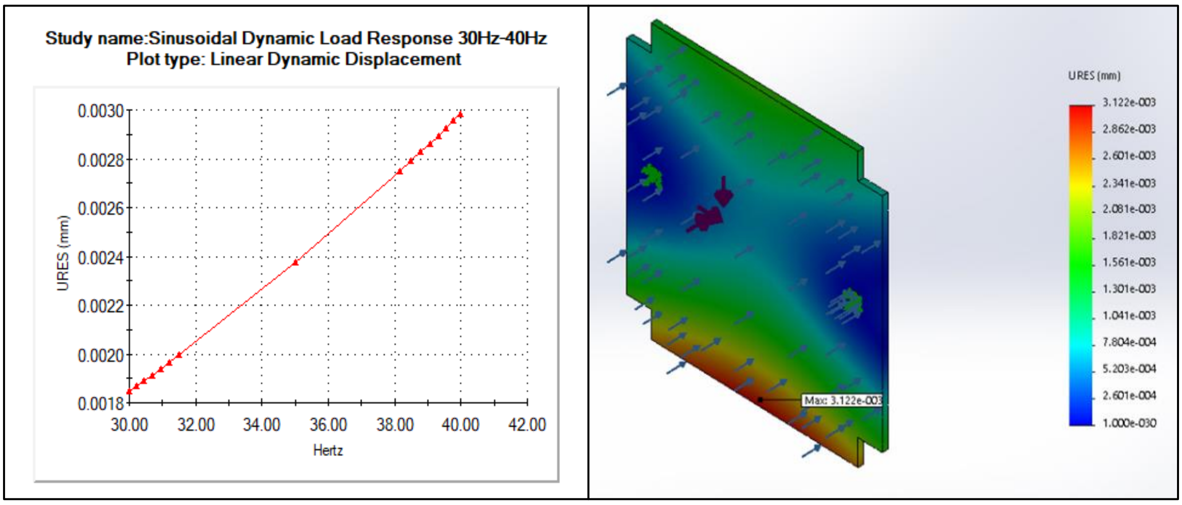

Appendix Figure O-30: Maximum lid displacement under longitudinal loading for frequency range 30Hz-40Hz

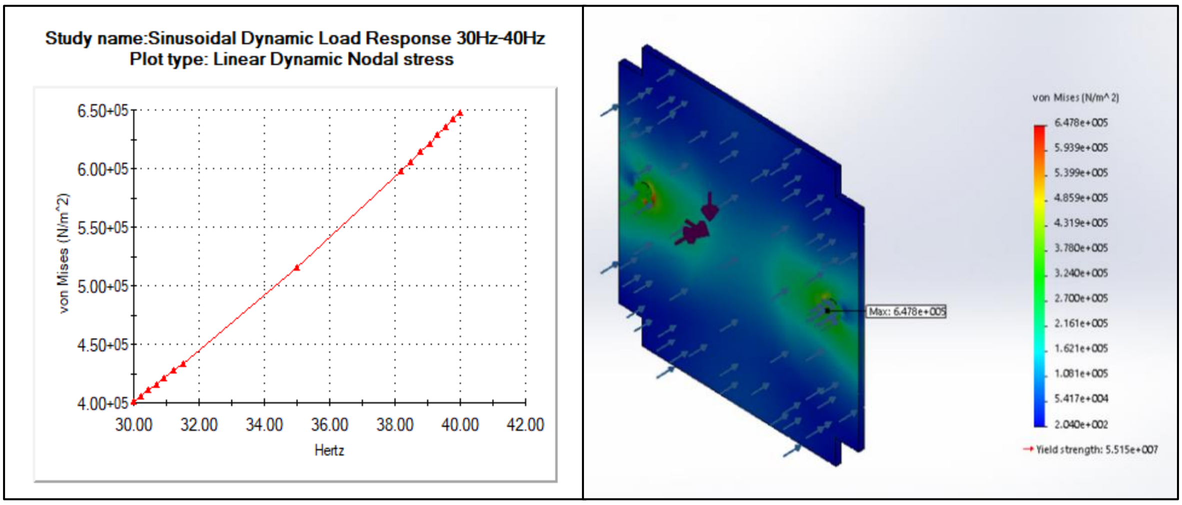

Appendix Figure O-31: von Mises stresses on the lid under longitudinal loading for frequency range of 30Hz-40Hz

The harmonic analysis results shown in appendix figure O-32 and appendix figure O-33 represents the displacement and von Mises stress for the sinusoidal frequency range of 40Hz-60Hz and a load of 0.5g. Based on harmonic analysis the maximum displacement and maximum von Mises were found to be 0.00649278 mm and 1.3872e+006 N/m^2 at 60Hz respectively.

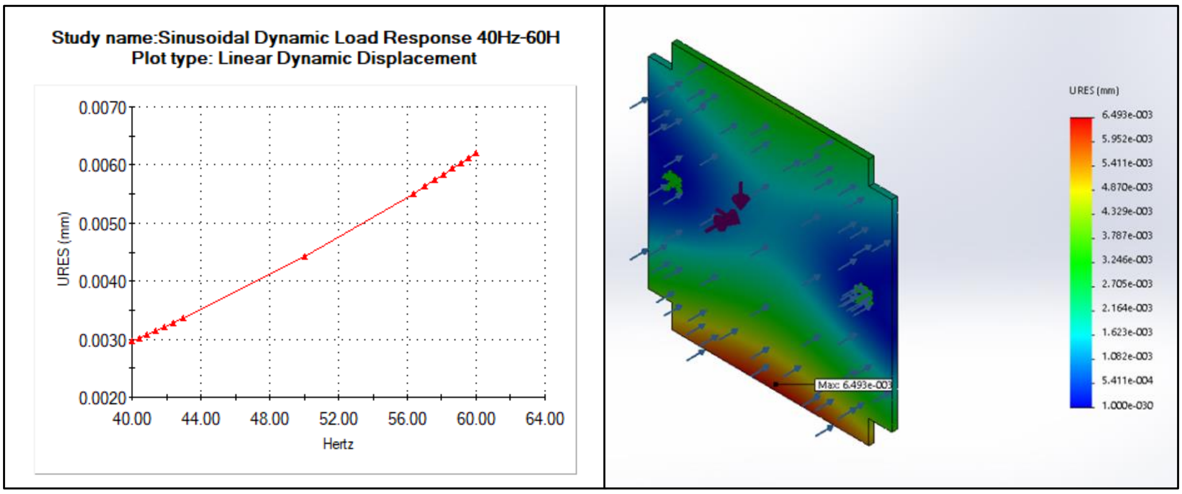

Appendix Figure O-32: Maximum lid displacement under longitudinal loading for frequency 40Hz-60Hz

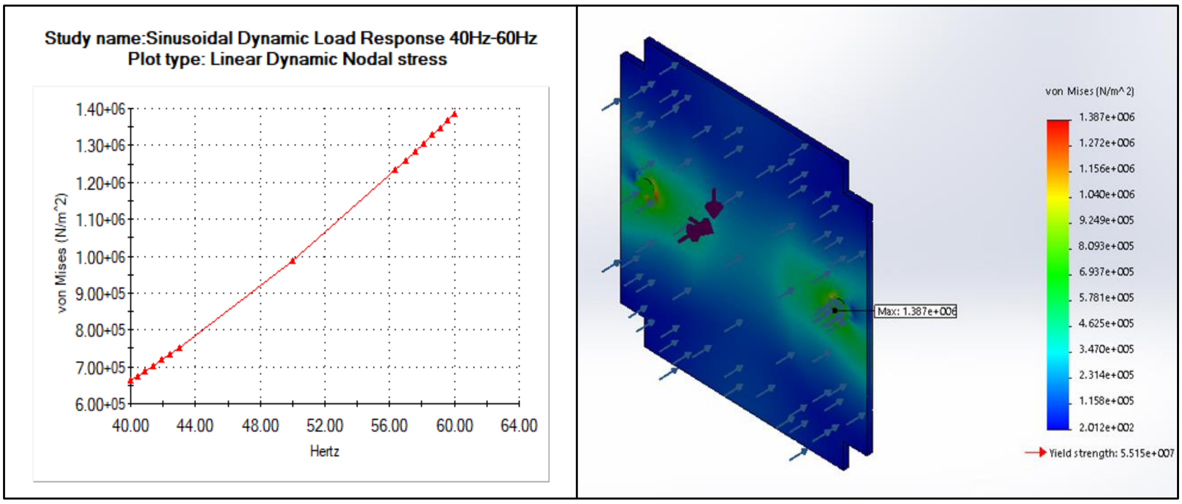

Appendix Figure O-33: Von Mises stress on the lid under longitudinal loading for frequency range 40Hz-60Hz

Appendix figure O-34 and appendix figure O-35 shows the response of the lid when it is exposed to a sinusoidal frequency range of 60Hz-100Hz and a load of 0.3 g. Based on harmonic analysis the maximum displacement was found to be 0.0173629 mm at 100Hz, and the von Mises stress was 3.70274e+006 N/m^2 at 100Hz.

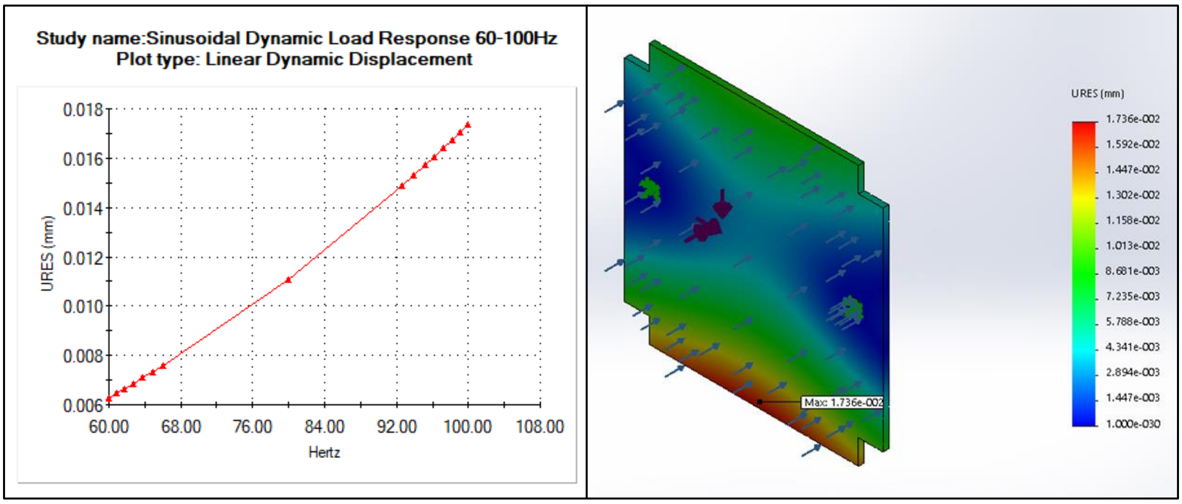

Appendix Figure O-34: Maximum lid displacement under longitudinal loading for frequency range 60Hz-100Hz

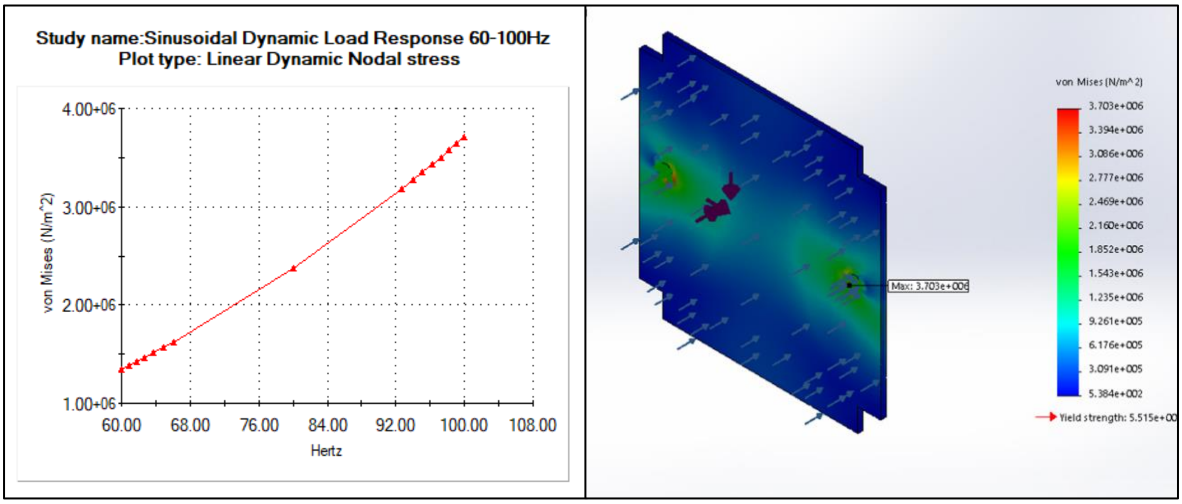

Appendix Figure O-35: Von Mises stress on the lid under longitudinal loading of frequency range 60Hz-100Hz

The following figures shows the response of the lid if the first natural frequency where to be reached. This serves as a worst-case scenario in which the frequency range was expanded to 500Hz-590Hz. Based on harmonic analysis displacement of 8mm at 583Hz is indicated in appendix figure O-36. Followed by the maximum von Mises stres of 1.76301e+009 N/m^2 at 583Hz.

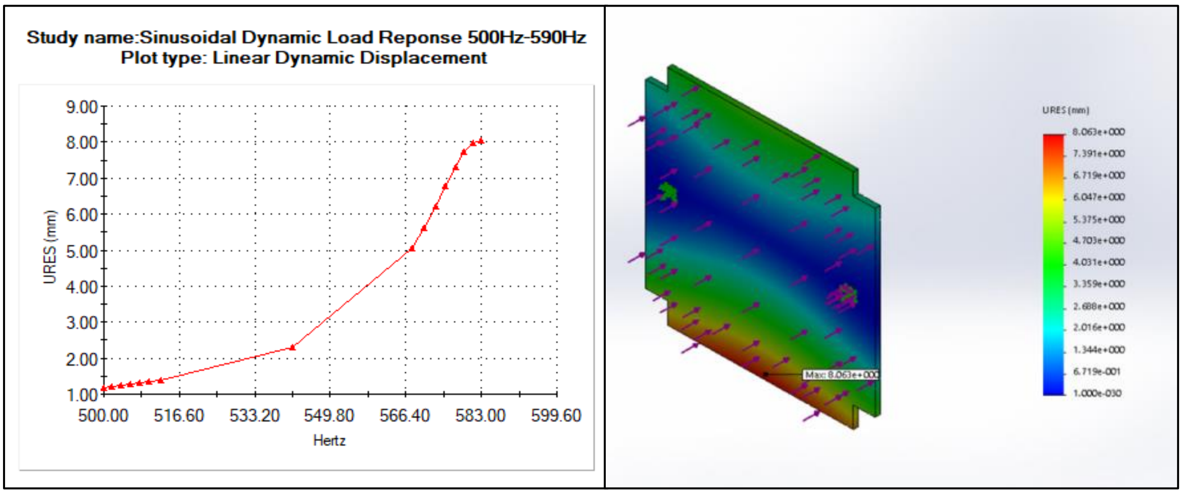

Appendix Figure O-36: Worst-case von Mises stress on the lid over frequency range of 500Hz-590Hz

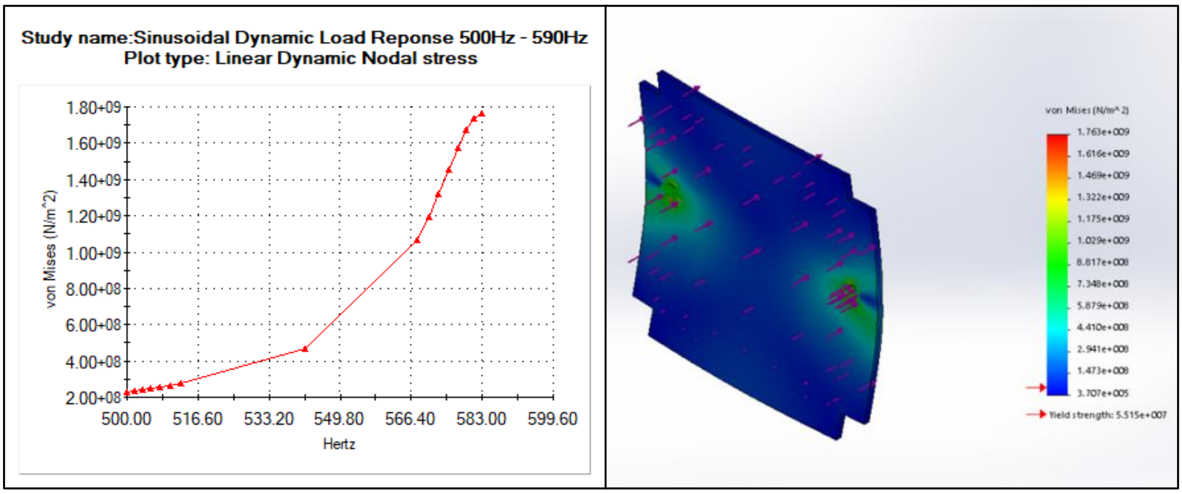

Appendix Figure O-37: Worst-case displacement of lid under longitudinal loading for frequency range 500Hz-590Hz

6. Sinusoidal Response of Lid under Lateral Loading

The following section shows the dynamic response of the lid under the lateral loading when only constrained by the M2 frangibolts. Appendix figure O-38 and appendix figure O-39 shows the displacement and von Mises at a sinusoidal frequency range of 1Hz-5Hz and a 0.4g load. Based on harmonic analysis the maximum displacement was 4.17432e-005 mm at 5Hz and the maximum von Mises stresses was 9057.4 N/m^2 at 5Hz.

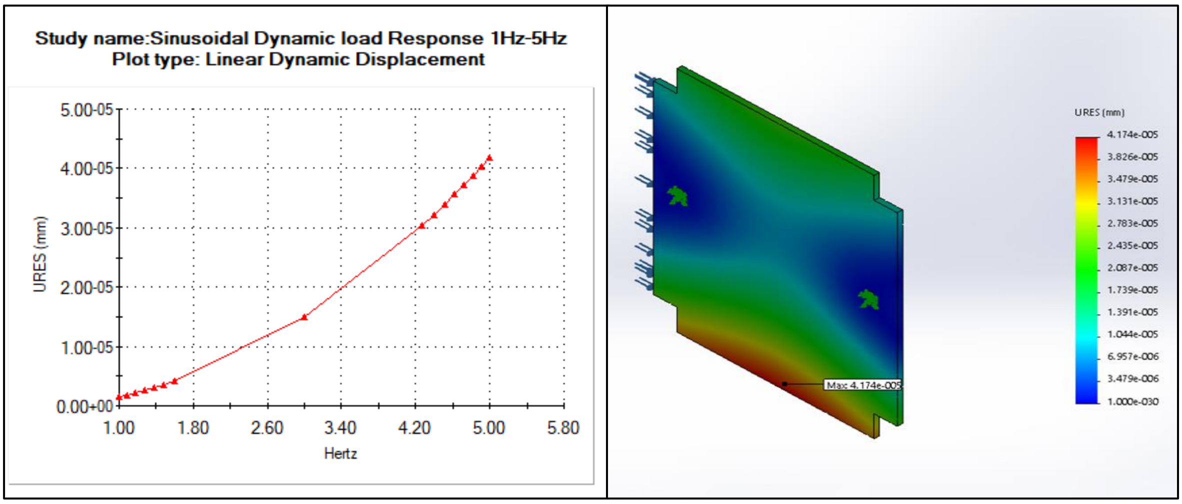

Appendix Figure O-38: Maximum lid displacement under lateral loading for frequency range of 1Hz-5Hz

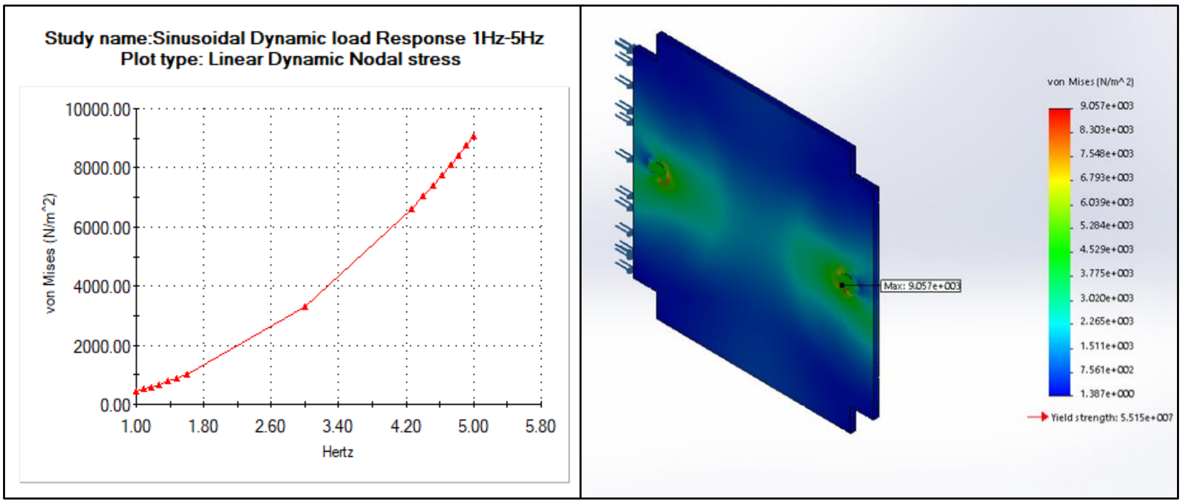

Appendix Figure O-39: Von Mises stress on the lid under lateral loading for frequency range of 1Hz-5Hz

The results shown below are based on harmonic analysis for the sinusoidal frequency range of 5Hz-10Hz under a load of 0.6g. Maximum displacement of 0.000167422 mm at 10Hz is shown inappendix figure O-40. This is followed by appendix figure O-41 which shows the maximum von Mises stress of 35970.4 N/m^2 at 10Hz.

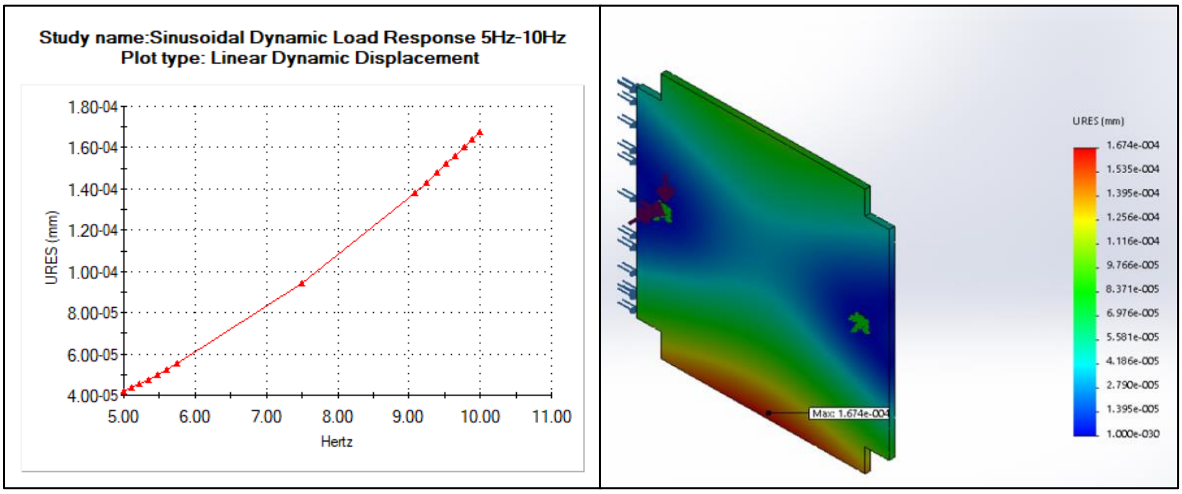

Appendix Figure O-40: Maximum lid displacement under lateral loading for frequency range 5Hz-10Hz

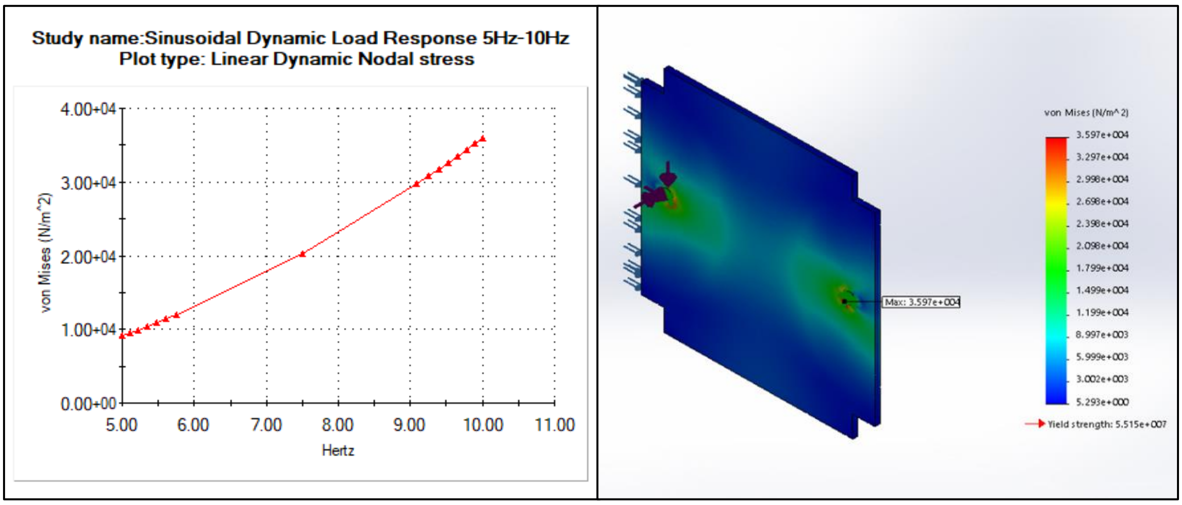

Appendix Figure O-41: von Mises Stress on the lid under lateral loading for frequency of 5Hz-10Hz

Dynamic response of the lid for sinusoidal frequency range of 10Hz-20Hz and load of 0.6g are shown in appendix figure O-42 and appendix figure O-43. Based on harmonic analysis the maximum displacement and von Mises stresses were 0.000670732 mm and 143608 N/m^2 at 20Hz respectively.

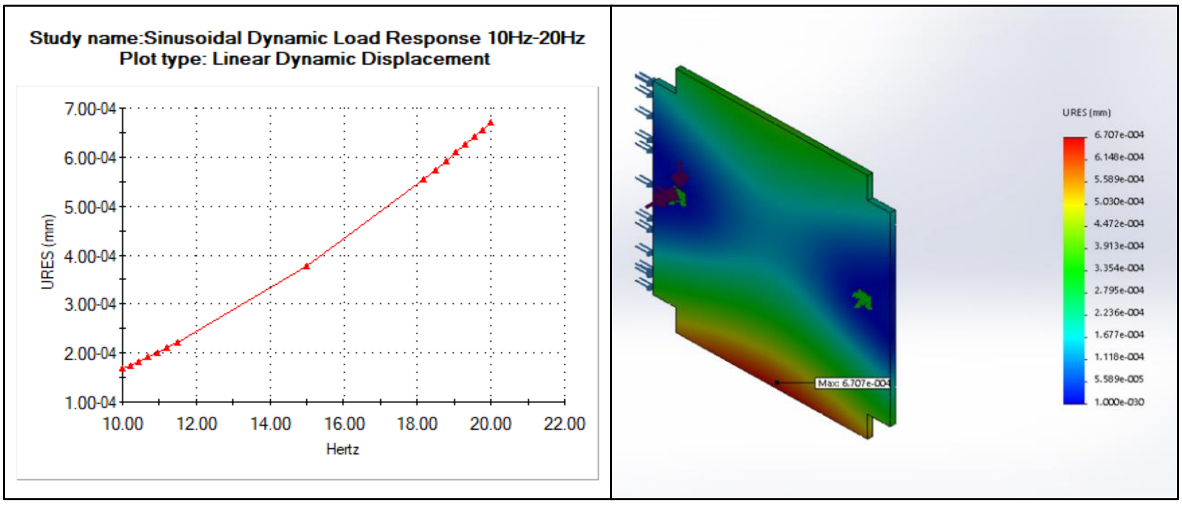

Appendix Figure O-42: Maximum lid displacement under lateral loading for frequency range 10Hz-20Hz

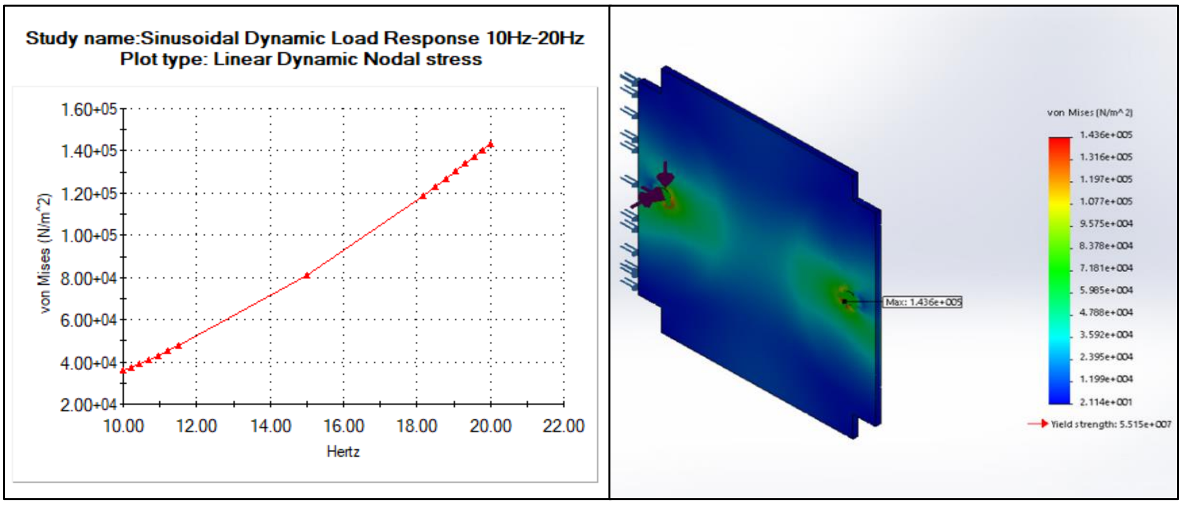

Appendix Figure O-43: von Mises stress on the lid under lateral loading for frequency range 10Hz-20Hz

Appendix figure O-44 and appendix figure O-45 shows the responses of the lid for sinusoidal frequency range of 20Hz-30Hz and a 0.4g load. Based on harmonic analysis the maximum displacement was 0.00152077 mm at 30Hz and the maximum von Mises stress was 326543 N/m^2 at 30Hz.

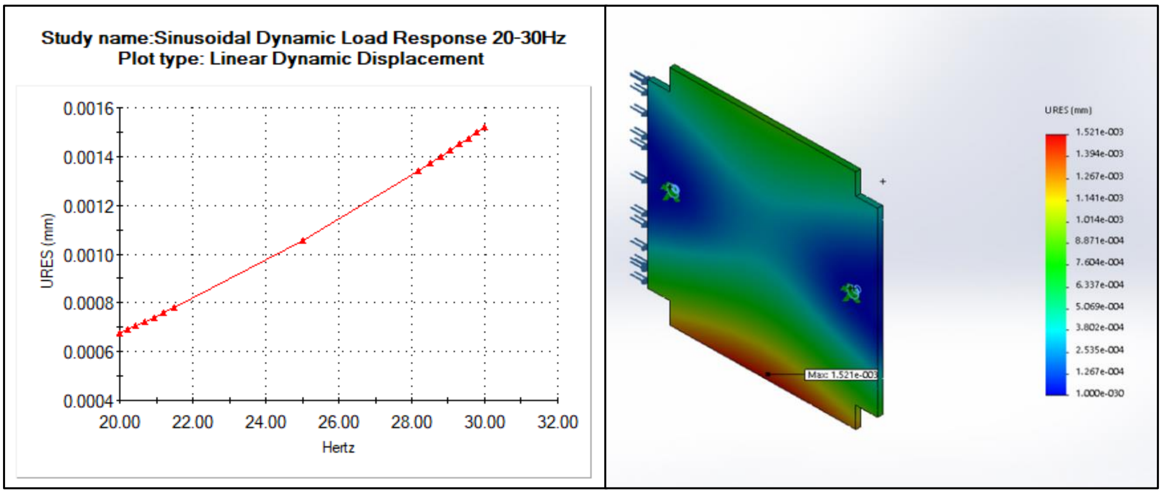

Appendix Figure O-44: Maximum lid displacement under lateral loading for frequency range 20Hz-30Hz

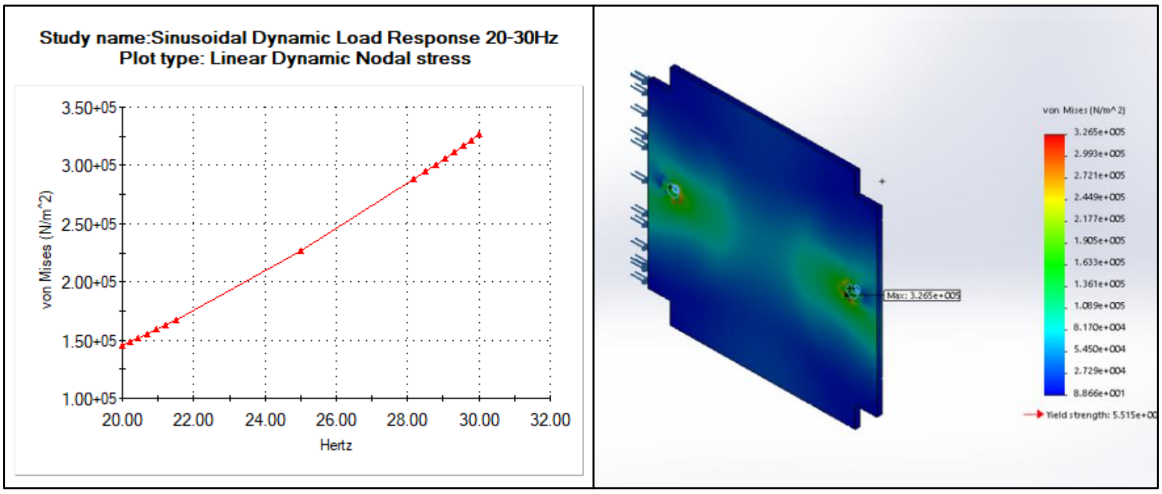

Appendix Figure O-45: von Mises stress on the lid under lateral loading for frequency range 20Hz-30Hz

The Dynamic response of the lid over the sinusoidal frequency range of 30Hz-40Hz and lateral load of 0.4g are shown in appendix figure O-46 and appendix figure O-47. Based on harmonic analysis the maximum displacement and von Mises stress were at 40Hz and were 0.00271086 mm and 562827 N/m^2.

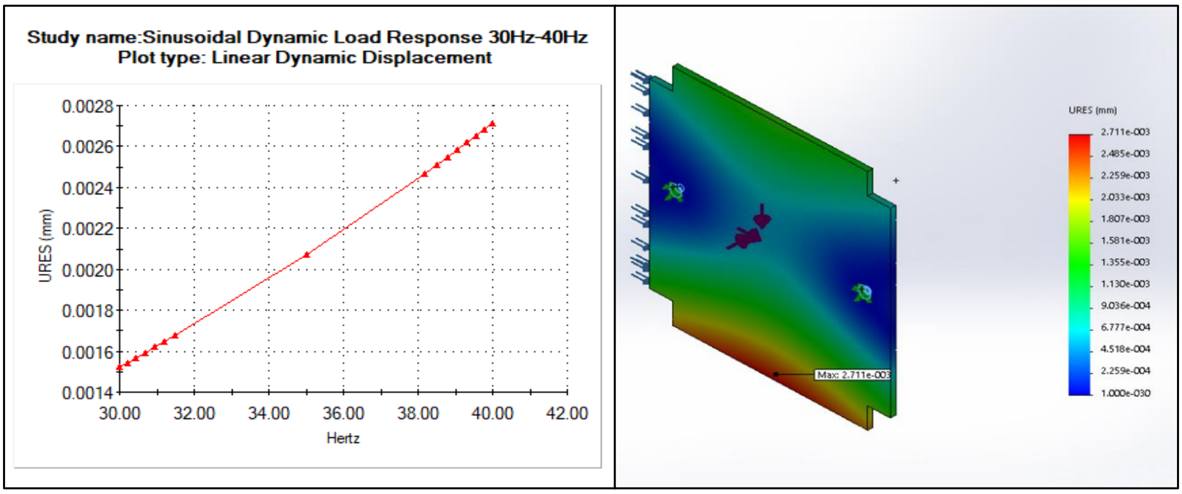

Appendix Figure O-46: Maximum lid displacement under lateral loading for frequency range of 30Hz-40Hz

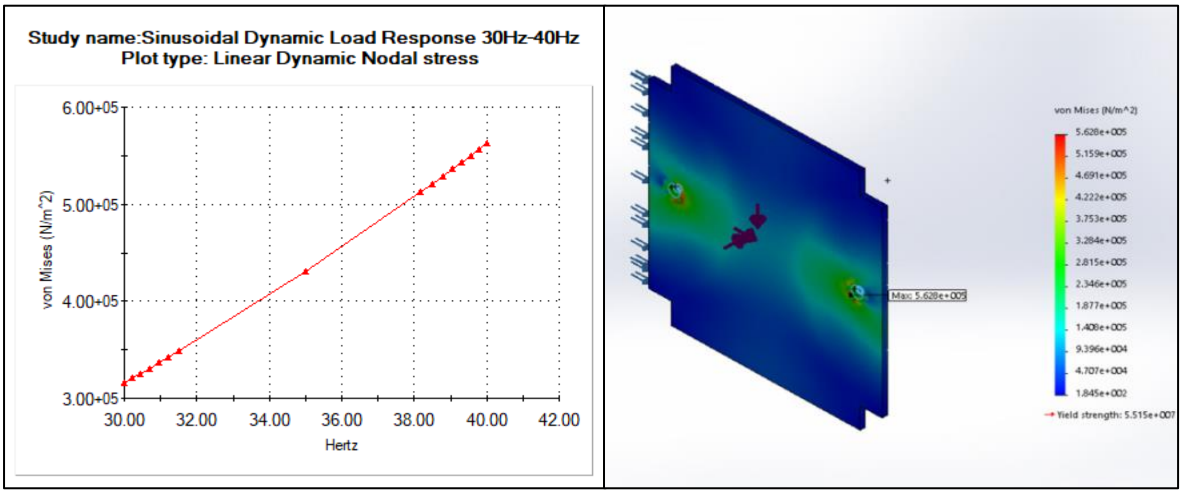

Appendix Figure O-47: von Mises stress on the lid under lateral loading and frequency range 30Hz-40Hz

The dynamic response of the lid over the sinusoidal frequency range of 40Hz-60Hz and under a lateral load of 0.3g are illustrated in appendix figure O-48 and appendix figure O-49. Harmonic analysis indicated that the maximum displacement and von Mises stress observed at 60Hz were found to be 0.0060833 mm and 1.29987e+006 N/m^2

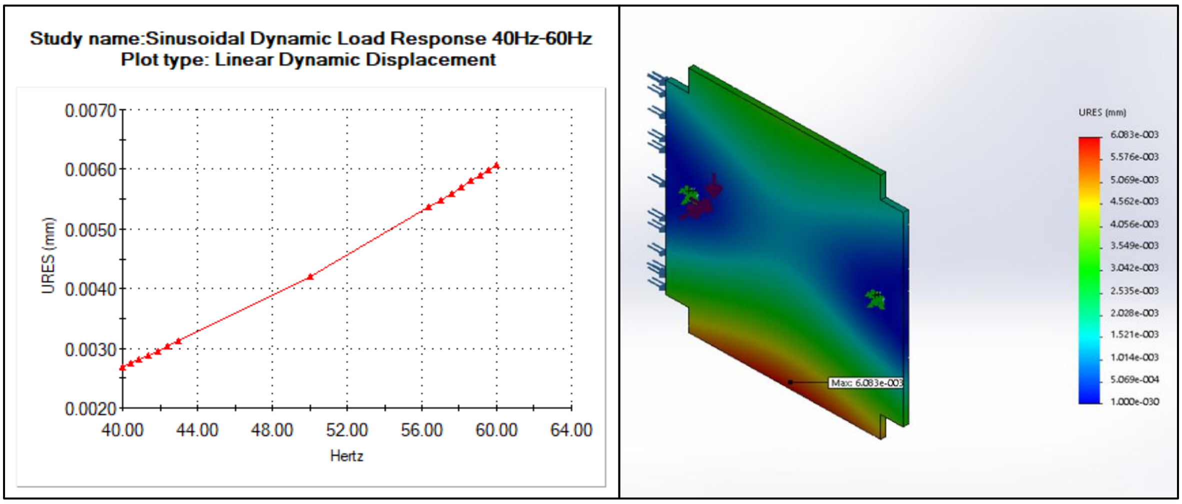

Appendix Figure O-48: Maximum lid displacement under lateral loading and frequency range 40Hz-60Hz

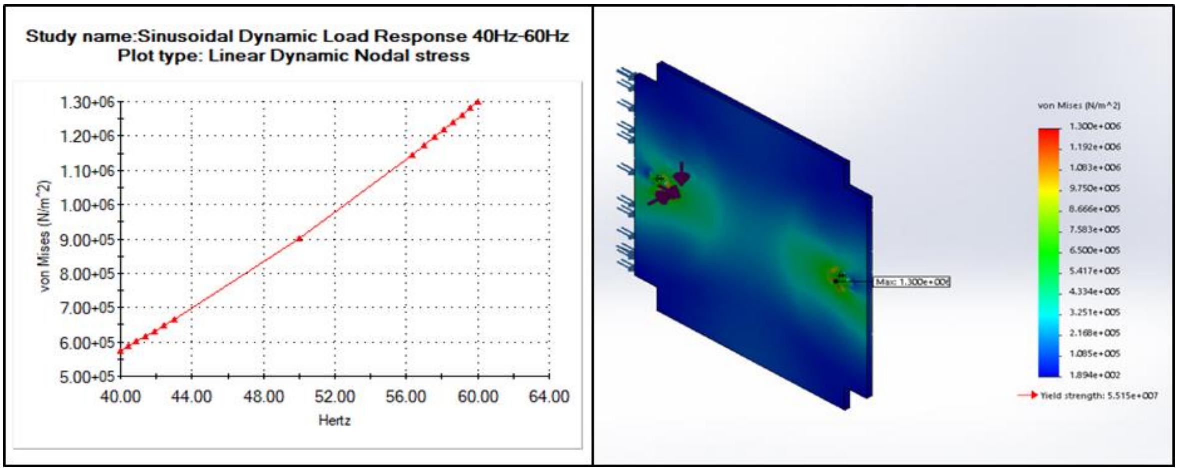

Appendix Figure O-49: von Mises stress on the lid under lateral loading for frequency range 40Hz-60Hz

The dynamic response of the lid over the sinusoidal frequency range of 60Hz-100Hz and under lateral load of 0.3g are illustrated in appendix figure O-50 and appendix figure O-51. Harmonic analysis showed the maximum displacement was observed at 100Hz and was found to be 0.017155 mm. The maximum von Mises stress was also at 100Hz with a value of 3.65853e+006 N/m^2.

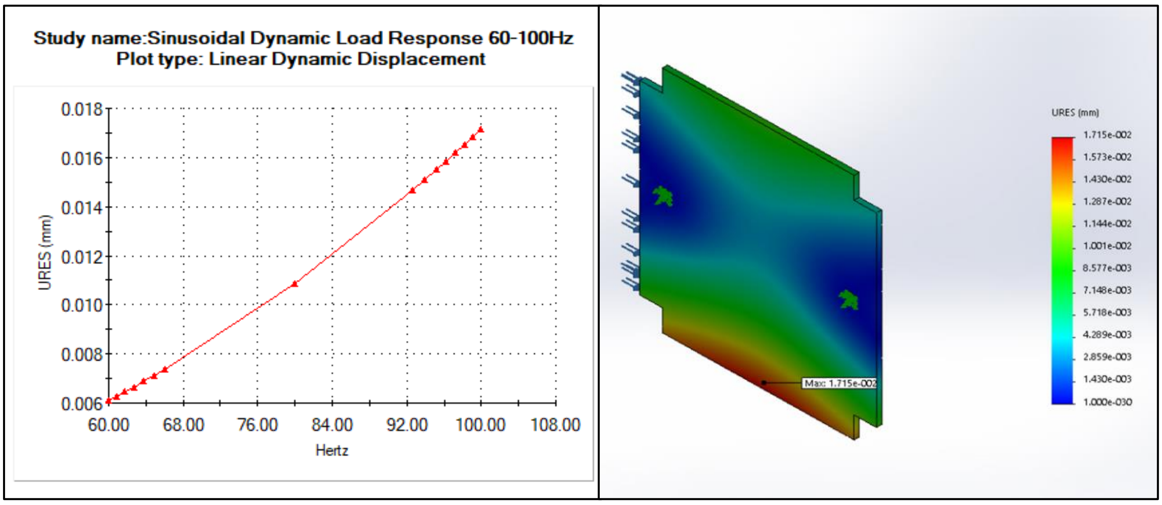

Appendix Figure O-50: Maximum lid displacement under lateral loading for frequency range 60Hz-100Hz

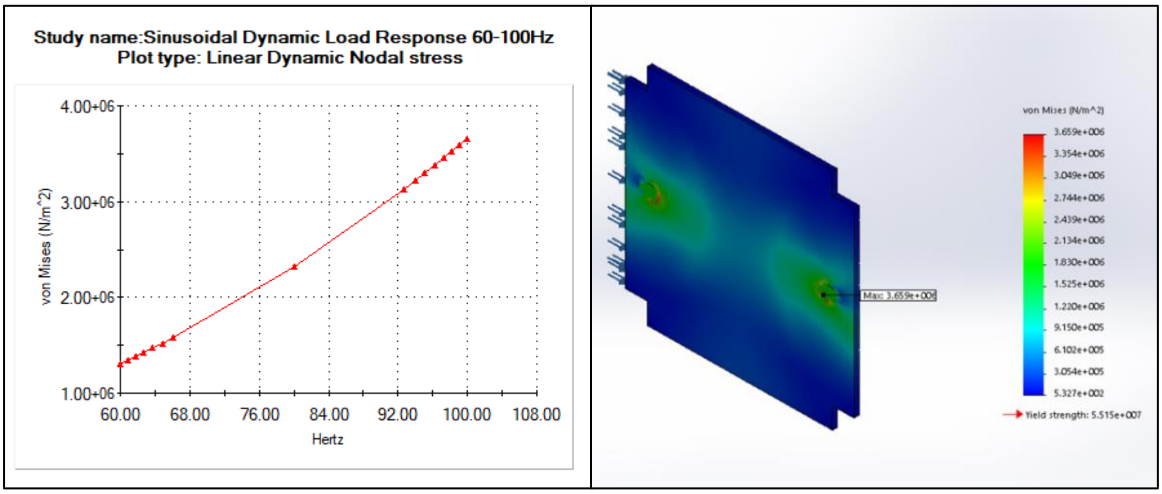

Appendix Figure O-51: von Mises stress on the lid under lateral loading for frequency range 60Hz-100Hz

The following figures shows the response of the lid if the first natural frequency where to be reached. This served as a worst-case scenario in which the sinusoidal frequency range was expanded to 500Hz-590Hz. Based on harmonic analysis displacement of 8mm at 583Hz was observed and is shown in appendix figure O-52 The maximum stress at observed was 1.75046e+009 N/m^2 at 590Hz shown in appendix figure O-53.

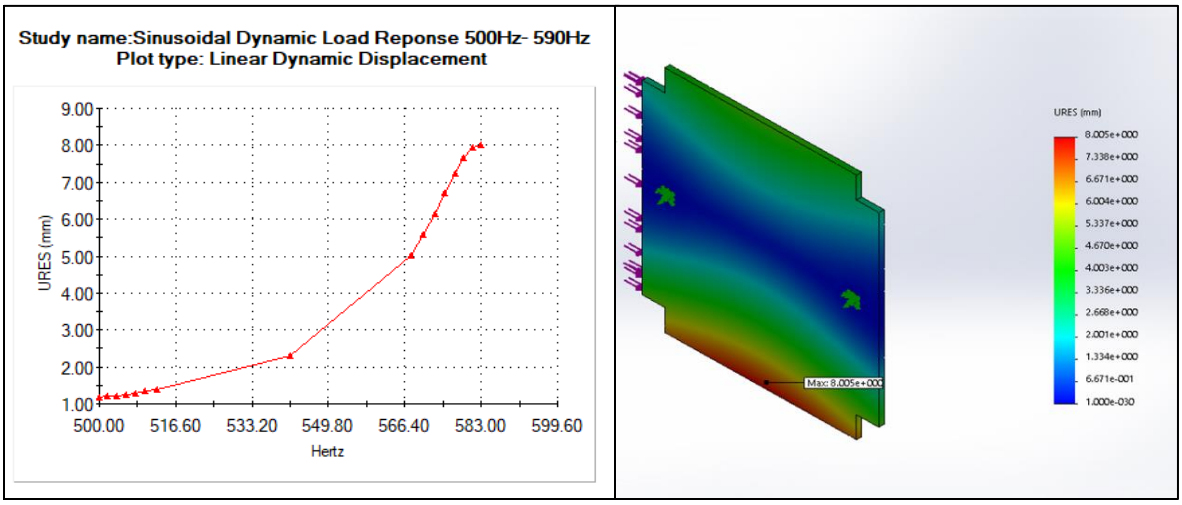

Appendix Figure O-52: Worst-case lid displacement under lateral loading for frequency range 500Hz-590Hz

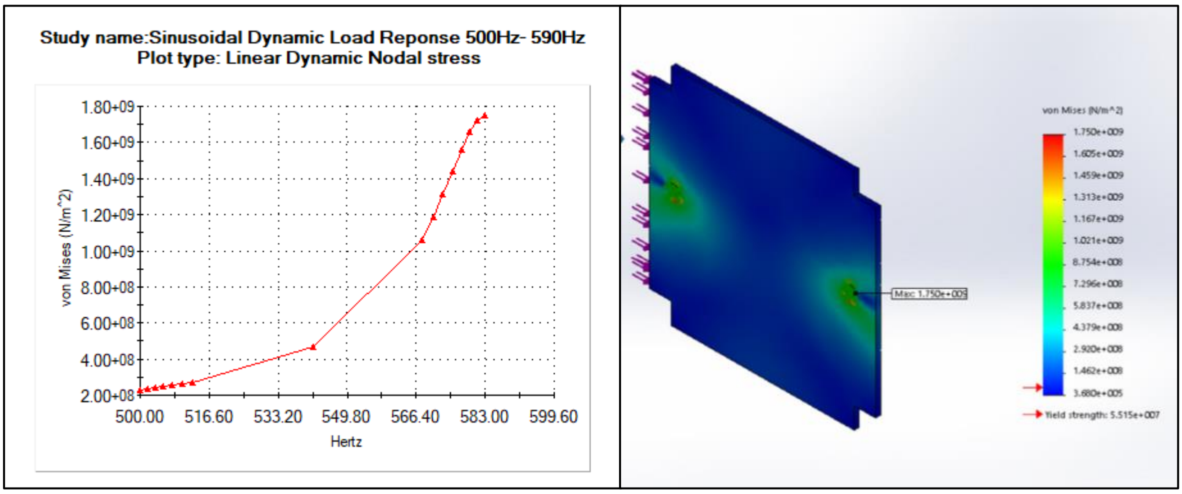

Appendix Figure O-53: Worst-case von Mises stress on the lid under lateral loading for frequency range 500Hz-590Hz

7. Sinusoidal Response of Housing under Longitudinal Loading

The following section shows the dynamic response of the housing under various longitudinal loading and corresponding sinusoidal frequencies when constrained at the four corners. Figure 6.82 and 6.83 shows the harmonic analysis results when the housing is under a 0.4g longitudinal load and frequency range of 1Hz-5Hz. Based on harmonic analysis appendix figure O-54 shows the maximum displacement occurs at 5Hz and was found to be 8.03677e-005 mm. The maximum von Mises stress shown in appendix figure O-55 was 35347.2 N/m^2 at 5Hz.

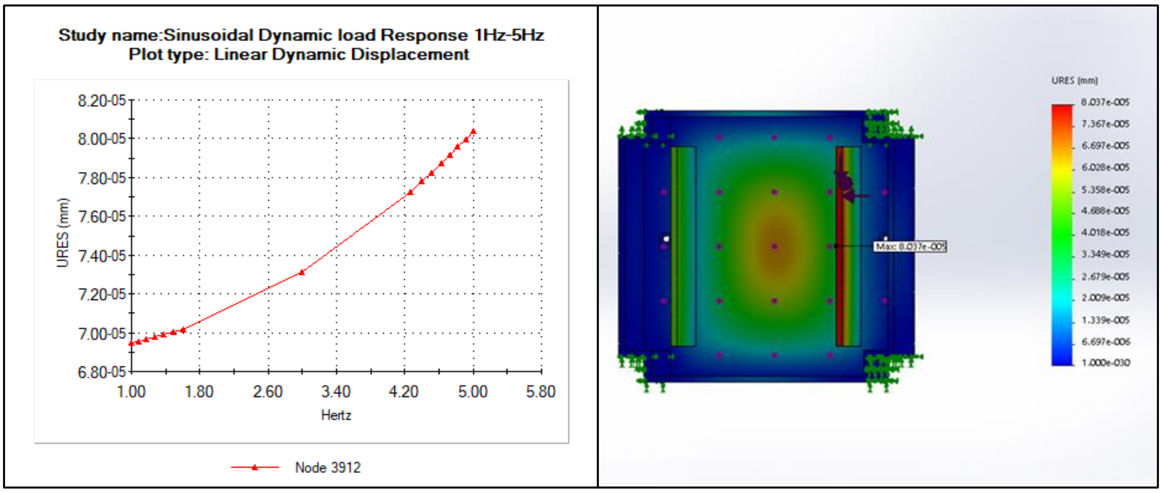

Appendix Figure O-54: Maximum housing displacement under longitudinal loading and frequency range 1Hz-5Hz

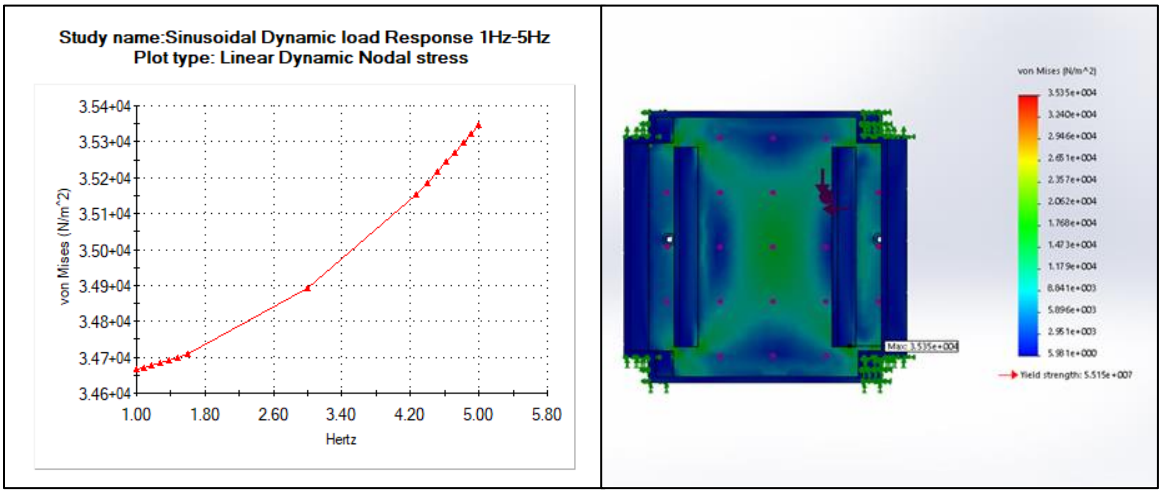

Appendix Figure O-55: Von Mises stress the housing under longitudinal loading and frequency range 1Hz-5Hz

Appendix figure O-56 and appendix figure O-57 shows the displacement and von Mises stress of the housing when exposed to a sinusoidal frequency range of 5Hz-10Hz and 0.6g longitudinal loading. Based on harmonic analysis the maximum displacement and stress were found at 10Hz and was 0.000128631 mm and 44469.3 N/m^2 respectively.

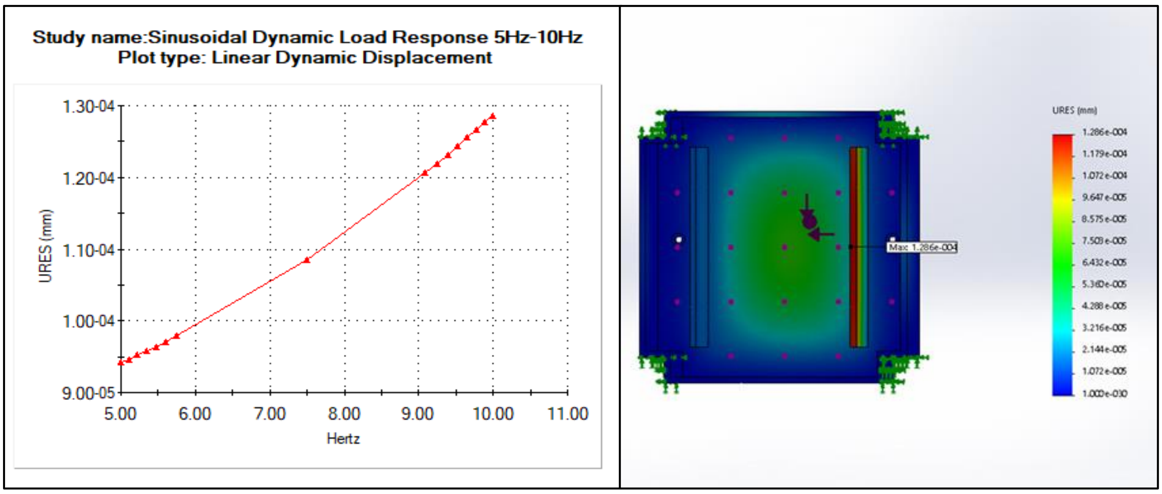

Appendix Figure O-56: Maximum lid displacement of the housing under longitudinal loading and frequency range 5Hz-10Hz

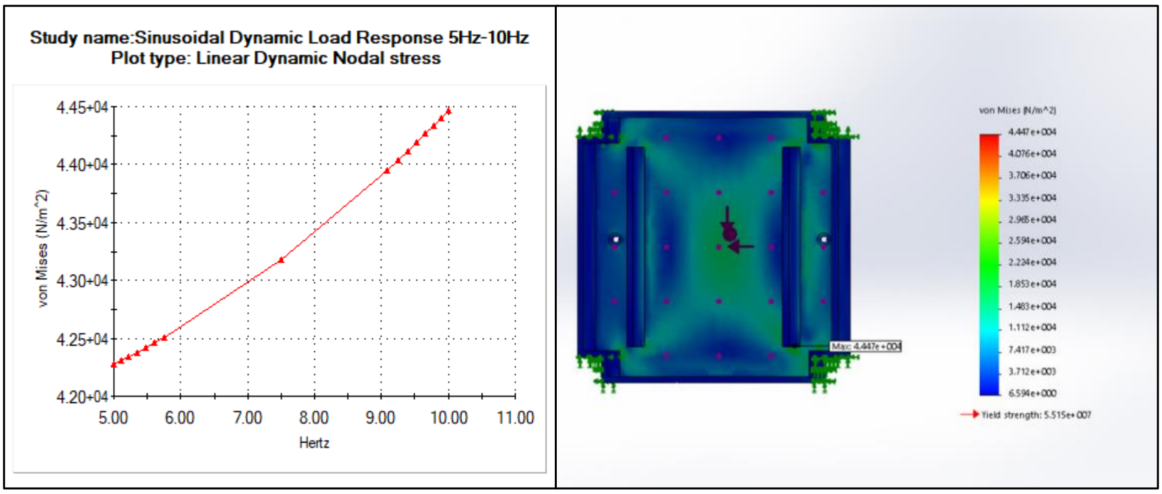

Appendix Figure O-57: von Mises stress on the housing under longitudinal loading for frequency range 5Hz-10Hz

Appendix figure O-58 and appendix figure O-59 shows the deformation and magnitude of the von Mises stresses of the housing when exposed to 0.8g longitudinal load and a dynamic sinusoidal frequency range of 10Hz-20Hz. Based on harmonic analysis the maximum deformation was 0.000323033 mm at 20Hz. The maximum von Mises stress was found at 20Hz with a magnitude of 81367.7 N/m^2.

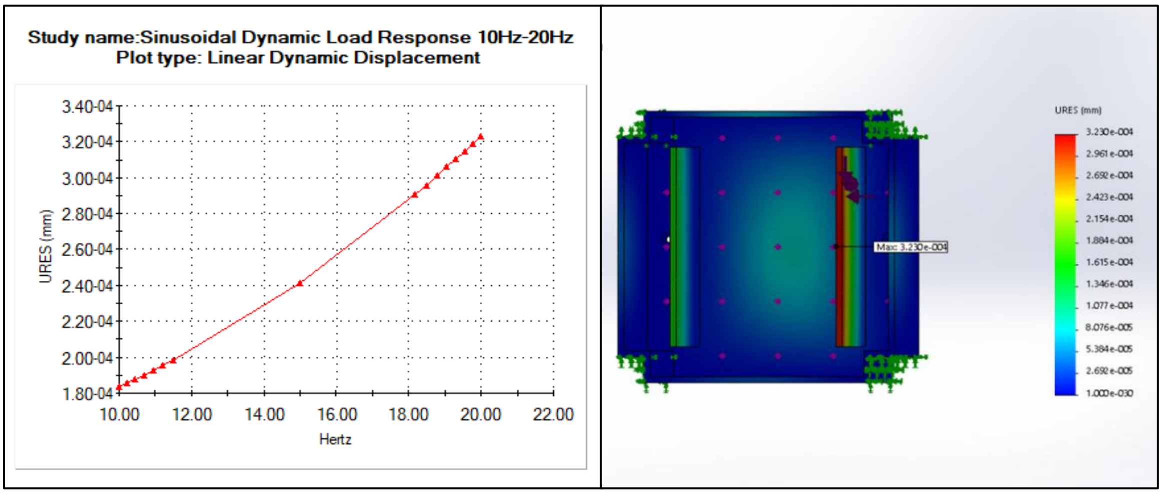

Appendix Figure O-58: Von Mises stress on the housing under longitudinal loading and frequency range 10Hz-20Hz

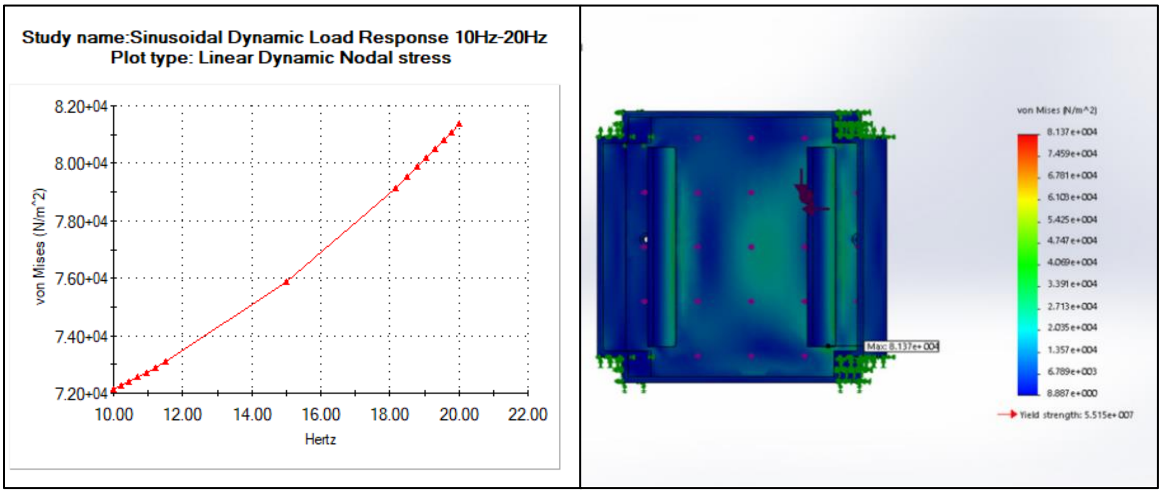

Appendix Figure O-59: Maximum housing displacement of the housing under longitudinal loading and frequency range 10Hz-20Hz

Appendix figure O-60 and appendix figure O-61 shows the deformation and magnitude of the von Mises stress of the housing when it is exposed to 0.8g longitudinal load and a sinusoidal frequency range of 20Hz-30Hz. Based on harmonic analysis the maximum deformation and maximum stress were found at 30Hz and had a value of 0.00055768 mm and 110919 N/m^2.

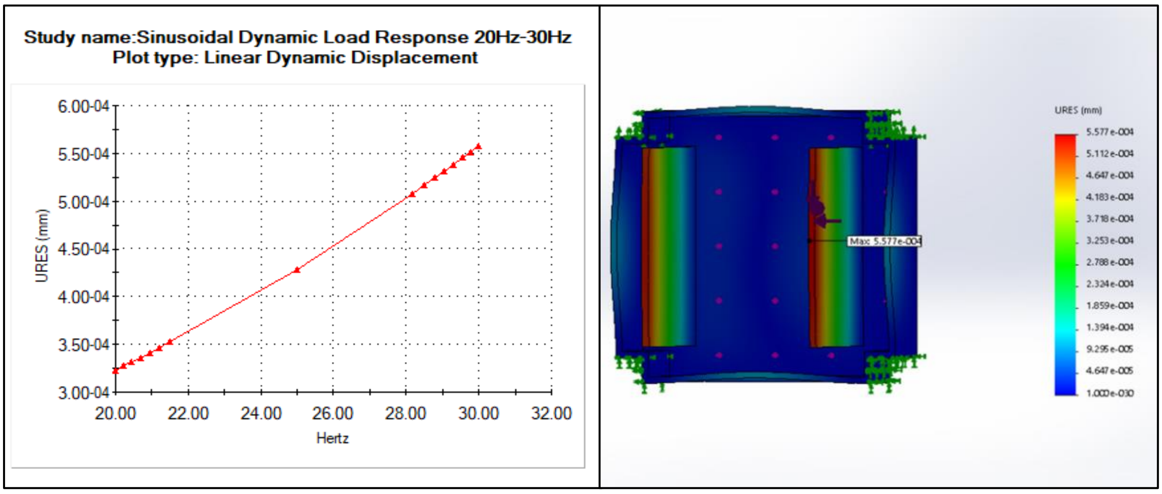

Appendix Figure O-60: Maximum housing displacement under longitudinal loading and frequency range 20Hz-30Hz

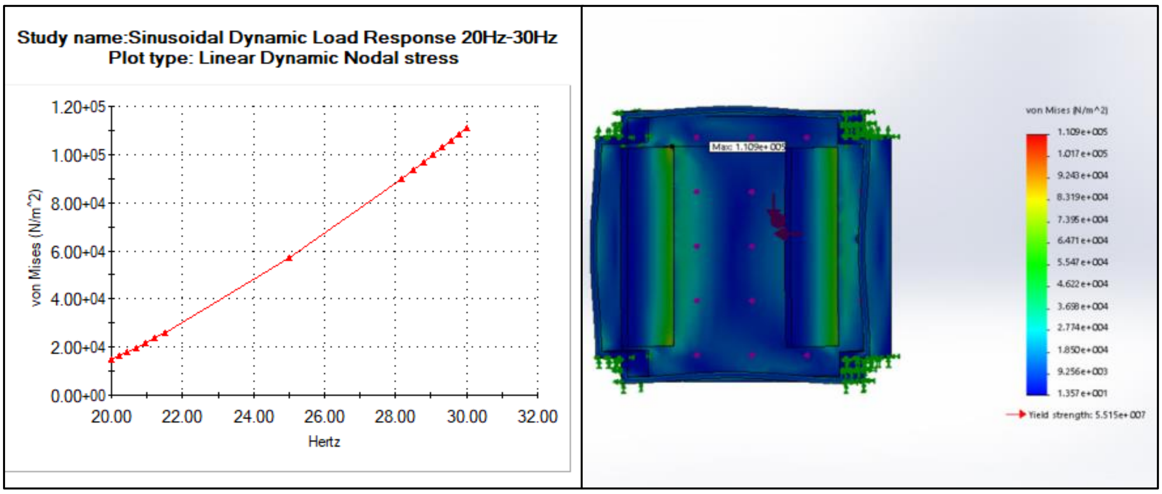

Appendix Figure O-61: Von Mises stress on the housing under longitudinal loading and frequency range 20Hz-30Hz

Appendix figure O-62 and appendix figure O-63 shows the response of the housing when it is exposed to a longitudinal load of 0.5g and sinusoidal frequency range of 30Hz-40Hz. Based on harmonic analysis the maximum deformation observed was 0.00112359 mm at 40Hz.The maximum von Mises occurred at 40Hz and magnitude of 275989 N/m^2.

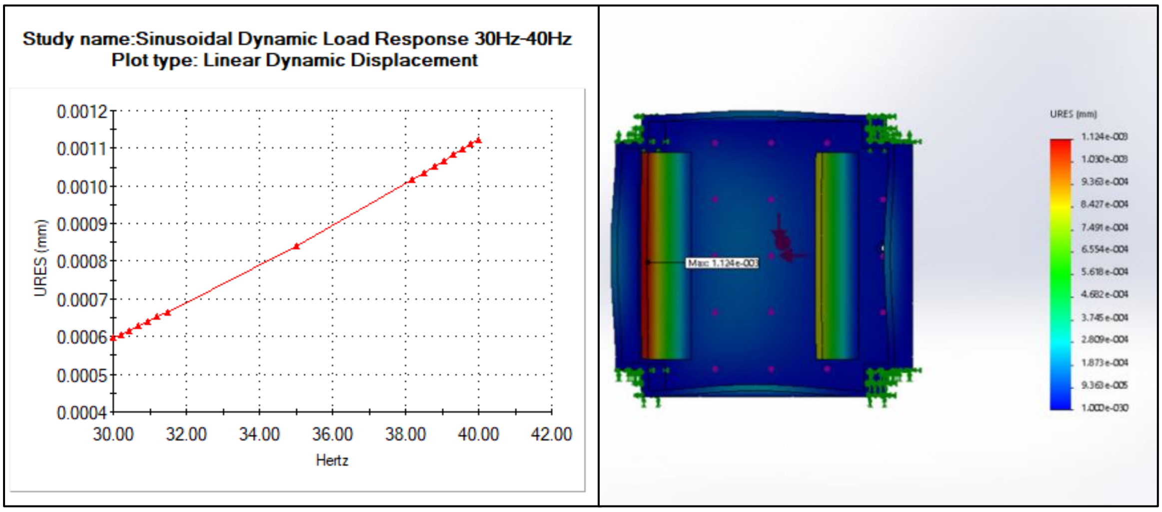

Appendix Figure O-62: Maximum housing displacement under longitudinal loading and frequency 30Hz-40Hz

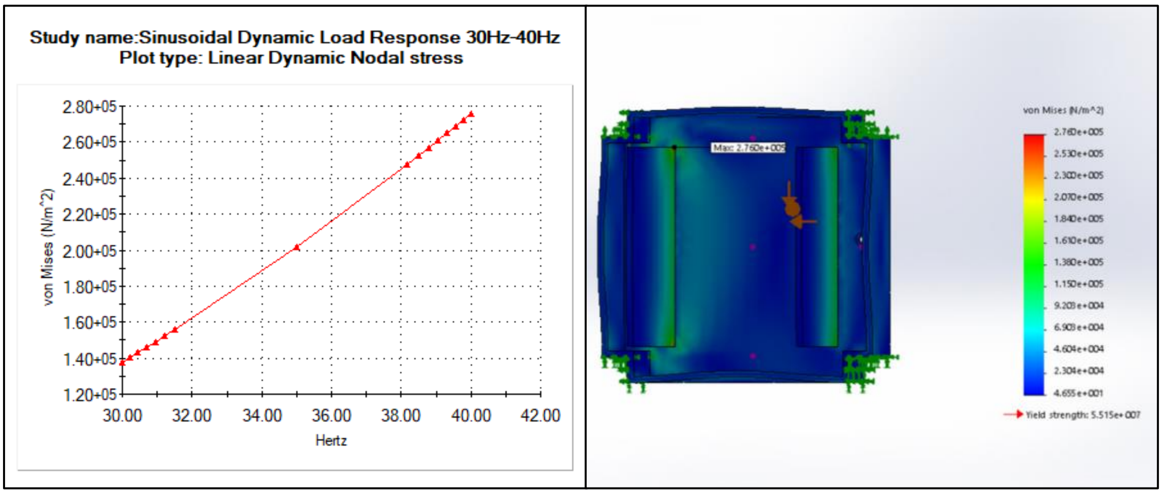

Appendix Figure O-63: von Mises stress on the housing under longitudinal loading and frequency range 30Hz-40Hz

Appendix figure O-64 and appendix figure O-65 shows the response of the housing when it is exposed to a longitudinal load of 0.5g and sinusoidal frequency range of 40Hz-60Hz. Based on harmonic analysis the maximum deformation occurred at 60Hz and was 0.00263419 mm. The maximum von Mises stress was observed at 60Hz and had a magnitude of 672216 N/m^2.

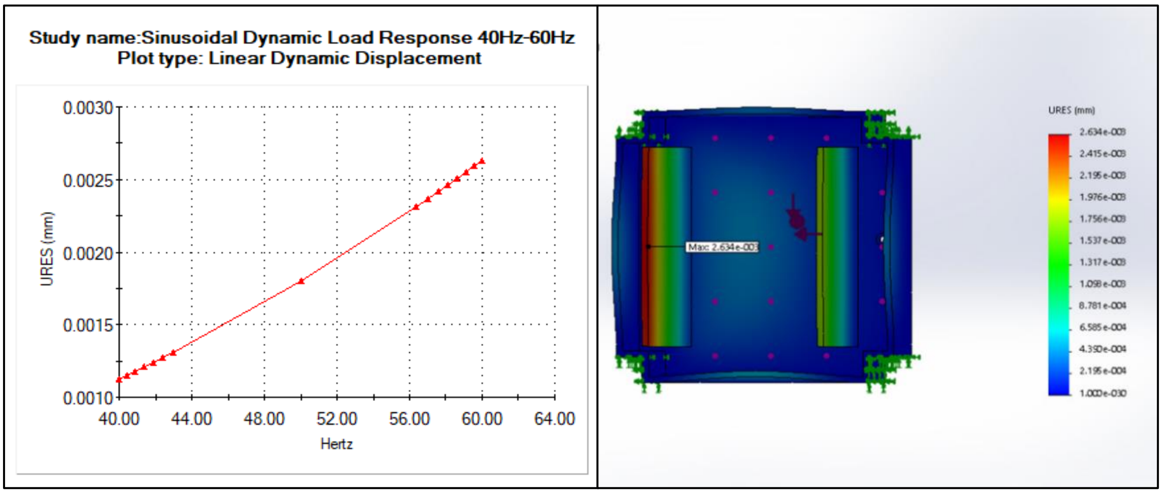

Appendix Figure O-64: Maximum housing displacement under longitudinal loading and frequency range 40Hz-60Hz

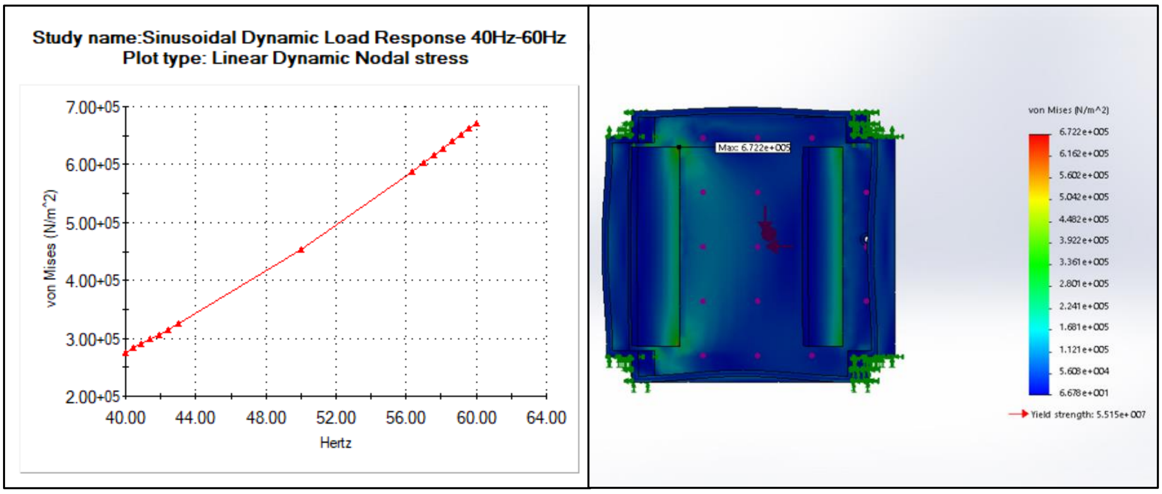

Appendix Figure O-65: von Mises on the housing under longitudinal loading and frequency range 40Hz-60Hz

Appendix figure O-66 to appendix figure O-67 displays the response of the housing when it is exposed to 0.3g longitudinal load and a sinusoidal dynamic load at a frequency range of 60Hz-100Hz.Based on harmonic analysis appendix figure O-66 shows, maximum deformation occurs at 100Hz with a value of 0.00754381 mm. The maximum von Mises stress is seen in appenid figure O-67 and has a magnitude of 1.96678e+006 N/m^2.

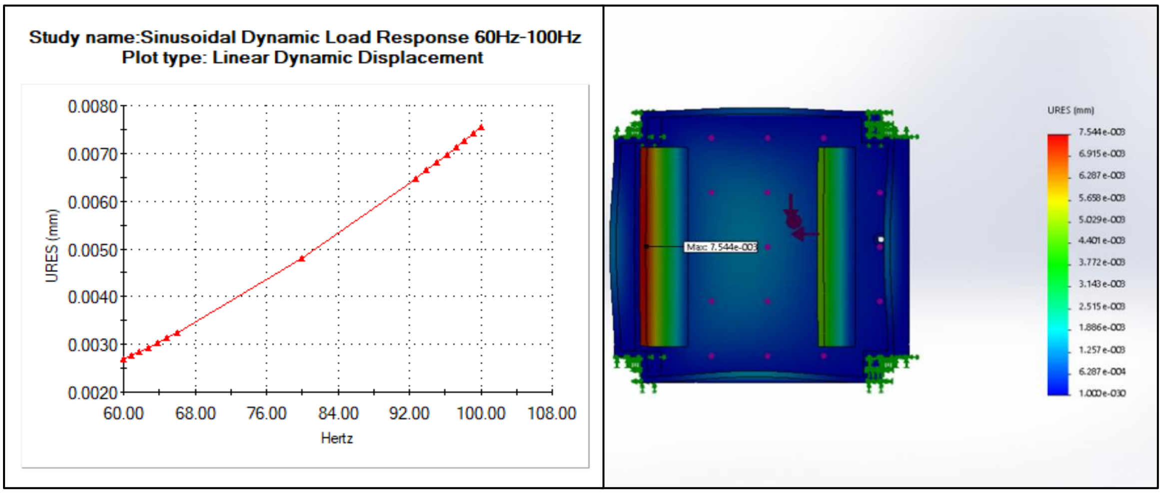

Appendix Figure O-66: Maximum housing displacement under longitudinal loading and frequency range 60Hz-100Hz

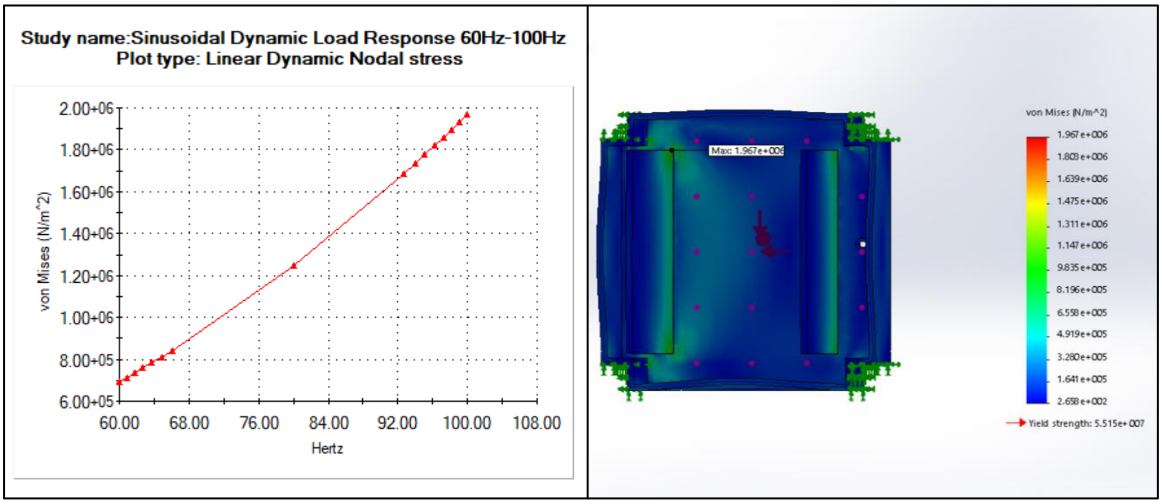

Appendix Figure O-67: von Mises stress on the housing under longitudinal loading and frequency range 60Hz-100Hz

The following figures show the response of the housing if the first natural frequency where to be reached. This served as a worst-case scenario in which the dynamic load frequency range was expanded to 950Hz-1070Hz. Based on harmonic analysis the results seen in appenidix figure O-68 shows a deformation of 12.9 mm at a frequency of 1066Hz .The von Mises stress is seen in appendix figure O-69 and has a magnitude of 2.37588e+009 N/m^2 at 1066Hz.

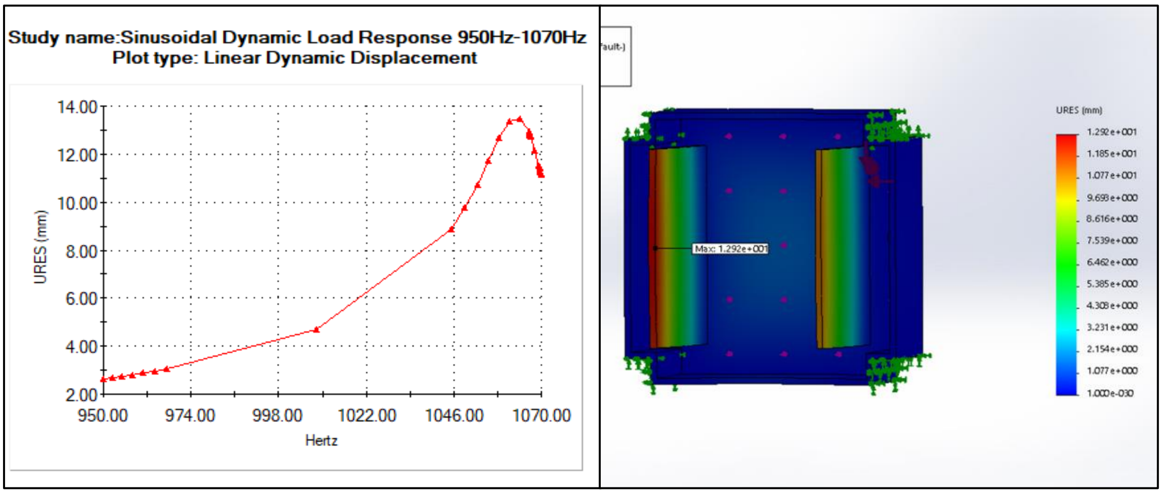

Appendix Figure O-68 : Worst-case housing displacement at a frequency range of 950Hz-1070Hz

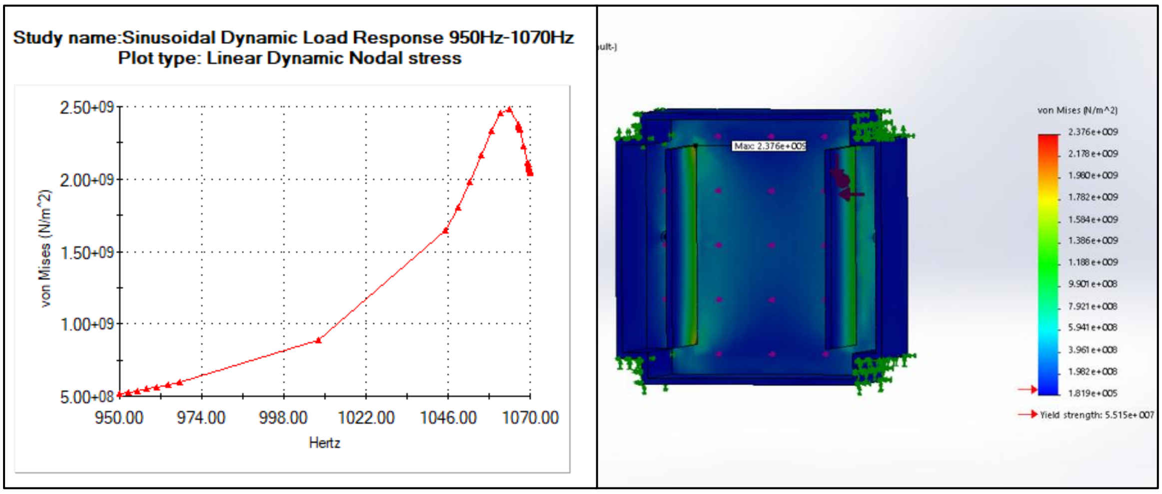

Appendix Figure O-69: Worst-case von Mises stress on the housing at a frequency range 950Hz-1070Hz

8. Sinusoidal Response of Housing under Lateral Loading

The following section shows the dynamic response of the housing under various lateral loading and the corresponding sinusoidal frequencies when constrained at all four corners. Appendix figure O-70 and appendix figure O-71 shows the displacement of the housing when it is exposed to lateral load of 0.4g and a sinusoidal dynamic load with a frequency range of 1Hz-5Hz. Bases on harmonic analysis the maximum displacement and von Mises stress both occurred at 1Hz and had a magnitude of 0.00210mm and 6.48e+004 N/m^2.

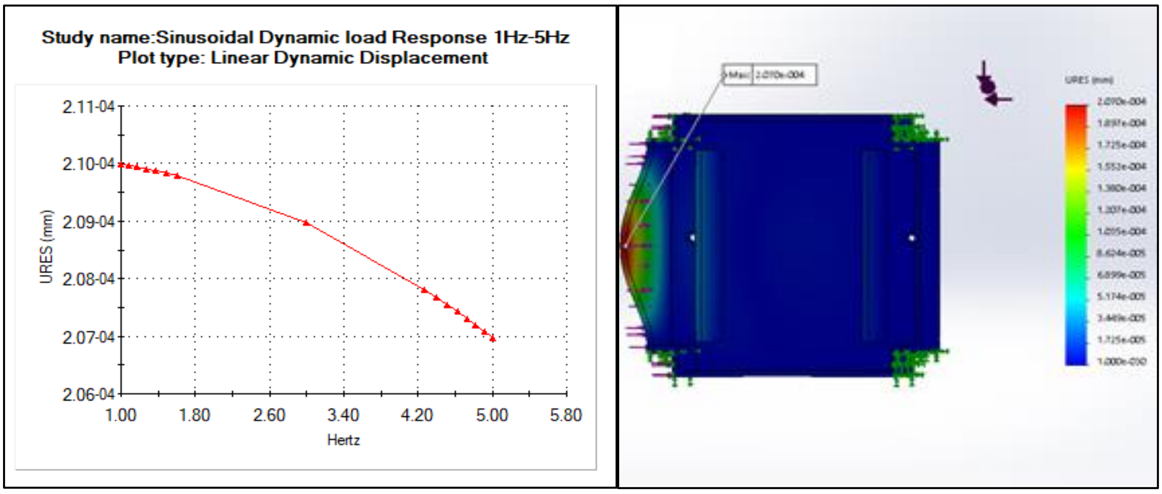

Appendix Figure O-70: Maximum housing displacement under lateral loading and frequency range 1Hz-5Hz

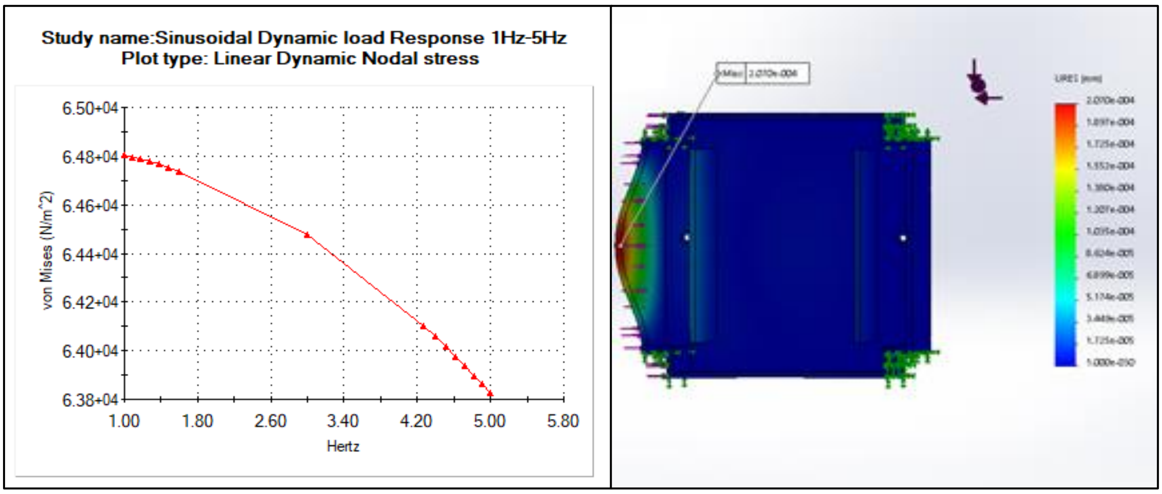

Appendix Figure O-71: von Mises stress on the housing under lateral loading and frequency range 1Hz-5Hz

Appendix figure O-72 and appendix figure O-73 shows the response of the housing when it is exposed to lateral load of 0.6g and a sinusoidal dynamic load with frequency range of 5Hz-10Hz. Harmonic analysis showed that the maximum displacement and von Mises stress occurs at the lower limit of the range which is 5Hz. Based on harmonic analysis the maximum displacement and stress had a magnitude of 0.00029mm and 8.672e+004 N/m^2 respectively.

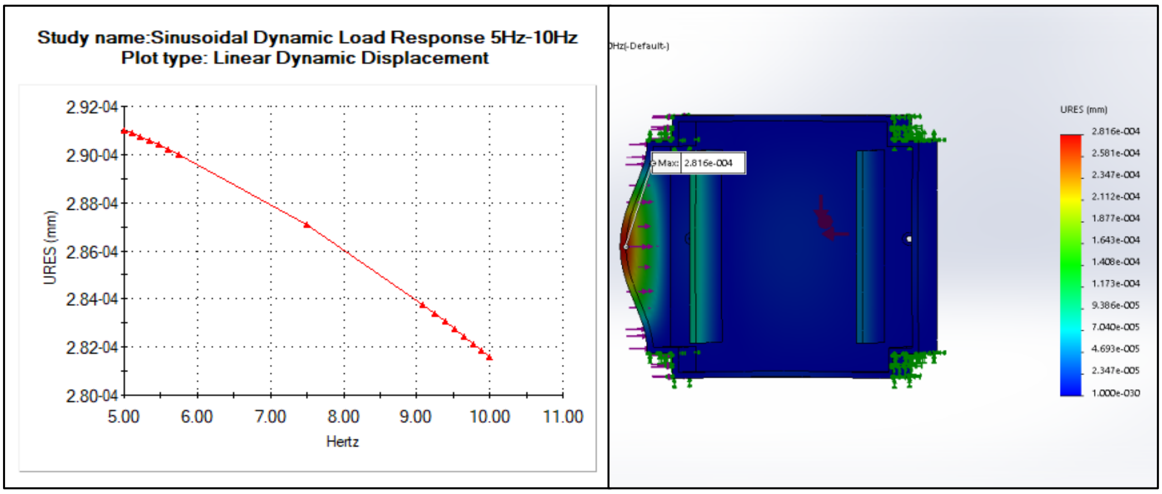

Appendix Figure O-72: Maximum housing displacement under lateral loading and frequency range 5Hz-10Hz

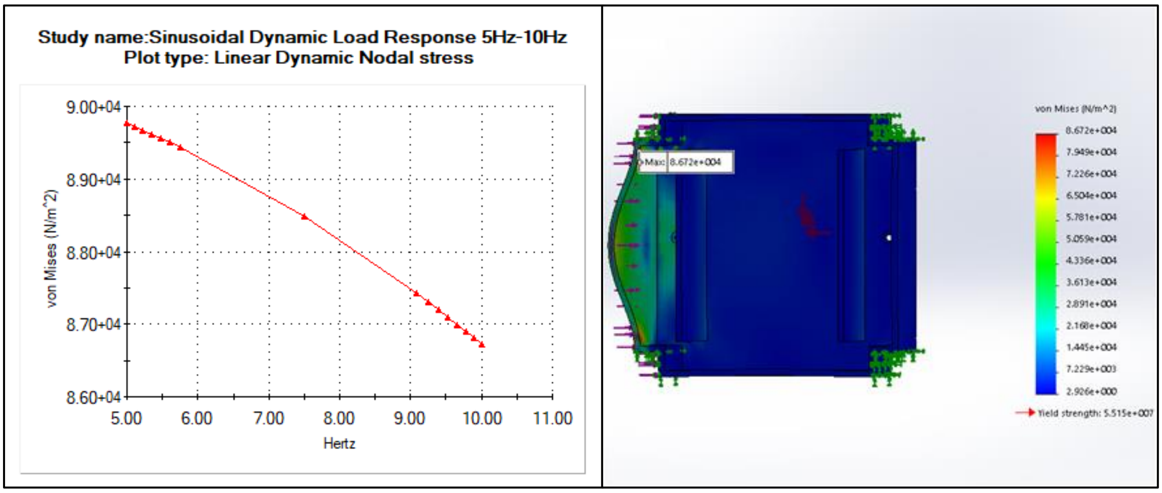

Appendix Figure O-73: von Mises stress on the housing under lateral loading and frequency range 5Hz-10Hz

The housing response under lateral load of 0.7g and sinusoidal dynamic load with frequency range of 10Hz-20Hz are shown in appendix figure O-74 and appendix figure O-75. Based on harmonic analysis the maximum deformation and stress occur at 20Hz with magnitude of 0.000318117 mm and 8.672e+004 N/m^2.

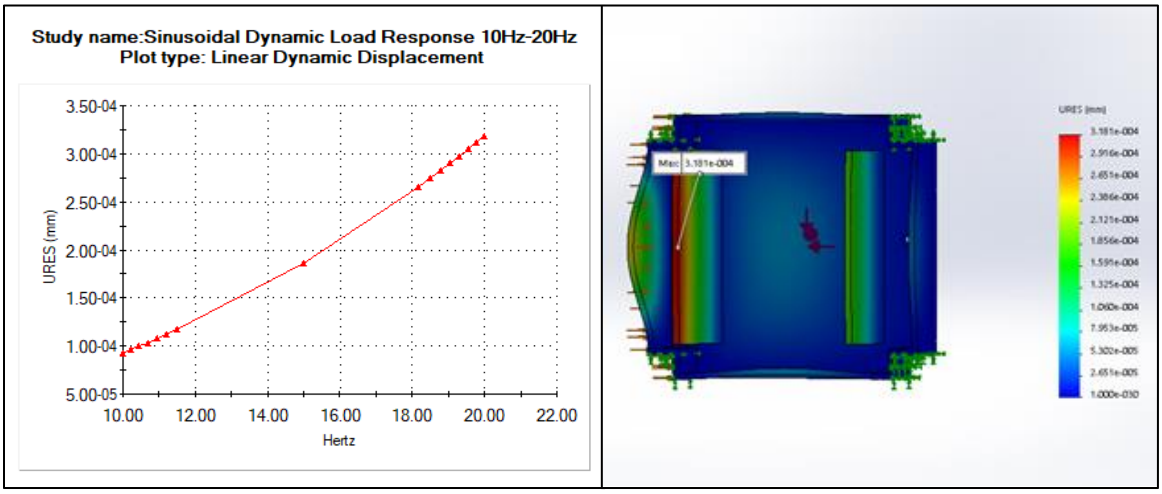

Appendix Figure O-74: Maximum housing displacement under lateral loading and frequency range 10Hz-20Hz

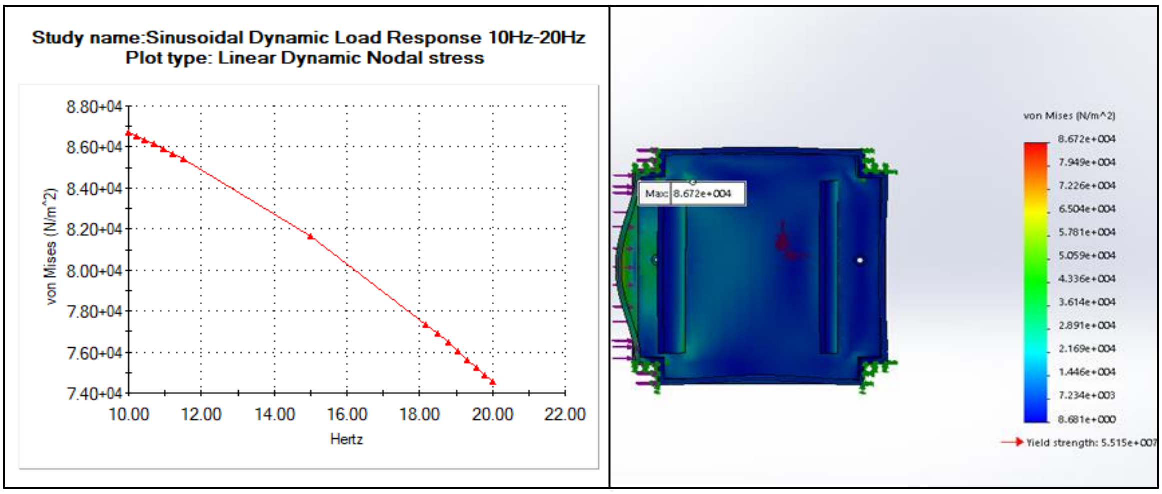

Appendix Figure O-75: von Mises stress on the housing under lateral loading and frequency range 10Hz-20Hz

The housing response under a lateral load of 0.4g and dynamic sinusoidal load with frequency range of 20Hz-30Hz are shown in appendix figure O-76 and appendix figure O-77.Harmonic analysis indicated that the maximum deformation and maximum von Mises stress occur at the upper limit of the range indicated as 40Hz. Based on harmonic analysis the displacement and von Mises stress had a magnitude of 0.000689604 mm and 170893 N/m^2 respectively.

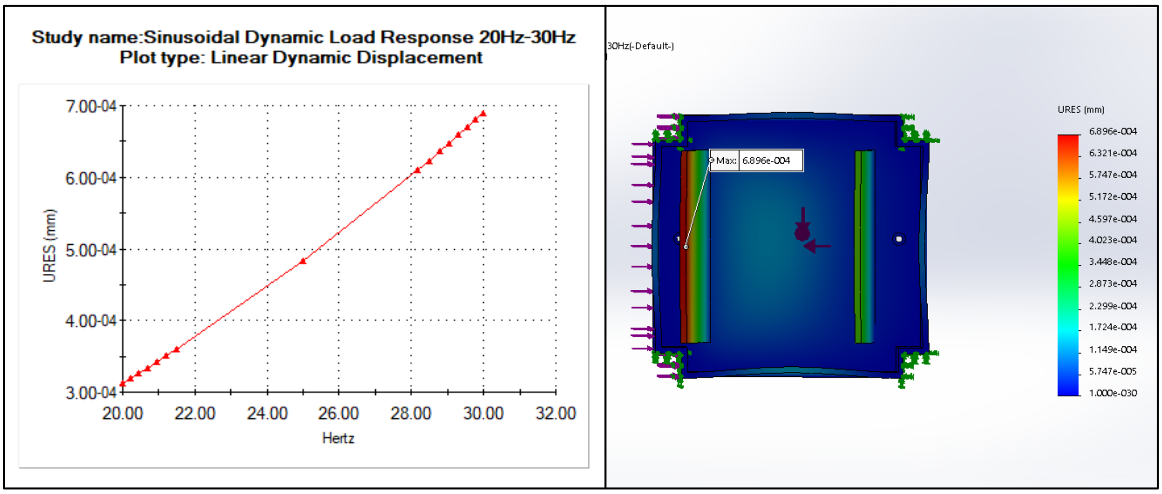

Appendix Figure O-76: Maximum housing displacement under lateral loading and frequency range 20Hz-30Hz

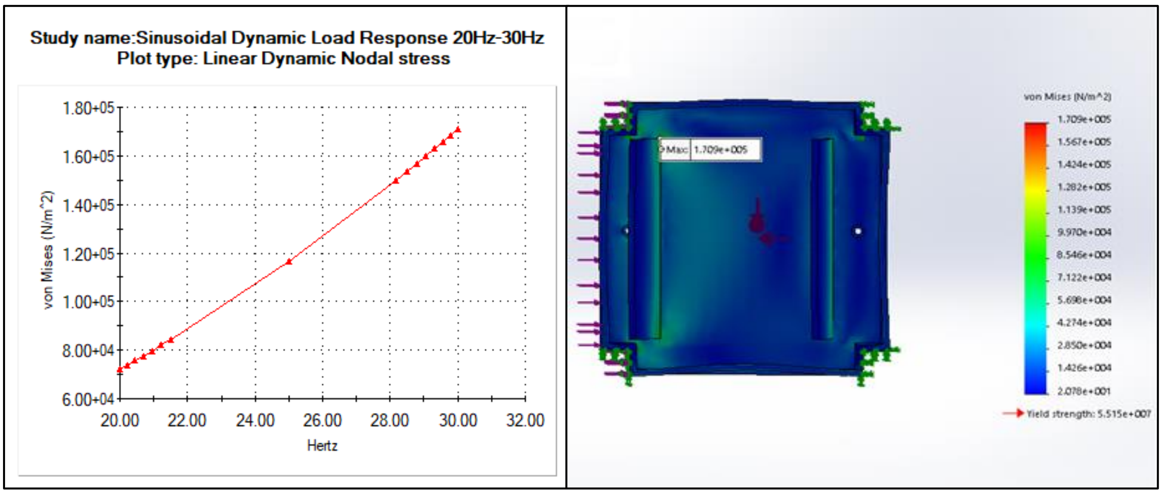

Appendix Figure O-77: von Mises stress on the housing under later loading and frequency range 20Hz-30Hz

The housing response under lateral load of 0.4g and sinusoidal dynamic load with frequency range of 30Hz-40Hz are displayed in appendix figure O-78 and appendix figure O-79. Based on harmonic analysis the maximum deformation and von Mises stress occurs at 40 Hz and was found to be 0.00121718 mm and 309377 N/m^2.

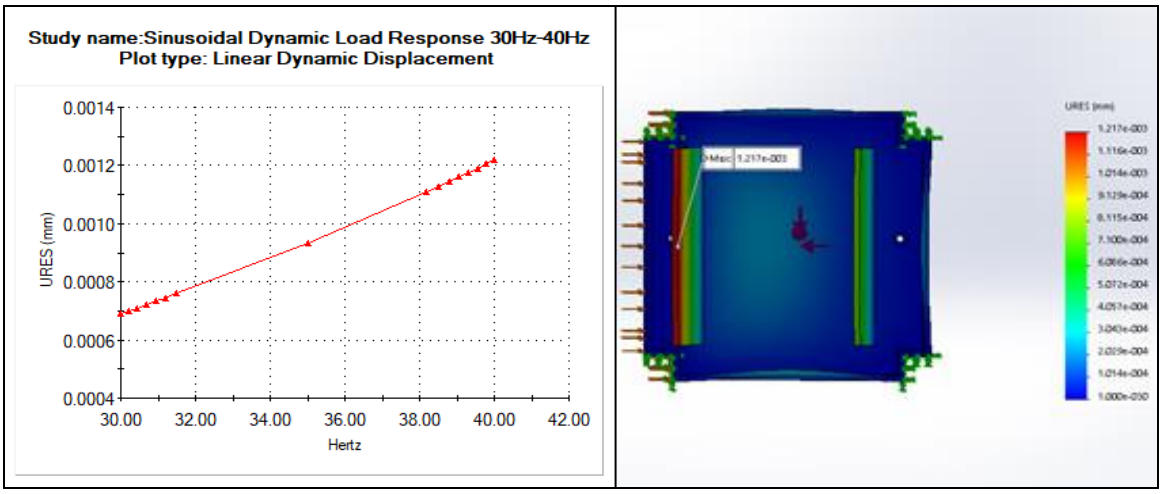

Appendix Figure O-78: Maximum housing displacement under lateral loading and frequency range 30Hz-40Hz

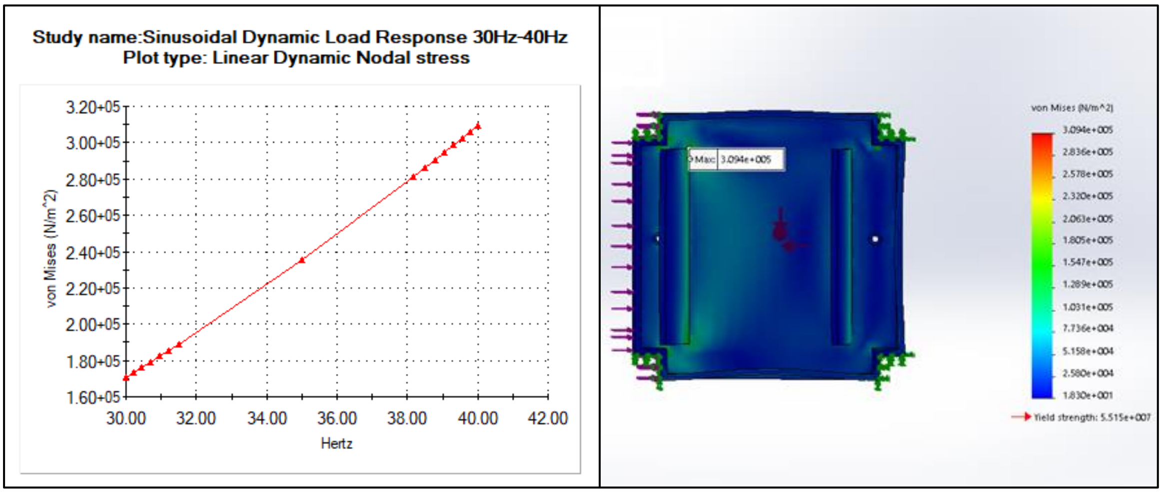

Appendix Figure O-79: von Mises stress of the housing under lateral loading and frequency range 30Hz-40Hz

The housing response under lateral load of 0.3g and sinusoidal dynamic load with frequency range of 40Hz-60Hz are shown in appendix figure O-80 and appendix figure O-81. Based on harmonic analysis the maximum displacement and von Mises stress observed occur at the upper limit of the range at 60Hz. The maximum deformation was 0.00272314 mm and the maximum stress 708479 N/m^2.

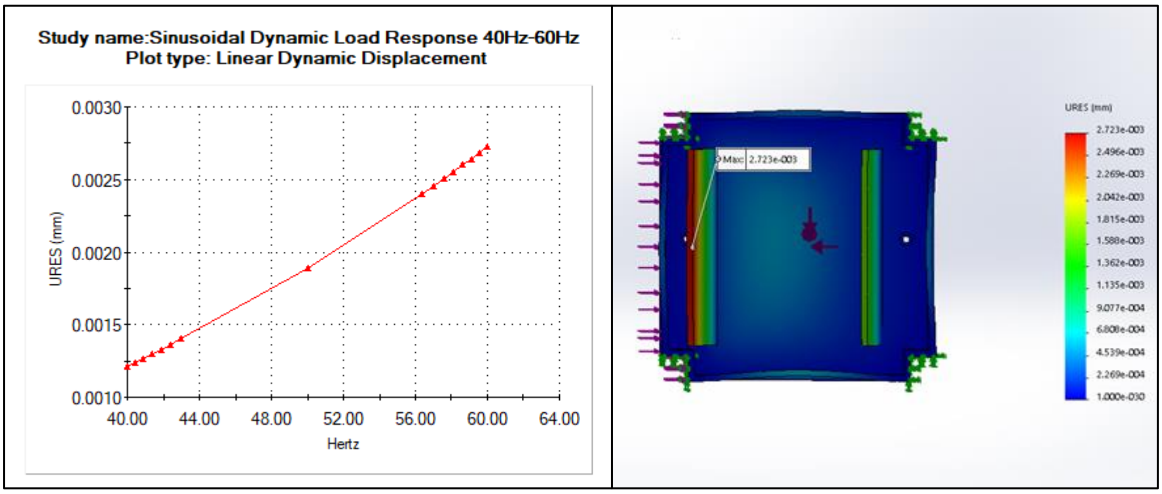

Appendix Figure O-80: Maximum housing displacement under lateral loading and frequency range 40Hz-60Hz

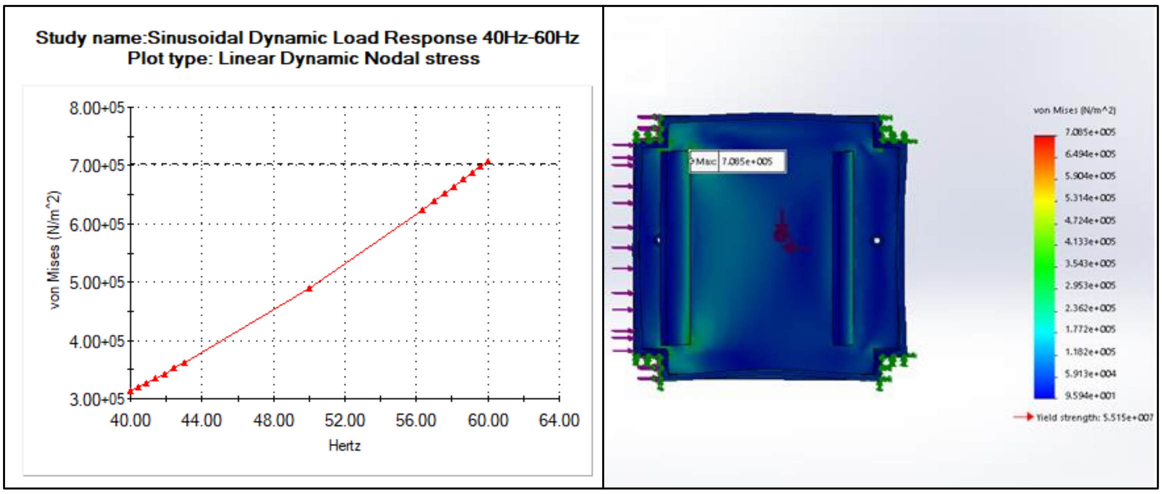

Appendix Figure O-81: von Mises stresses on the housing under lateral loading and frequency range 40Hz-60Hz

The housing response under lateral load 0.3g and sinusoidal dynamic load with frequency range of 60Hz-100Hz are shown in appendix figure O-82 and appendix figure O-82. Harmonic analysis indicated the maximum displacement and von Mises occur at the upper limit of the frequency range given as 100Hz.The maximum displacement and von Mises stress were found to be 0.00759229 mm and 1.98288e+006 N/m^2

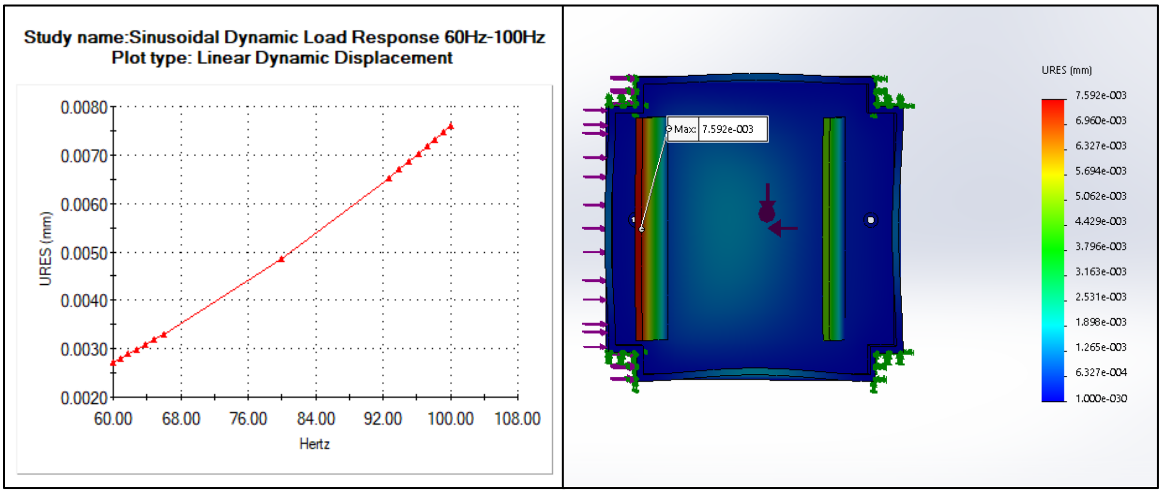

Appendix Figure O-82: Maximum housing displacement under lateral loading and frequency 60Hz-100Hz

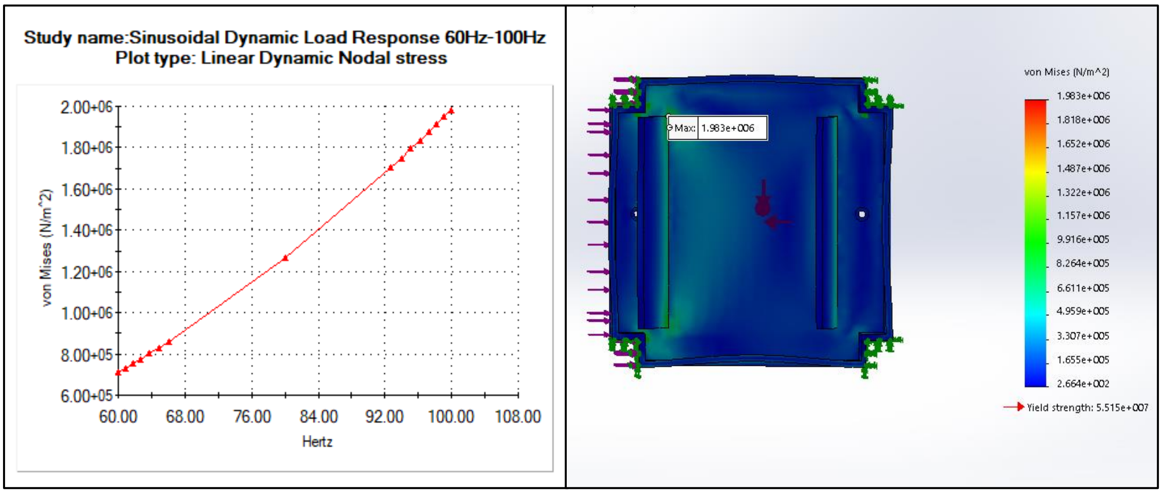

Appendix Figure O-83: von Mises on the housing under lateral loading and frequency range 60Hz-100Hz

Appendix figure O-84 and appendix figure O-85 shows the response of the housing if the first natural frequency where to be reached under lateral loading conditions and a sinusoidal dynamic load frequency range of 950Hz-1070Hz. Based on harmonic analysis the results indicated a displacement of 12 mm at 1066Hz and a von Mises stress of 2.50e+009 N/m^2.From the results shown in the figures below, it is obvious that if this frequency is reached it will result in catastrophic failure of the housing and may cause damage to other satellite components.

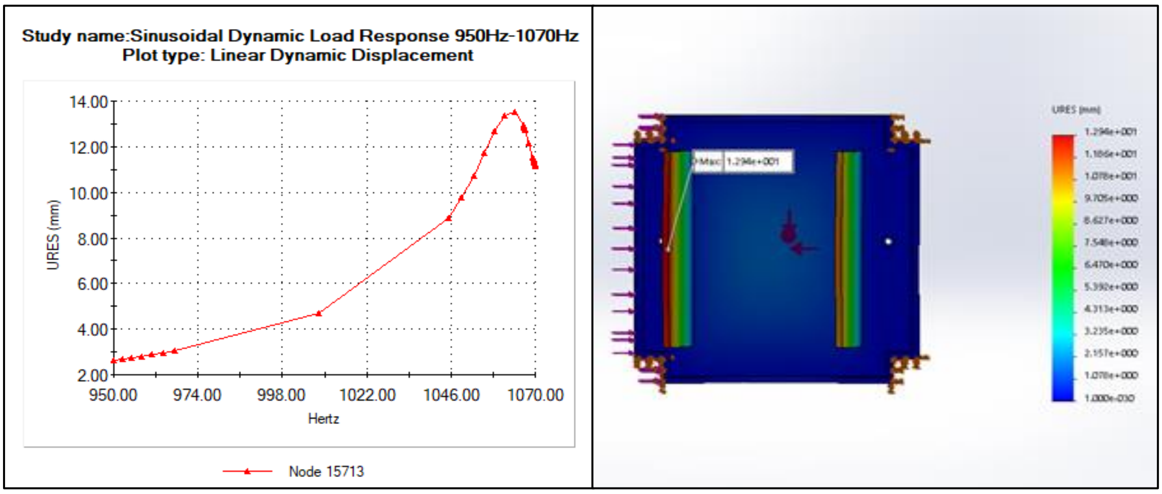

Appendix Figure O-84: Worst-case von Mises stress under lateral loading and frequency range 950Hz-1070Hz

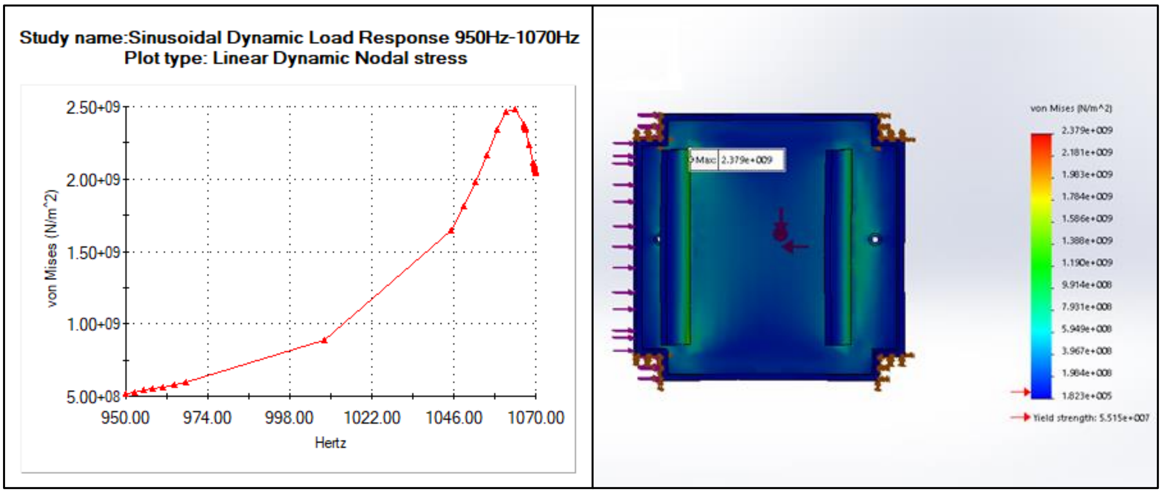

Appendix Figure O-85: Worst-case housing displacement under lateral loading and frequency range 950Hz-1070Hz

9. Sinusoidal Response of Assembled Structure under Longitudinal Loading.

This section illustrates the response of the concept as a complete structure under longitudinal loading and the corresponding sinusoidal frequency ranges. The structure is constrained at the four counters to replicate the integration/fixing point of the structure and CubeSat. The response of the structure under longitudinal loading and sinusoidal dynamic load with frequency range of 1Hz-5Hz are shown in appendix figure O-86 and appendix figure O-87. Harmonic analysis indicated that the maximum deformation and stress occur at the lower limit of the range, which is given as 1Hz. The maximum displacement and stress observed at 1Hz were 4.80e-005 mm and 2.153e+004 N/m^2.

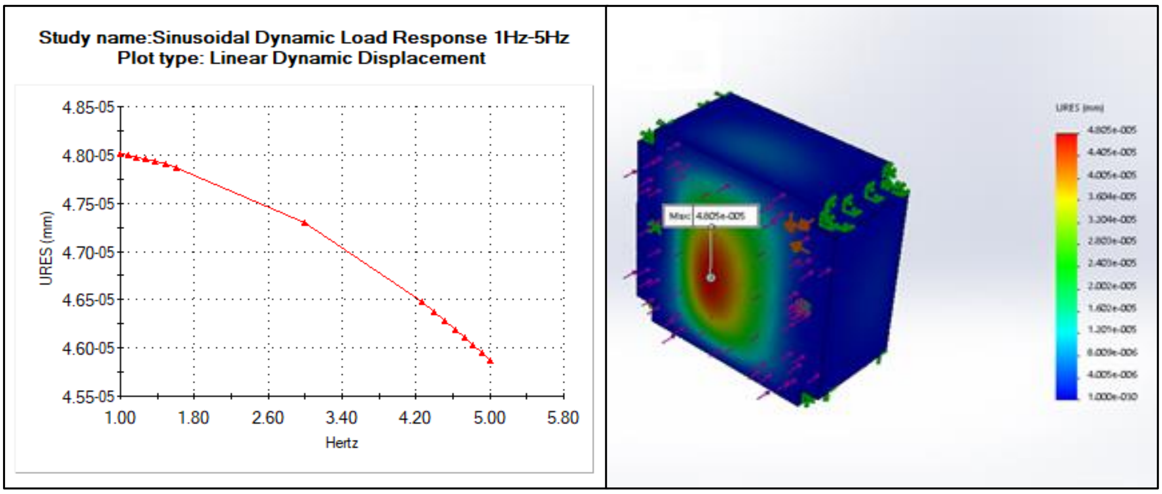

Appendix Figure O-86: Maximum displacement of the structure under longitudinal loading and frequency range 1Hz-5Hz

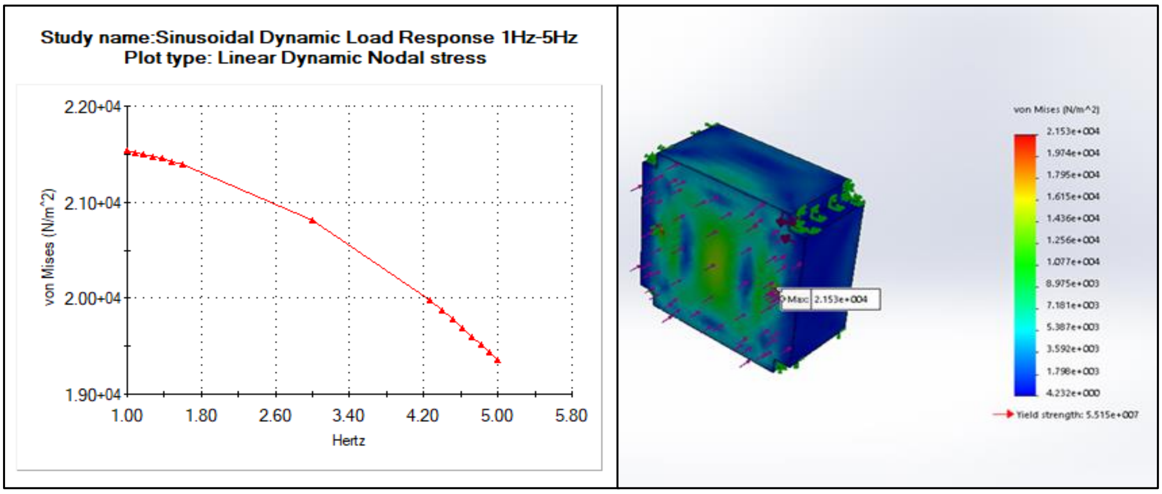

Appendix Figure O-87: von Mises stress on the structure under longitudinal loading and frequency range 1Hz-5Hz

Appendix figure O-88 and appendix figure O-89 shows the results of the structure under a longitudinal load of 0.4g and sinusoidal dynamic load with frequency a range of 5Hz-10Hz. Harmonic analysis indicated that the maximum displacement and von Mises stress occur at the lower end of the range, given as 5Hz. The displacement and von Mises observed at 5Hz were 6.197e-005 mm and 2.65e+004N/m^2

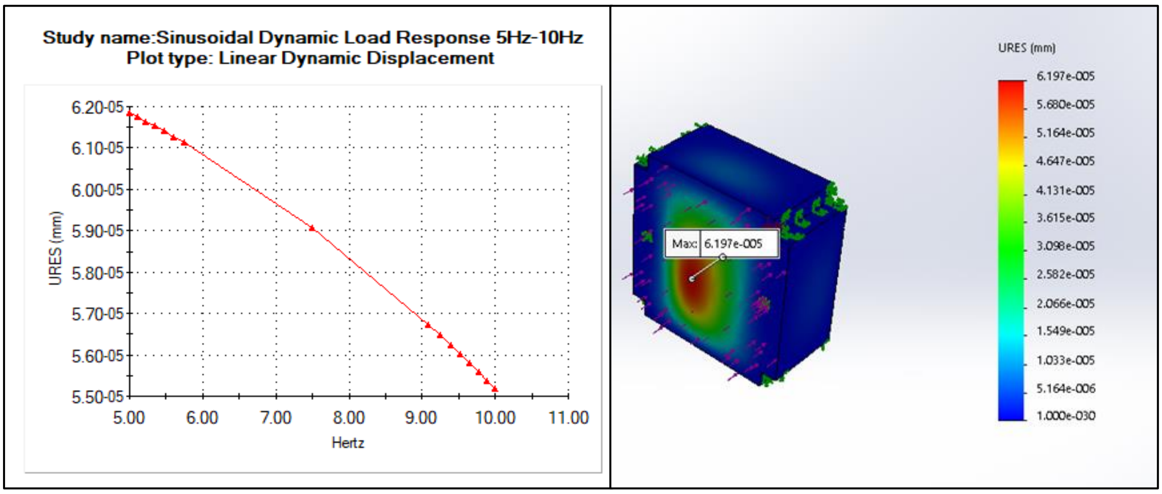

Appendix Figure O-88: Maximum displacement of the structure under longitudinal loading and frequency range 5Hz-10Hz

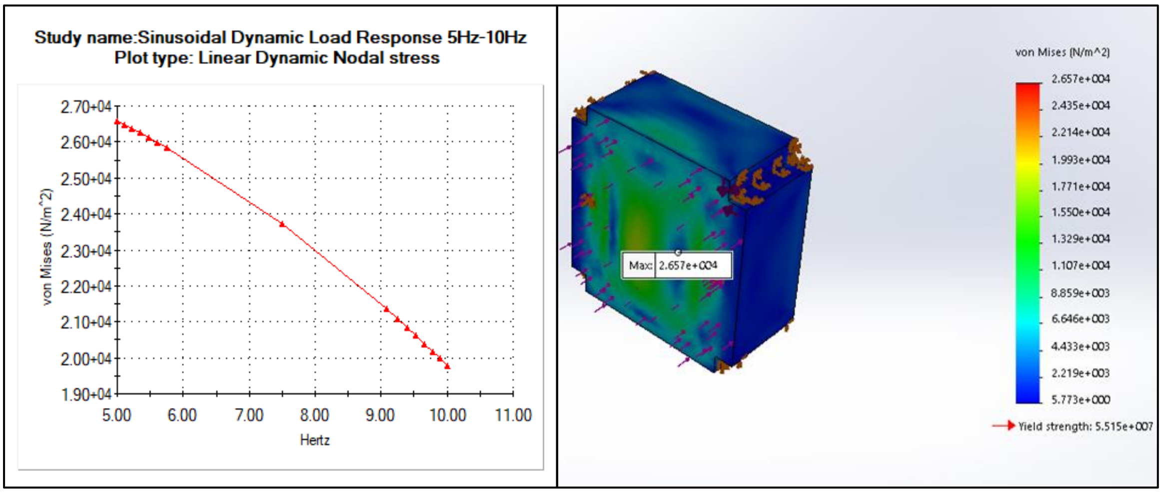

Appendix Figure O-89: von Mises on the structure under longitudinal loading and frequency range 5Hz-10Hz

Appendix figure O-90 and appendix figure O-91 shows the displacement and von Mises stress experienced by the structure when it is exposed to a 0.8g longitudinal load and sinusoidal dynamic loading with frequency range of 10Hz-20Hz. Harmonic analysis indicated that the maximum displacement and stress both occur at the lower limit of the frequency range which is given as 10Hz. The magnitude of the displacement and stress observed was 1.09e-004 mm and 4.015e+004

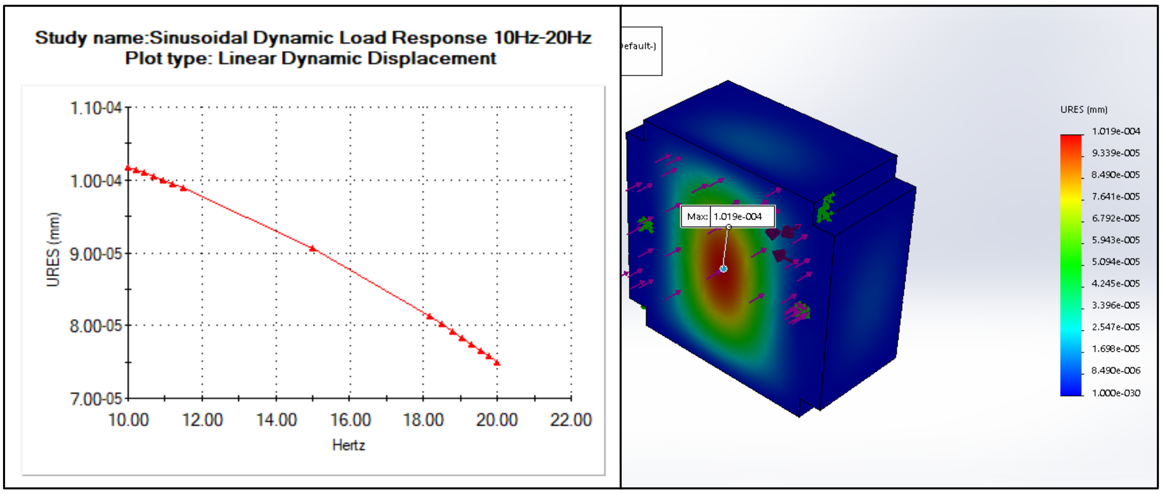

Appendix Figure O-90: Maximum displacement of the structure under longitudinal loading and frequency range 10Hz-20Hz

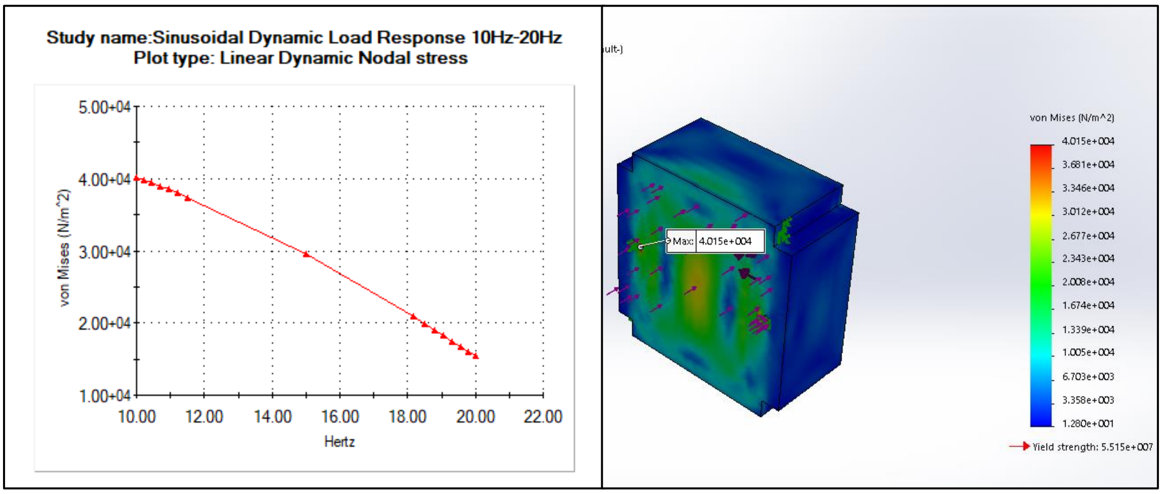

Appendix Figure O-91: von Mises stress on the structure under longitudinal loading and frequency range 10Hz-20Hz

KKK

The response of the structure when it is exposed to a longitudinal load of 0.8g and sinusoidal dynamic load with frequency range of 20Hz-30Hz are shown in appendix figure O-92 and appendix figure O-93. Based on harmonic analysis the maximum displacement observed occurred at the lower limit(20Hz) and had a magnitude of 7.513e-005 mm. Oppositely, the maximum von Mises stress occurred at the upper limit(30Hz) and has a magnitude of 3.61e+004.

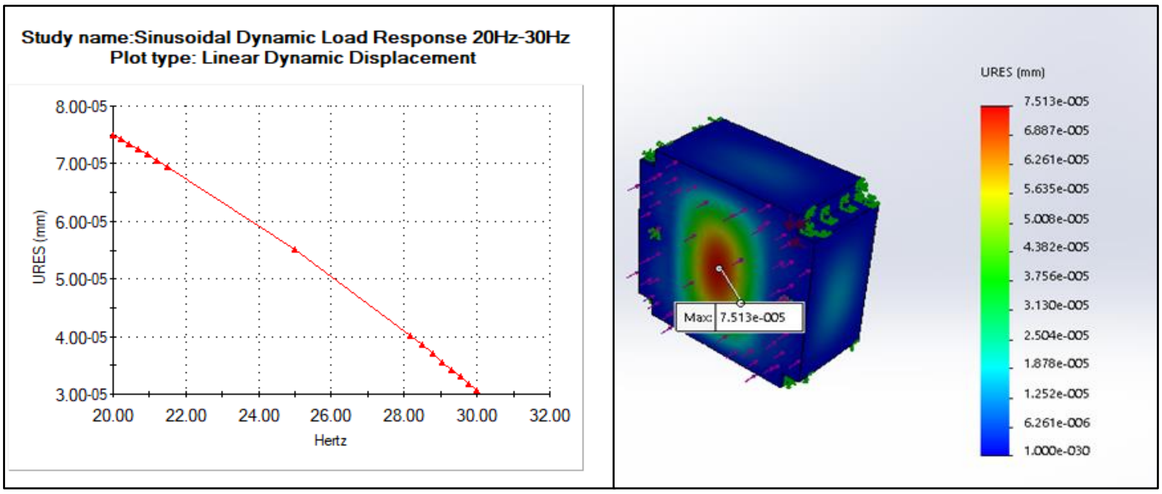

Appendix Figure O-92: Maximum displacement of the structure under longitudinal loading and frequency range 20Hz-30Hz

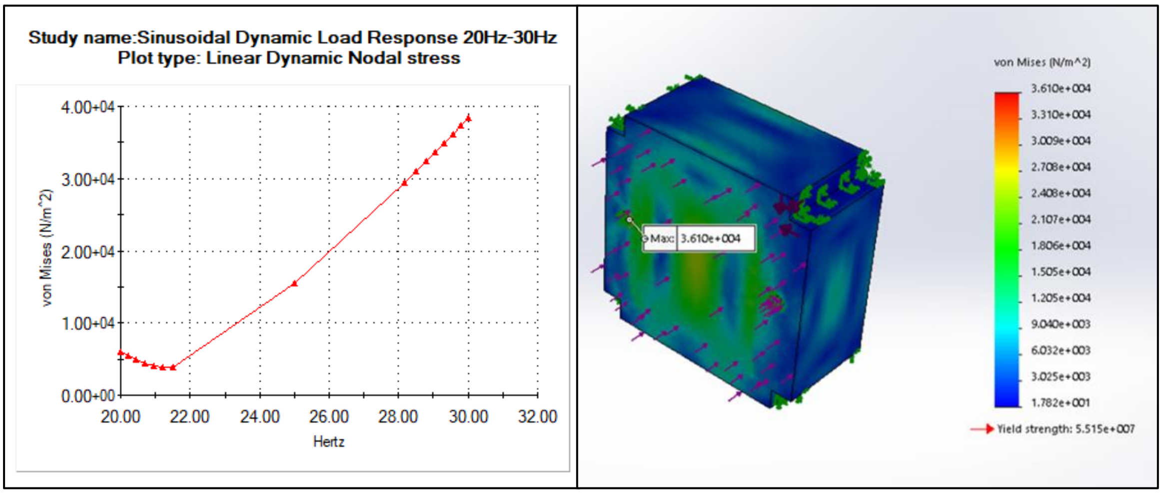

Appendix Figure O-93: von Mises on the structure under longitudinal loading and frequency range 20Hz-30Hz

Appendix figure O-94 and appendix figure O-95 shows the response of the structure when it is exposed to longitudinal load of 0.5g and a sinusoidal dynamic load with a frequency range of 30Hz-40Hz. Harmonic analysis indicated that the maximum deformation and von Mises observed occurred at 40Hz with a magnitude of 1.61e-004 mm and 1.164e+005 N/m^2.

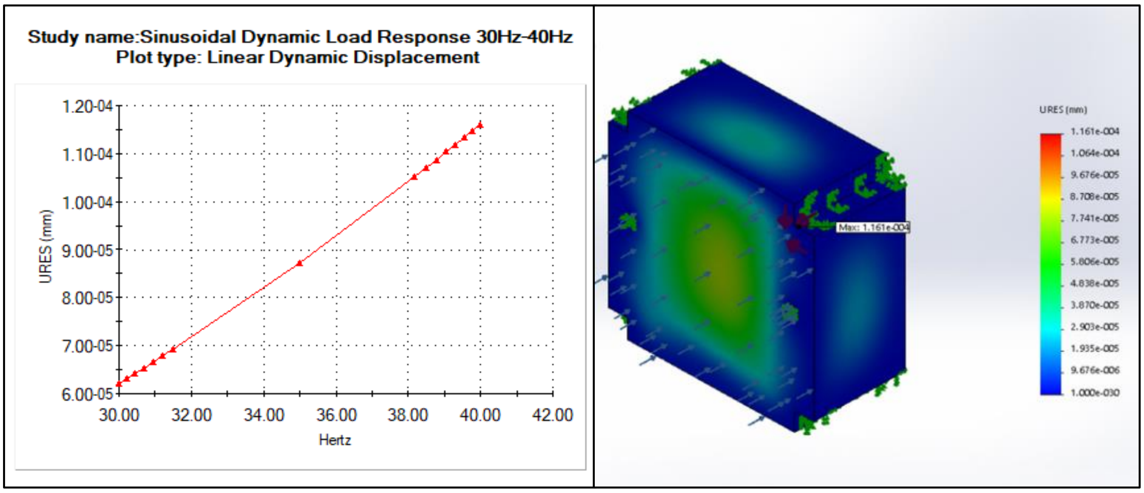

Appendix Figure O-94: Maximum displacement of the structure under longitudinal loading and frequency range 30Hz-40Hz

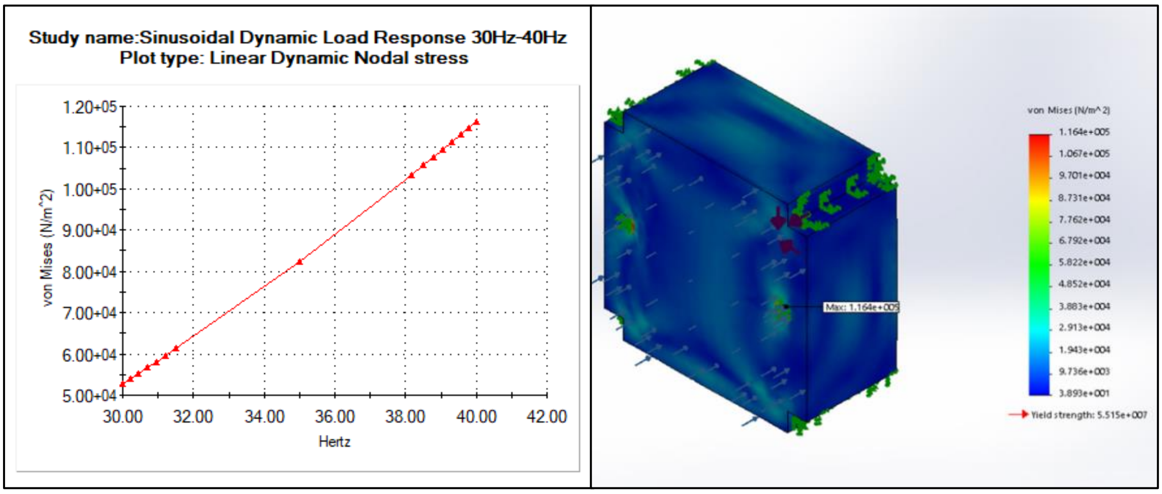

Appendix Figure O-95: von Mises on the structure under longitudinal loading and frequency range 30Hz-40Hz

Appendix figure O-96 and appendix figure O-97 shows the results of the structure under a longitudinal load of 0.5g and a sinusoidal dynamic load with a frequency range of 40Hz-60Hz. Based on harmonic analysis the maximum deformation and von Mises stress both occurred at the upper limit of the range and had the magnitude of 0.000269945 mm and 2.98e+005 N/m^2.

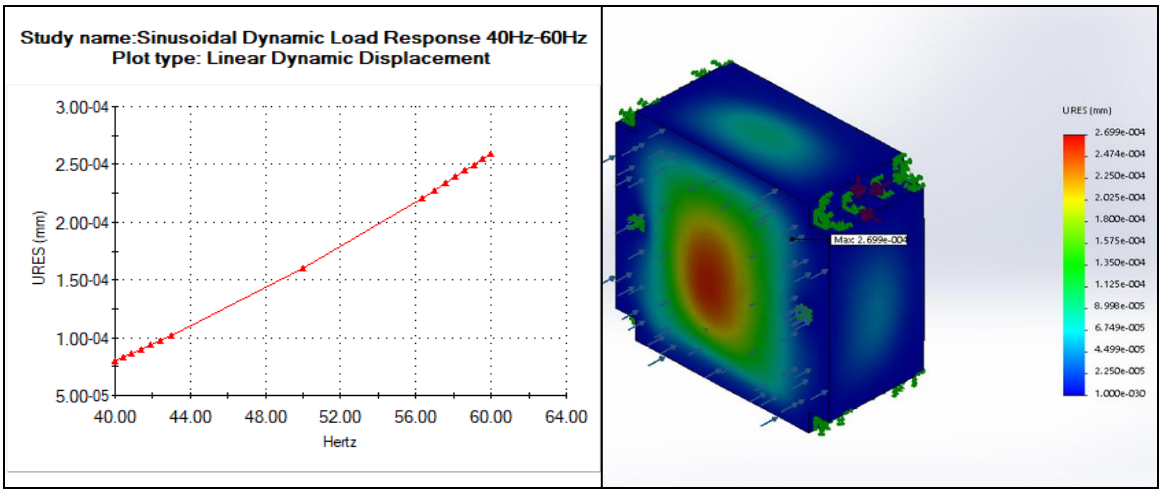

Appendix Figure O-96: Maximum displacement of the structure under longitudinal loading and frequency range 40Hz-60Hz

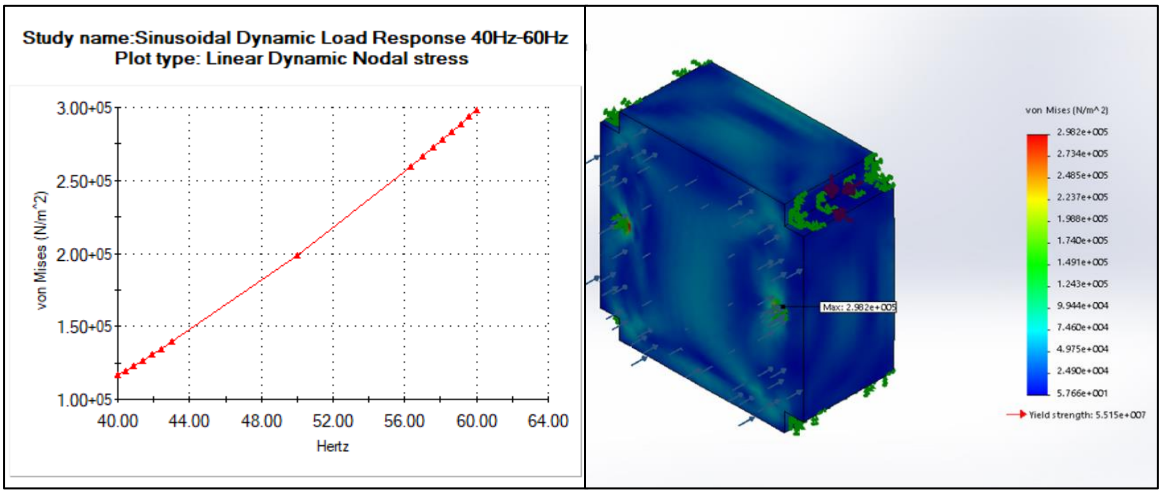

Appendix Figure O-97: von Mises on the structure under longitudinal loading and frequency range 40Hz-60Hz

The response of the structure under a longitudinal load of 0.3g and sinusoidal dynamic load with a frequency range of 60Hz-100Hz are shown in appendix figure O-98 and appendix figure O-99. Based on harmonic analysis the maximum deformation and stress occurred at the upper limit of the range and was found to be 0.000858284 mm and 8.9e+005 N/m^2 respectively.

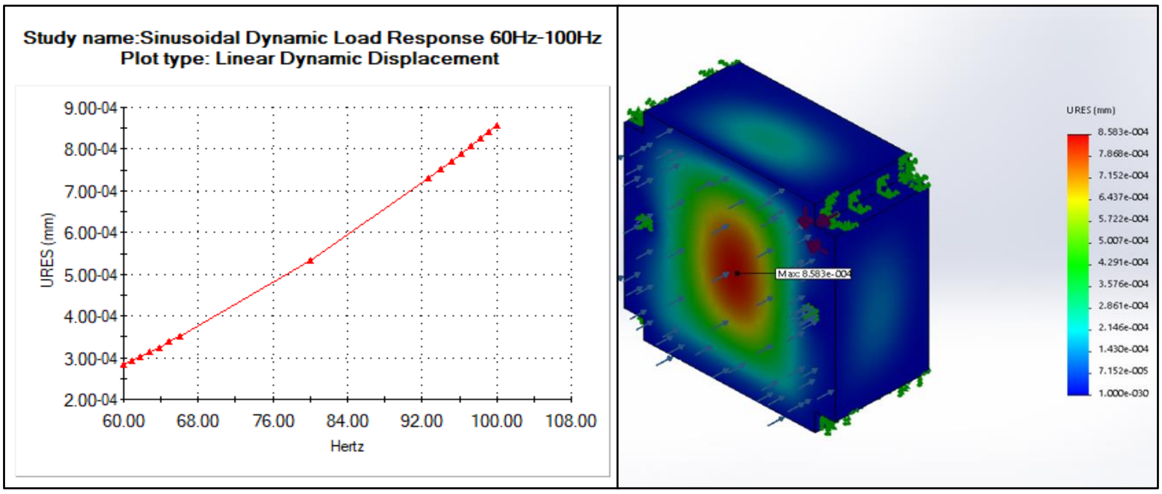

Appendix Figure O-98: Maximum displacement of the structure under longitudinal loading and frequency range 60Hz-100Hz

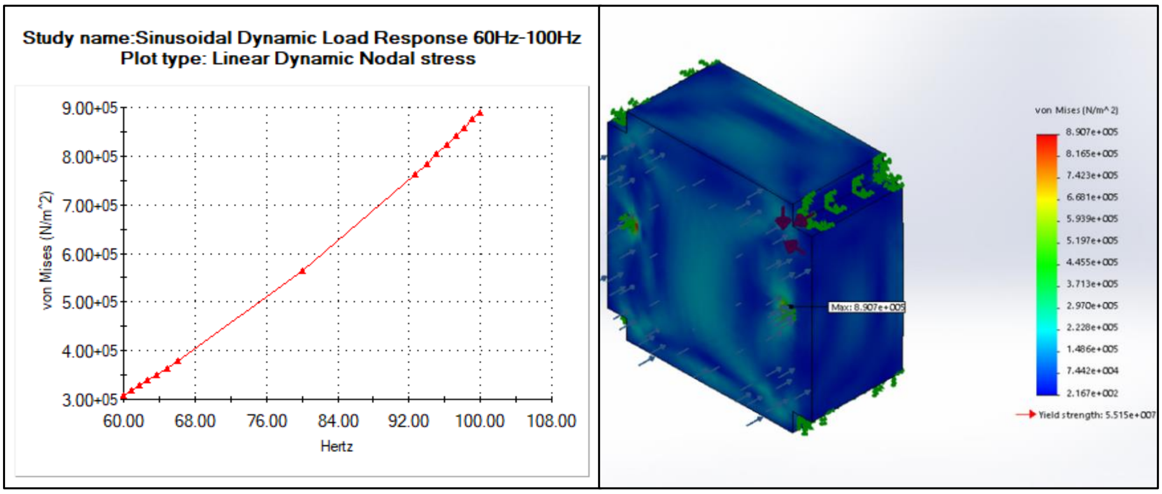

Appendix Figure O-99: von Mises stress on the structure under longitudinal loading and frequency range 60Hz-100Hz

Appendix figure O-100 and appendix figure O-101 shows the response of the structure if the first natural frequency where to be reached under longitudinal loading conditions and a sinusoidal dynamic load frequency range of 3100Hz-3200Hz. Harmonic analysis indicated a displacement of 49.5 mm at 3200Hz and a von Mises stress of 2.89811e+010 N/m^2 .From the results shown in the figures below, it is clear that if this frequency is reached it will result in disastrous failure of the entire structure and will cause damage to other satellite components**.**

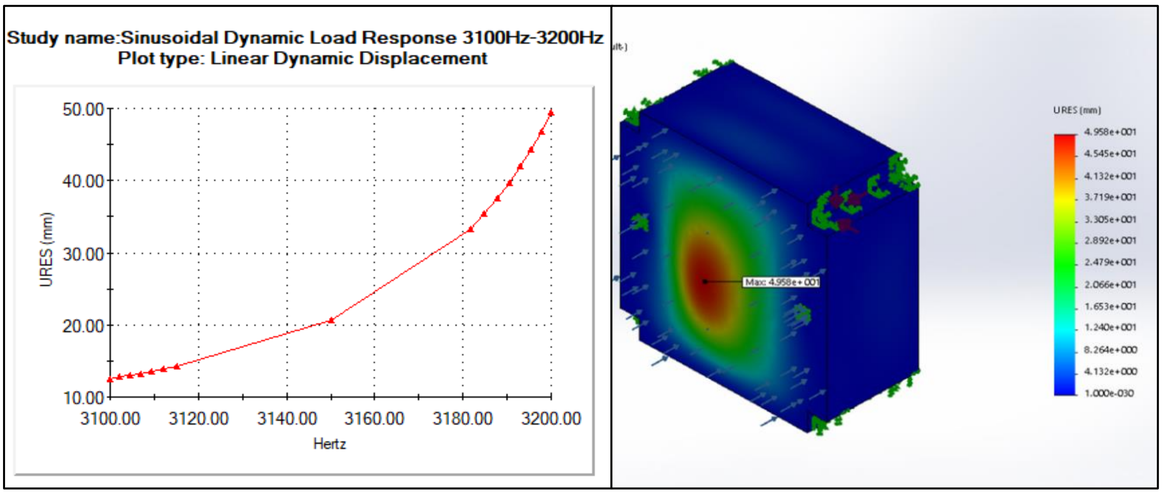

Appendix Figure O-100: Worse-case displacement of the structure under longitudinal loading and frequency range 3100Hz-3200Hz

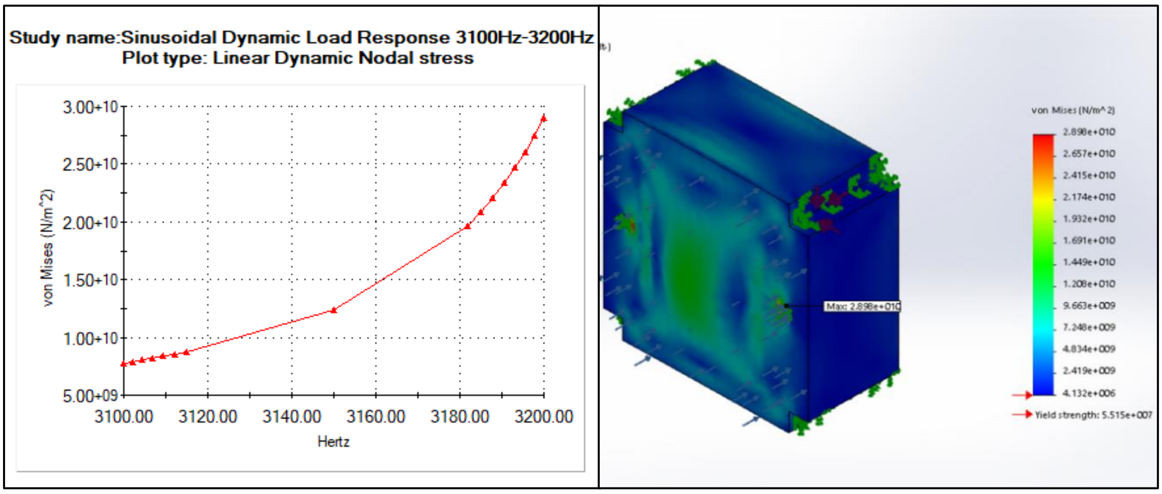

Appendix Figure O-101: Worst-case von Mises stress on the structure under longitudinal loading and frequency range 1300Hz-3200Hz

10. Sinusoidal Response of Structure under Lateral Loading.

The following section shows the results of the assembled structure when it is exposed to various lateral load and sinusoidal dynamic loads with frequencies ranging from 1Hz-100Hz. Appendix figure O-102 and appendix figure O-103 shows the response of the structure when it is exposed to a 0.4g lateral load and sinusoidal dynamic loading with a frequency range of 1H-5Hz. Based on harmonic analysis the maximum deformation and von Mises stress observed occurred at the lower limit(1Hz) of the range with magnitude of 4.80e-005 mm and 2.15e+004 N/m^2.

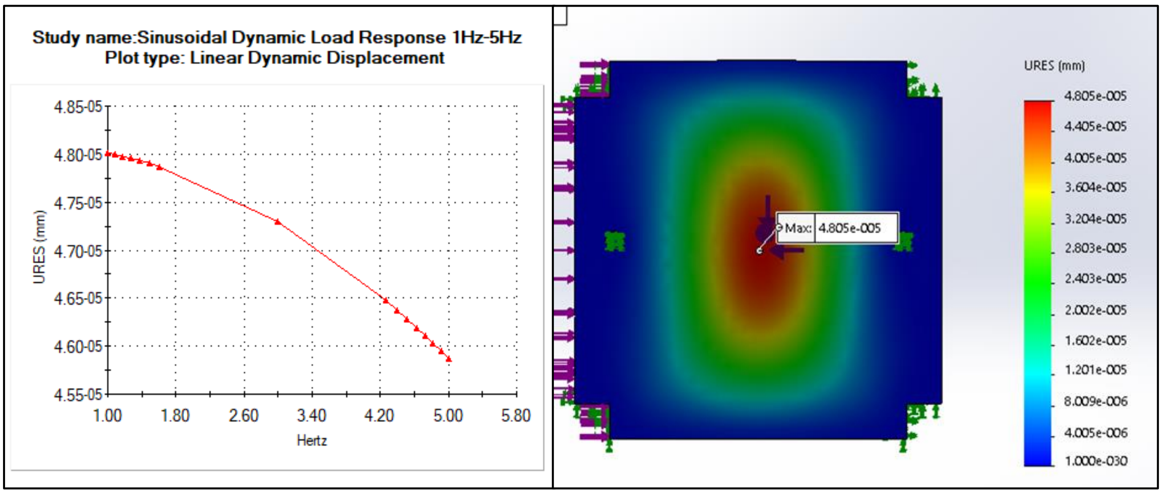

Appendix Figure O-102: Maximum displacement of the structure under lateral loading and frequency range 1Hz-5Hz

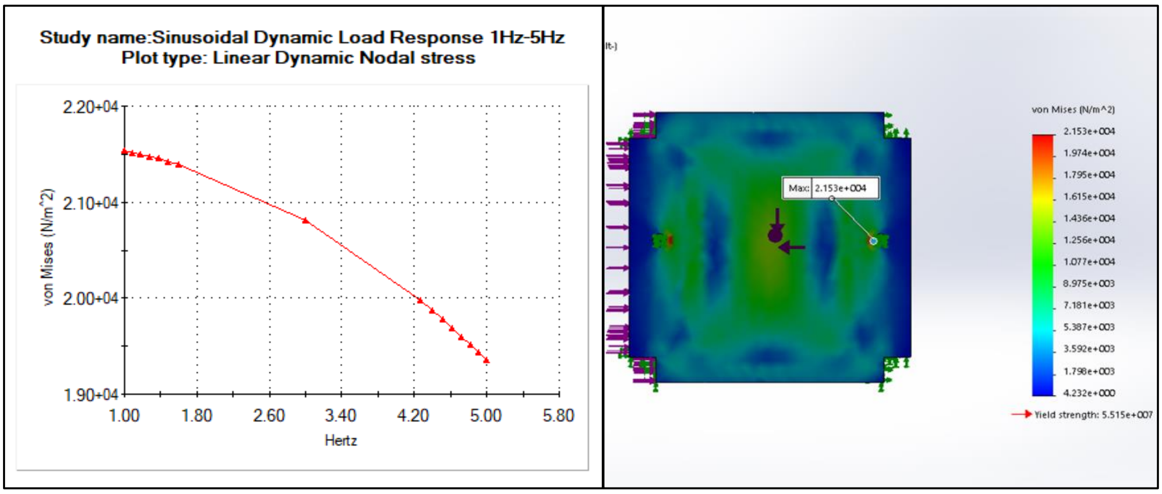

Appendix Figure O-103: von Mises on the structure under lateral loading and frequency range 1Hz-5Hz

The response of the structure when it is exposed to a lateral load of 0.6 g and sinusoidal dynamic load with a frequency range of 5Hz-10Hz are shown in appendix figure O-104 and appendix figure O-105. Harmonic analysis indicated that the maximum deformation and von Mises stresses observed occurred at 5Hz with magnitude 6.19e-005 mm and 2.65e+004 N/m^2 respectively.

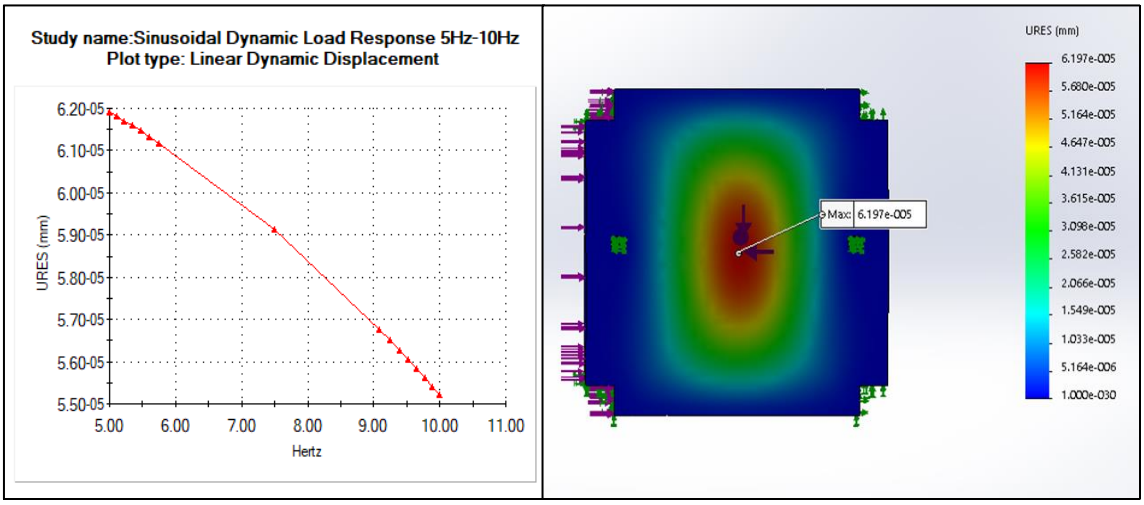

Appendix Figure O-104: Maximum displacement of the structure under lateral loading and frequency range 5Hz-10Hz

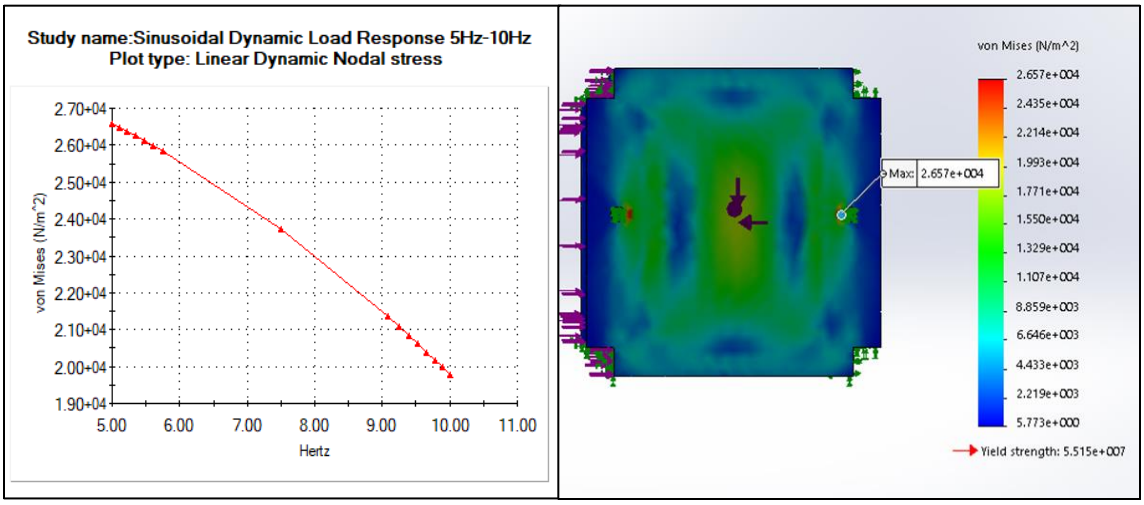

Appendix Figure O-105: von Mises on the structure under lateral loading and frequency range 5Hz-10Hz

Appendix figure O-106 and appendix figure O-107 shows the response of the structure when it is exposed to a lateral load of 0.6g and a sinusoidal dynamic loading with a frequency range of 10Hz-20Hz. Based on harmonic analysis the maximum deformation and von Mises stress occurred at 10Hz and had a magnitude of 1.019e-004 mm and 4.0e+004 N/m^2 respectively.

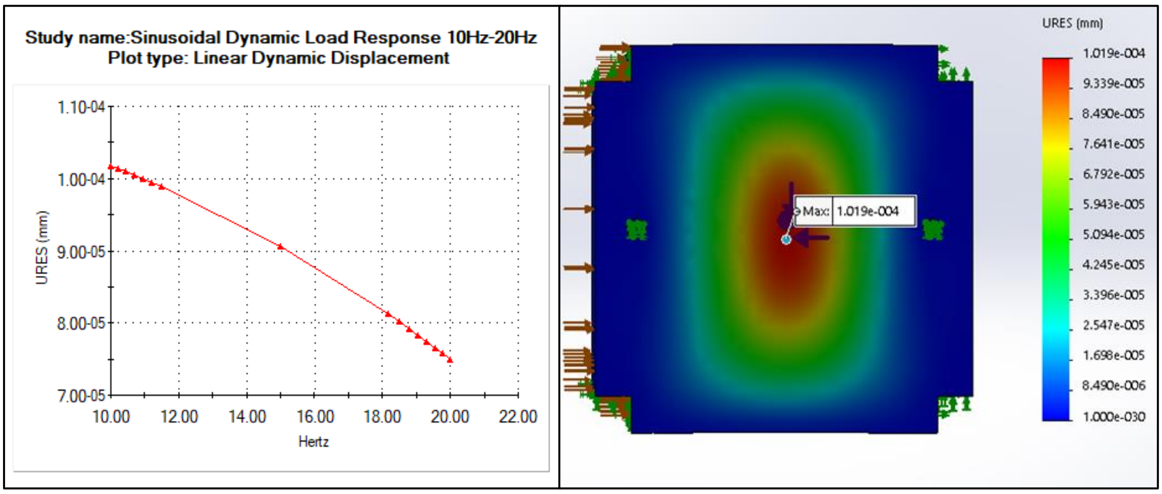

Appendix Figure O-106: Maximum displacement of the structure under lateral loading and frequency range 10Hz-20Hz

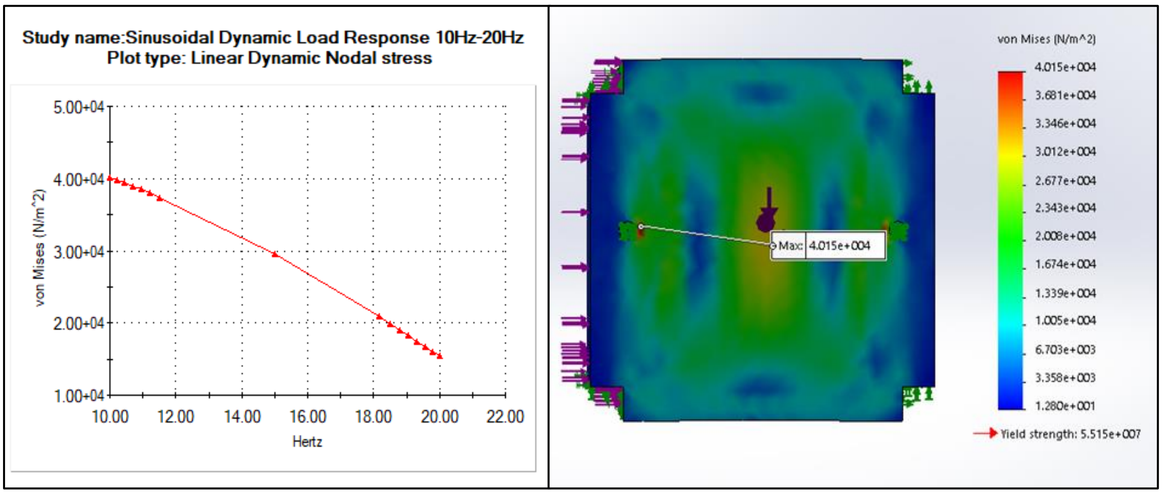

Appendix Figure O-107: von Mises on the structure under lateral loading and frequency range 10Hz-20Hz

The response of the structure when it is exposed to a lateral load of 0.4g and sinusoidal dynamic load with a frequency range of 20Hz-30Hz are shown in appendix figure O-108 and appendix figure O-109 .Harmonic analysis indicated that the maximum deformation occurred at the lower limit of the range (20Hz) and was found to be 7.5e-005 mm. Oppositely, the maximum von Mises stress occurs at the upper limit of the range (30Hz) and had a magnitude of 3.6+004 N/m^2.

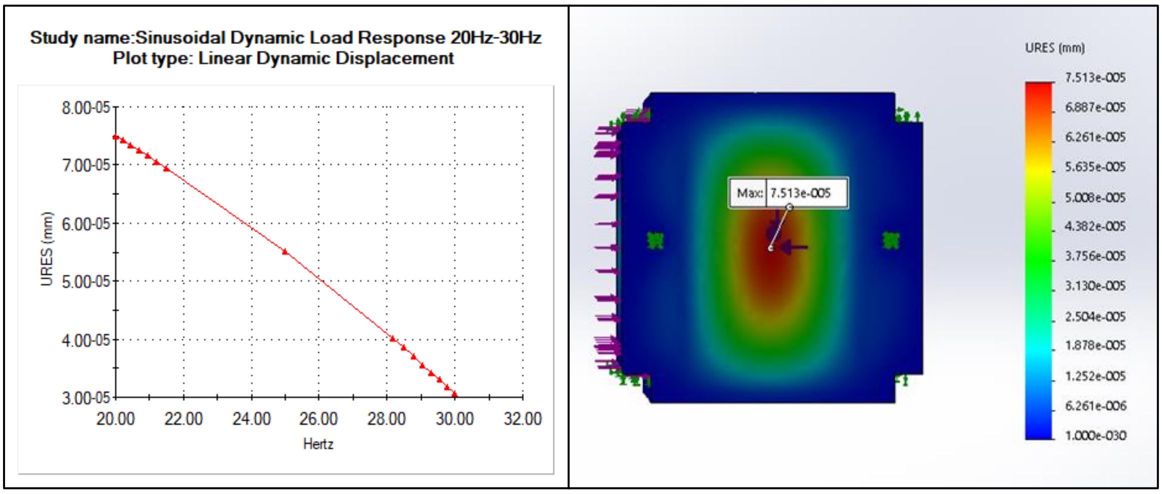

Appendix Figure O-108: Maximum displacement of the structure under lateral loading and frequency range 20Hz-30Hz

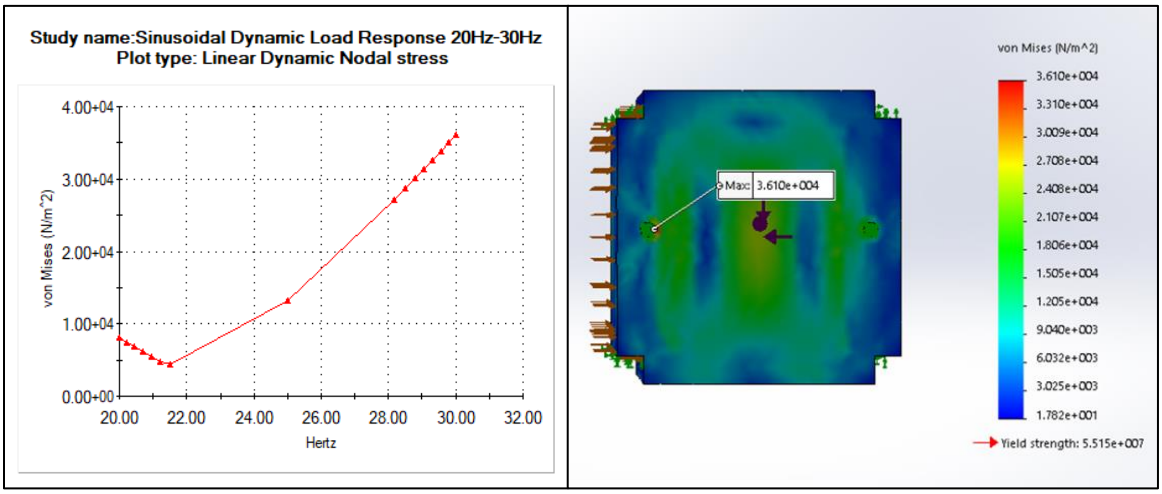

Appendix Figure O-109: von Mises stress on the structure under later loading and frequency range 20Hz-30Hz

The response of the structure under a lateral load of 0.4g and sinusoidal dynamic loading with a frequency range of 30Hz-40Hz are shown in appendix figure O-110 and appendix figure O-111. Harmonic analysis indicated that the maximum deformation and von Mises stress occurred at the upper limit of the range(40Hz) and had a magnitude of 1.47e-004 mm and 1.45e+005 N/m^2.

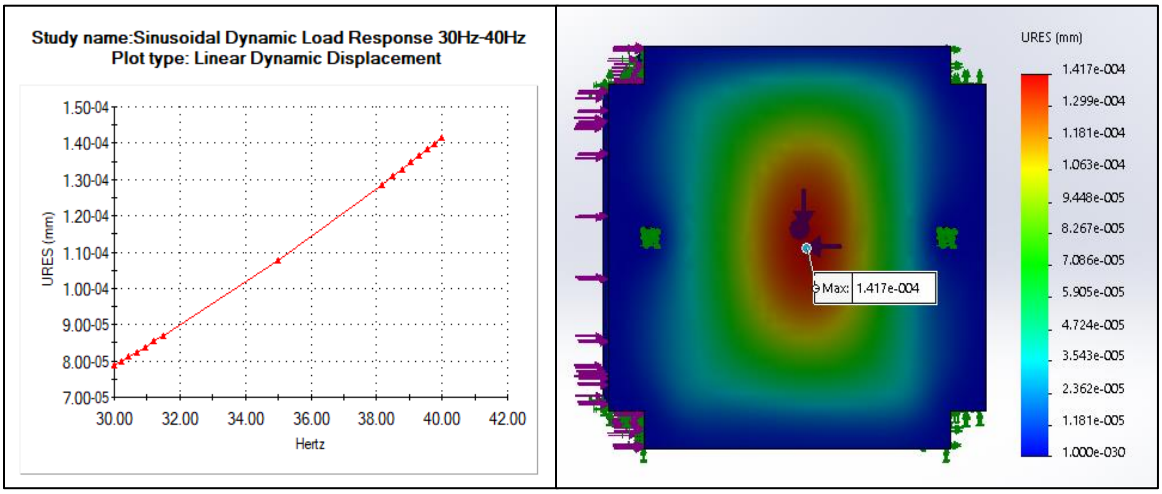

Appendix Figure O-110: Maximum displacement of the structure under lateral loading and frequency range 30Hz-40Hz

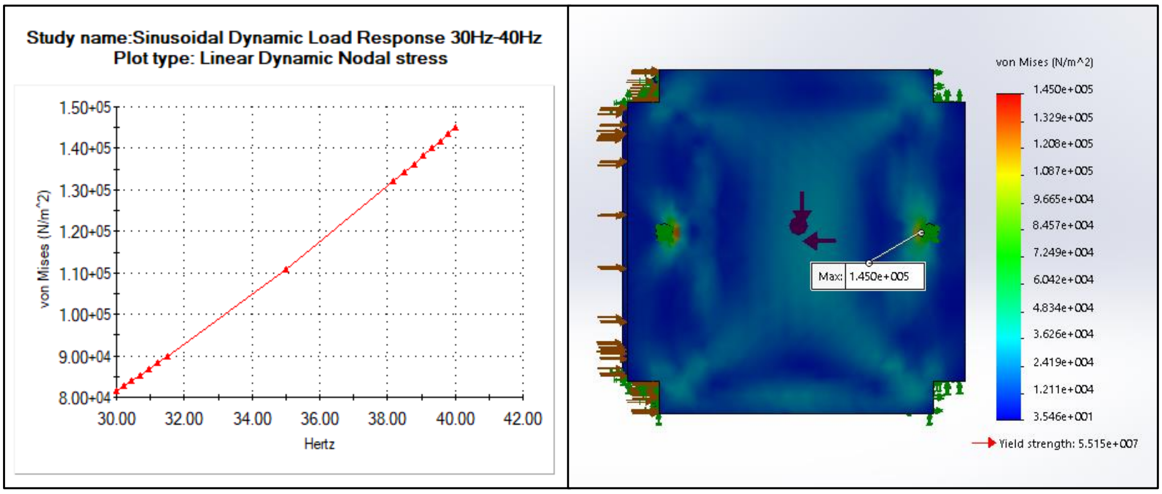

Appendix Figure O-111: von Mises stress on the structure under lateral loading and frequency range 30Hz-40Hz

Appendix figure O-112 and appendix figure O-113 shows the response of the structure when exposed to a lateral load of 0.3g and a sinusoidal dynamic load with a frequency range of 40Hz-60Hz. Harmonic analysis indicated that the maximum displacement and von Mises stress occurred at 60Hz and has a magnitude of 3.215e-004 mm and 3.268e+005 N/m^2.

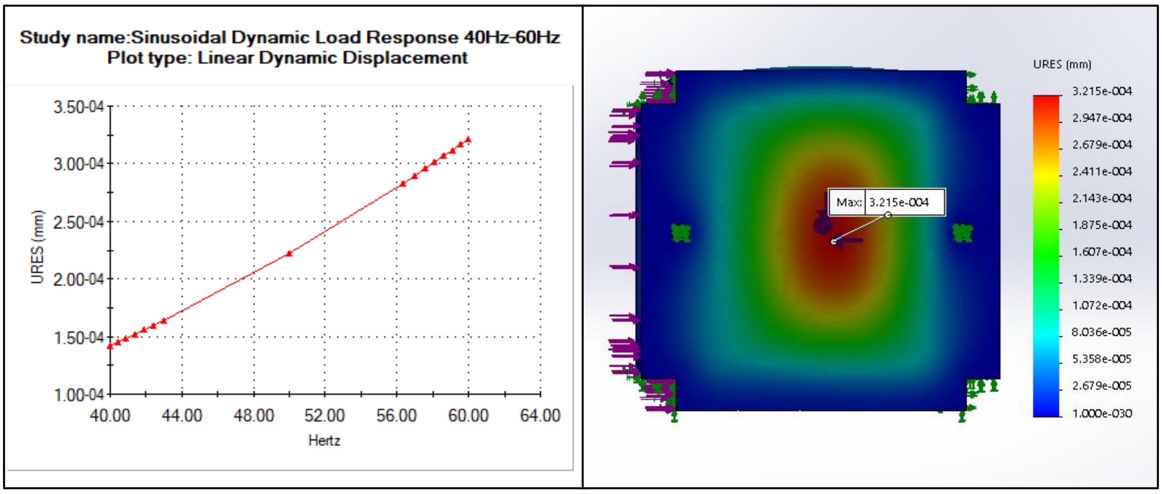

Appendix Figure O-112: Maximum displacement of the structure under lateral loading and frequency range 40Hz-60Hz

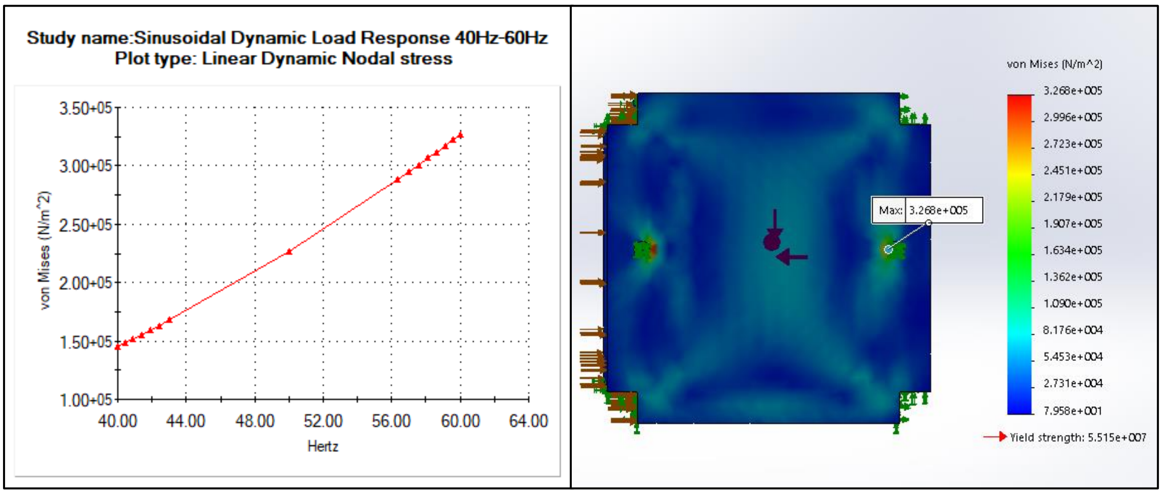

Appendix Figure O-113: von Mises stress on the structure under lateral loading and frequency range 40Hz-60Hz

Appendix figure O-114 and appendix figure O-115 shown the response of the structure when it is exposed to lateral load of 0.3g and a sinusoidal dynamic load with a frequency range of 60Hz-100Hz. Based on harmonic analysis the maximum displacement occurs at 100Hz and was found to be 8.96e-004 mm. The maximum von Mises also occurred at 100Hz and has a magnitude of 9.085e+005 N/m^2.

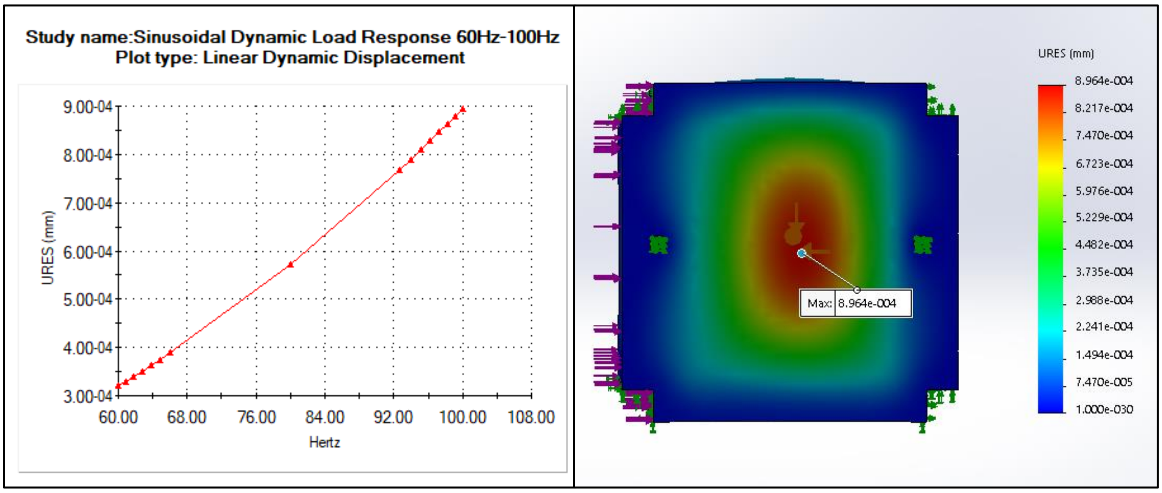

Appendix Figure O-114: Maximum displacement of the structure under lateral loading and frequency range 60Hz-100Hz

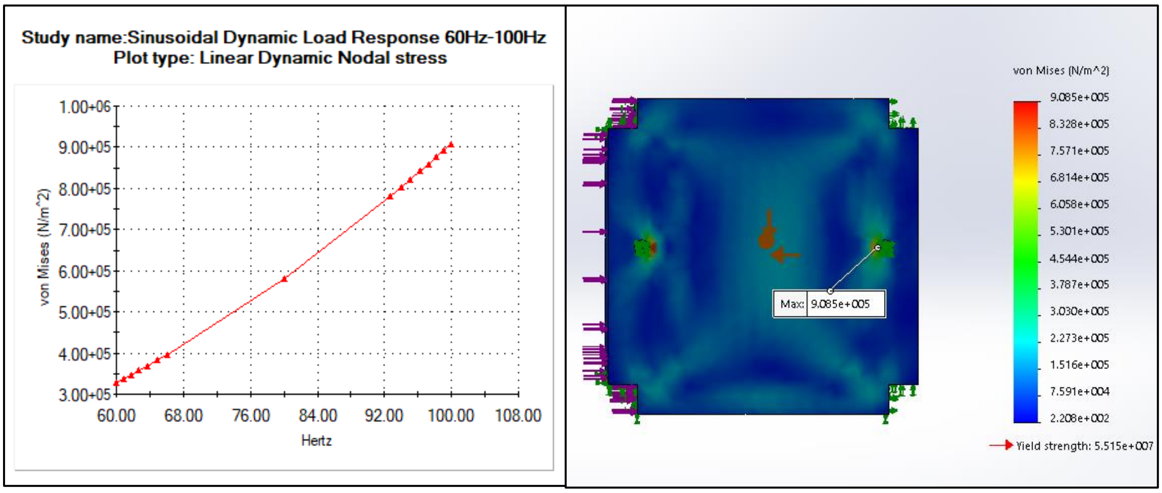

Appendix Figure O-115: von Mises stresses on the structure under lateral loading and frequency range 60Hz-100Hz

Appendix figure O-116 and appendix figure O-117 shows the response of the structure if the first natural frequency the response of the structure if the first natural frequency where to be reached under lateral loading conditions and a sinusoidal frequency range of 3100Hz-3200Hz**.** Based on harmonic analysis a displacement is observed at 3200Hz with a magnitude of 49.5mm. Similarly, the maximum von Missis stress observed at 3200Hz had a magnitude of 2.89841e+010 N/m^2.

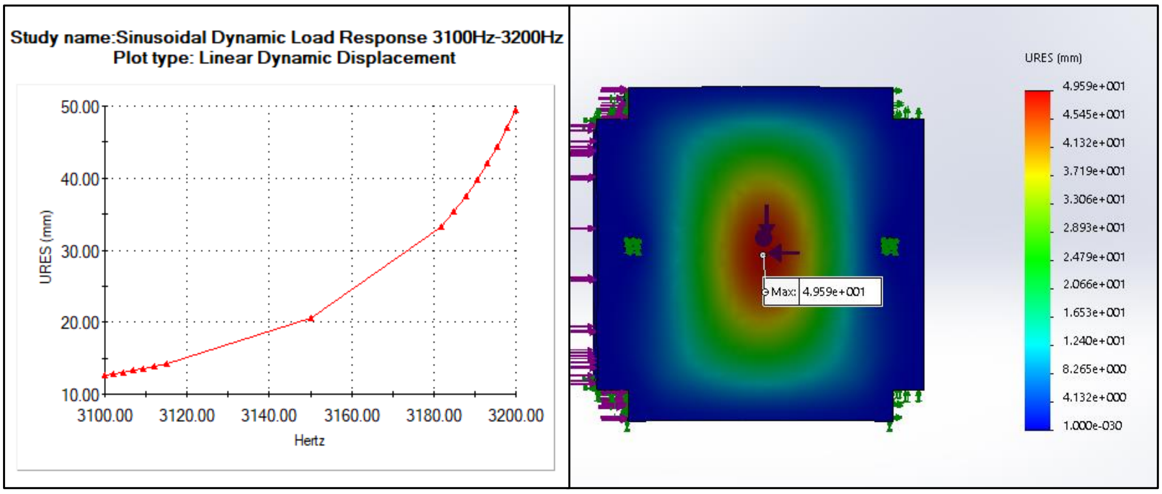

Appendix Figure O-116: Worst-case displacement of the structure under lateral loading and frequency range 3100Hz-3200Hz

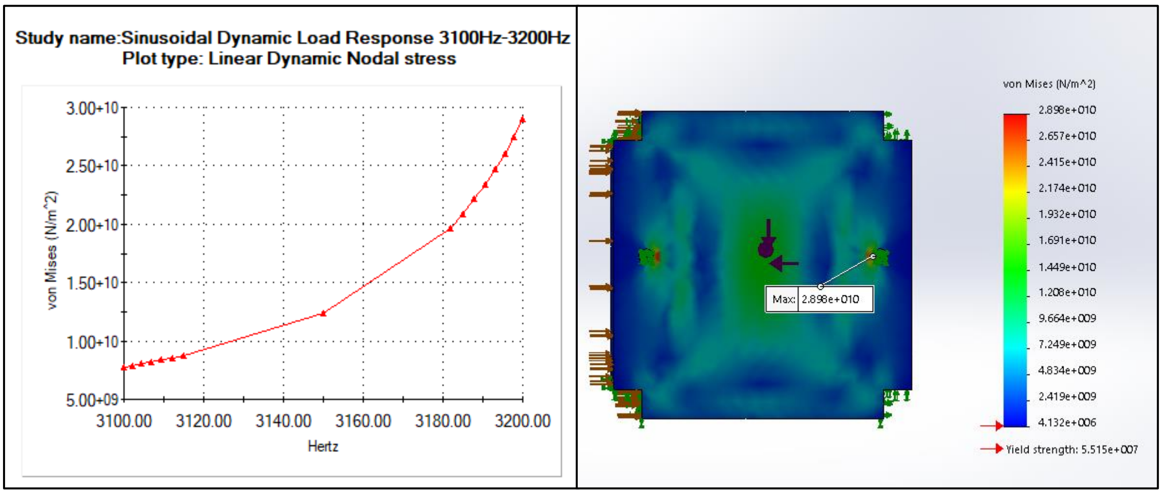

Appendix Figure O-117: : Worst-case von Mises stress on the structure under lateral loading and frequency range 3100Hz-3200Hz